Abschlußbericht
zum BMBF Vorhaben 0326801G
(HTGT-Turbotech Projekt 1.1.2.10)

Entwicklung verbesserter Turbulenzmodelle zur Berechnung der Strömung in Schaufelgittern

von

W. Rodi, N.-H. Cho, E. Papanicolaou, A.W. Date,
V. Michelassi, G. Theodoridis

November 1996

INSTITUT FÜR HYDROMECHANIK
UNIVERSITÄT KARLSRUHE

Abschlußbericht
zum BMBF Vorhaben 0326801G
(HTGT-Turbotech Projekt 1.1.2.10)

Entwicklung verbesserter Turbulenzmodelle zur Berechnung der Strömung in Schaufelgittern

von

W. Rodi, N.-H. Cho, E. Papanicolaou, A.W. Date,
V. Michelassi, G. Theodoridis

November 1996

INSTITUT FÜR HYDROMECHANIK
UNIVERSITÄT KARLSRUHE

INHALTSVERZEICHNIS

Berichtsblatt

1. ISBN oder ISSN	2. Berichtsart Schlußbericht

3a. Titel des Berichts
Entwicklung verbesserter Turbulenzmodelle zur Berechnung der Strömung in Schaufelgittern

3b. Titel der Publikation
siehe beiliegendes Blatt

4a. Autoren des Berichts (Name, Vorname(n))
Rodi, W., Cho, N.-H., Papanicolaou, E., Date, A., Michelassi, V., Theodoridis, G.

4b. Autoren der Publikation (Name, Vorname(n))
siehe beiliegendes Blatt

5. Abschlußdatum des Vorhabens
31.3.1996

6. Veröffentlichungsdatum
November 1996

7. Form der Publikation
Proceedings

8. Durchführende Institution(en) (Name, Adresse)
Institut für Hydromechanik
Universität Karlsruhe
Kaiserstr. 12
76128 Karlsruhe

9. Ber.Nr. Durchführende Insitution

10. Förderkennzeichen *)
0326801G

11a. Seitenzahl Bericht
247

11b. Seitenzahl Publikation

12. Literaturangaben
170

13. Fördernde Institution (Name, Adresse)
Bundesministerium für Bildung, Wissenschaft, Forschung und Technologie (BMBF)

53170 Bonn

14. Tabellen
3

15. Abbildungen
136

16. Zusätzliche Angaben

17. Vorgelegt bei (Titel, Ort, Datum)

18. Kurzfassung

Die Berechnung der reibungsbehafteten Strömung in Schaufelgittern als Grundlage für eine optimale Gitterauslegung erfordert ein Turbulenzmodell, das die wichtigsten, zu den Verlusten beitragenden Turbulenzphänomene zu beschreiben vermag. Bei Vorhabenbeginn existierende Modelle hatten Schwierigkeiten mit dem laminar-turbulenten Umschlag und beim Auftreten größerer Ablösezonen; es war auch unklar, in wieweit sie bei stark dreidimensionalen Situationen mit Sekundärströmung geeignet waren. Ziel des Vorhabens war die Entwicklung und das Testen verbesserter Turbulenzmodelle. Dazu wurde das Ausgangs-k-ε-Modell mit Wandfunktionen zu einem Zweischichtenmodell erweitert, welches die wandnahe viskose Unterschicht mit einem Eingleichungsmodell auflöst. Diesem wurden empirische Umschlagmodelle beigefügt. Das Ausgangs-k-ε-Modell sowie die verbesserten Modelle wurden an grundlegenden Strömungen sowie an verschiedenen 2D und 3D Gitterströmungen getestet. Das Ausgangs-k-ε-Modell kann die Kernströmung und Druckverteilung in vielen Fällen schon mit akzeptabler Genauigkeit berechnen, während für die Simulierung der Grenzschicht bei Auftreten von Umschlag oder Relaminarisierung unbedingt das Zweischichtenmodell gebraucht wird. Dieses gibt auch deutlich bessere Ergebnisse beim Vorliegen größerer Ablösezonen. Für das Austesten mußte das vorhandene Finite-Volumen Verfahren stark erweitert werden; es steht jetzt ein leistungsfähiges Verfahren für alle Geschwindigkeitsbereiche zur Verfügung.

19. Schlagwörter
Schaufelgitterströmung, Reibungseinflüsse, numerische Rechnungen, Turbulenzmodelle, Finite-Volumen Verfahren, Grenzschichten, Sekundärströmungen, laminar-turbulenter Umschlag

20. Verlag	21. Preis

*) Auf das Förderkennzeichen des BMBF soll auch in der Veröffentlichung hingewiesen werden.

Document Control Sheet

1. ISBN or ISSN	2. Type of Report Final Report

3a. Report Title

Development of improved turbulence models for calculating the flow through cascades

3b. Title of Publication

see separate sheet

4a. Author(s) of the Report (Family Name, First Name(s))	5.End of Project
Rodi, W., Cho, N.-H., Papanicolaou, E., Date, A., Michelassi, V., Theodoridis, G.	31/3/1996
4b. Author(s) of the Publication (Family Name, First Name(s))	6. Publication Date
see separate sheet	November 1996
	7. Form of Publication
	Proceedings
8. Performing Organization(s) (Name, Address)	9. Originator's Report No.
Institut für Hydromechanik Universität Karlsruhe Kaiserstr. 12 76128 Karlsruhe	
	10. Reference No.
	0326801G
	11a. No. of Pages Report
	247
	11b. No. of Pages Publication
13. Sponsoring Agency (Name, Address)	12. No. of References
Bundesministerium für Bildung, Wissenschaft, Forschung und Technologie (BMBF)	170
	14. No. of Tables
	3
53170 Bonn	15. No. of Figures
	136

16. Supplementary Notes

17. Presented at (Title, Place, Date)

18. Abstract

The calculation of viscous flow in turbine cascades for optimising the cascade design requires a turbulence model which allows to describe the most important turbulence phenomena contributing to the losses. The models that existed at the beginning of the project had difficulties with the laminar-turbulent transition and when larger separation zones occurred; it was also unclear how suitable these models were for strongly three-dimensional situations with secondary flow. The goal of the project was the development and the testing of improved turbulence models. For this, the existing k-ε model with wall functions was extended to a two-layer model, which resolves the viscous sublayer with a one-equation model. Empirical transition models were added to this. The basic k-ε model is able to calculate the core flow and the pressure distribution in many cases with acceptable accuracy, while in cases with transition or relaminarisation the boundary layer can be simulated well only with the two-layer model. This also yields significantly better results in situations with larger separation zones. For the test calculations, the availabe finite-volume method had to be extended significantly; a powerful method is now available for all velocity ranges.

19.Keywords
turbine cascade flow, viscous effects, numerical calculations, turbulence models, finite-volume procedures, boundary layers, secondary flow,transition

20. Publisher	21. Price

Anlage zum Berichtsblatt/Appendix to document control sheet:

Angaben zu Publikationen/Information on Publications

1. Low-speed turbine computation by pressure-correction and time-marching methods,
Michelassi, Vittorio, Theodoridis, Georgios, Papanicolaou, Elias,
Proceedings AD-Vol. 49, Computation of Fluid Dynamics in Aeropropulsion, ASME, 1995.

2. A comparison of the time-marching and pressure-correction algorithms for transonic turbine blades,
Michelassi, Vittorio, Papanicolaou, Elias, Theodoridis, Georgios,
Proceedings AD-Vol. 49, Computation of Fluid Dynamics in Aeropropulsion, ASME, 1995.

3. Computation of separated-flow transition using a two-layer model of turbulence,
Papanicolaou, Elias, Rodi, Wolfgang,
submitted to 1997 ASME Gas Turbine Conference, Orlando, USA.

4. Experimental and numerical investigation of boundary-layer and wake development in a transonic turbine cascade,
Michelassi, Vittorio, Rodi, Wolfgang, Gieß, P.-A.
submitted to 1997 ASME Gas Turbine Conference, Orlando, USA.

1 EINLEITUNG

Bei der Auslegung von Verdichtern und Turbinen ist die strömungsmechanische Optimierung mit dem Ziel einer Minimierung der Verluste eine wichtige Aufgabe. Hierzu werden zuverlässige Berechnungsverfahren benötigt. Solche Verfahren erfordern, vor allem auch zur Erfassung der Verluste, eine realistische Simulierung der turbulenten Austauschvorgänge mit Hilfe eines Turbulenzmodells. Dieses muß auch den Umschlag von einer laminaren in eine turbulente Grenzschicht entlang der Gitterschaufeln zu beschreiben vermögen. Eine wirkliche Optimierung auf der Grundlage von Rechenverfahren ist nur möglich, wenn die Effekte des Umschlags sowie von Ablösungen und Sekundärströmungen bei der numerischen Simulation realistisch beschrieben werden können, da die aerodynamischen Verluste und damit der Wirkungsgrad stark durch solche Effekte beeinflußt werden. Die zu Beginn des Vorhabens im Einsatz befindlichen Turbulenzmodelle hatten schon bei der Berechnung zweidimensionaler Strömungen durch ebene Schaufelgitter Schwierigkeiten beim Auftreten größerer Ablösezonen und mit dem laminar-turbulenten Umschlag, sowie mit der Stoß/Grenzschicht-Wechselwirkung bei transsonischen Strömungen. In wirklichen Gitterkanälen, in denen zusätzlich dreidimensionale Effekte, vor allem in Form von Sekundärströmungen auftreten, war die Anwendbarkeit der existierenden Turbulenzmodelle noch fraglicher und die Berechenbarkeit der wichtigsten Strömungsphänomene wesentlich ungesicherter. Der Rückstand bei der Entwicklung von Turbulenzmodellen war ganz wesentlich auch darauf zurückzuführen, daß keine ausreichenden Meßdaten zum Austesten und Verifizieren von Turbulenzmodellen zur Verfügung standen. Ziel des Vorhabens war es daher, unter Zuhilfenahme der Ergebnisse der begleitenden experimentellen Untersuchungen in den Parallelprojekten 1.1.1.7 und 1.1.1.12 des Verbundvorhabens verbesserte Turbulenzmodelle und auch Umschlagmodelle zu entwickeln und diese an Hand der experimentellen Ergebnissen abzusichern. Die resultierenden Modelle sollten beim Einsatz in Navier-Stokes Verfahren in der Lage sein, alle wesentlichen Turbulenzphänomene in wirklichen Gitterströmungen zu simulieren.

Für die Entwicklung und das Austesten von Turbulenzmodellen wurde eine schrittweise Vorgehensweise gewählt: Ausgangspunkt war das Standard k-ε Turbulenzmodell, das in ein 3D Finite-Volumen Verfahren zur Lösung der Strömungsdifferentialgleichungen für inkompressible Strömungen eingebaut war; eine zweidimensionale Version lag ebenfalls vor. Zunächst sollte für den einfacheren Fall zweidimensionaler Strömungen eine bessere Beschreibung von Ablösungserscheinungen und des laminar-turbulenten Umschlags in Angriff genommen werden, zuerst für inkompressible Strömungen sowie dann auch für kompressible transsonische Strömungen mit Stoß/Grenzschicht-Wechselwirkung. Sodann sollte in ähnliche Weise für die komplexeren dreidimensionalen Situationen mit Sekundär-

strömungen eine Weiterentwicklung und ein ausführliches Austesten von Turbulenzmodellen vorgenommen werden, und zwar zunächst wieder für inkompressible und dann für kompressible Strömungen. Neben der Weiterentwicklung der Turbulenzmodelle mußte auch erhebliche Arbeit in die Anpassung bzw. Weiterentwicklung der Finite-Volumen Verfahren zur Lösung der Strömungsdifferentialgleichungen für Gitterströmungen geleistet werden, so eine Erweiterung zur Berücksichtigung periodischer Ränder und von Rechennetzen, die durch die Schaufel verlaufen, vor allem aber eine Erweiterung für kompressible Strömungen.

Ein besonders wichtiger Arbeitspunkt war das Nachrechnen der in den Parallelvorhaben 1.1.1.7 und 1.1.1.12 experimentell untersuchten Schaufelgitterströmungen. Leider haben sich die experimentellen Arbeiten in diesen Projekten stark verzögert, so daß die Ergebnisse wesentlich später als vorgesehen zur Verfügung standen und deshalb die Laufzeit des Vorhabens (kostenneutral) um 7 Monate verlängert werden mußte. Aber trotz dieser Verlängerung standen Messungen aus Projekt 1.1.1.7 für dreidimensionale Ringgitterkonfigurationen nicht rechtzeitig zur Verfügung, so daß nur die 2D Strömung durch das ebene Gitter berechnet werden konnte. Weiter wurden im Projekt 1.1.1.12 keine Messungen in kompressibler Strömung durchgeführt, so daß keine Verifikationsrechnungen für 3D kompressible Gitterströmungen durchgeführt werden konnten. Das entwickelte Rechenverfahren ist aber prinzipiell zur Berechnung solcher Strömungen geeignet. Zum Arbeitsablauf sei noch bemerkt, daß durch einen Wechsel des Hauptsachbearbeiters Verzögerungen auftraten und auch deshalb leider nicht alle ursprünglich vorgesehenen Testrechnungen durchgeführt werden konnten.

Nachfolgend werden die Entwicklungs- und Testarbeiten beschrieben sowie die Ergebnisse des Vorhabens vorgestellt. Einige in sich geschlossenen Teile der Arbeiten sind detailliert in englischer Sprache in den Anhängen A bis E beschrieben. Für diese Teile wird im Hauptteil des Berichts nur eine kurze Zusammenfassung gegeben; es wird dabei auf Bilder in den Anhängen verwiesen, wobei den Bildnummern in den Anhängen der den jeweiligen Anhang kennzeichnende Buchstabe vorangestellt wird.

2 GRUNDZÜGE UND WEITERENTWICKLUNG DES NUMERISCHEN VERFAHRENS

Das zu Beginn des Vorhabens zur Verfügung stehende 3D Finite-Volumen Verfahren zur Lösung der Strömungsgleichungen für inkompressible Strömungen mußte zur Berücksichtigung des branch cuts bei Einzelprofilen, der periodischen Ränder bei Gitterrechnungen und zur Berücksichtigung der Kompressibilität bei Strömungen mit höherer

Geschwindigkeit und vor allem transsonischen Gitterströmungen erweitert werden. Nachfolgend wird kurz das Ausgangsverfahren beschrieben und anschließend die genannten Erweiterungen.

2.1 Ausgangsverfahren

Zu Beginn des Vorhabens war ein am Institut für Hydromechanik entwickeltes 3D Finite-Volumen Verfahren FAST3D vorhanden, mit dem sich für inkompressible Strömungen die Strömungsgleichungen auf nicht-orthogonalen krummlinigen (aber strukturierten) Rechengittern lösen lassen. Ebenfalls vorhanden war eine 2D Version des Verfahrens (FAST 2D). Die Verfahren verwenden zellzentrierte Variablenanordnung (nicht-versetzte Gitter) und kartesische Geschwindigkeits-komponenten. Das Rhie-Chow Interpolationsverfahren zur Bestimmung der Massenflüsse an den Zellrändern wird zur Vermeidung unphysikalischer Oszillationen der Strömungsgrößen eingesetzt, die sonst bei Verwendung der zellzentrierten Variablenanordnung auftreten. Die Druck/Geschwindigkeitskopplung wird mit Hilfe der SIMPLE Predictor-Korrektor Methode (Druckkorrekturverfahren) bewerkstelligt. Verschiedene Diskretisierungs-methoden für die konvektiven Glieder können aufgerufen werden, so das hybride Zentral/Aufwinddifferenzenverfahren, das genauere, aber zur Instabilität neigende QUICK Verfahren, das nicht zur Lösung der im k-ε Turbulenzmodell auftretenden Gleichungen für k und ε eingesetzt werden kann, sowie das von Zhu [1] entwickelte HLPA (Hybrid Linear Parabolic Approximation) Verfahren, das wenig numerische Diffusion einführt und dabei doch stabil ist. Die Lösung des Systems der resultierenden linearen algebraischen Differenzengleichungen erfolgt entweder mit dem Tridiagonal-Algorithmus oder der Methode der unvollständigen LU Zerlegung nach Stone. Das Rechenprogramm ist weitgehend vektorisiert und läuft sehr effizient auf dem Siemens SNI 600/20 Vektorrechner der Universität Karlsruhe. Als Standard-Turbulenzmodell ist das k-ε Modell eingebaut. Das Verfahren ist im Detail in [2] beschrieben.

2.2 Erweiterung zur Berücksichtigung von branch cuts

Die zu entwickelnden Turbulenz- und Umschlagmodelle sollten zunächst an Strömungen um Einzelprofile getestet werden, da hierfür umfangreichere Meßdaten für die Validierung zur Verfügung standen. Für eine gute numerische Auflösung muß bei der Berechnung von Einzelprofilen ein C-Rechennetz verwendet werden. Dieses läuft um das Profil herum. Im Nachlaufgebiet berühren sich zwei Gittergrenzen und bilden mitten im Berechnungsgebiet eine künstliche Trennlinie, den sogenannten branch cut (siehe Bild 1). Da an dieser Berührungslinie nicht die üblichen Randbedingungen vorgegeben werden können, sondern eine geschlossene Lösung über die Berandung hinweg gewünscht wird, sind die Berechnungs-

gebiete über den branch cut hinweg so zu koppeln, daß die künstliche Grenze keinen Einfluß auf die numerische Lösung hat. Aus Stabilitätsgründen wurde eine semi-implizite Kopplung der beiden Gebiete gewählt, d.h. bei der Berechnung der geometrischen Größen und Koeffizienten am branch cut als auch bei der Lösung des Gleichungssystems wird jeweils Information von der anderen Gitterseite mitverwendet. Es kommt auch ein spezieller Tridiagonal-Algorithmus zur Lösung der Gleichungen zum Einsatz, der die am branch cut gegenüber liegendenden Zonen miteinander koppelt.

Für das Problem der Kopplung der Berechnungsgebiete am branch cut wird zunächst das Berechnungsgebiet für den Lösungsalgorithmus in die Zonen A und B zerlegt (siehe Bild 1). Dann wird in der Zone A mit einem linieniterativen Tridiagonalalgorithmus das Gleichungssystem gelöst, wobei die Information des ersten Knotens in der dem branch cut gegenüber liegenden Zone B mit verwendet wird. Der Variablenwert des ersten Kontrollvolumens in dieser Zone ist aus den vorherigen Iterationen bekannt. Für Zone B erfolgt daraufhin dieselbe Lösungsprozedur, wobei die neu berechneten und jetzt bekannten Variablenwerte der Zone A in den ersten Kontrollvolumen am branch cut als Randinformation für die Lösung in Zone B verwendet werden.

Die Erweiterung zur Berücksichtigung des branch cuts wurde zunächst ausführlich an laminaren Profilumströmungen getestet und erst dann für Rechnungen mit Turbulenzmodellen eingesetzt.

2.3 Änderungen zur Verwendung von I-Gittern

H- und C-Gitter eignen sich nicht gut zur Auflösung des Hinterkantenbereichs von Profilen - ideal wäre dort ein O-Gitter, das aber für Schaufelkanalrechnungen mit periodischen Rändern nicht geeignet ist. Es wurde deshalb auf die Verwendung von I-Gittern ausgewichen, bei denen auch Gitterlinien in der Schaufel verlaufen, die an der Nase ein- und an der Hinterkante wieder austreten (siehe als Beispiel Bild 13). Solche Gitter erlauben deshalb eine wesentlich bessere Auflösung im Hinterkantenbereich (und gegenüber H-Gittern auch im Vorderkantenbereich). Zur Erzeugung solcher Gitter hat Michelassi [3] ein Programm entwickelt, das auch hier eingesetzt wurde. Bei der Anwendung des Finite-Volumen-Verfahrens FAST3D/2D muß der Teil des Rechennetzes im Inneren der Schaufel ausgeblockt werden. Dazu mußte das Rechenverfahren entsprechend angepaßt werden.

2.4 Behandlung periodischer Ränder

Bei Gitterströmungen wird im allgemeinen nur eine Gitterteilung berechnet. Dies führt zum Auftreten periodischer Ränder des Rechengebiets, entweder ausgehend von Vorder- und Hinterkante oder in der Mitte des Gitterkanals zwischen zwei Profilen. Auf entspre-

chenden Punkten der beiden periodischen Ränder (z.B. a und b in Bild 2) sind alle Strömungsgrößen gleich und dieser Sachverhalt stellt die Randbedingungen an den periodischen Rändern dar. Das Ausgangs-Rechenverfahren mußte zur Aufprägung dieser periodischen Randbedingungen entsprechend modifiziert und ausgetestet werden. Zunächst wurden die in Bild 2a skizzierten Punkt-zu-Punkt-periodischen Rechennetze verwendet, bei denen die Quergitterlinien gezwungen werden, von einem Punkt (a) auf der unteren periodischen Grenze zum entsprechenden Punkt (b) auf der oberen periodischen Grenze zu verlaufen. Solche Gitter ermöglichen eine einfache Aufbringung der periodischen Randbedingungen, so daß die Strömungsgrößen in den Punkten (a) und (b) gleich sind. Die Erzwingung dieses Gitterverlaufs führt aber zu stark verzerrten Gittern, vor allem im Hinterkantenbereich (siehe Beispiel in Bild 17). Solche verzerrten Gitter verursachen Konvergenzschwierigkeiten bei der numerischen Lösung. Daher wurde auf nicht-Punkt-zu-Punkt periodische Rechennetze übergegangen, wie sie in Bild 2b skizziert sind. Dabei enden die vom unteren periodischen Rand ausgehenden Quergitterlinien (z.B. von Punkt a) nicht auf den entsprechenden Punkten (z.B. b) auf dem oberen periodischen Rand, so daß zur Aufbringung der periodischen Randbedingungen eine Interpolation notwendig wird.

Es lassen sich auf diese Weise vor allem im Hinterkantenbereich wesentlich weniger verzerrte Gitter erzeugen, die bei der numerischen Lösung günstiger sind (siehe z.B. Bilder 17, 18, 28). Für die Interpolation zur Formulierung der Randbedingungen wurde entlang der periodischen Ränder ein Überlappungsgebiet eingeführt. Die Details dazu sind in Anhang B zu finden.

2.5 Erweiterung für kompressible, transsonische Strömungen

Das Ausgangsverfahren ist nur zur Berechnung inkompressibler Strömungen geeignet. Bei Anwendung auf kompressible Strömungen muß die Variation der Dichte mitberücksichtigt werden, und bei transsonischen Strömungen muß das Verfahren in der Lage sein, Verdichtungsstöße mit starken Gradienten der Strömungsgrößen zu erhalten und nicht durch die Numerik zu verschmieren. Zur Berücksichtigung der Dichteänderung muß die Druckkorrekturgleichung modifiziert werden. Bei transsonischen Strömungen muß die Gleichung im Unterschallbereich elliptisch und im Überschallbereich hyperbolisch sein, d.h. sie muß beim Übergang von der einen zur anderen Strömungsart den Typ ändern. Dies wird erreicht durch ein spezielles Diskriminierungsverfahren, das bei der Interpolation der Dichte an den Zellrändern aus den in den Zellzentren gespeicherten Werten des Drucks wirksam wird. Es wird in Abhängigkeit von der lokalen Machzahl eine gemischte lineare/Aufwindinterpolation eingeführt, d.h. für Machzahlen < 1 wird linear interpoliert und

für Machzahlen > 1 wird die Aufwindinterpolation verwendet, und zwar wird umso stärker Aufwind gewichtet, je größer die Machzahl ist, so daß ein allmählicher Übergang erreicht wird. Die Details dieser Modifikation sind im Anhang A beschrieben.

Mit der oben skizzierten Erweiterung ist das Finite-Volumen-Verfahren anwendbar für alle Geschwindigkeiten und es erlaubt eine gute Simulierung von Verdichtungsstößen. Da die Geschwindigkeitskomponenten selbst als abhängige Variable beibehalten wurden (in ähnlichen Verfahren in der Literatur wurde die Dichte mal Geschwindigkeitskomponenten als abhängige Variable eingeführt), hielten sich die im inkompressiblen Ausgangsprogramm durchzuführenden Änderungen in Grenzen.

Das modifizierte Rechenprogramm wurde zunächst anhand einiger reibungsfreier transsonischer Strömungen getestet. So wurde die Strömung durch eine konvergent-divergente Düse mit senkrechtem Verdichtungsstoß berechnet. Bild A5c zeigt, daß ein recht scharfer Stoß erhalten werden konnte. Weiter wurde die Strömung durch einen Kanal mit 10%iger und 4%iger Einengung auf der einen Kanalseite berechnet (bump flow). Im ersten Fall mit Unterschallausströmung stellt sich auf der Rückseite der Einschnürung ein Verdichtungsstoß ein. Im zweiten Fall mit Überschallabströmung geht vom Beginn der Einschnürung ein Verdichtungsstoß aus, der von der gegenüberliegenden Wand reflektiert wird und zusammen mit dem vom Ende der Einschnürung ausgehenden Stoß ein kompliziertes λ-Stoßsystem bildet. Dieses konnte realistisch und unter guter Erhaltung der Stoßschärfe berechnet werden (Bilder A10b und A11b). Die Ergebnisse stimmen auch recht gut mit denen überein, die mit einem Zeitschrittverfahren für kompressible Strömungen berechnet wurden.

Wie im Anhang C näher beschrieben, wurde das erweiterte Verfahren auch in Rechnungen der reibungsfreien Strömung durch ein Nuovo-Pignone Gitter getestet, und zwar für Austritts-Machzahlen im Bereich 0,7 - 1,6. Dabei konnte für den gesamten Bereich eine realistische Strömungsausbildung erhalten werden - insbesondere konnten die Stöße mit guter Schärfe simuliert werden (siehe Bild C5). Die berechnete isentrope Machzahlverteilung um die Schaufel stimmt in weiten Bereichen gut mit den Messungen überein - auf der Saugseite gibt es im hinteren Bereich gewisse Unterschiede, die hauptsächlich von der Vernachlässigung von Reibungseffekten herrühren (siehe Bild C6, 7). Auch diese Ergebnisse wurden mit entsprechenden Rechnungen verglichen, die mit einem Zeitschrittverfahren für kompressible Strömungen durchgeführt wurden.

3 TURBULENZMODELLIERUNG

3.1 Basis k-ε Modell mit Wandfunktionen

Ausgangspunkt der Turbulenzmodellentwicklungen war das Standard k-ε Modell (siehe z.B. [4]), das in dem vorhandenen Computerprogramm eingebaut war. Dieses Modell verwendet das Wirbelviskositätsprinzip, d.h. es bezieht die in den zu lösenden gemittelten Bewegungsgleichungen auftretenden turbulenten Spannungen zu den Geschwindigkeitsgradienten über eine künstlich eingeführte Wirbelviskosität μ_t. Diese wird ihrerseits in Beziehung gesetzt zu zwei Turbulenzparametern, nämlich zur kinetischen Energie der Turbulenz k und der Dissipationsrate ε:

$$\mu_t = c_\mu \rho \frac{k^2}{\varepsilon} \tag{1}$$

Die Verteilung der Turbulenzparameter k und ε über das Strömungsgebiet wird durch Lösen von Modelltransportgleichungen für diese beiden Größen erhalten:

$$\frac{\partial k}{\partial t} + U_j \frac{\partial k}{\partial x_j} = \frac{\partial}{\partial x_j}\left(\frac{\nu_t}{\sigma_k}\frac{\partial k}{\partial x_j}\right) + \underbrace{\nu_t\left(\frac{\partial U_i}{\partial x_j} + \frac{\partial U_j}{\partial x_i}\right)\frac{\partial U_i}{\partial x_j}}_{P_k} - \varepsilon \tag{2}$$

$$\frac{\partial \varepsilon}{\partial t} + U_j \frac{\partial \varepsilon}{\partial x_j} = \frac{\partial}{\partial x_j}\left(\frac{\nu_t}{\sigma_\varepsilon}\frac{\partial \varepsilon}{\partial x_j}\right) + c_{\varepsilon 1}\frac{\varepsilon}{k}P_k - c_{\varepsilon 2}\frac{\varepsilon^2}{k} \tag{3}$$

Für die in den obigen Modellgleichungen auftretenden empirischen Konstanten werden die Standardwerte [4] verwendet.

Diese Basisversion des k-ε Modells ist nicht anwendbar in der viskosen Unterschicht in direkter Wandnähe. Diese Schicht wird bei Verwendung des Standardmodells nicht aufgelöst, sondern der erste Gitterpunkt muß außerhalb der viskosen Unterschicht gelegt werden, idealerweise in einen Bereich, in dem der dimensionslose Wandabstand $y^+ = yU_\tau/\nu$ den Wert 30 - 100 hat, wo bei anliegenden Grenzschichten das universelle logarithmische Wandgesetz für die Geschwindigkeitsverteilung gilt und die Turbulenz näherungsweise im lokalen Gleichgewicht ist (Produktion = Dissipation). Die Geschwindigkeit U_{res} parallel zur Wand sowie k und ε am ersten Gitterpunkt werden dann über die folgenden Wandfunktionen zur Wandschubspannung τ_w in Beziehung gesetzt:

$$\frac{U_{res}}{U_\tau} = \frac{1}{\kappa}\ln\left(\frac{y_1 U_\tau}{\nu}E\right) \qquad , U_\tau = \sqrt{\tau_w/\rho} \tag{4}$$

$$\frac{k}{U_\tau^2} = \frac{1}{\sqrt{c_\mu}} \quad , \varepsilon = \frac{U_\tau^3}{\kappa\, y_1} \tag{5}$$

wobei y_1 der Abstand des ersten Gitterpunkts von der Wand ist. Die diesen Wandfunktionen zu Grunde liegenden Annahmen (logarithmische Geschwindigkeitsverteilung, lokales Gleichgewicht) gelten in Ablösegebieten nicht, weshalb dort Wandfunktionen nicht so geeignet sind. Außerdem sind sie nicht anwendbar für transitionale Grenzschichten; zur Berechnung dieser muß die viskose Unterschicht aufgelöst werden.

3.2 Zweischichtenmodelle

Die Auflösung der viskosen Unterschicht ist möglich mit sogenannten low-Re Versionen des k-ε Modells, und es gibt eine Vielfalt solcher Versionen (siehe [5, 6]). Diese Modelle erfordern, vor allem wegen des steilen Gradienten von ε in direkter Wandnähe eine sehr hohe numerische Auflösung mit 20 bis 30 Gitterpunkten allein in der viskosen Unterschicht und deshalb einen hohen Rechenaufwand. Es wurde daher als Alternative ein Zweischichtenmodell entwickelt, bei dem in der viskosen Unterschicht auf ein einfacheres Eingleichungs-Turbulenzmodell umgeschaltet wird, das keine ε-Gleichung löst, sondern die Längenmaßverteilung empirisch vorgibt. Zunächst wurde als Eingleichungsmodell das Norris-Reynolds [7] Modell eingeführt. Dieses berechnet die Wirbelviskosität aus

$$\mu_t = \rho\, k^{1/2}\, l_\mu \tag{6}$$

wobei k aus der k-Gleichung (2) (aber mit ν_t/σ_k im Diffusionsglied ersetzt durch $\nu_t/\sigma_k + \nu$) berechnet wird. Das Längenmaß l_μ wird mit der folgenden empirischen Beziehung vorgegeben:

$$l_\mu = C_l\, y \underbrace{\left(1 - \exp\left(-\frac{Re_y}{A_\mu}\frac{25}{A^+}\right)\right)}_{f_\mu} \quad , \text{mit } c_l = \kappa c_\mu^{-3/4}, \quad A_\mu = 50.5 \tag{7}$$

wobei f_μ eine Dämpfungsfunktion ähnlich der van Driestschen Dämpfungsfunktion im Mischungswegmodell ist (mit $Re_y = y\, k^{1/2}/\nu$). In voll-turbulenten Strömungen wird $A^+ = 25$ gesetzt, während eine Variation von A^+ die Simulierung des laminar-turbulenten Umschlags erlaubt (siehe 3.5). ε in der k-Gleichung (2) wird aus

$$\varepsilon = \frac{k^{3/2}}{l_\varepsilon} \tag{8}$$

berechnet. Das darin auftretende Längenmaß l_ε wird bestimmt aus

$$l_\varepsilon = \frac{C_l\, y}{1 + 5.3 / Re_y} \tag{9}$$

Dieses Modell wird nur in direkter Wandnähe eingesetzt, während die wandferneren Strömungsgebiete mit dem durch Gleichungen (1) - (3) beschriebenen k-ε Modell berechnet werden. Als Umschaltkriterium wird das Verhältnis von Wirbelviskosität zu molekularer Viskosität μ_t/μ genommen, und es wird hierfür normaleweise ein Wert von ca. 30 eingesetzt.

Eine weitere Variante des Zweischichtenmodells wurde untersucht, bei der ein alternatives Eingleichungsmodell verwendet wird, das auf der Basis direkter numerischer Simulationsdaten (DNS) vom Projektleiter und seiner Gruppe entwickelt wurde [8]. Hierbei wird statt dem im Norris-Reynolds Modell verwendeten $\sqrt{k}$ als Geschwindigkeitsmaßstab für die Turbulenzbewegung der auf den Schwankungen normal zur Wand basierende Maßstab $(\overline{v'^2})^{1/2}$ verwendet, da die Querschwankungen ursächlich für den turbulenten Impulsaustausch in Wandnähe verantwortlich sind. Die Wirbelviskositätsbeziehung wird deshalb geschrieben

$$\mu_t = \rho \left(\overline{v'^2}\right)^{1/2} l_{\mu,v} \tag{10}$$

und für das neue Längenmaß $l_{\mu,v}$ wurde aus den DNS Daten die folgende einfache Beziehung hergeleitet

$$l_{\mu,v} = C_{l,\mu} y \quad , \quad c_{l,\mu} = 0.33 \tag{11}$$

in der keine Dämpfungsfunktion mehr auftritt. ε in der k-Gleichung wird in diesem Modell aus Gleichung

$$\varepsilon = \frac{\left(\overline{v'^2}\right)^{1/2} k}{l_{\varepsilon,v}} \tag{12}$$

berechnet, wobei das Längenmaß nach der folgenden Beziehung bestimmt wird:

$$l_{\varepsilon,v} = 1.3\, y \Big/ \left(1 + 2.12 \frac{\nu}{\sqrt{\overline{v'^2}\, y}}\right) \tag{13}$$

Es wird weiter angenommen, daß das Verhältnis $\overline{v'^2}/k$ in direkter Wandnähe einer universellen Beziehung folgt, die aus den DNS Daten abgeleitet wurde:

$$\frac{\overline{v'^2}}{k} = 4.65\times10^{-5}y^{*2} + 4.00\times10^{-4}y^{*} \quad , \qquad y^{*} = k^{1/2}y/\nu \qquad (14)$$

k wird wie im Norris-Reynolds Modell aus der k-Gleichung berechnet. Die Beziehung (14) übernimmt quasi die Dämpfungsfunktion, was physikalisch realistischer ist als die Dämpfung im Norris-Reynolds Modell, weil es die Querschwankungen sind, die durch den Einfluß der Wand gedämpft werden. Außerdem verhält sich Beziehung (14) numerisch besser als die in (7) verwendete f_μ-Funktion.

3.3 Testrechnungen für einfache Geometrien

Die zwei Varianten des Zweischichtenmodells (TLK und TLV unter Verwendung der Geschwindigkeitsmaßstäbe $\sqrt{k}$ und $(\overline{v'^2})^{1/2}$ wurden für Grenzschichten und ebene Kanalströmungen ausführlich getestet, und zwar durch einen Vergleich mit den DNS Daten (siehe [8]). Es ergab sich dabei eine Überlegenheit des Modells TLV bezüglich der Simulation von Turbulenzgrößen in Wandnähe, aber nur wenig Unterschied bei den Geschwindigkeitsverteilungen. Als nächstes wurden relativ einfache Strömungen mit Ablösungen berechnet, und zwar zunächst der oft verwendete Testfall der Strömung über eine Stufe. Es wurde die von Driver und Seegmiller [9] experimentell untersuchte Stufe herangezogen (Expansionsverhältnis von 1,125, Reynoldszahl von 3×10^5 und relativ dünne Grenzschicht im Kanal vor der Stufe). In Bild 3 sind die berechneten Verteilungen des Reibungsbeiwerts c_f entlang der unteren Kanalwand nach der Stufe sowie Profile der Geschwindigkeit und der turbulenten Schubspannung $\overline{uv}$ an verschiedenen Stellen dargestellt. Die zwei Varianten des Zweischichtenmodells ergeben nahezu identische Ergebnisse (bei den Profilen sind sie nicht zu unterscheiden). Für die c_f-Verteilung sind auch die mit dem Standard k-ε Modell mit Wandfunktionen berechneten Ergebnisse eingetragen. Die Zweischichtenmodelle ergeben eine längere Ablösezone als das k-ε Modell und liegen daher näher an den Experimenten - sie führen aber zu etwas zu großen negativen Geschwindigkeiten im Rückströmgebiet. Dies sieht man auch aus den Geschwindigkeitsverteilungen, die jedoch insgesamt eine gute Übereinstimmung mit dem Experiment zeigen. Die berechnete Schubspannung $\overline{uv}$ ist etwas zu groß, was daher rührt, daß in dem in der abgelösten, gekrümmten Scherschicht zur Anwendung kommenden k-ε Modell der stabilisierende Einfluß der Krümmung nicht berücksichtigt wird.

Als weiterer Testfall wurde die Strömung über einen 2D Modellhügel berechnet. In diesem Fall liegt der Ablösepunkt nicht fest. Bild 4 vergleicht die mit verschiedenen Turbulenzmodellen berechneten Stromlinien mit den experimentell bestimmten. Das Standard k-

ε Modell mit Wandfunktionen berechnet die Ablösung zu spät und das Ablösegebiet wesentlich zu kurz. Weitaus realistischere Ergebnisse erhält man mit den Zweischichtenmodellen, die eine gute Übereinstimmung mit den Messungen zeigen. Auch in diesem Fall sind wieder keine signifikanten Unterschiede zwischen den Varianten TLK und TLV zu finden. Da aber das TLK Modell insgesamt schon wesentlich umfangreicher erprobt wurde, wird im weiteren nur noch das TLK Zweischichtenmodell verwendet.

3.4 Testrechnungen für Einzelprofile

Die Strömung um Einzelprofile wurde zunächst als Testfall herangezogen, da gegenüber 2D Gitterströmungen umfangreichere und detailliertere Testdaten zur Verfügung standen, insbesondere auch für Situationen, bei denen keine laminaren Ablöseblasen mit Umschlag auftraten, so daß zunächst Testrechnungen ohne dieses komplizierende Phänomen durchgeführt werden konnten. Es wurde die Strömung um ein superkritisches von Nakayama [10] experimentell untersuchtes Profil bei 4° Anstellwinkel berechnet. Dabei tritt keine Ablösung auf, so daß es sich hier nicht um einen besonders anspruchsvollen Testfall handelt. Als Testfall interessanter ist die Strömung um ein NACA 4412 Profil bei einem Anstellwinkel $\alpha = 13{,}87°$ und einer Reynoldszahl von $Re = cU_0/\nu = 1.5 \times 10^6$, wobei c die Sehnenlänge ist. In den Experimenten von Coles und Wadcock [11] wurde der laminar-turbulente Umschlag durch Aufbringen von Rauheitsstreifen in Vorderkantennähe herbeigeführt, so daß in diesem Fall keine Tendenz zu laminarer Ablösung vorlag und kein Umschlag simuliert werden mußte. Es tritt aber eine turbulente Ablösung auf der Saugseite in Hinterkantennähe auf, was in Bild 5 zu erkennen ist. Die Rechnungen mit dem Standard k-ε Modell mit Wandfunktionen sowie mit dem TLK Zweischichtenmodell ergaben wenig Unterschiede. Die Strömung im Hinterkantenbereich wird recht gut berechnet, so die Ablösestelle und die Größe der (kleinen) Ablösezone. Auch die in Bild 5d gezeigte Entwicklung der Geschwindigkeitsprofile zeigt gute Übereinstimmung für beide Modelle. Größere Unterschiede treten bei der Verwendung unterschiedlicher Diskretisierungsverfahren auf und dieser Testfall zeigt, daß Aufwindverfahren zu große numerische Diffusion einführen und für ein Austesten von Turbulenzmodellen ungeeignet sind. Andererseits lassen sich mit dem HLPA Hybrid Linear Parabolic Approximation Verfahren von Zhu [1] und dem QUICK Verfahren numerisch ausreichend genaue Ergebnisse erzielen, wobei das letztere Verfahren allerdings zur Instabilität neigt und nicht auf die k- und ε-Gleichungen angewandt werden kann.

3.5 Berechnung des Umschlags bei anliegender Grenzschicht

In Zweischichtenmodellen kann sehr einfach ein empirisches Umschlagmodell eingebaut werden: dem Vorbild von Mischungswegmodellen folgend wurde die Steuerung des Umschlags über den Parameter A^+ in der Dämpfungsfunktion f_μ (7) erzielt. In laminaren Grenzschichten wird A^+ ein großer Wert (300) zugeordnet, so daß die resultierende Wirbelviskosität sehr klein wird, während in voll turbulenten Grenzschichten $A^+ = 25$ gesetzt wird. Im Transitionsbereich, der durch

$$Re_{tr} \le Re_\theta \le 2\,Re_{tr} \tag{15}$$

festgelegt ist, wird folgende Übergangsformel verwendet:

$$A^+ = A_t^+(300 - A_t^+)\left(1 - \sin\left(\frac{\pi}{2}\frac{Re_\theta - Re_{tr}}{Re_{tr}}\right)\right)^3 \tag{16}$$

Hierbei ist Re_θ die lokale Impulsverlustdicken-Reynoldszahl und Re_{tr} eine kritische, den Beginn des Umschlags festlegende Reynoldszahl, die durch folgende empirische Formel von Abu Ghannam (siehe [12, 13]) bestimmt wird:

$$Re_{tr} = 163 + \exp\left(F(\lambda_2) - \frac{F(\lambda_2)\,Tu}{6.91}\right)$$

$$F(\lambda_2) = \begin{cases} 6.91 + 12.75\,\lambda_2 + 63.64\,\lambda_2^2, & \lambda_2 \le 0 \\ 6.91 + 2.48\,\lambda_2 - 12.27\,\lambda_2^2, & \lambda_2 > 0 \end{cases} \qquad \lambda = -\frac{\theta^2}{\mu_t U_e}\frac{dP}{dx} \tag{17}$$

Danach hängt der Beginn des Umschlags vom Längsdruckgradienten dP/dx und vom Außenturbulenzgrad Tu ab. Dieses Umschlagmodell wurde schon erfolgreich eingesetzt zur Berechnung des Umschlags in verschiedensten Plattengrenzschichten [12] und des Umschlags an Schaufelprofilen [13].

Die TLV Variante des Zweischichtenmodells verwendet keine Dämpfungsfunktion; hier muß der Umschlag über einen Intermittenzfaktor γ eingeführt werden, mit dem die Wirbelviskosität μ_t multipliziert wird. Dieser Parameter geht vom Wert 0 in der laminaren Grenzschicht zum Wert 1 in der turbulenten Grenzschicht. Der Übergang wird mit einer ähnlichen Formel wie in (16) beschrieben. Der Beginn des Umschlags wird dann mit einer modifizierten Version der empirischen Funktion von Abu Ghannam erzielt. Sieger et al. [14] haben dieses Modell erfolgreich zur Berechnung des Umschlags in einer Reihe verschiedener Plattengrenzschichten eingesetzt.

4 MODELLIERUNG DES UMSCHLAGS IN ABLÖSEBLASEN

4.1 Physikalisches Phänomen und gewähltes Umschlagmodell

Der laminar-turbulente Umschlag an Schaufeln in Turbinen- und Verdichtergittern findet häufig in Ablöseblasen statt (siehe den Übersichtsartikel von Mayle [15]). Die Situation ist in Bild 6 skizziert. Auf Grund eines positiven Druckgradienten (abfallende Außengeschwindigkeit U_e) löst die von der Vorderkante anwachsende laminare Grenzschicht an einem bestimmten Punkt (x_{sep}) ab. Es bildet sich eine Ablöseblase aus mit einer abgelösten laminaren Scherschicht und einer Rückströmung darunter. Diese abgelöste Scherschicht wird nach einer gewissen Lauflänge bei x_{tr} instabil und es beginnt ein Umschlag in eine turbulente Strömung, der sich über eine gewisse Lauflänge (bis x_T) hinzieht. Die energiereichere, turbulente Strömung legt sich nun wieder an die Wand an (x_R). Es bildet sich anschließend eine turbulente anliegende Grenzschicht aus. Im Bereich der Ablösung tritt wie skizziert ein Druckplateau mit geringem Längsdruckgradienten auf, aus dem man aus Druckmessungen (allerdings schwierig) das Auftreten von Ablöseblasen erkennen kann. Eindeutiger lassen sie sich mit Anstrichbildern bestimmen.

Das in 3.5 beschriebene Umschlagmodell für anliegende Grenzschichten ist zur Beschreibung des Umschlags in Ablöseblasen nicht geeignet, da die Wanddämpfungsfunktion f_μ, in welcher der zur Steuerung des Umschlags verwendete Paramter A^+ auftritt, nicht die Verhältnisse in der abgelösten Scherschicht beschreibt und die empirischen Beziehungen aus Experimenten für anliegende Grenzschichten hergeleitet wurden. Es ist jedoch eine ähnliche Vorgehensweise im Rahmen des Zweischichtenmodells möglich. Ähnlich wie bei dem Umschlagmodell von Sieger et al. [14] für anliegende Grenzschichten wird die Steuerung des Umschlags über eine Intermittenzfunktion γ vorgenommen, die die mit dem Turbulenzmodell berechnete Wirbelviskosität multipliziert. Diese Funktion nimmt den Wert 0 in laminaren Strömungsgebieten und den Wert 1 in voll turbulenten ein; im Transitionsgebiet findet ein Anstieg von 0 auf 1 statt. Hierfür wurden verschiedene empirische Formeln vorgeschlagen und zu Beginn auch ausprobiert. Es wurde schließlich die von Rodi und Schönung [16] vorgeschlagene und in einem Mischungswegmodell für die Simulierung des Umschlags an Turbinenschaufeln getestete Form verwendet:

$$\gamma(x) = 1 - \exp\left[-G(x - x_{tr})\int_{x_{tr}}^{x}\frac{dx}{U_\infty}\right] \quad \text{wobei:} \quad G = \frac{\exp(0.99\,T\,u)}{100}\frac{U_\infty^{\,3}}{\nu^2}\,Re_{\theta,\,sep}^{\;-8/3} \qquad (18)$$

Es handelt sich hierbei um eine erweiterte Version der von Chen und Thyson [17] eingeführten Umschlagbeziehung, wobei vor allem der Einfluß des Außenturbulenzgrads mit

hereingebracht wurde. Der Beginn des Umschlags wird ebenfalls mit Hilfe einer von Rodi und Schönung [16] entwickelten empirischen Formel berechnet:

$$Re^2_{\theta,tr} = \left(1 + \frac{0.05}{\exp(0.365\ T\ u)}\right) Re^2_{\theta,sep} + \frac{17000}{\exp(0.509\ T\ u)} \qquad (19)$$

Hierbei ist $Re_{2,sep}$ die an der Ablösestelle herrschende Impulsverlustdicken-Reynoldszahl. $Re_{2,tr}$ ist die kritische Impulsverlustdicken-Reynoldszahl, bei welcher der Umschlag beginnt (x_{tr}). Diese Formel für den Beginn des Umschlags in Ablöseblasen wurde von Rodi und Schönung anhand der experimentellen Daten von Gotthardt [18] und Haas et al. [19] für Modellschaufeluntersuchungen optimiert. Das hier beschriebene Umschlagmodell wird nur aufgerufen, wenn zuvor eine laminare Ablösung in der Rechnung auftritt. Die Details der Implementierung des Modells sind im Anhang D beschrieben.

4.2 Testrechnungen

Mit verschiedenen Umschlagmodellen wurden zunächst Testrechnungen für Einzelprofile vom Typ NACA 66_3-018 und Eppler 387 durchgeführt, bei denen in Experimenten laminare Ablöseblasen mit Umschlag beobachtet wurden. In den Rechnungen trat aber nur zum Teil Ablösung auf, so daß das Modell nicht immer eingeschaltet wurde und in manchen Fällen keine realistische Simulation ergab; in anderen konnte jedoch der Umschlag in der Ablöseblase in relativ guter Übereinstimmung mit dem Experiment beschrieben werden. Insgesamt waren diese Testfälle aber nicht so geeignet, da wie erwähnt, die Ablöseblase teilweise schwer zu erhalten war und der Turbulenzgrad bei Tragflügelumströmungen äußerst niedrig und damit nicht repräsentativ für Schaufelumströmungen ist.

Die Testrechnungen wurden daher verlagert auf die Strömung in einem Kanal mit geneigter Stufe an der unteren Wand bei relativ niedriger Reynoldszahl, in der die ankommende Strömung eine ausgebildete laminare Kanalströmung war. Zu diesem Testfall lagen detaillierte Messungen von Makiola [20] vor. Der Turbulenzgrad in der ankommenden Strömung war etwas höher als bei den Tragflügelprofilen, aber immer noch relativ gering. Der Testfall erwies sich ebenfalls als nicht sehr geeignet, da sowohl auf der unteren Kanalwand mit Stufe als auch auf der oberen, ebenen Kanalwand eine Ablösung mit Umschlag auftrat, so daß insgesamt eine äußerst komplexe Strömungssituation vorlag. Der Testfall wurde auch deshalb aufgegeben, weil inzwischen geeignetere Testfälle vorlagen, die von der ERCOFTAC* Special Interest Group on Transition ausgegeben wurden. Es handelte sich

---

* European Research Community on Flow, Turbulence and Combustion

hier um die Strömung über eine kleine 90° Stufe und um die Strömung um eine Profilnase. Messungen für den ersten Fall wurden an der Universität Cambridge durchgeführt und für den zweiten Fall bei der Firma Rolls-Royce, Derby, UK. Die beiden Strömungssituationen sind in Bild D1 skizziert. Die Details zu den Rechnungen sowie die ausführlichen Ergebnisse für diese zwei Testfälle sind in Anhang D zu finden.

Bei der Stufenströmung mit ankommender laminarer Grenzschicht liegt der Ablösepunkt an der Stufenecke fest. Die Kanalströmung mit Stufe hat einen Expansionsverhältnis von 1,012, d.h. die Stufenhöhe war nur sehr klein im Vergleich zur Kanaltiefe. Außerdem herrschte ein extrem niedriger Turbulenzgrad von Tu $\approx 10^{-2}$% im Kanal. Experimentelle Ergebnisse lagen für drei Reynoldszahlen vor, es konnten jedoch nur Rechnungen für die höchste Reynoldszahl von Re = 4095 (gebildet mit der Stufenhöhe H und der Anströmgeschwindigkeit) simuliert werden. Bei den niedrigeren Reynoldszahlen traten auf Grund des äußerst kleinen Turbulenzgrads numerische Instabilitäten auf. Die Ergebnisse sind in den Bildern D24 - 27 wiedergegeben. Es bildet sich eine Rückströmzone hinter der Stufe mit einer Länge von 9.5h aus. Die Verteilung der Impulsverlustdicke und des Formparameters deuten darauf hin, daß das Ablösegebiet gut berechnet wird. Im Ablösegebiet beginnt der Umschlag bei x = 4,85H und endet stromab des Wiederanlegepunkts bei ca. 18H. Der Umschlag scheint ebenfalls realistisch berechnet worden zu sein, da die Geschwindigkeitsprofile nach dem Wiederanlegen gut mit den Messungen übereinstimmen; in der Ablösezone sind gewisse Unterschiede mit dem Experiment festzustellen, wobei aber im Rückströmgebiet die Hitzdrahtmessungen etwas zweifelhaft sind.

Für den Testfall der Umströmung einer Profilnase wurden alle 6 Fälle berechnet, die im Experiment untersucht wurden (siehe Tabelle D1). Dabei wurde die Reynoldszahl Re (gebildet mit Körperdurchmesser D und der Anströmgeschwindigkeit) im Bereich Re = 1646 - 6586 variiert und der Freistromturbulenzgrad im Bereich 0,17 - 5,56%. Für alle Fälle wurde eine Ablöseblase berechnet; die Charakteristika dieser Blase sind für die einzelnen Testfälle in Tabelle D2 zusammengestellt. Im Anhang D sind die Stromlinien, die Verteilung des Intermittenzparameters γ~x sowie die Verteilungen der Grenzschichtdicke δ, der maximalen Geschwindigkeit in der Außenströmung $U_{max,,}$ des Formparameters H und des Reibungsbeiwerts c_f gegeben sowie Profile der Geschwindigkeit U und der Turbulenzenergie k an verschiedenen Stellen, die mit Messungen der Längsschwankungen $\overline{u'^2}$ verglichen werden. Insgesamt ist die Übereinstimmung zwischen Rechnung und Messung gut, wenn auch der berechnete Formparameter im Ablösegebiet eine zu hohe Spitze aufweist. Jedoch sind Länge und Lage der Ablöseblase jeweils gut berechnet, und auch die Entwicklung des Geschwindigkeitsprofils und der turbulenten Schwankungsenergie sind

realistisch - jedoch wird in der ausgebildeten turbulenten Grenzschicht weiter stromab die Turbulenzenergie in Wandnähe zu klein berechnet, was eine bekannte Schwäche des verwendeten TLK Zweischichtenmodells ist.

5 TESTRECHNUNGEN FÜR 2D GITTERSTRÖMUNGEN

5.1 Kreisbogenverdichtergitter von Zierke und Deutsch

Das von Zierke und Deutsch [21] experimentell untersuchte Verdichtergitter wurde für Testrechnungen gewählt, weil es eines der wenigen Testfälle mit zweidimensionaler Gitterströmung ist, in dem auch die Grenzschicht im Detail ausgemessen wurde. Die Versuche wurde an einem Gitter mit 5 Schaufeln (Bild 7) durchgeführt, die sehr dünn sind und Kreisbogengeometrie haben. Die Messungen erfolgten an der mittleren Schaufel. Durch die Versuchsanordnung wurde gute Zweidimensionalität und Periodizität sichergestellt. Die Einströmprofile wurden 0,16 C (C = chord = Sehnenlänge = 228,6 mm) stromauf der Vorderkante gemessen und Abströmprofile 0,5c stromab der Hinterkante. Die Zuströmgeschwindigkeit war 133m/s, so daß inkompressible Strömung angenommen werden konnte, die Reynoldszahl war $Re = C \cdot V_1 / \nu \approx 500.000$ und der Anström-Turbulenzgrad 0,18%. Die Teilung betrug 106,8 mm, und es wurden Messungen durchgeführt für die Anströmwinkel β_1 (Definition siehe Bild 7) von 44,5°, 51,5° und 58°. Zierke und Deutsch präsentieren gemessene Verteilungen des Druckbeiwerts c_p, der Verdrängungsdicke δ^*, der Impulsverlustdicke θ, des Formparameters H und des Reibungsbeiwerts c_f (oder der Wandschubspannung τ_w) entlang der Druck- und der Saugseite für alle drei genannten Winkel β_1. Allerdings wurden die Grenzschichtgrößen abgeleitet für „rekonstruierte" Grenzschichten, um den Einfluß der starken Druckgradienten normal zur Wand (verursacht durch die starke Krümmung der Schaufelwand) auszuschalten. Die Wandschubspannung τ_w wurde nicht direkt gemessen, sondern in laminaren Grenzschichtbereichen durch Vergleich mit Faulkner Skan Lösungen erzielt und im turbulenten Bereich durch Abgleich mit dem Coles´schen Nachlaufgesetz. Zum Teil treten laminare Ablöseblasen mit Umschlag in der Ablösezone und turbulentem Wiederanlegen auf und diese wurden bestimmt mit Hilfe von Sublimations-Sichtbarmachung und Anstrichbildern.

Die hauptsächlichen Rechnungen wurden in einem relativ frühen Stadium des Forschungsprojekts durchgeführt, als noch H-Netze verwendet wurden. Bild 8 zeigt das für diese Rechnungen eingesetzte 67 x 72 H-Netz, und zwar für zwei Schaufelkanäle (gerechnet wurde allerdings nur einer), um die Netzverhältnisse an den periodischen Rändern sichtbar machen zu können. In Bild 8 ist auch der Bereich der Vorderkante vergrößert dargestellt.

Die Bilder zeigen, daß vor allem in diesem Bereich, und ähnlich natürlich im Hinterkantenbereich die Auflösung relativ schlecht und das Netz stark verzerrt ist. Eine wesentlich bessere Auflösung mit kaum verzerrten Netzen ist mit den später entwickelten I-Gittern möglich (siehe Bild 13). Die Ein- und Ausström-Geschwindigkeitsprofile wurden aus den Messungen übernommen und als Einström-Turbulenzgrad wurde 1,8% gewählt, um die numerische Stabilität nicht zu gefährden. Ein solcher Wert wurde auch schon in früheren Rechnungen [22] verwendet. Es wurden Rechnungen sowohl mit dem k-ε Modell mit Wandfunktionen durchgeführt als auch mit dem TLK Zweischichtenmodell zusammen mit dem in 3.5 beschriebenen Umschlagmodell für anliegende Grenzschichten. Das erstere Modell erlaubt natürlich keine Simulierung des Umschlags, sondern nimmt an, daß die Grenzschicht von der Vorderkante ausgehend turbulent ist. Bei Verwendung des Zweischichtenmodells wurde zwar die gleiche Gitterpunktzahl verwendet, aber die Gitterpunkte waren in Wandnähe konzentrierter. Das Modell für den Umschlag in Ablöseblasen war zum Zeitpunkt dieser Rechnungen noch nicht entwickelt, so daß dieses Phänomen nicht simuliert werden konnte.

Die berechneten und gemessenen Druckverteilungen sind für die drei Anströmwinkel in Bild 9 dargestellt. Auf der Druckseite herrscht im allgemeinen gute Übereinstimmung; nur bei den kleineren Anströmwinkeln 51,5° und 44,5° gibt es Abweichungen im Hinterkantenbereich bei den Rechnungen mit dem Zweischichtenmodell. Auf der Saugseite zeigen die Rechnungen bei diesem Winkel eine gewisse Verschiebung gegenüber den Experimenten und bei 44,5° tritt eine größere Abweichung im Vorderkantenbereich auf. Diese, und die oben genannten Abweichungen im Hinterkantenbereich der Saugseite sind sicherlich eine Folge des dort nicht besonders idealen Rechennetzes.

Ein direkter Vergleich der berechneten und von Zierke und Deutsch berichteten Verdrängungs- und Impulsverlustdicken ist nicht sehr sinnvoll, da es sich bei den letzteren um aus dem Experiment rekonstruierte Werte handelt. Der Einfluß dieser Rekonstruktion auf den Formparameter H dürfte jedoch geringer sein und die Wandschubspannung kann direkt verglichen werden; sie wurde allerdings nicht direkt gemessen. In den Bildern 10 - 12 sind für die drei untersuchten Anströmwinkel jeweils der Formparameter H, die Wandschubspannung τ_w sowie die Verteilung des in der Rechnung auftretenden Parameters A^+ für die Saug- und Druckseite gegeben. Die Verteilung von A^+ gibt direkten Aufschluß über den Grenzschichtzustand in der Rechnung: bei A^+-Werten von 300 ist die Grenzschicht laminar und bei einem Wert von 25 voll turbulent und dazwischen transitional.

Bei $\beta = 58°$ (Bild 10) wurde im Experiment der laminar-turbulente Umschlag in einer kurzen Ablöseblase bei 3,6% der Sehnenlänge C (= chord) beobachtet; der voll turbulente

Zustand der Grenzschicht liegt ab 8 - 12%C vor und es tritt eine turbulente Ablösung bei ca. 65%C auf. Auch in der Rechnung erfolgte ein früher Umschlag bei ca. 3%C (allerdings ohne Ablöseblase), so daß die Grenzschicht auf dem allergrößten Teil der Saugseite turbulent war und deshalb wenig Unterschiede im Formparameter zwischen Standard k-ε Modell- und Zweischichtenmodell-Rechnungen zu sehen sind. In guter Übereinstimmung mit der Messung löst die Strömung auch in der Rechnung bei ca. 64%C ab und der Anstieg des Formparameters im hinteren Bereich der Saugseite ist ebenfalls gut berechnet. Andererseits werden die aus der Messung abgeleiteten hohen Wandschubspannungswerte in der Rechnung nicht erzielt. Es sollte beachtet werden, daß der Betrag der Wandschubspannung aufgetragen ist, so daß diese nicht negativ wird, obwohl eine Ablösezone auftritt. Auf der Druckseite bleibt die Grenzschicht im Experiment bis 68%C laminar und hat dann transitionales Verhalten bis zur Hinterkante. In der Rechnung tritt der Umschlag schon etwas früher bei ca. 50%C ein und auch hier ist die Strömung anschließend transitional, so daß eine gute qualitative Übereinstimmung vorliegt. In diesem Fall mit Transition ist die mit dem Zweischichten- und Umschlagmodell berechnete H-Verteilung wesentlich besser als die mit dem Standard k-ε Modell berechnete und auch die Schubspannungsverteilung ist wesentlich näher an der über die Faulkner Skan Lösungen aus dem Experiment abgeleitete.

Beim Anströmwinkel $\beta_1 = 51{,}5°$ (Bild 11) tritt im Experiment der Umschlag auf der Saugseite schon relativ früh ein (aber es gibt keine direkte Zahlenangabe). Das Zweischichtenmodell zeigt einen Umschlag im Bereich 25 - 46%C voraus und anschließend eine voll turbulente Grenzschicht. Im Experiment löst die Grenzschicht bei ca. 70%C ab; aus den berechneten Geschwindigkeitswerten ist an dieser Stelle ebenfalls eine Ablösung abzuleiten, doch steigt der Formparameter H nicht wie im Experiment an. Auch hier ist die Wandschubspannung mit dem Zweischichtenmodell wesentlich besser berechnet als mit dem Standard k-ε Modell. Auf der Druckseite zeigen die Experimente eine laminare Ablösung bei 40%C und ein turbulentes Wiederanlegen bei 50%C. Die Rechnung sagt hier einen Umschlag bei anliegender Grenzschicht bei 40%C voraus mit anschließenden Relaminarisierungstendenzen und ab 68%C dann eine voll turbulente Grenzschicht. Der Formparameter wird mit dem Zweischichtenmodell ganz gut berechnet und im voll turbulenten Bereich auch mit dem Standard k-ε Modell. Die Wandschubspannung wird ebenfalls vor allem im vorderen Bereich mit laminarer und transitionaler Grenzschicht vom Zweischichten-modell wesentlich besser berechnet.

Beim Anströmwinkel $\beta_1 = 44{,}5°$ (Bild 12) tritt im Experiment eine laminare Ablösung bei ca. 40%C auf, ein Umschlag in der Blase bei 50 - 55%C und die turbulente Strömung legt

bei ca. 60%C wieder an. Es kommt hier also zur Ausbildung einer längeren Ablösblase, was sich auch im starken Anstieg des Formparameters H im Ablösebereich wiederspiegelt. Dies kann natürlich in der Rechnung mit Umschlagmodell für anliegende Grenzschichten nicht nachvollzogen werden. Der Umschlag der anliegenden Grenzschicht beginnt in der Rechnung bei ca. 38%C und die Grenzschicht ist voll turbulent ab 55%C. Beide Modelle berechnen den Formparameter H im voll turbulenten Bereich in guter Übereinstimmung mit dem Experiment, und auch die mit dem Zweischichtenmodell berechnete Wandschubspannung stimmt außer im Bereich der Ablösezone ganz gut mit den Messungen überein. Auf der Druckseite gab es im Experiment eine frühe Ablösung mit turbulentem Wiederanlegen bei ca. 10%C. Hier erfolgt der Umschlag in der Rechnung erst ab 33%C, anschließend wird der Formparameter von beiden Modellen gut berechnet und die mit dem Zweischichtenmodell berechnete Wandschubspannung stimmt im ganzen Bereich mit den aus den Messungen abgeleiteten Werten überein.

Die bisher vorgestellten Testrechnungen für das Kreisbogenverdichtergitter zeigen insgesamt, daß das Zweischichtenmodell wesentlich realistischere Ergebnisse bei der Berechnung der Grenzschicht gibt, wenn ein Umschlag auftritt und wenn die Grenzschichten teilweise laminar oder transitional sind. Allerdings konnte mit dem verwendeten Umschlagmodell kein Umschlag in Ablöseblasen simuliert werden. Für den Anströmwinkel β_1 = 44,5°, bei dem im Experiment die größte Ablöseblase auftrat, wurde deshalb die Rechnung später mit dem in 4.1 beschriebenen Umschlagmodell wiederholt. Dabei wurde auch ein wesentlich geeigneteres I-Rechennetz mit 201 x 124 Gitterpunkten (Bild 13) verwendet, das vor allem im Vorder- und Hinterkantenbereich wesentlich weniger verzerrt ist und dort auch eine wesentlich bessere Auflösung ergibt. Dies führt, vor allem im Vorderkantenbereich, zu einer verbesserten Druckverteilung (siehe Bild 9). In dieser Rechnung wurde im Bereich 40 - 46%C eine Ablöseblase erhalten, die allerdings sehr dünn ist (siehe Bild 14) und auch kürzer als die im Experiment beobachtete. Die berechnete H-Verteilung (Bild 15) zeigt nun wegen des Auftretens einer Ablöseblase ebenfalls einen starken Anstieg zu dem im Experiment beobachteten Niveau, aber der Bereich mit erhöhtem H ist gegenüber dem Experiment zu kleineren x-Werten verschoben, da die Blase zu kurz berechnet wird. Die in den neuen Rechnungen erhaltene Wandschubspannung ist zwar im Ablösebereich realistischer als die alte, da sie negative Werte aufweist, aber außerhalb dieses Bereiches ergibt sich eine schlechtere Übereinstimmung mit dem Experiment als mit der alten Rechnung. Dies ist schwer zu verstehen und bedarf noch einer Klärung.

5.2 DLR T5.1 Turbinenlaufradgitter

Im Parallelvorhaben 1.1.1.7 wurde bei der DLR in Göttingen die Strömung durch ein ebenes T5.1 Laufradgitter experimentell untersucht [23, 24], und zwar für die Austritts-Machzahlen 0,3 und 1,1. Der erste Fall ist näherungsweise inkompressibel und der zweite transsonisch; beide wurden als Testfälle der TURBOTECH Arbeitsgruppe „Navier-Stokes Verfahren" an die Partner des Gemeinschaftsprogramms sowie an kommerzielle Softwareanbieter zur Nachrechnung ausgegeben. Die Gitterkonfiguration ist in Bild 16 gegeben. Die Druckverteilung entlang der Schaufelwände wurde in der Mittelebene an zwei gegenüberliegenden Schaufeln gemessen. Mit einer Keilsonde im Nachlauf stromab des Gitters wurde der Totaldruck, der statische Druck und der Strömungswinkel gemessen. Das Strömungsfeld im Schaufelkanal wurde mit einem Laser2-Fokusverfahren bestimmt. Die Grenzschichtmessungen im hinteren Bereich der Schaufel an den ebenfalls in Bild 16 gezeigten Stellen wurden mit einer Fischmaulsonde durchgeführt. Schließlich wurden Schlierenbilder und Anstrichbilder aufgenommen.

Inkompressible Strömungsberechnungen bei $Ma_2 = 0{,}3$. Über mehrere Jahre wurden Rechnungen für den inkompressiblen Testfall durchgeführt und die Ergebnisse an die Arbeitsgruppe „Navier-Stokes Verfahren" abgeliefert. Es wurden sowohl zweidimensionale wie auch dreidimensionale Rechnungen der ebenen Gitterströmung durchgeführt; letzere ergaben im Mittelschnitt aber dieselben Ergebnisse bezüglich des Druckverlusts und des Abströmwinkels im Nachlauf wie die zweidimensionalen Rechnungen; deshalb werden hier nur die zweidimensionalen Rechnungen vorgestellt. Für die ersten Rechnungen wurden H-Gitter verwendet, die naturgemäß stark verzerrt waren und keine gute Auflösung im Vorder- und Hinterkantenbereich erlaubten. Es wurde deshalb zu I-Gittern übergegangen, zunächst zu Gittern, die an den Rändern Punkt-zu-Punkt periodisch waren. Der in Bild 17 dargestellte Ausschnitt eines 108 x 41 Gitters zeigt, daß ein solches I-Gitter wegen der erzwungenen Punkt-zu-Punkt Periodizität im Hinterkantenbereich stark verzerrt ist. Ähnliches gilt für den Vorderkantenbereich. Es wurde deshalb schließlich ein Gitter verwendet, das eine Punkt-zu-Punkt Periodizität an den Rändern nicht erzwingt und das wesentlich weniger verzerrt ist (siehe Bilder 17 und 18). Nachfolgend werden nur die mit diesem Gitter erzielten Ergebnisse dargestellt, die auch die endgültigen an die Arbeitsgruppe „Navier-Stokes Verfahren" abgelieferten Ergebnisse waren (Version 4).

Es kam bei diesen Rechnungen nur das Standard k-ε Turbulenzmodell mit Wandfunktionen zum Einsatz, d.h. die Grenzschicht wurde entlang der ganzen Schaufel voll turbulent berechnet. Die wirkliche Grenzschichtentwicklung konnte damit natürlich nicht realistisch simuliert werden, da in den Experimenten die Grenzschicht auf der Saugseite bis ca. 80%

Sehnenlänge laminar war und auf der Druckseite im ganzen Bereich weitgehend transitional. Aus Zeitgründen konnten jedoch für den inkompressiblen Fall keine Rechnungen mit dem Zweischichtenmodell kombiniert mit einem Umschlagmodell durchgeführt werden. Dies wurde für den nachfolgend besprochenen kompressiblen Fall nachgeholt.

Die Rechnungen wurden mit verschiedenen Diskretisierungsverfahren für die konvektiven Glieder durchgeführt. Dabei wurden sowohl das hybride Zentral-/ Aufwinddifferenzenverfahren, das quadratische Aufwinddifferenzenverfahren QUICK (aber nur für die Impulsgleichungen) und das hybride linear parabolische Approximationsverfahren (HLPA) verwendet. Der Zuströmrand lag x/t = 1.8 stromauf der Vorderkante; dort wurde konstante Einströmgeschwindigkeit angenommen mit einem Turbulenzgrad von 0,5% und zur Festlegung des Einströmwerts von ε ein Verhältnis von Wirbelviskosität zu molekularer Viskosität $\mu_t/\mu = 10$. Bild 19 zeigt den Einfluß der Diskretisierungsverfahren und der Gitterfeinheit auf die berechnete Druckverteilung sowie den Druckverlustbeiwert und Abströmwinkel im Nachlauf. Daraus kann geschlossen werden, daß die mit HLPA sowie mit QUICK (plus HLPA für k- und ε-Gleichungen) auf dem feineren Gitter erzielten Ergebnisse gitterunabhängig und numerisch genau sind. Bild 20 vergleicht berechnete und gemessene Verteilungen des Strömungswinkels und der Machzahl an verschiedenen axialen Stellen (aufgetragen gegen y_{ax}/t). Stromauf der Hinterkante ($x/l < 1$) ist die Übereinstimmung gut. In kurzem Abstand stromab der Hinterkante ($x/l = 1{,}111$) gibt es Abweichungen; die Strömung im Nahbereich der Hinterkante ist sehr komplex mit einer Ablösung, die möglicherweise instationär ist (vortex shedding) und mit dem Standard k-ε Modell sicher nicht ausreichend genau berechnet werden kann.

Die Bilder 21 - 23 zeigen Druckverteilungen entlang der Schaufeloberflächen sowie Verteilungen des Abströmwinkels und des Druckverlustbeiwerts im Nachlauf hinter dem Gitter. Diese Bilder sind dem Bericht der Arbeitsgruppe „Navier-Stokes Verfahren" [25] entnommen und vergleichen die eigenen Rechnungen (Bezeichnung IHm - V3) mit denen anderer Gruppen und den Messungen der DLR. Bild 21 zeigt, daß die Druckverteilung von allen Gruppen in recht guter Übereinstimmung mit den Messungen berechnet werden konnte. Die eigenen Ergebnisse für den Abströmwinkel (Bild 22) sind über 75% der Teilung in guter Übereinstimmung mit den Messungen und damit besser als die meisten anderen Ergebnisse; im Nachlaufbereich wird das Minimum des Abströmwinkels allerdings nicht so gut simuliert, ein Problem, das auch in den anderen Ergebnissen wiederzufinden ist. Die in Bild 23 dargestellten Druckverlustbeiwerte zeigen, daß hier das hybride Differenzenverfahren wesentlich zu große Verluste erzeugt. Bei Verwendung des HLPA Verfahrens sind diese zwar immer noch zu groß, aber dies ist eigentlich zu erwarten, da ja

kein Umschlagmodell verwendet und die Grenzschicht von der Vorderkante ausgehend turbulent gerechnet wurde. Damit werden die Grenzschichten zu dick berechnet (siehe Profile Bild 24) und die Verluste natürlich zu hoch. Die Verteilung des Verlustbeiwerts wird allerdings relativ realistisch simuliert, doch mit dem Maximum bei etwas zu großem y, was von dem zu groß berechneten Abströmwinkel β_2 im Nachlauf herrührt.

Bild 24 vergleicht berechnete und gemessene Geschwindigkeitsprofile in der Grenzschicht an den im Bild 16 gekennzeichneten Meßstellen. Auf der Saugseite ist an der Stelle D_{ss} die Grenzschicht im Experiment noch laminar und sehr dünn. Hier ergibt die von der Vorderkante ausgehende voll turbulente Rechnung mit dem k-ε Modell natürlich eine wesentlich zu dicke turbulente Grenzschicht. Dies führt dazu, daß auch in den weiter stromab gelegenen Stellen in der Nähe der Hinterkante die Grenzschicht noch zu dick berechnet wird, selbst wenn sie dort nun auch im Experiment turbulent ist. Die Abweichungen bezüglich der Verteilung sind allerdings nicht mehr so groß. Auf der Druckseite (Profil A_{ds}) beschreibt das Modell zumindest den Trend richtig, nämlich daß dort die Grenzschicht wesentlich dünner ist als auf der Saugseite. Jedoch ist die berechnete Grenzschicht auch hier in der voll turbulenten Rechnung mindestens doppelt so dick wie im Experiment. Realistischere Simulationen der Grenzschichtprofile können nur unter Verwendung eines Modells erhalten werden, das die anfänglich laminaren Grenzschichten berücksichtigt und den Umschlag zu simulieren vermag.

Transsonische Strömungsberechnung bei $Ma_2 = 1.1$. Rechnungen für den transsonischen Testfall konnten erst nach dem endgültigen Abgabetermin der Arbeitsgruppe „Navier-Stokes Verfahren" durchgeführt werden, so daß diese Ergebnisse nicht in den Bericht der Arbeitsgruppe [25] aufgenommen werden konnten. Die Rechnungen sind im Anhang E ausführlich beschrieben. Sie wurden mit der in 2.5 vorgestellten kompressiblen Version des Computercodes FAST 3 (allerdings für 2D Rechnungen abgespeckt) durchgeführt. Dabei kamen folgende Turbulenzmodelle zum Einsatz: k-ε Model mit Wandfunktionen, TLK Zweischichtenmodell mit und ohne Umschlagmodell sowie TLV Zweischichtenmodell mit und ohne Umschlagmodell. Die TLK und TLV Modelle gaben sehr ähnliche Ergebnisse. Zum Vergleich wurden auch Rechnungen mit einem Zeitschrittverfahren [26] durchgeführt unter Verwendung des k-ω Modells zusammen mit einem Umschlagmodell. Es kamen I-Gitter zum Einsatz, und zwar ein 241 x 110 Gitter (Bild E4) unter Verwendung von Wandfunktionen und ein 273 x 115 Gitter bei Verwendung der Zweischichtenmodelle. Wie Bild E14 zeigt, konnten die Verdichtungsstöße gut erhalten werden. Die isentrope Machzahlverteilung entlang der Saug- und Druckseite stimmt insgesamt gut mit den Messungen überein; auf der Saugseite fällt Ma in Hinterkantennähe unrealistisch ab,

wenn kein Umschlagmodell verwendet wird. Beim Zuschalten dieses Modells wird die Verteilung dort realistisch, wenn auch nicht in völliger Übereinstimmung mit den Messungen berechnet. Auch die Grenzschichtentwicklung wird bei Verwendung des Umschlagmodells auf der Saugseite wesentlich besser berechnet, als wenn die Grenzschichten von der Vorderkante an turbulent berechnet werden. Auf der Saugseite ist die Grenzschicht bis zum Auftreffen des von der Hinterkante des Nachbarprofils ausgehenden Verdichtungsstoßes laminar und schlägt dann um, wobei dies im Experiment in einer sehr kleinen Ablöseblase vor sich geht. Bei Zuschaltung des Umschlagmodells findet der Umschlag ebenfalls an der Stelle des Auftreffens des Verdichtungsstoßes statt, bei dem verwendeten Zweischichtenmodell allerdings ohne Ablösung. Der nachfolgende Anstieg der Grenzschichtdicke bis zur Hinterkante wird durch das Modell sehr gut vorhergesagt (Bild E21). Ohne Umschlagmodell wird die Grenzschicht auf der Saugseite insgesamt zu dick berechnet, wie schon beim vorher besprochenen inkompressiblen Fall. Auf der Druckseite findet eine starke Beschleunigung statt, die die Grenzschichtdicke zur Hinterkante reduziert, und es wird mit dem Zweischichtenmodell dort die sehr dünne vermutlich transitionale Grenzschicht realistisch beschrieben. Die Verteilung von Machzahl und Strömungswinkel im Nachlauf ist nicht so stark von den Modellvarianten abhängig und wird von der Rechnung näherungsweise richtig wiedergegeben. Andererseits ist die berechnete Verteilung des Gesamtdrucks im Nachlauf zu eng und dadurch der Minimalwert zu klein, was auf mangelnde Vermischung im Nachlauf hindeutet. Es gibt Hinweise, daß an der Hinterkante des Profils instationäre Wirbelablösung (vortex shedding) auftrat, welche die wesentlich stärkere Vermischung im Experiment erklären würde. Dieses instationäre Phänomen kann bei den durchgeführten stationären Rechnungen natürlich nicht simuliert werden.

6 TESTRECHNUNGEN FÜR DREIDIMENSIONALE INKOMPRESSIBLE GITTERSTRÖMUNGEN

Mit dem FAST3D Code, erweitert zur Behandlung periodischer Ränder, wurden in einem relativ frühen Projektstadium dreidimensionale Rechnungen für das von Schulz und Gallus [27] experimentell untersuchte Axialverdichterringgitter durchgeführt. Für verschiedene Anströmwinkel α_2 haben Schulz und Gallus umfangreiche Messungen vorgenommen, so Sichtbarmachung der Strömung um Schaufeln und Nabe, Druckverteilung an den Schaufeln, der Nabe und dem Gehäuse, Druckverlust und Abströmwinkel im Nachlauf und Grenzschichtmessungen. Der Umschlag fand in einer laminaren Ablöseblase statt, die auf der Saugseite mit zunehmendem Anströmwinkel α_2 nach vorne wanderte. Im Schaufel/Nabenbereich trat eine turbulente Ablösung auf , die für $\alpha_2 > 45°$ auch den Mittelschnitt erreichte. Für die verschiedenen Anströmwinkel wurden Rechnungen durchgeführt,

und zwar mit einem 97 x 52 x 52 H-Gitter, das 5 Gitterpunkte über den Spalt zwischen der Schaufelspitze und dem Gehäuse aufwies. Dieses Gitter ist im Nachlauf sicher nicht fein genug. Für die Rechnung wurde die inkompressible Ausgangsversion verwendet. Im Experiment war die Strömungsgeschwindigkeit von der Größenordnung 100 m/s, so daß dort schon gewisse Kompressibilitätseinflüsse auftraten. In der Rechnung kam das k-ε Modell mit Wandfunktionen zum Einsatz, das die Details der Grenzschichtentwicklung und natürlich auch den Umschlag in Ablöseblasen nicht nachvollziehen kann. Trotzdem konnte das Grobverhalten der Strömung wie Ablösung im Schaufel-/Nabenbereich und die Druckverteilung auf den Schaufeln sowie der Nabe und dem Gehäuse realistisch simuliert werden, und zwar mindestens so gut wie in den früheren Rechnungen von Gallus et al. [28]. Die Grenzschichtentwicklung und auch der Abströmwinkelwinkel waren dabei jedoch nicht in guter Übereinstimmung mit den Meßergebnissen. Die durchgeführten Rechnungen können nur als vorläufig gelten, weshalb hier keine Ergebnisse vorgestellt werden. Sie müßten wiederholt werden mit der kompressiblen Version des Codes, mit einem feineren numerischen Gitter und mit dem entwickelten Umschlagmodell für Ablöseblasen, doch konnten solche Rechnungen aus Zeitgründen leider nicht mehr durchgeführt werden.

6.1 Ebenes Turbinengitte von Gregory-Smith und Cleak

Über mehrere Jahre wurden 3D Testrechnungen für das von Gregory-Smith und Cleak [29] experimentell untersuchte ebene Turbinengitter durchgeführt. Dieses wurde auch als Testfall für eine Serie von ERCOFTAC * Workshops ausgegeben, und für zwei dieser Workshops wurden Rechenergebnisse eingereicht. Die Versuchsanordung und die Profilkontur sind in Bild 25 dargestellt, das auch die wichtigsten Daten bezüglich des Gitters und der ankommenden Grenzschicht auf den Endplatten gibt sowie die Lage der Meßebenen. Es wurden Druckverteilungen um das Schaufelprofil gemessen, Totaldruck und statischer Druck in den Meßebenen sowie die Geschwindigkeiten, aus denen die Sekundärströmung und der Strömungswinkel bestimmt werden konnten. Außerdem wurde die Turbulenzenergie gemessen. Detaillierte Messungen in den Grenzschichten liegen nicht vor, doch wurde in [30] über Intermittenzmessungen in der Nähe der verschiedenen Wände berichtet, die Aufschluß über das Grenzschichtverhalten geben. Es bilden sich verschiedene Sekundärströmungswirbel aus, so auf Grund der Krümmung ein relativ großer und ausgeprägter Kanalwirbel, sowie zwei Äste des von der Ecke zwischen Vorderkante und Seitenwand ausgehenden Hufeisenwirbels. Auf der Saugseite verläuft dieser Wirbel in der Ecke zwischen Schaufel und Seitenwand, während der druckseitige Ast den Kanal

---

* European Research Community on Flow, Turbulence and Combustion

überquert und sich mit dem großen Kanalwirbel verbindet. Der Kanalwirbel beginnt in der Nähe der Druckseite an der Seitenwand, wandert dann hin zur Saugseite und von der Seitenwand weg. Der Kanalwirbel schert die ankommende Seitenwandgrenzschicht in einen sogenannten Verlustkern ab, und eine neue Seitenwandgrenzschicht bildet sich stromab aus. Die Intermittenzmessungen deuten an, daß diese weitgehend zunächst laminar ist und erst später wieder umschlägt. Außerdem zeigen die Messungen, daß auf der Saugseite die Grenzschicht bis 80% der Sehnenlänge im Mittelschnitt laminar ist und nur in Seitenwandnähe schon früher turbulent wird. Auf der Druckseite stellt sich zunächst eine turbulente Grenzschicht ein, die aber im hinteren Bereich auf Grund der starken Beschleunigung relaminarisiert. Insgesamt sind also die Strömungsverhältnisse trotz der noch relativ einfachen Geometrie des ebenen Gitters äußerst komplex.

Der Testfall wurde in einem relativ frühen Stadium des Projekts zunächst mit einem 108 x 36 x 22 H-Gitter berechnet, und zwar nur unter Verwendung des Standard k-ε Modells mit Wandfunktionen. Es wurden dabei jedoch verschiedene Diskretisierungsverfahren für die konvektiven Glieder getestet, und Bild 26 zeigt die axiale Entwicklung der querschnittsgemittelten Werte des Totaldruckverlustbeiwerts und des Sekundärströmungskoeffizienten, der die in der Sekundärströmung enthaltene kinetische Energie charakterisiert. Das Bild zeigt, daß bei Verwendung des hybriden Zentral/Aufwinddifferenzenverfahrens (HDS) die Verluste wesentlich zu groß berechnet werden und die durch dieses Verfahren eingeführte numerische Diffusion auch die sekundäre Strömung dämpft. Mit den genaueren QUICK und HLPA Verfahren liegen dagegen die Ergebnisse wesentlich näher an den experimentellen Werten. In Bild 27 sind über die Teilung gemittelte Werte des Strömungswinkels, des Druckverlustbeiwerts, des Sekundärströmungsbeiwerts und der turbulenten kinetischen Energie in Spannweitenrichtung (von der Seitenwand, $z = 0$ bis zum Mittelschnitt) aufgetragen. Auch hier zeigt sich ganz klar, daß das hybride Differenzenverfahren zu große Verluste und eine Dämpfung der Sekundärströmung bewirkt. Mit diesem Verfahren erzielte Ergebnisse sollen daher nicht weiter betrachtet werden. In Bild 27 sind auch Ergebnisse mit dem genaueren HLPA-Verfahren dargestellt, und zwar für zwei verschiedene Werte des Verhältnisses der Wirbelviskosität zur molekularen Viskosität, μ_t/μ, am Einströmquerschnitt, welche das Längenmaß der Turbulenz dort festlegt. Die mit dem niedrigeren Wert $\mu_t/\mu = 10$ durchgeführten Rechnungen zeigen im allgemeinen eine wesentlich bessere Übereinstimmung mit den Messungen, außer für die Turbulenzenergie, welche hier wesentlich zu niedrig vorhergesagt wird. Bei Verwendung von $\mu_t/\mu = 100$ wird zwar das richtige Niveau der Turbulenzenergie vorhergesagt, doch führt dieser Wert zu einer Verschmierung der Verteilungen der anderen Größen und deshalb zu schlechterer Übereinstimmung mit den Meßergebnissen.

In einer späteren Phase des Projekts wurden die Rechnungen mit wesentlich verbesserten I-Gittern durchgeführt, wobei diese nicht-Punkt-zu-Punkt periodisch waren und deshalb nur wenig verzerrt. Es kam außerdem nur noch das genauere HLPA Diskretisierungsverfahren zum Einsatz. Bei diesen neueren Rechnungen wurden sowohl das k-ε Modell mit Wandfunktionen eingesetzt als auch das Zweischichten-TLK-Turbulenzmodell. Die Rechnungen mit dem ersteren Modell wurden auf einem 148 x 63 x 35 Gitter durchgeführt, das in Bild 28 dargestellt ist, die Rechnungen mit dem Zweischichtenmodell auf einem feineren 183 x 94 x 41 Gitter. Außerdem wurde $\mu_t/\mu = 100$ verwendet, um das Niveau das Turbulenzenergie richtig zu erhalten. Die Druckverteilungen entlang der Saug- und der Druckseite sind für verschiedene Abstände von der Seitenwand in Bild 29 dargestellt. Es ergeben sich keine signifikanten Unterschiede zwischen den beiden Turbulenzmodellen und beide liefern eine relativ gute Übereinstimmung mit den gemessenen Druckverteilungen. Die dem Bild 27 entsprechenden Ergebnisse für über die Teilung gemittelte Werte aus der neuen Rechnung sind in Bild 30 dargestellt für die Mittenebene 10 stromab der Hinterkante. Wieder sind keine allzu großen Unterschiede zwischen den beiden Turbulenzmodellen zu erkennen. Die Übereinstimmung mit den Experimenten ist insgesamt nicht schlecht, doch werden Strömungswinkel, Druckverlustbeiwert und auch Sekundärströmungsbeiwert nicht so gut berechnet wie in der früheren Rechnung mit $\mu_t/\mu = 10$ (Bild 27). Wie dort gezeigt, werden bei Verwendung von $\mu_t/\mu = 100$ die Verteilungen zu sehr verschmiert. Allerdings wird nun der Sekundärströmungsverlustkern auch bei Verwendung von $\mu_t/\mu = 10$ erhalten, was auf die Verwendung des feineren numerischen Gitters zurückzuführen ist. Außerdem ergeben die neuen Rechnungen wegen Verwendung des höheren μ_t/μ-Werts das richtige Niveau für die Turbulenzenergie.

In Bild 31 ist, ähnlich wie in Bild 26, die axiale Verteilung von querschnittsgemittelten Werten für den Verlustbeiwert, den Sekundärströmungsbeiwert und die turbulente kinetische Energie aufgetragen. Es ergeben sich auch hier keine großen Unterschiede zwischen den zwei Turbulenzmodellen und die Übereinstimmung mit dem Experiment ist insgesamt mittelmäßig. Insbesondere sind die Verluste noch etwas zu hoch, was daher rühren könnte, daß die Grenzschicht voll turbulent gerechnet wurde, während im Experiment der größere Teil laminar bzw. transitional war. In Bild 32 werden berechnete und gemessene Sekundärströmungsvektoren an den Meßquerschnitten 5, 8 und 10 verglichen. An allen drei Querschnitten ist die Größe der Sekundärbewegung zu klein berechnet. Beim Querschnitt 5 ist das Zentrum der Sekundärströmungswirbel außerdem weiter von der Ecke zwischen Saugseite und Seitenwand entfernt als in der Messung; das Meßergebnis ist allerdings an dieser Stelle etwas im Widerspruch zur allgemeinen Beobachtung, daß der Kanalwirbel von der Seitenwand an der Druckseite ausgeht und erst im Verlauf des

Durchwanderns des gekrümmten Kanals zur Saugseite hinwandert. Beim Meßquerschnitt 8 in der Nähe der Hinterkante ist die Lage des Wirbelzentrums recht gut berechnet, während stromab der Hinterkante beim Meßquerschnitt 10 der berechnete Wirbel etwas zu nah an der Saugseite und nicht weit genug von der Seitenwand entfernt zu liegen kommt. Die Konturen des Druckverlustbeiwertes (Bild 33) werden realistisch mit zwei Maxima berechnet, wobei allerdings die Maximalwerte etwas zu groß berechnet werden. Ähnliche Übereinstimmung ist aus den Konturen des statischen Drucks zu erkennen, wobei aber hier das Maximum zur Ecke Saugseite/Seitenwand hin verlagert ist. Die Übereinstimmung für die Wirbelstärke und die Strömungswinkel ist ähnlich (Bild 33).

Insgesamt geben die neueren Rechnungen mit der wesentlich besseren numerischen Auflösung aber bei Verwendung des höheren Einströmwerts μ_t/μ zu viel Verlust und ein zu starkes Verschmieren der Verteilungen der einzelnen Strömungsgrößen, und zwar ohne große Unterschiede zwischen dem Zweischichtenmodell und dem k-ε Modell mit Wandfunktionen. Mit beiden werden die Grenzschichten als voll turbulent betrachtet und berechnet, und eine Reduzierung der Verluste und der Verschmierung könnte sich ergeben, wenn das Zweischichtenmodell mit einem Umschlagmodell kombiniert wird, so daß die im Experiment beobachteten teilweise laminaren und transitionalen Grenzschichten simuliert werden können.

6.2 3D Schaufelkanalströmung von Vorhaben 1.1.1.12 (RWTH Aachen)

Als letzter Testfall wurde die 3D Schaufelkanalströmung nachgerechnet, die im Parallelvorhaben 1.1.1.12 an der RWTH Aachen experimentell untersucht wurde [31]. Es handelt sich hierbei um ein vereinfachtes Turbinengitter, bei dem in einem ebenen Strömungskanal eine Schaufel in der Mitte plaziert wurde und die Kanalwände so konturiert waren, daß sie das Vorhandensein von Nachbarschaufeln approximierten (siehe Bild 34). Mit dieser Versuchsanordnung wurde allerdings keine volle Periodizität erreicht. Im Parallelvorhaben wurde die inkompressible Schaufelkanalströmung untersucht, und zwar durch Sichtbarmachungsexperimente, Messung der Wanddruckverteilungen, der Grenzschichten auf dem Boden und der Schaufel mit Einsensor-Hitzdrahtsonden, des Strömungsfeldes im Schaufelkanal und im Nachlauf mit Dreisensor-Hitzdrahtsonden und der Totaldruckverteilung mit Pitot-Sonden Es wurden zwei Versuche durchgeführt, einer davon war mit laminarer Anströmung, wobei die Schaufel auf der Grenzschicht weitgehend laminar blieb, so daß dieser Fall für Turbulenzmodelltestrechnungen nicht geeignet ist. In einem zweiten Versuch wurde ein Gitter zur Erzeugung einer turbulenten Anströmung mit Tu = 0,8% vorgeschaltet. Außerdem wurde, um eine Relaminarisierung der Grenzschicht auf der Schaufel zu vermeiden und definierte Transitionspunkte zu erhalten, sowohl auf der Druck- wie auf

der Saugseite bei 10% Sehnenlänge ein Stolperdraht angebracht. Es wurde nur dieser zweite Fall nachgerechnet; da bei ihm die Grenzschicht praktisch von der Vorderkante an sowie auch auf dem Boden voll turbulent war, kam nur das k-ε Modell mit Wandfunktionen zum Einsatz. Das Rechengebiet ist in Bild 34 dargestellt; es reicht vom Kanalboden bis zum Mittelschnitt (z = 191 mm). Die Einströmebene liegt 300 mm stromauf der Vorderkante und die Ausströmebene 450 mm stromab der Hinterkante, wobei die Sehnenlänge der Schaufel 300 mm ist. Für die Konturen des Kanals und die Schaufelgeometrie wurden die vom Parallelvorhaben vorgegebenen Daten verwendet. Bild 35 zeigt das für die Rechnung verwendete 120 x 82 x 20 I-Gitter, das eine Verfeinerung in der Nähe der Schaufelwände und der konturierten Seitenwände des Kanals aufweist.

In Bild 36 sind die im Mittelschnitt berechneten Druckkonturen dargestellt. Das Bild zeigt klar, daß die Druckverteilung in den beiden durch die Schaufel gebildeten Kanälen zwar ähnlich, aber nicht gleich ist, so daß in der Tat keine periodischen Verhältnisse vorliegen. In Bild 37 sind die Druckverteilungen entlang der Druck- und Saugseite der Schaufel in verschiedenen Abständen vom Boden dargestellt. Auf der Druckseite stimmen die berechneten Verteilungen recht gut mit den gemessenen überein, während auf der Saugseite das Druckminimum nicht richtig berechnet wird und die flache Druckverteilung eine zu geringe Beschleunigung im Mittelbereich der Saugseite andeutet. Dies wird auch durch die in Bild 38 gezeigten Geschwindigkeitsprofile bestätigt. Diese Unterschiede zwischen Rechnung und Messung sind schwer zu verstehen und zu erklären; eine mögliche Erklärung wäre, daß die in der Rechnung vorgegebene Geometrie des konturierten Schaufelkanals etwas von der im Experiment verwendeten abweicht. Es genügen hier schon relativ geringe Abweichungen in der Kontur der Kanalwände, um die Druckverteilung relativ stark zu ändern. In Bild 38 sind Profile der Längsgeschwindigkeit entlang Schnitten senkrecht zur Saugseite in verschiedenen Abständen vom Boden und bei verschiedenen Längspositionen x dargestellt. Es zeigt sich hier klar die zu gering berechnete Beschleunigung der Strömung im Mittenbereich der Saugseite, während im vorderen Bereich und auch im Hinterkantenbereich das Geschwindigkeitsniveau und die Verteilung im allgemeinen richtig vorhergesagt wird; auch weiter von der Schaufeloberfläche entfernt stimmt das Geschwindigkeitsniveau im allgemeinen gut mit den Messungen überein.

Bild 39 zeigt, daß die Verteilung der Geschwindigkeit in der Grenzschicht der Saugseite insgesamt sehr gut berechnet wird, wenn auch im vorderen Bereich die Auflösung mit dem verwendeten Rechennetz nicht besonders gut war und deshalb dort nur wenige Gitterpunkte in der Grenzschicht zu liegen kommen. In diesem Bild ist die lokale Geschwindigkeit in der Grenzschicht mit der Geschwindigkeit U_a am Grenzschichtrand (Stelle des Geschwindigkeitsmaximums) dimensionslos gemacht, so daß die in Abb. 38 zutage getre-

tenen Unterschiede im Niveau der Geschwindigkeit in der Nähe der Saugseite hier nicht auftreten. In Bild 39 sind ebenfalls die Verteilungen der Längsturbulenzschwankungen $\sqrt{\overline{u'^2}}/U_a$ in der Grenzschicht der Saugseite dargestellt. Die berechneten Werte wurden aus den berechneten k-Werten unter der Annahme $\overline{u'^2} \approx k$ bestimmt, die in Wandnähe gilt, aber für die wandferneren Bereiche $\overline{u'^2}$ im Vergleich zu k etwas zu groß angibt. Deshalb stimmen in Wandnähe die Rechnungen recht gut mit den Messungen überein, während im wandfernen Bereich im allgemeinen die berechneten Längsschwankungen höher als die gemessenen liegen. Auch hier wirkt sich im vorderen Bereich natürlich die mangelnde Auflösung aus. Entsprechende Geschwindigkeits- und Längsschwankungsprofile sind für die Bodengrenzschicht entlang einer Linie mit Abstand y/t = 0.14 von der Saugseite in Bild 40 dargestellt. Da in Bodennähe das Rechennetz nicht so stark verfeinert ist wie in der Nähe der Schaufelwände, ist die Auflösung der Bodengrenzschicht insgesamt nicht so gut wie diejenige der Schaufelgrenzschicht, was sich durch eckige Verteilungen bemerkbar macht. Trotzdem wird aber insgesamt die Form des Geschwindigkeitsprofils näherungsweise richtig berechnet. Allerdings kann mit dem relativ groben Gitter das in den Messungen beobachtete Maximum der Längsschwankungen in direkter Wandnähe nicht erhalten werden; dafür liegt der erste Gitterpunkt zu weit von der Wand weg. Weiter entfernt von der Wand wird die Verteilung jedoch richtig wiedergegeben.

In Bild 41 sind berechnete und gemessene Vektoren der Sekundärströmungsgeschwindigkeit in verschiedenen axialen Querschnitten dargestellt, und zwar jeweils Geschwindigkeiten relativ zu den entsprechenden Sekundärgeschwindigkeiten im Mittelschnitt. Bei x/l_{ax} = 0.18 ist der im Uhrzeigersinn drehende Hufeisenwirbel in der Ecke zwischen Schaufel und Boden klar zu erkennen. Weiter ist der noch schwache, im Gegenuhrzeigersinn drehende Kanalwirbel zu sehen, der von der Druckseite und vom Boden ausgeht. Beim Durchlaufen des gekrümmten Kanals nimmt dieser Kanalwirbel an Stärke zu und bewegt sich zur Saugseite hin. Er verdrängt dort den Hufeisenwirbel bzw. löst ihn auf - im Experiment befindet er sich zunächst noch in der Ecke, ist aber schwer sichtbar und wird dann vom Kanalwirbel auf der Schaufel nach oben gedrängt. In der Rechnung ist er allerdings ab $x/l_{ax} \approx 0.5$ nicht mehr identifizierbar; er wird dort durch den gegendrehenden, viel stärkeren Kanalwirbel aufgelöst. Im Nachlauf befindet sich das Zentrum des Wirbels bei ca. 8% der Teilung von der Hinterkantenlinie entfernt; der vom anderen Kanal ausgehende Wirbel hat sein Zentrum in der Nähe der als Saugseite des Nachbarprofils fungierenden Kanalwand. Die Übereinstimmung zwischen Rechnung und Messung bezüglich des Wirbels im Nachlauf ist gut. Insgesamt wird die Entwicklung des Kanalwirbels in guter Übereinstimmung

mit der Messung berechnet, und zwar sowohl die Lage wie auch die Stärke und die Ausdehnung.

Zusammenfassend kann zu diesem Testfall gesagt werden, daß die Druckverteilung auf der Saugseite und entsprechend auch die Absolutwerte der Geschwindigkeit relativ große Abweichungen zu den Messungen zeigen, was eventuell von gewissen Abweichungen der in Rechnung und Messung verwendeten Kanalkontur herrührt. Die relativen Sekundärgeschwindigkeiten (bezogen auf Werte im Mittelschnitt) und insbesondere die Ausbildung des Kanalwirbels wird jedoch gut vorhergesagt, während der wesentlich schwächere Hufeisenwirbel in der Rechnung im Verlauf des Durchwanderns des gekrümmten Kanals verloren geht. Auch die Grenzschichtentwicklung auf der Saugseite der Schaufel wird insgesamt gut berechnet. Es sollte jedoch angemerkt werden, daß es sich diesbezüglich hier nicht um einen besonders anspruchsvollen Testfall handelte, da weder Umschlag noch Ablösung auftraten. Deshalb konnten die Rechnungen auch erfolgreich mit dem Standard k-ε Modell mit Wandfunktionen durchgeführt werden.

7 SCHLUSSBEMERKUNGEN

Es wurden numerische Verfahren zur Berechnung turbulenter Strömungen in Schaufelgittern entwickelt und getestet. Dabei ging es primär um die Verbesserung und das Austesten von Turbulenzmodellen zur Beschreibung der turbulenten Austauschvorgänge, aber für das Austesten mußten auch geeignete numerische Verfahren bereitgestellt und weiterentwickelt werden. Dies erforderte mehr Arbeitsaufwand, als ursprünglich vorgesehen war, vor allem, da sich H-Rechennetze und Punkt-zu-Punkt periodische Rechennetze für die Gitterströmungsberechnungen als nicht so geeignet erwiesen. Das Finite-Volumen Verfahren wurde deshalb zur Verwendung von I-Rechennetzen und nicht-Punkt-zu-Punkt periodischen Rechennetzen modifiziert, wobei erstere eine wesentlich verbesserte Auflösung im Vorder- und Hinterkantenbereich erlauben und letztere zu bedeutend weniger verzerrten Rechennetzen führen. Mit diesen Netzen konnte die numerische Genauigkeit und die Konvergenz des Lösungsverfahrens wesentlich gesteigert werden. Einen erheblichen Aufwand erforderte auch die Erweiterung des ursprünglich inkompressiblen Finite-Volumen Verfahrens zur Berechnung kompressibler transsonischer Strömungen und das Austesten des neuen Verfahrens, wobei vor allem auf eine gute Erhaltung von Verdichtungsstößen geachtet werden mußte. Als Ergebnis der umfangreichen Entwicklungsarbeiten steht jetzt ein leistungsstarkes Finite-Volumen Verfahren auf der Basis der Druckkorrekturmethode zur Verfügung, das für den gesamten Geschwindigkeitsbereich von völlig inkompressiblen

Strömungen bis zu Überschallströmungen eingesetzt werden kann und auf die besonderen Eigenarten von Gitterströmungen angepaßt ist.

Den Schwerpunkt der Turbulenzmodellentwicklung stellte die Einführung von Zweischichtenmodellen dar. Dabei wurde von den im Ausgangs-k-ε-Turbulenzmodell verwendeten Wandfunktionen abgegangen und es wird bei Zweischichtenmodellen die viskose Unterschicht in direkter Wandnähe mit einem Eingleichungsmodell aufgelöst. Es wurden zwei Varianten des Eingleichungsmodells eingeführt und getestet, und zwar eine Variante mit $\sqrt{k}$ als Geschwindigkeitsmaßstab der Turbulenz und eine zweite Variante, die auf der Basis direkter numerischer Simulationsdaten entwickelt wurde, mit den Querschwankungen $(\overline{v'^2})^{1/2}$ als Geschwindigkeitsmaßstab. Das letztere Modell ist vom Konzept her überlegen und beschreibt die Details der Turbulenz in der Nähe von Kanalwänden besser, aber bei Strömungen mit Ablösung ergaben sich keine merkbaren Unterschiede in den Ergebnissen. Da das auf $\sqrt{k}$ basierende Modell (TLK) inzwischen auch schon anderweitig wesentlich ausführlicher getestet wurde, kam diese Version bei den Rechnungen für Gitterströmungen zum Einsatz. Die vergleichenden Testrechnungen mit dem Ausgangs-k-ε-Modell mit Wandfunktionen und dem Zweischichtenmodell haben ergeben, daß der Einsatz des Zweischichtenmodells unbedingt erforderlich ist, wenn der laminar-turbulente Umschlag oder Relaminarisierung erfaßt werden sollen. Weiter konnten mit diesem Modell im Vergleich zum Modell mit Wandfunktionen bei Situationen mit größeren Ablösegebieten wesentliche Verbesserungen der Rechenergebnisse erzielt werden. Natürlich muß dies mit erhöhtem Rechenaufwand bezahlt werden, da bei Verwendung des Zweischichtenmodells ca. 10 - 15 zusätzliche Gitterpunkte in das jetzt aufzulösende wandnahe Gebiet gelegt werden müssen.

In Verbindung mit dem Zweischichtenmodell wurden zwei zusätzliche Modelle zur Simulierung des laminar-turbulenten Umschlags eingeführt, und zwar ein Modell bei Umschlag in der anliegenden und eine zweite Variante bei Umschlag in der abgelösten Grenzschicht. Beide Modelle verwenden empirische Beziehungen für den Beginn des Umschlags und für den Transitionsbereich, die unterschiedlich sind; außerdem unterscheiden sich die beiden Modelle dadurch, daß im Modell für anliegende Grenzschichten der Umschlag über den Dämpfungsparameter A^+ im Eingleichungsmodell gesteuert wird und im Umschlagmodell für abgelöste Grenzschichten über die Intermittenzfunktion γ. Die Umschlagmodelle wurden erfolgreich getestet an Schaufelprofilen sowie für das Modell für den Umschlag in Ablöseblasen auch an Strömungen über eine Stufe und um eine Profilnase, wobei die Leistungsfähigkeit über einen weiten Parameterbereich gezeigt werden konnte.

Das Ausgangs-k-ε-Modell sowie die verbesserten Modelle wurden anhand einer Reihe verschiedener 2D und 3D Verdichter- und Turbinengitterströmungen getestet. Die hierbei gesammelten Erfahrungen haben gezeigt, daß die Kernströmung in den Schaufelkanälen inklusive der Sekundärströmung sowie auch die Druckverteilung an den Wänden meist schon recht gut mit dem Ausgangs-k-ε-Modell mit Wandfunktionen berechnet werden kann, außer in Bereichen mit Stoß/Grenzschichtwechselwirkung. Allerdings traten bei den untersuchten Testfällen keine größeren Ablösungen auf. Insbesondere wird für eine für praktische Zwecke ausreichend realistische Simulierung des Kanalwirbels keine verfeinerte Turbulenzmodellierung benötigt. Andererseits wird die Grenzschichtentwicklung stark durch das verwendete Turbulenzmodell beeinflußt. Hier werden beim Auftreten von Umschlag in der anliegenden oder abgelösten Grenzschicht realistische Ergebnisse nur mit dem Zweischichtenmodell zusammen mit dem entsprechenden Umschlagmodell erhalten. Die eingeführten Umschlagmodelle haben sich in den Testrechnungen bewährt. Allerdings waren die Rechnungen bisher hauptsächlich auf zweidimensionale Situationen beschränkt und es fehlen umfangreichere Untersuchungen bei dreidimensionalen Situationen. In einem relativ frühen Stadium wurde das Zweischichtenmodell auch an Partner der Vorhabensgruppe 1.1.2 übergeben und dort zum Teil in deren Navier-Stokes-Berechnungsverfahren eingesetzt.

Zum Schluß sei erwähnt, daß die nachfolgenden Anhänge B und C in den Proceedings des 1995 ASME International Mechanical Engineering Congress and Exposition, San Francisco, veröffentlicht wurden und auch zur Veröffentlichung im ASME Journal of Turbomachinery eingereicht sind. Etwas gekürzte Fassungen der Anhänge D und E wurden zur Präsentation auf der 1997 ASME Gas Turbine Conference in Orlando eingereicht, wobei in die Veröffentlichung zum Anhang E auch die experimentellen Ergebnisse aus dem Parallelvorhaben 1.1.1.7 aufgenommen wurden und es sich um eine gemeinsame Veröffentlichung mit diesem Vorhaben handelt.

8 LITERATURVERZEICHNIS

1. Zhu, J.: „A low-diffusive and oscillating-free convective scheme", Communications in Applied Num. Meth., Vol. 7, pp. 225-232, 1991

2. Majumdar, S., Rodi, W., Zhu, J.: „Three-dimensional finite-volume method for incompressible flows with complex boundaries", J. Fluids Eng., Vol. 114, pp. 496-503, 1992.

3. Michelassi, V.: „The Meshho programme 1.06", Report No. 1/1994, Department of Energetics, University of Florence, Italy, 1994.

4. Rodi, W.: „*Turbulence Models and their Application in Hydraulics*“, 3rd edition, Balkema Publishers, Rotterdam, 1993.

5. Patel, V.C., Rodi, W., Scheuerer, G.: „Turbulence models for near-wall and low-Reynolds-number flows: a review“, AIAA Journal, Vol. 23, pp. 1308-1319, 1985.

6. Rodi, W., Mansour, N.N.: „Low-Reynolds-number k-ε modelling with the aid of direct simulation data“, J. Fluid Mech., Vol. 250, pp. 509-529, 1993.

7. Norris, H.I., Reynolds, W.C.: „Turbulent channel flow with a moving wavy boundary“, Dept. Mech. Eng., Report FM10, Stanford University, 1975.

8. Rodi, W., Mansour, N.N., Michelassi, V.: „One-equation near-wall turbulence modelling with the aid of direct simulation data“, J. Fluids Eng., Vol. 115, pp. 196-205, 1993.

9. Driver, D.M., Seegmiller, H.L.: „Features of a reattaching turbulent shear layer in divergent channel flow“, AIAA J., Vol. 23, pp. 163-171, 1985.

10. Nakayama, A.: „Characteristics of the flow around conventional and supercritical airfoils“, J. Fluid Mech., Vol. 160, p. 155, 1985.

11. Coles, D.E., Wadcock, A.J.: „Flying-hot-wire study of flow past a NACA4412 airfoil at maximum lift, AIAA J., Vol. 117, p. 321, 1979.

12. Rodi, W.: „Experience with two-layer models combining the k-ε model with a one-equation model near the wall“, Paper AIAA-91-0216, 1991.

13. Cho, N.H., Liu, X., Rodi, W., Schönung, B.: „Calculation of wake-induced unsteady flow in a turbine cascade“, J. of Turbomachinery, Vol. 115, pp. 675-686, 1993.

14. Sieger, K., Schiele, R., Kaufmann, F., Wittig, S., Rodi, W.: „A two-layer turbulence model for the calculation of transitional boundary layers“, ERCOFTAC Bulletin No. 24, pp. 21-25, March 1995.

15. Mayle, R.E.: „The role of laminar-turbulent transition in gas turbine engines“, J. of Turbomachinery, Vol. 113, pp. 509-537, 1991.

16. Rodi, W., Schönung, B.: „Interaktives-inverses Grenzschichtverfahren zur Berechnung von lokalen Ablöseblasen an Turbinenschaufeln“, Zeitschrift für Flugwissenschaften und Weltraumforschung, Vol. 11, pp. 271-280, 1987.

17. Chen, K.K., Thyson, N.A.: „Extension of Emmons´ spot theory to flows on blunt bodies“, AIAA J., Vol. 9, pp. 821-825, 1971.

18. Gotthardt, H.: „Theoretische und experimentelle Untersuchungen an ebenen Turbinengittern mit Pfeilung und V-Stellung“, Dissertation, Universität Braunschweig, 1983.

19. Haas, W., Rodi, W., Schönung, B., Swamy, N.V.C.: „Experimentelle Untersuchung von lokalen Ablöseblasen an Gasturbinenschaufeln“, Z. Flugwiss. Weltraumforschung, Vol. 11, pp. 261-270, 1987.

20. Makiola, B.: „Experimentelle Untersuchungen zur Strömung über die schräge Stufe", Dissertation, Universität Karlsruhe, 1992.

21. Deutsch, S., Zierke, W.C.: „The measurement of boundary layers on a compressor blade in cascades", parts I, II, III, ASME Papers 87-GT-248/249/250, 1987.

22. Suryavamshi, N., Lakshminarayana, B.: „Numerical prediction of wakes in cascades and compressor rotors including the effects of mixing: part I - cascade wakes including the effects of incidence and free-stream turbulence", ASME J. of Turbomachinery, Vol. 114, pp. 607-616, 1992.

23. Giess, P.-A.: „Grenzschichtmessungen auf der Schaufeloberfläche bei transsonischer und inkompressibler Durchströmung ebener Turbinengitter", DLR Bericht IB 223-94A08, 1994.

24. Kost, F.: „Messungen des Geschwindigkeitsfeldes mit dem L2F-Velocimeter bei transsonischer und inkompressibler Durchströmung ebener Turbinengitter", DLR Bericht IB 223-94A09, 1994.

25. Klimetzek, F.R.: AG TURBO/TURBOTECH-Arbeitsgruppe „Navier-Stokes Verfahren: Abschlußbericht des Verfahrensvergleichs".

26. Michelassi, V., Martelli, F.: „3D implicit Navier Stokes solver for internal turbulent compressible flows", Journal de Phys. III, France, Vol. 3, pp. 223-235, 1993.

27. Schulz, H.D., Gallus, H.E.: „Experimental investigation of the three-dimensional flow in an annular compressor cascade", J. of Turbomachinery, Vol. 110, pp. 467-478, 1988.

28. Gallus, H.E, Hah, C., Schulz, H.D.: „Experimental and numerical investigation of the three-dimensional viscous flows and vortex motion inside an annular compressor blade row", Paper ASME 90, GT-155, 1990.

29. Gregory-Smith, D.E. and Cleak, J.G.E.: „Secondary flow measurements in a turbine cascade with high inlet turbulence", J. of Turbomachinery, Vol. 114, pp. 173-183, 1992.

30. Moore, H., Gregory-Smith, D.G.: „Transition effects on secondary flows in a turbine cascade", Paper ASME 96-GT-100, 1996.

31. Krause, E., Limberg, W., Zapp, T.: „Strömungsmessungen zur Validierung von Turbulenzmodellen in beschaufelten Kanälen mit gekrümmten Wänden", Abschlußbericht des TURBOTECH-Vorhabens 1.1.1.12, Aerodynamisches Institut der RWTH Aachen, 1996.

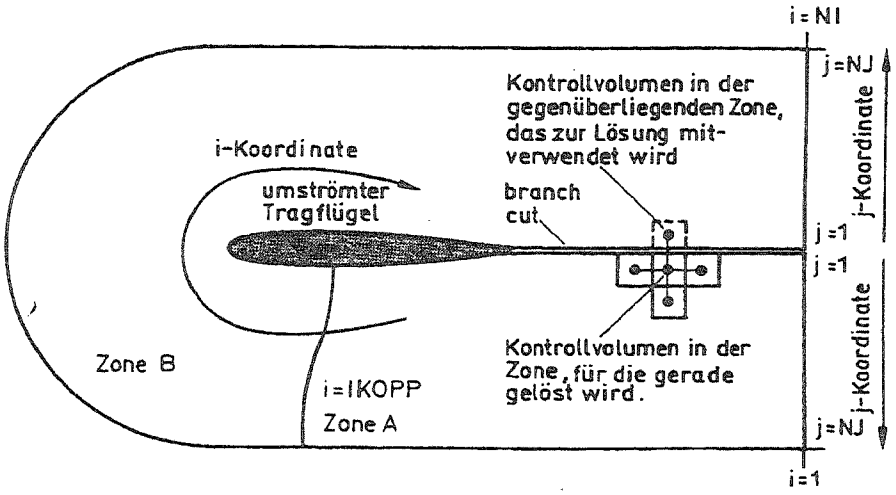

Bild 1 Die Behandlung des branchcuts bei der Verwendung von C-Gittern

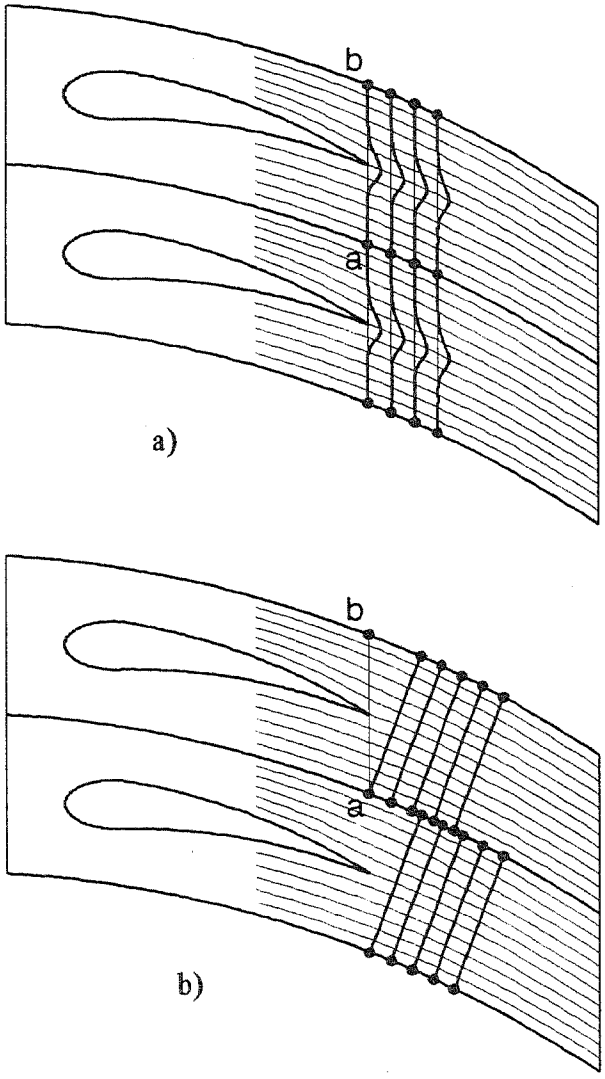

Bild 2 Punkt-zu-Punkt periodisches Gitter (a) und Nicht-Punkt-zu-Punkt periodisches Gitter (b)

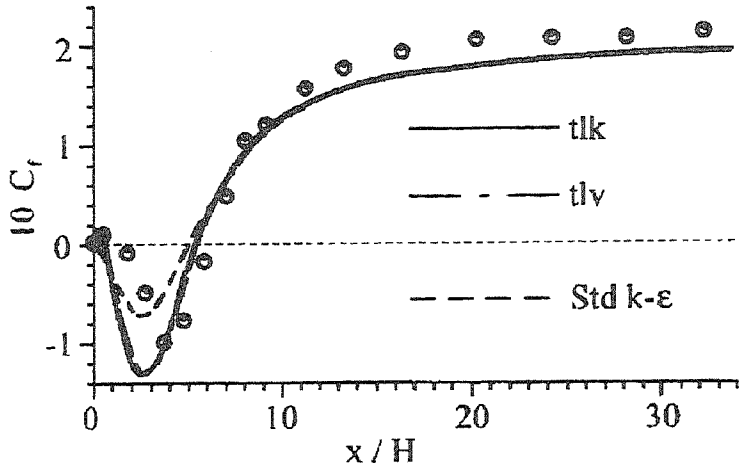

a) Verteilung des Reibungsbeiwerts entlang der unteren Wand

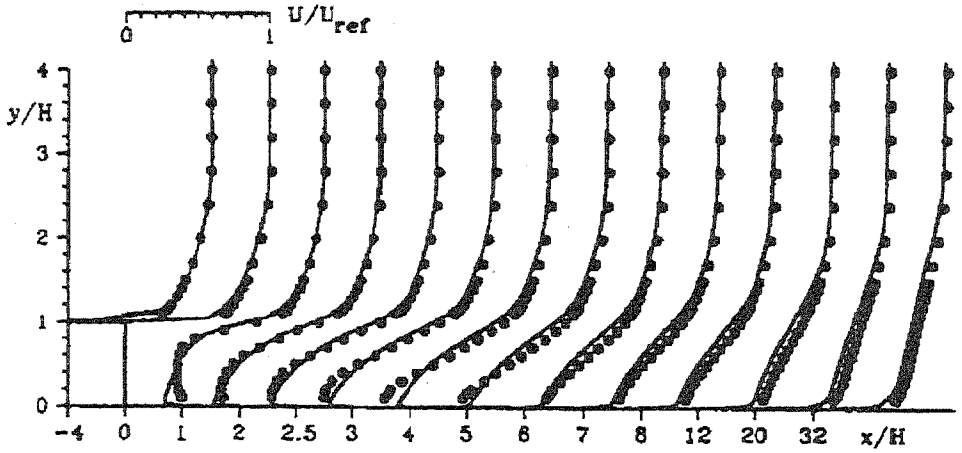

b) Geschwindigkeitsprofile

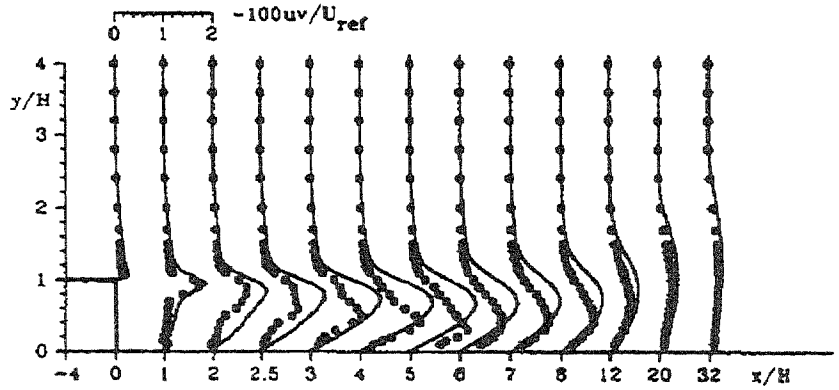

c) Schubspannungsprofile

Bild 3 Strömung über eine rückspringende Stufe; Linien sind Rechnungen, Symbole Messungen [9]

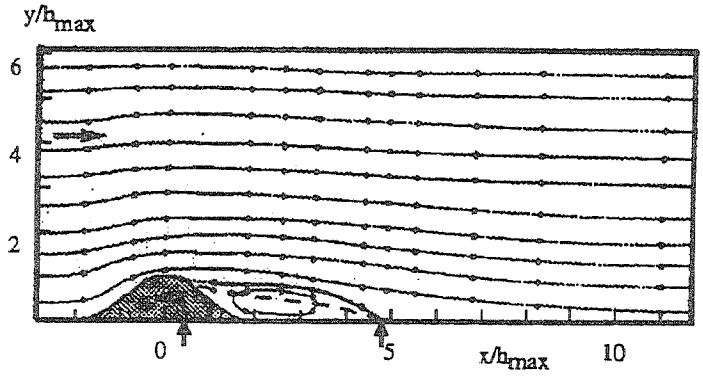

a) Experiment

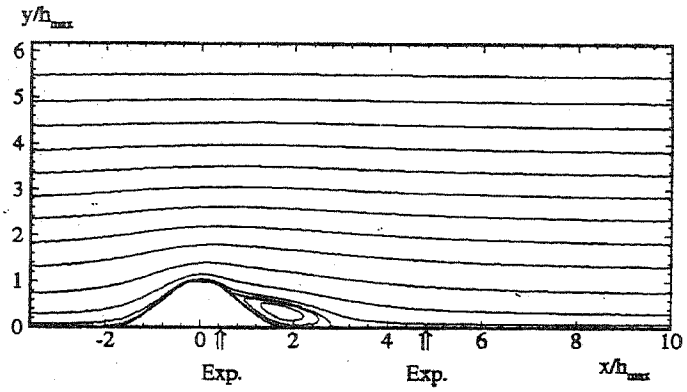

b) k-ε + WF

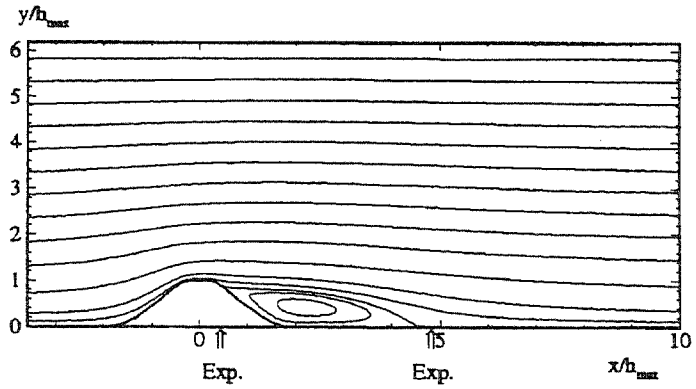

c) TLK

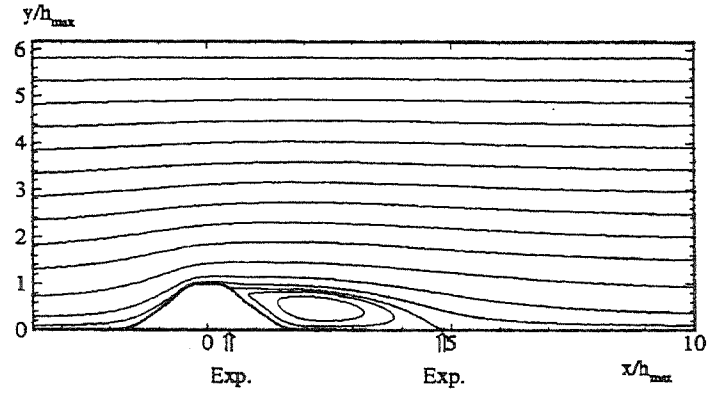

d) TLV

Bild 4 Strömung über einen 2D Modellhügel, Vergleich berechneter und gemessener Stromlinien

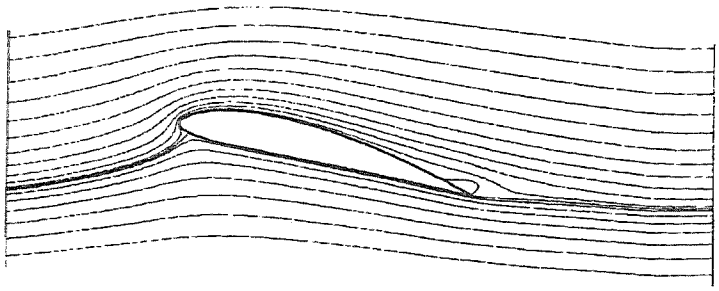

a) Berechnete Stromlinien (Zweischichtenmodell, HLPA-Verfahren)

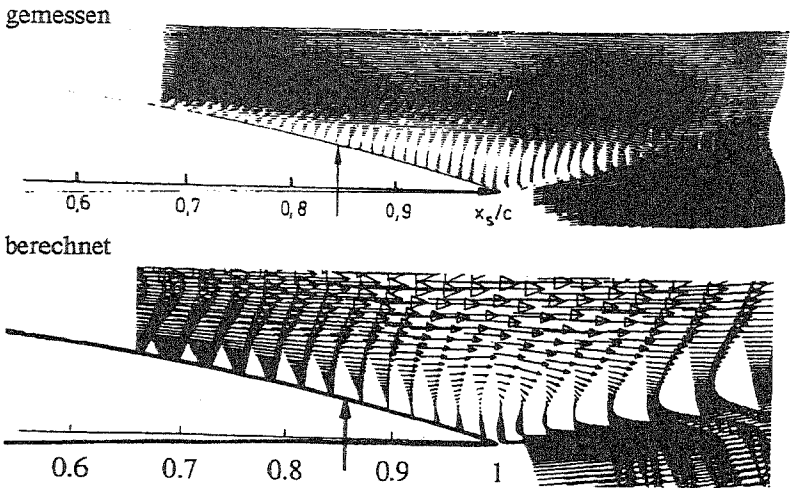

b) Geschwindigkeitsvektoren nahe der Hinterkante

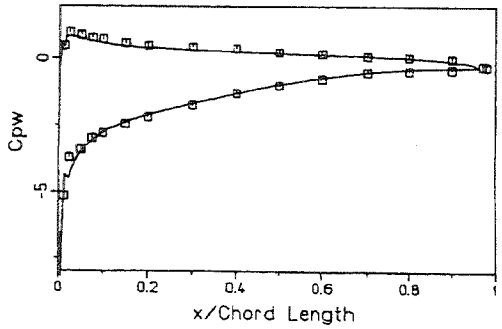

c) Druckverteilung, – Rechnung mit dem Zweischichtenmodell und HLPA-Verfahren, □ Experimente

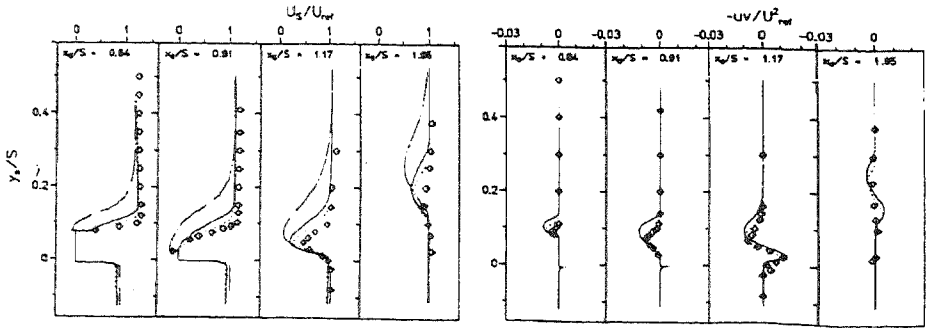

d) Verteilung von Geschwindigkeit (U_s) und Schubspannung ($\overline{uv}$); Rechnungen:
– Zweischichtenmodell mit HLPA, --- k-ε Modell mit QUICK,
. . . k-ε Modell mit Hybrid-Zentral/Aufwindverfahren, ◊ Experimente

Bild 5 Strömung um ein NACA 4412 Tragflügelprofil

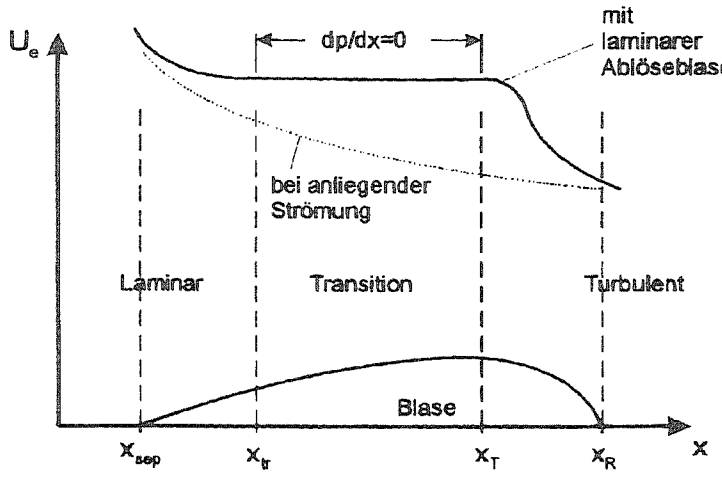

Bild 6 Prinzipskizze für Ablöseblase mit laminar-turbulentem Umschlag

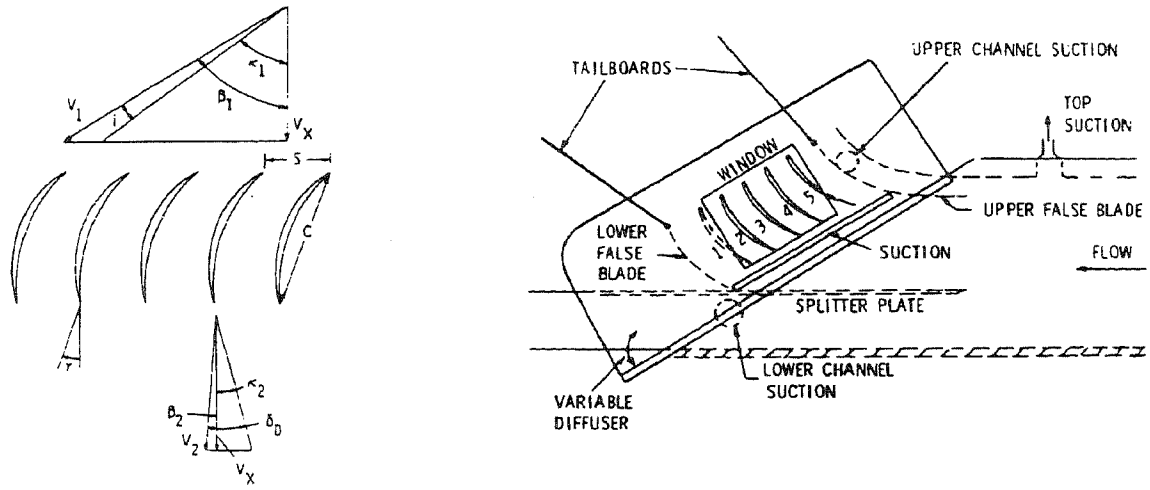

Bild 7 Versuchsaufbau für Kreisbogenverdichtergitter (von [21])

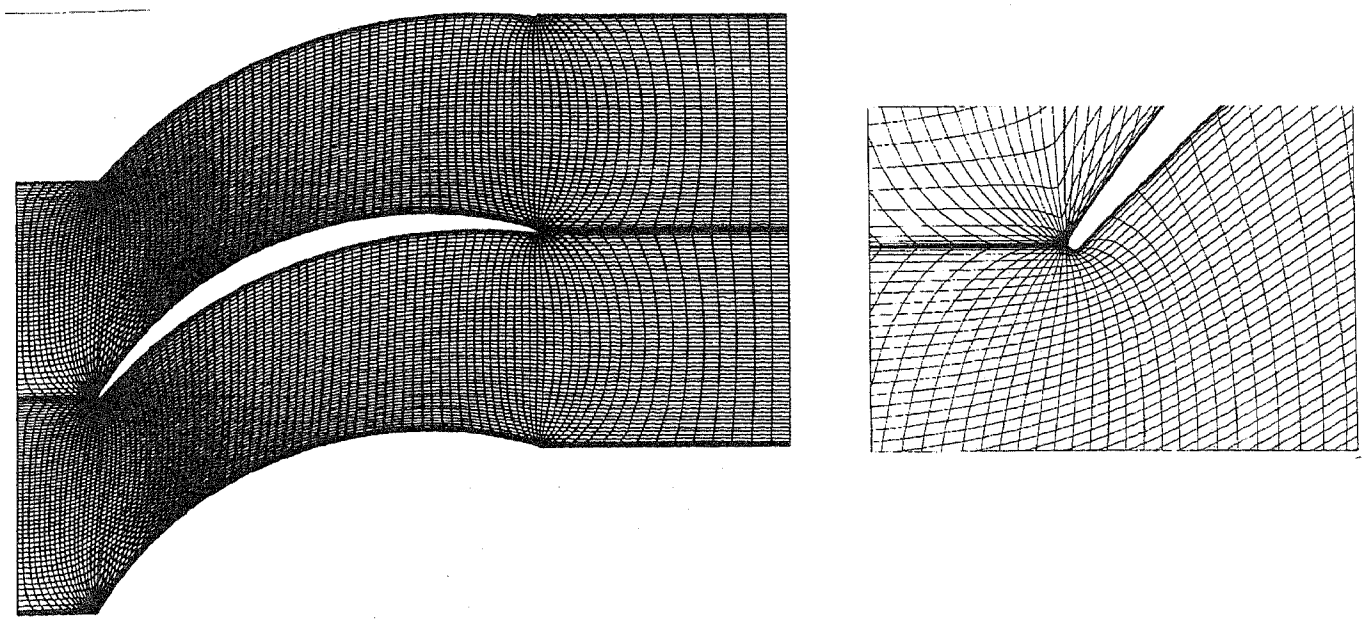

Bild 8 Rechennetz für das Kreisbogenverdichtergitter

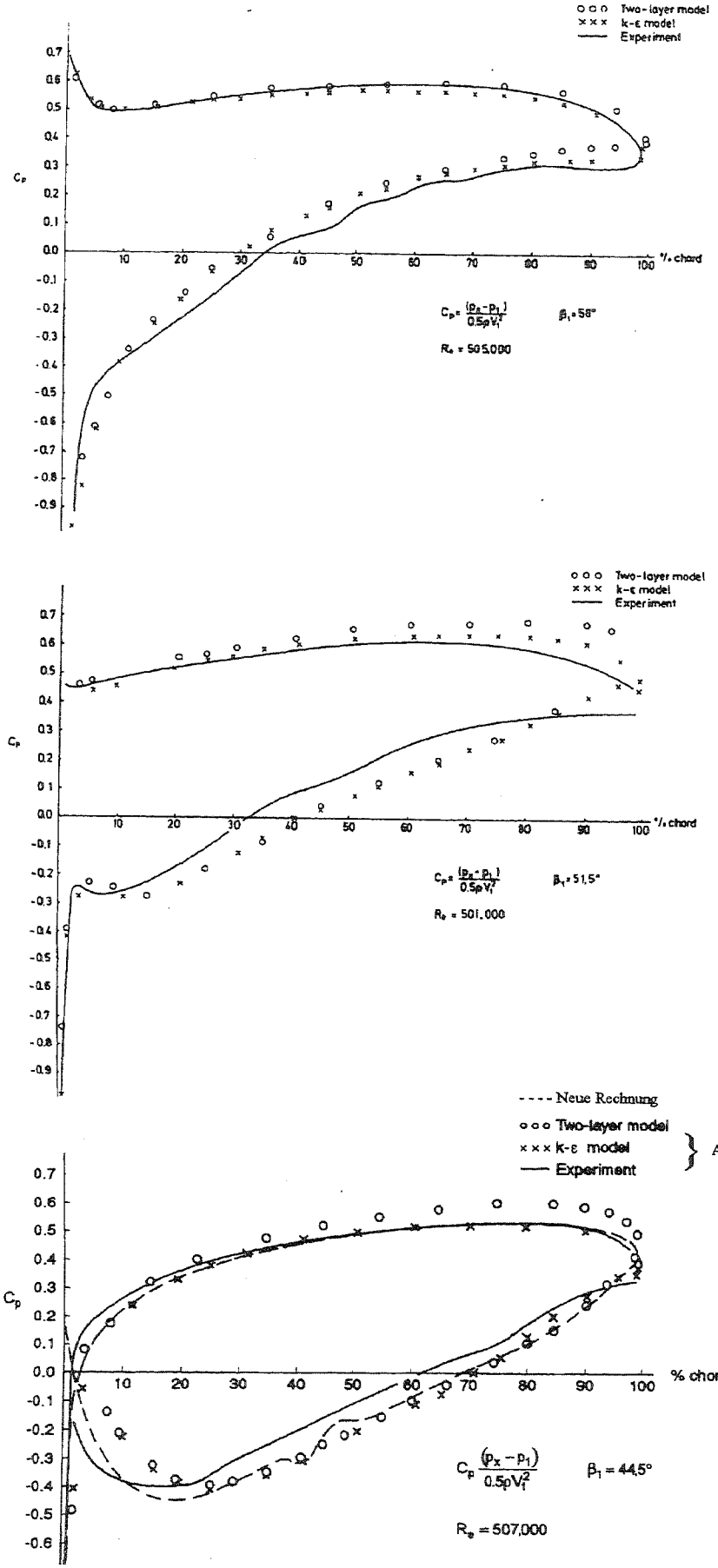

Bild 9 Druckverteilungen entlang der Druck- und Saugseite für das Kreisbogenverdichtergitter;Experimente von Zierke und Deutsch [21]

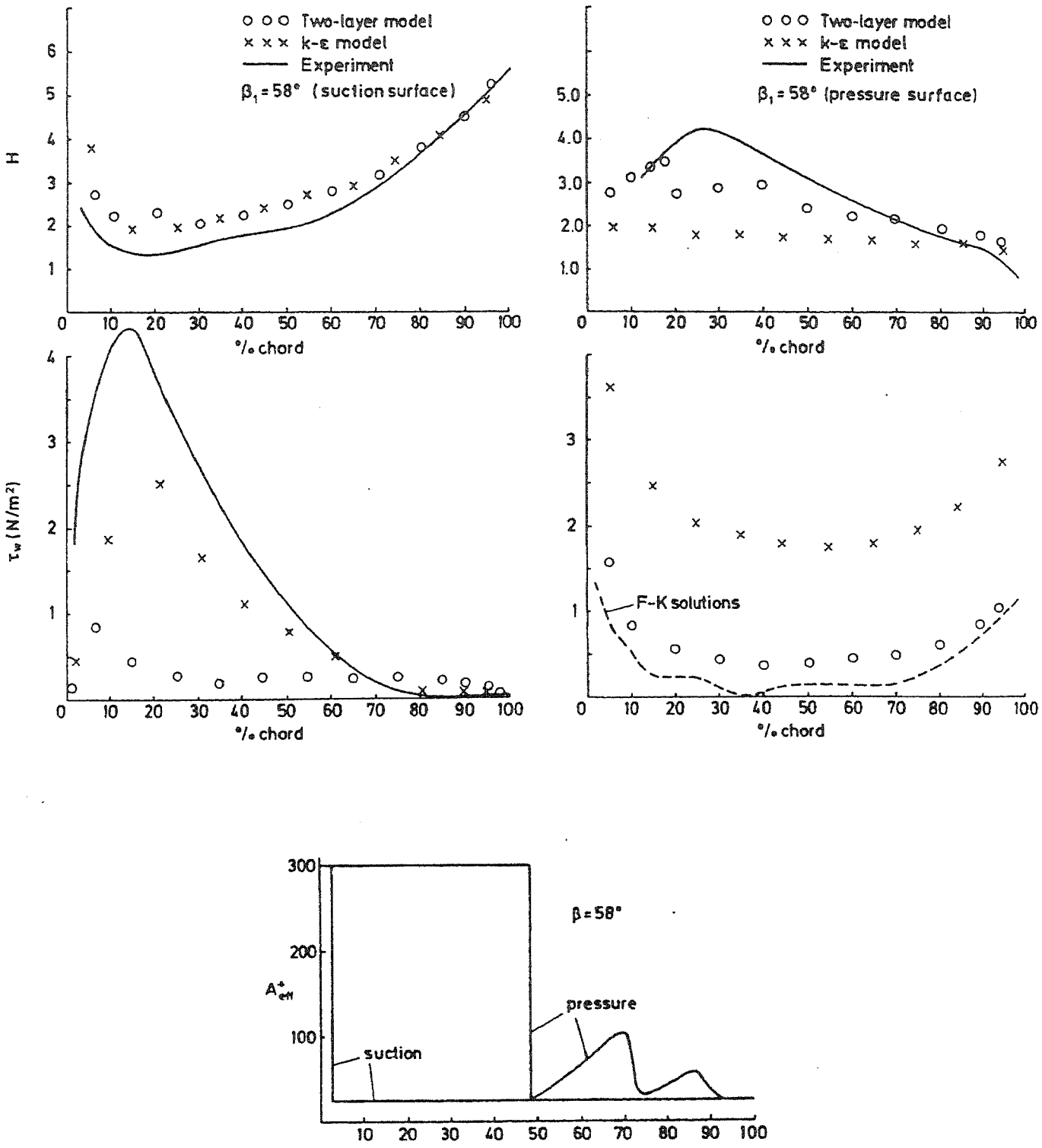

Bild 10 Verteilung von Formparameter und Wandschubspannung entlang der Schaufel des Kreisbogenverdichtergitters, Anströmwinkel $\beta_1 = 58^\circ$

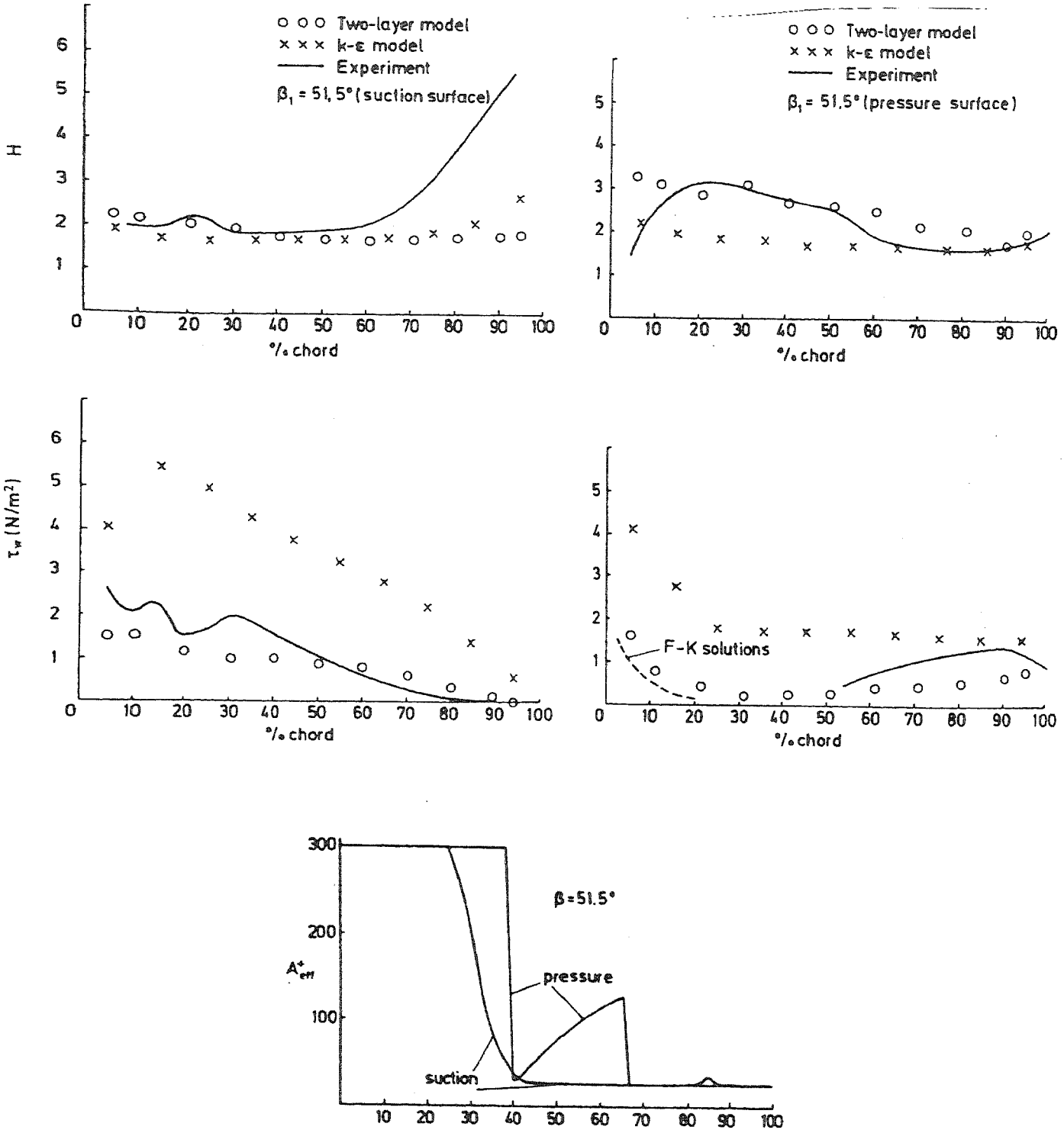

Bild 11: Verteilung von Formparameter und Wandschubspannung entlang der Schaufel des Kreisbogenverdichtergitters, Anströmwinkel $\beta_1 = 51{,}5°$

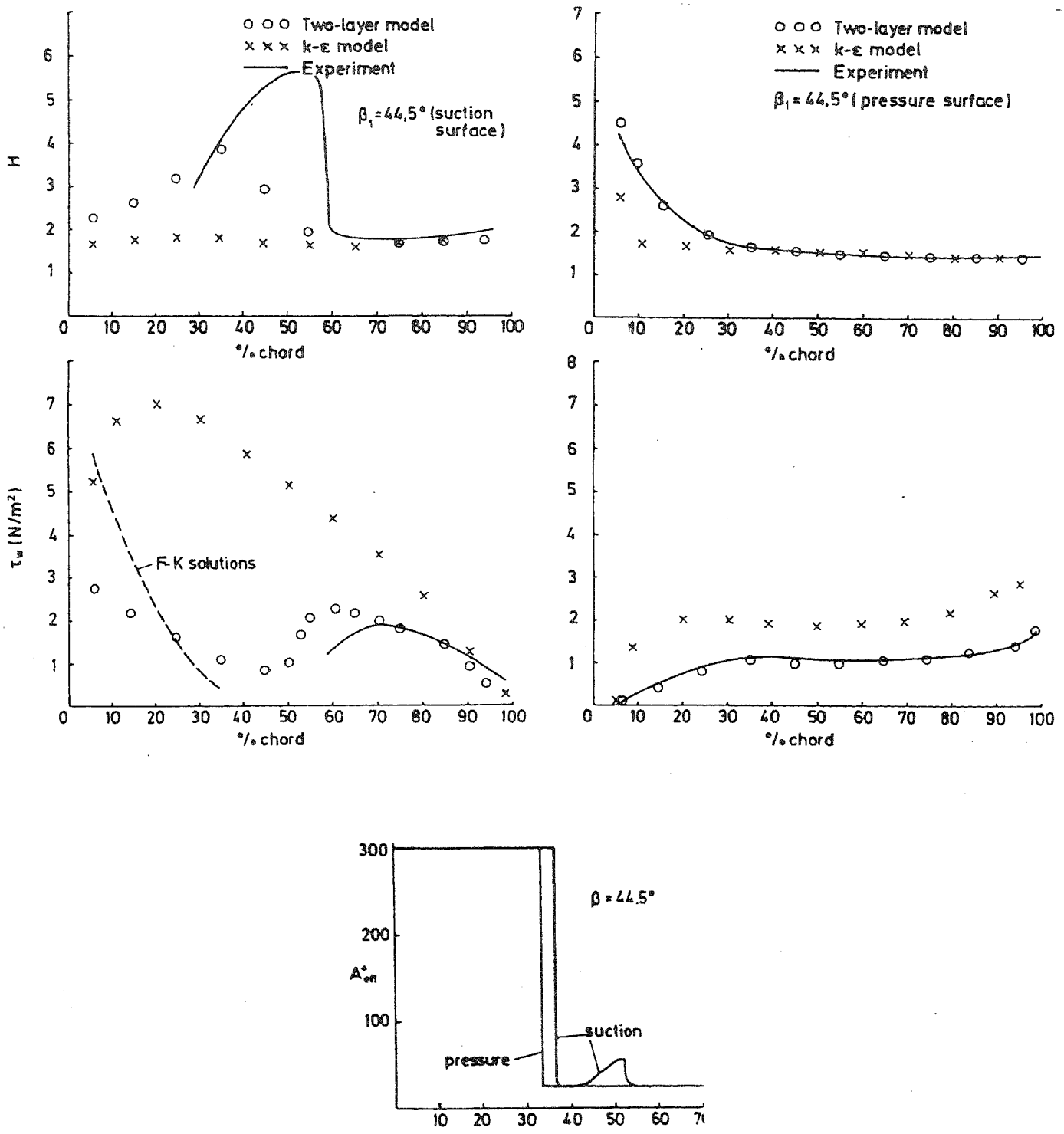

Bild 12 Verteilung von Formparameter und Wandschubspannung entlang der Schaufel des Kreisbogenverdichtergitters, Anströmwinkel $\beta_1 = 44{,}5°$

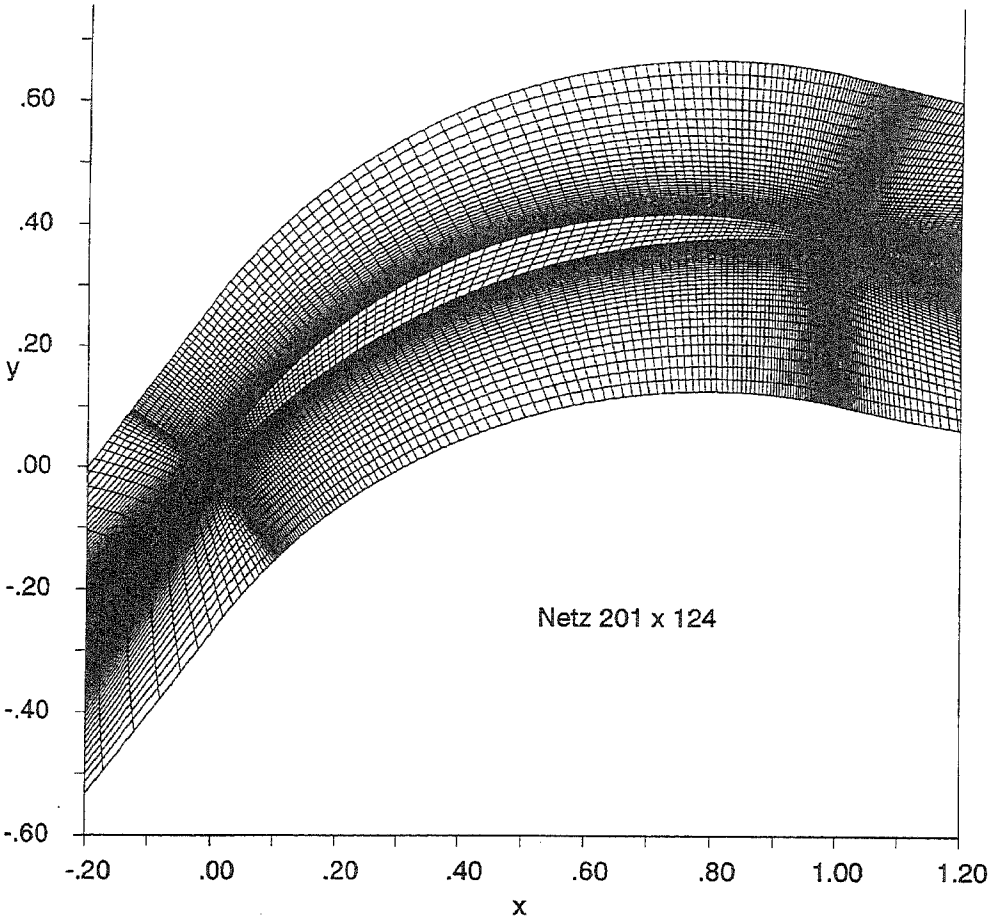

Abbildung 1

Bild 13 I-Rechennetz für neuere Rechnungen des Kreisbogenverdichtergitters

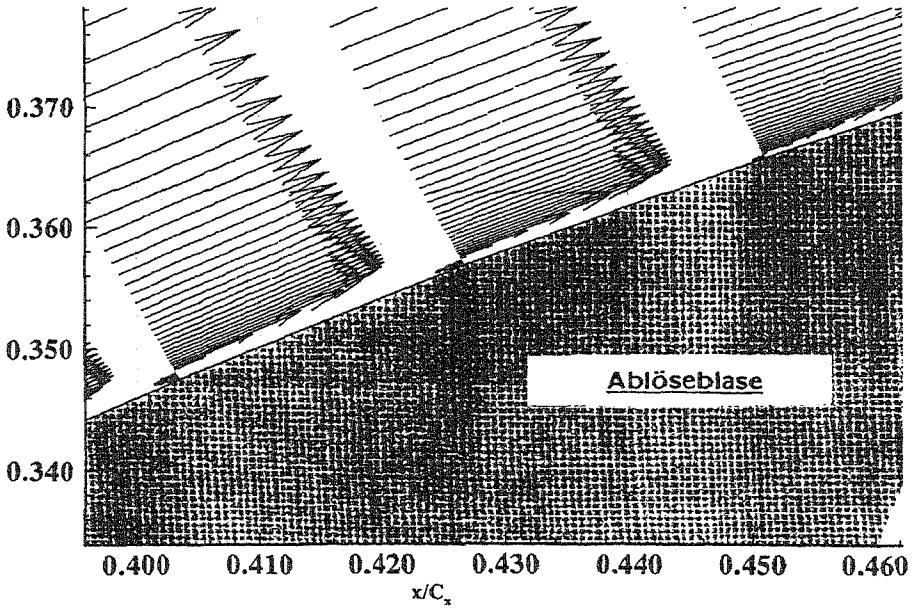

Bild 14 Berechnete Ablöseblase auf der Saugseite des Kreisbogenverdichtergitters

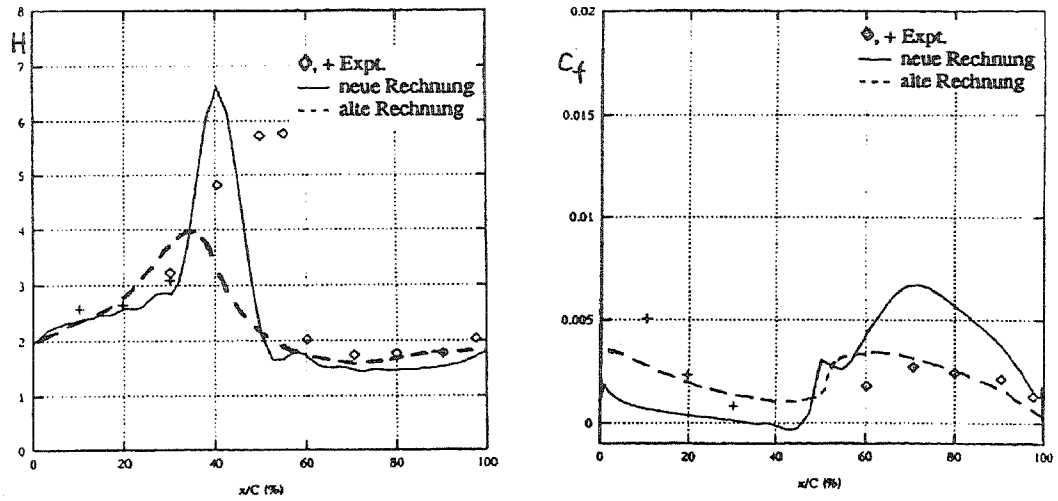

Bild 15 Formparater H und Reibungsbeiwert c_f entlang der Saugseite des Kreisbogenverdichtergitters, Vergleich von alter und neuer Rechnung

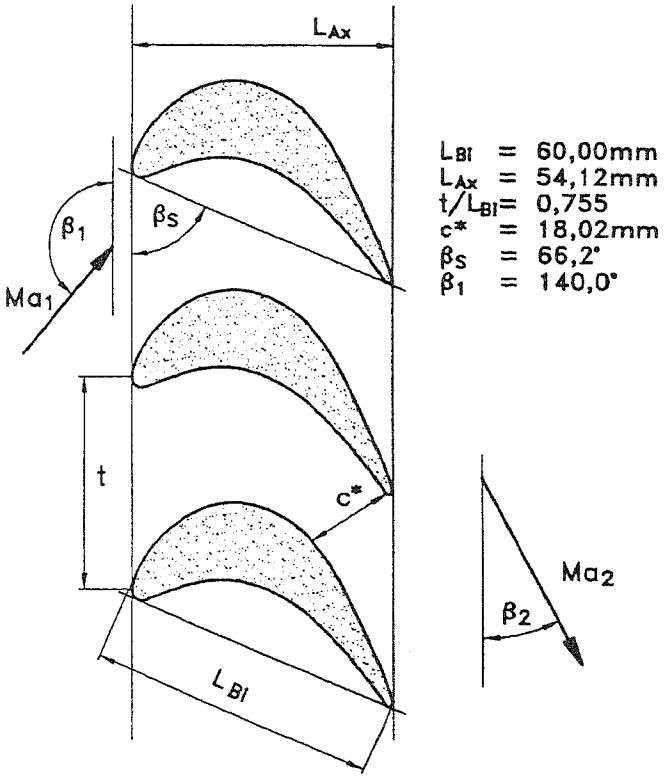

a) Gitterkonfiguration

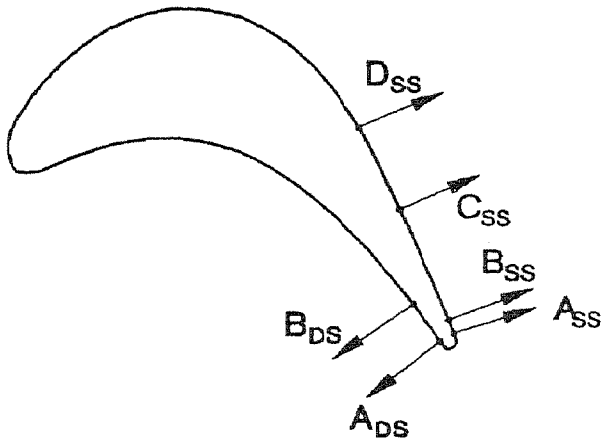

b) Meßstellen für Grenzschichtmessungen

Bild 16 Ebenes Laufradgitter T5.1

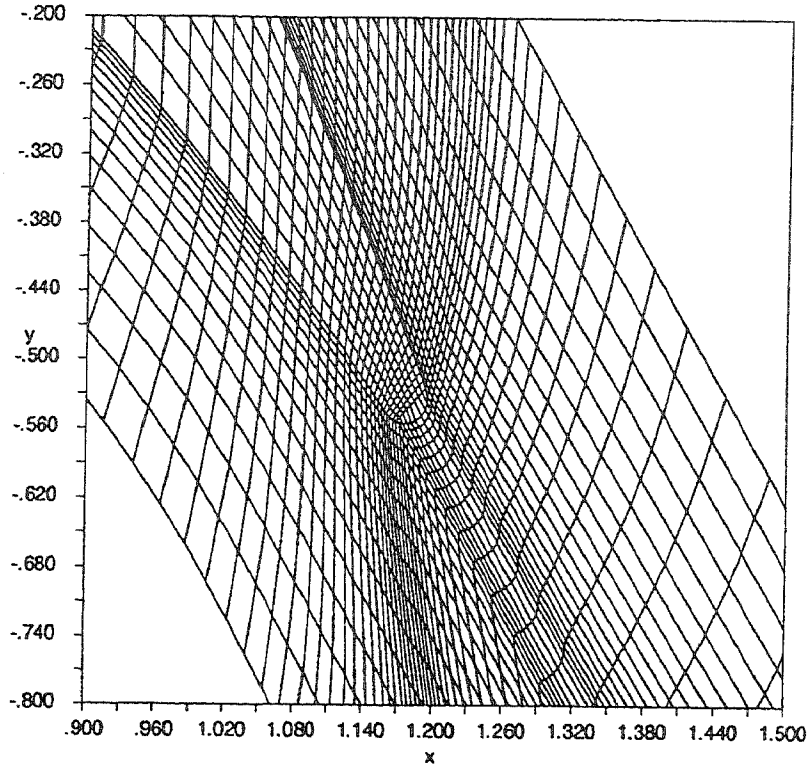

a) Punkt-zu-Punkt periodisches Rechennetz

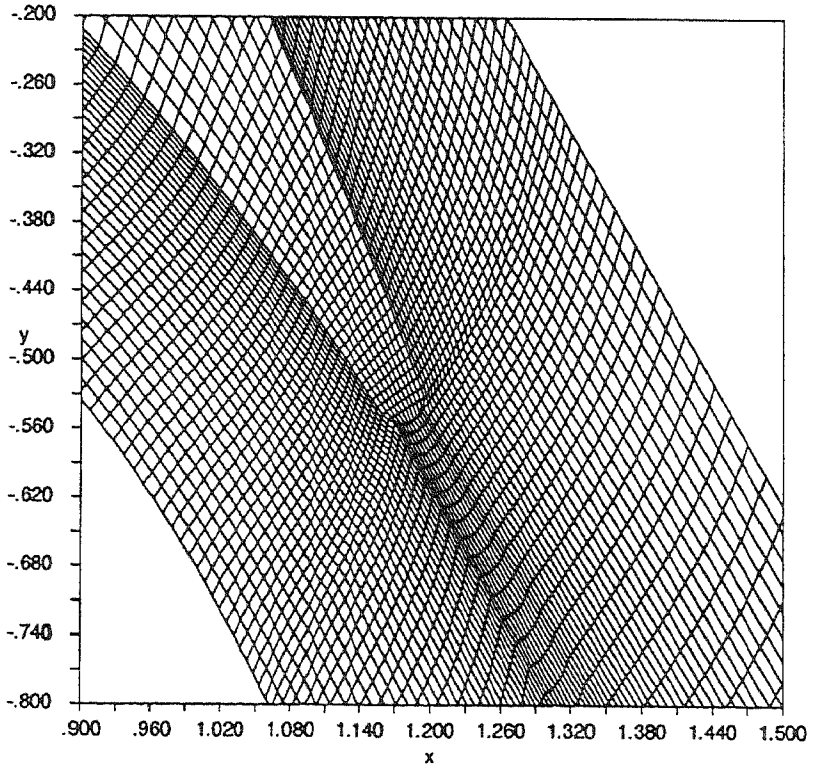

b) Nicht-Punkt-zu-Punkt periodisches Rechennetz

Bild 17 Rechennetz im Hinterkantenbereich des T 5.1 Gitters

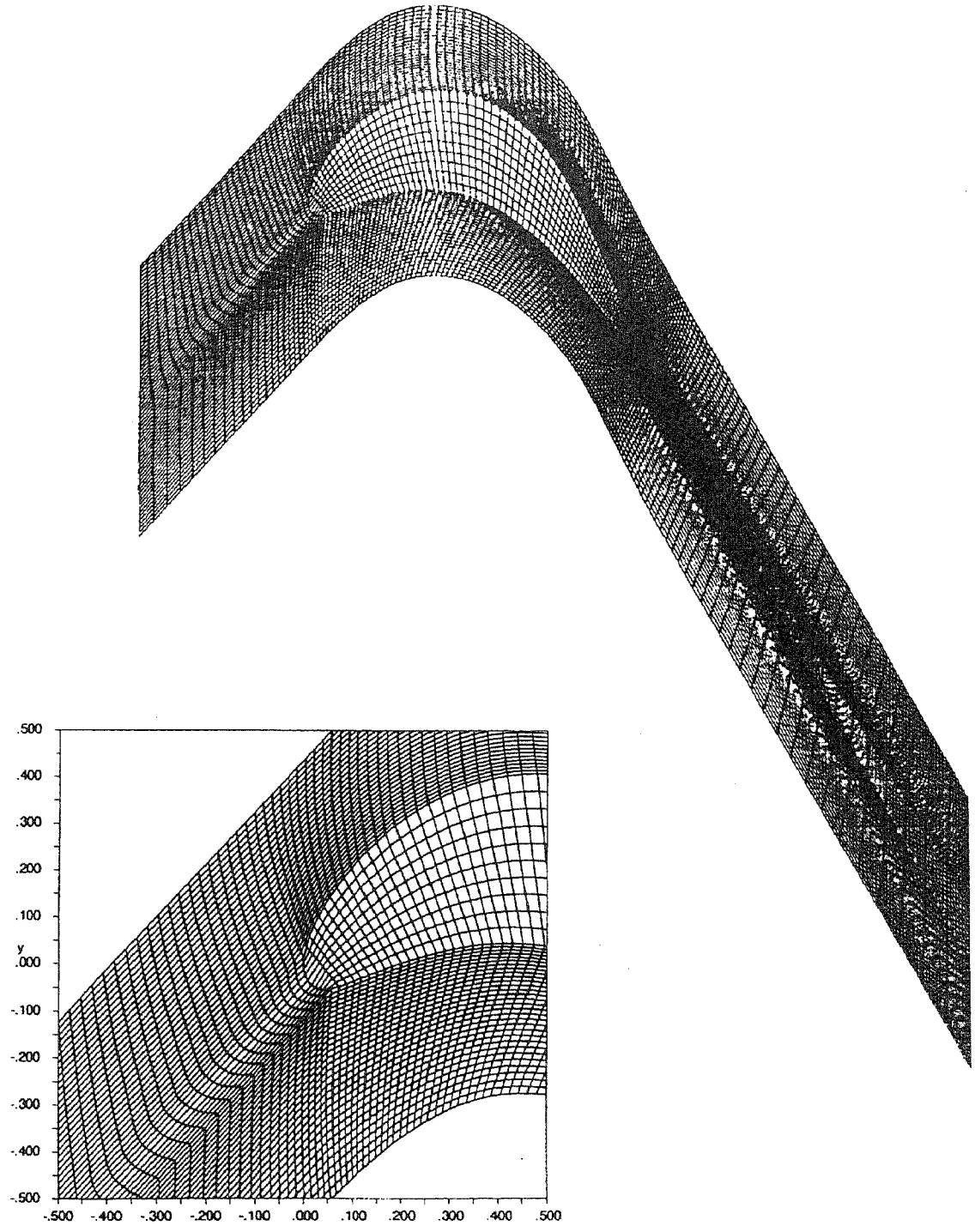

Bild 18 Gesamt-nicht-Punkt-zu-Punkt periodisches Rechennetz für das T5.1 Gitter und vergrößerte Darstellung des Vorderkantenbereichs

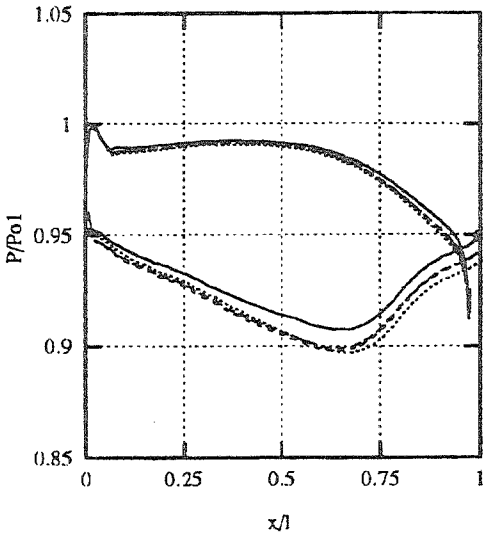

a) Druckverteilung um Schaufel

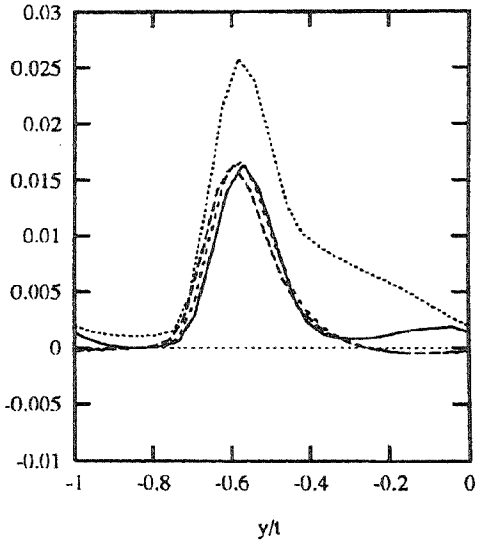

b) Druckverlustbeiwert bei x/l = 1.46

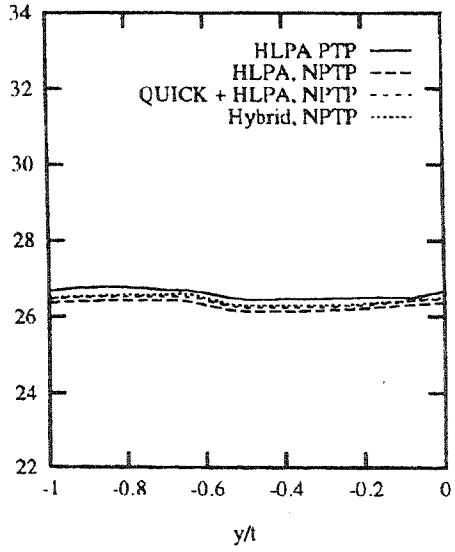

c) Abströmwinkel bei x/l = 1.46

Bild 19 Einfluß numerischer Parameter auf die Berechnung der inkompressiblen Strömung um das T5.1 Gitter

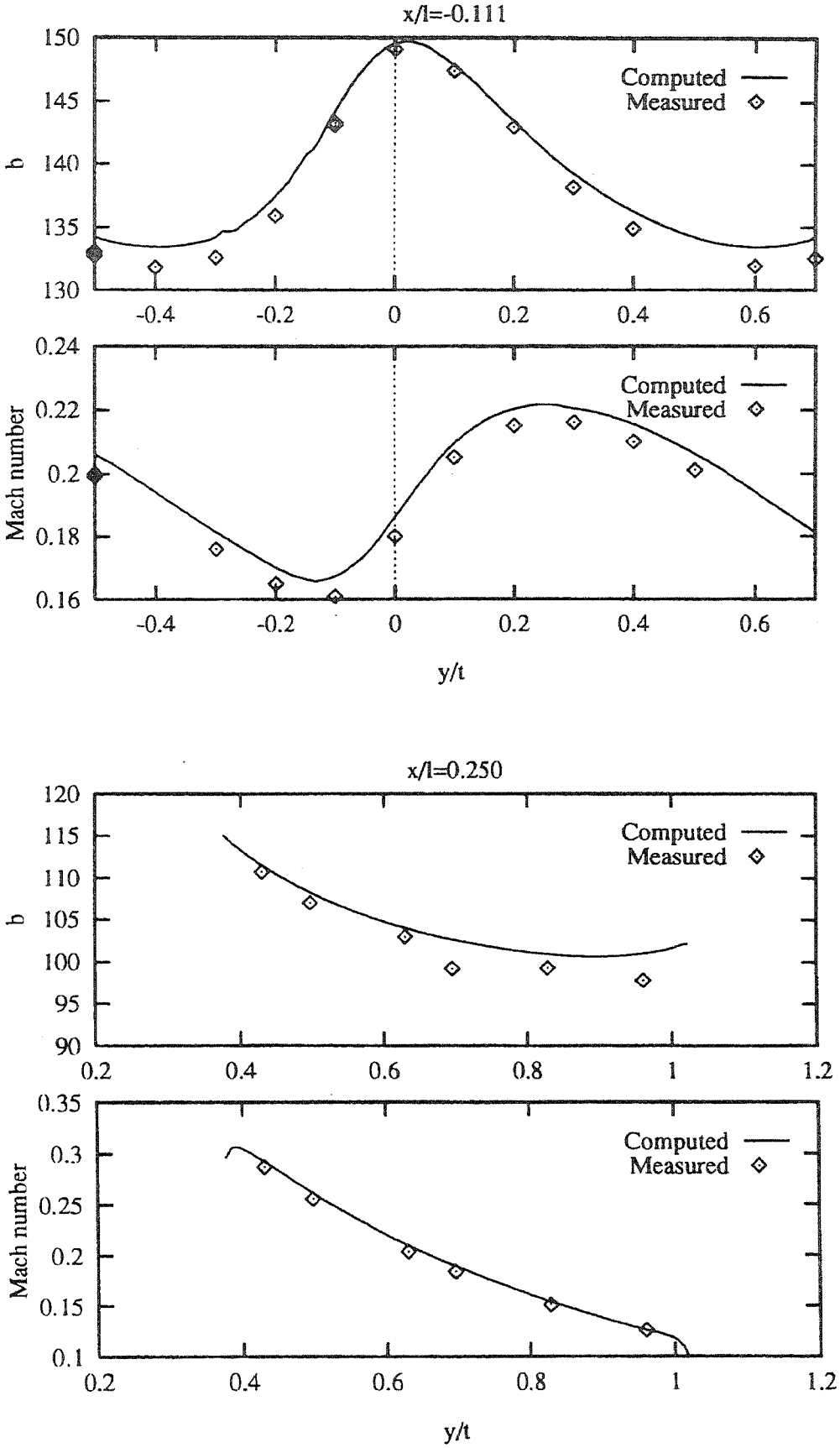

Bild 20 Verteilung von Strömungswinkel und Machzahl über den Gitterkanal an verschiedenen axialen Meßquerschnitten, T5.1 Gitter ($Ma_2 = 0.3088$)

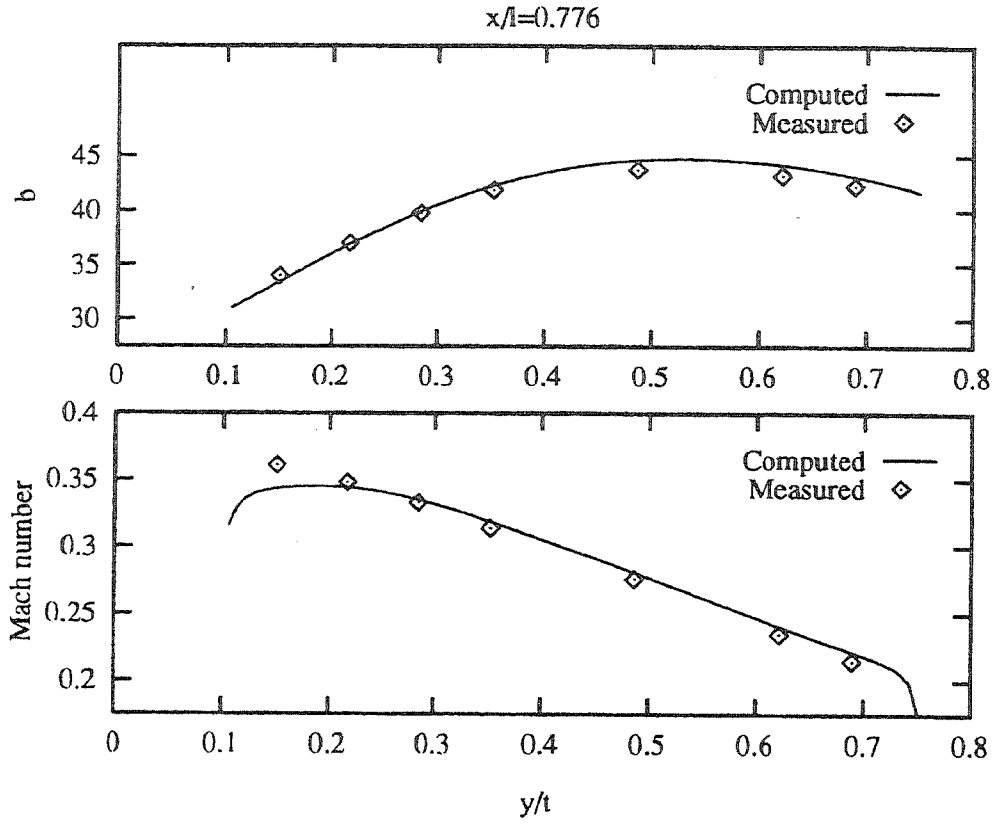

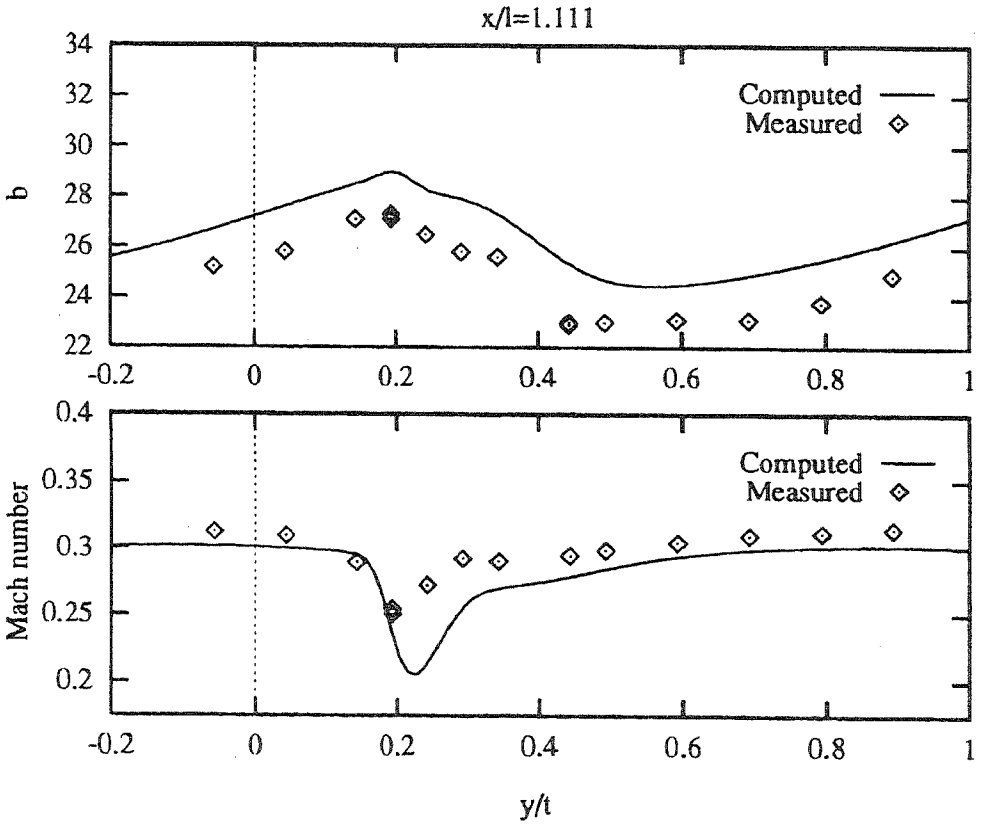

Bild 20 Fortsetzung

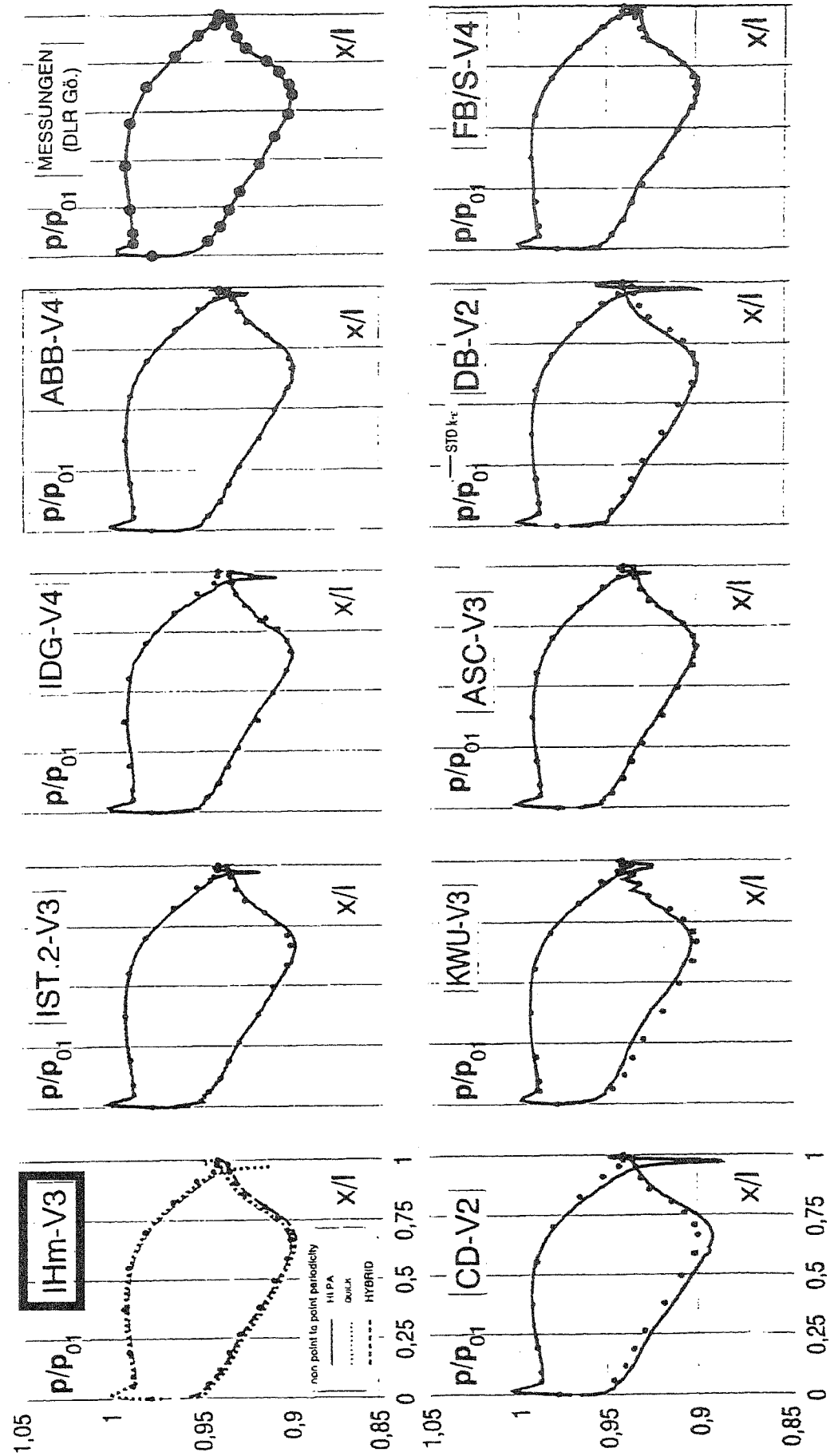

Bild 21: Druckverteilung entlang der T5.1 Schaufel bei inkompressibler Strömung ($Ma_2 = 0.3088$)
Vergleich der an die Navier-Stokes Arbeitsgruppe abgelieferten Rechnungen mit den DLR Messungen
(aus [25])

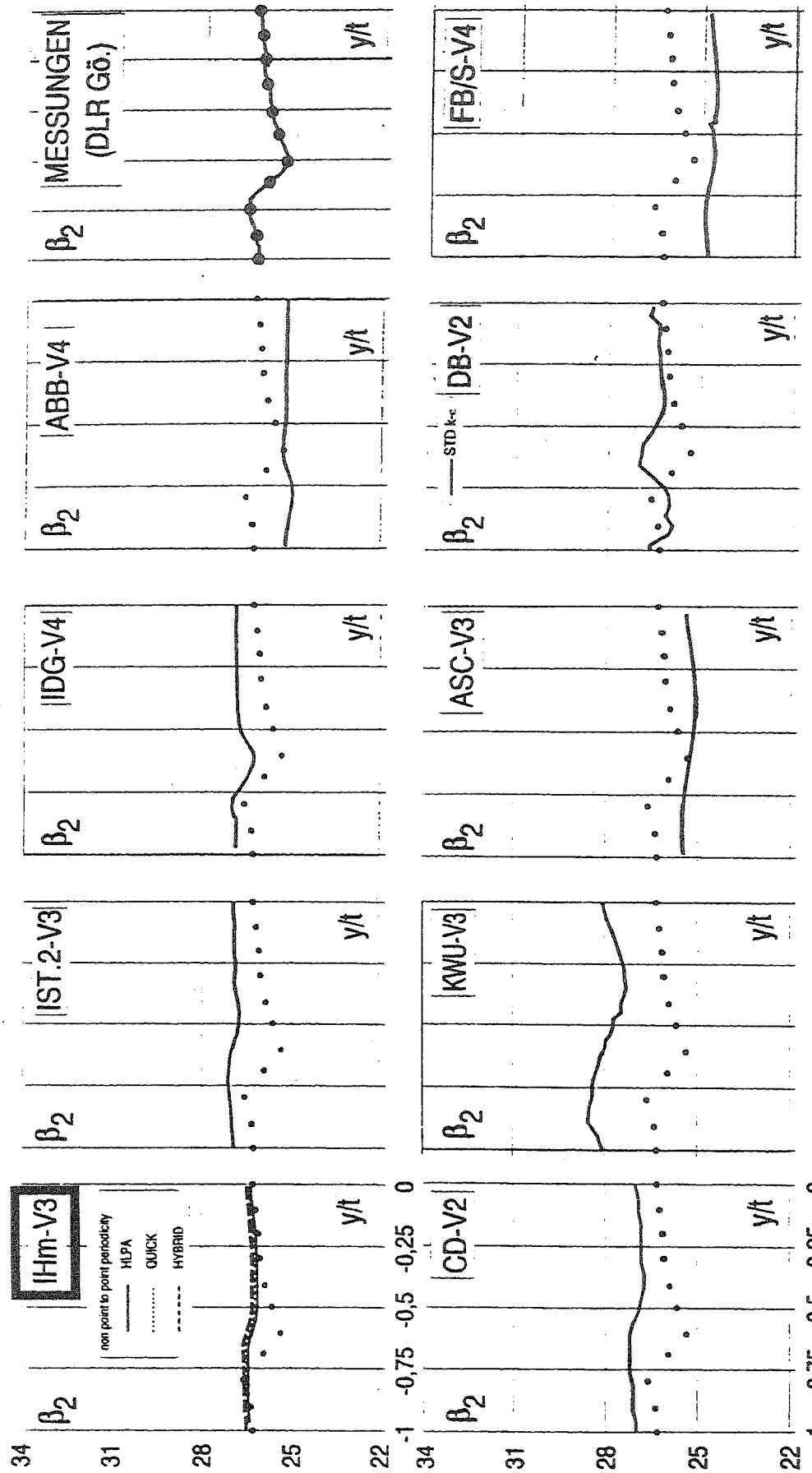

Bild 22 Abströmwinkel hinter der T5.1 Schaufel bei inkompressibler Strömung ($Ma_2 = 0.3088$)

Vergleich der an die Navier-Stokes Arbeitsgruppe abgelieferten Rechnungen mit den DLR Messungen

(aus [25])

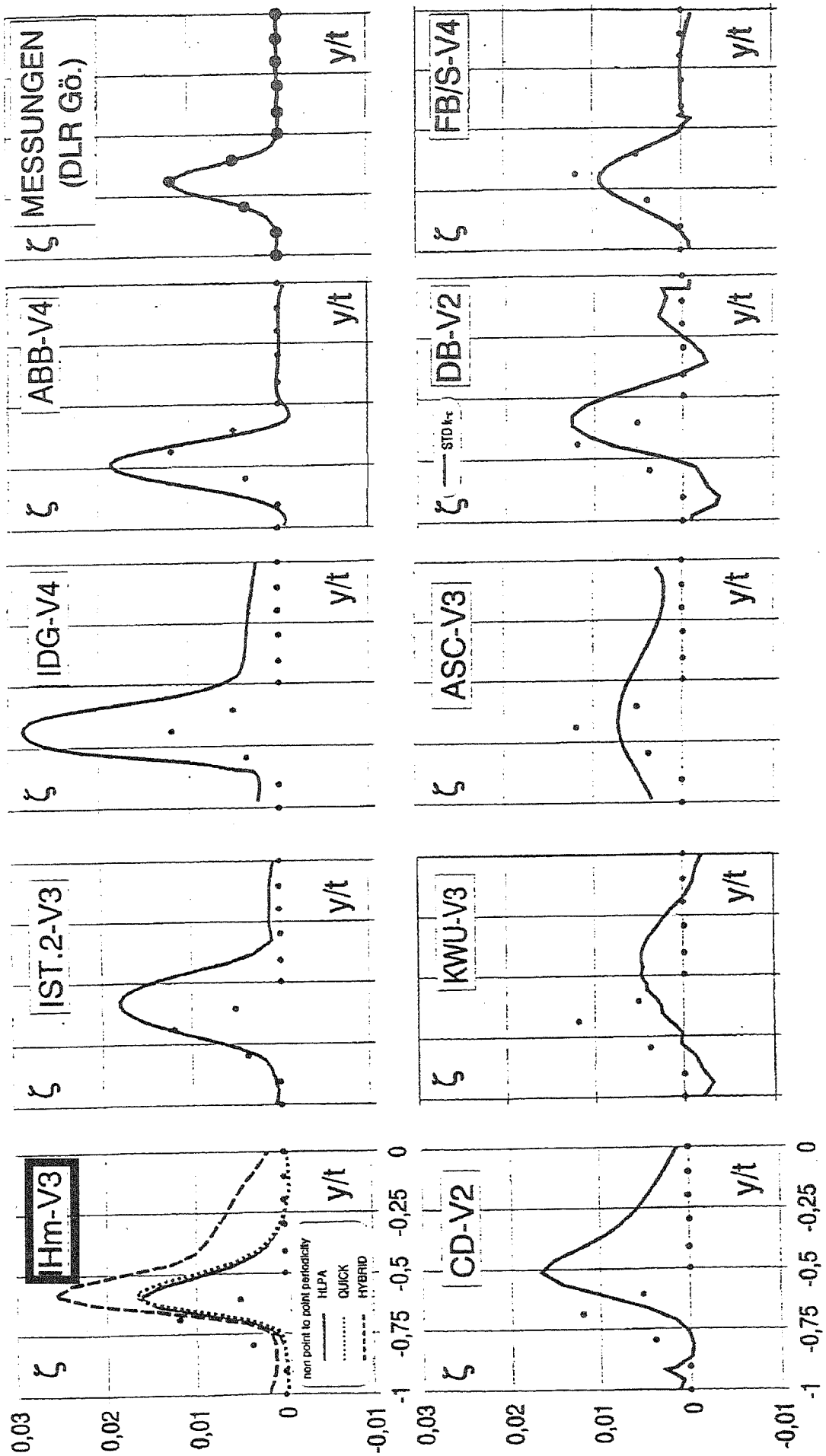

Bild 23 Gesamtdruckverlustbeiwert hinter der T5.1 Schaufel bei inkompressibler Strömung (Ma = 0.3088)
Vergleich der an die Navier-Stokes Arbeitsgruppe abgelieferten Rechnungen mit den DLR Messungen
(aus [25])

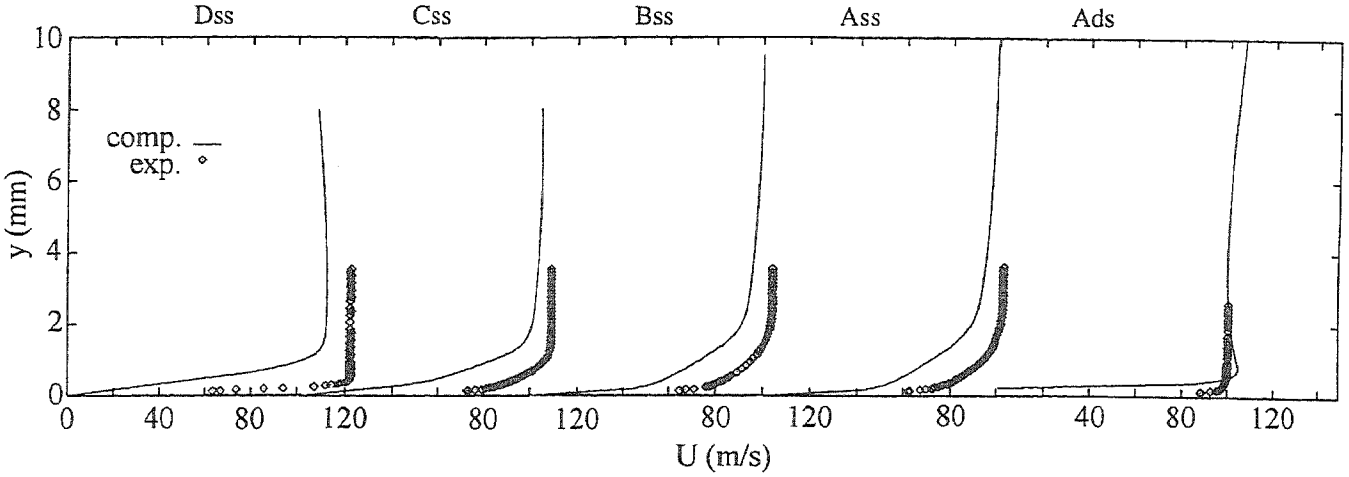

Bild 24 Geschwindigkeitsprofile (an den Meßstellen - siehe Bild 16)in der Grenzschicht der T5.1 Schaufel bei bei inkompressibler Strömung ($Ma_2 = 0.3088$)

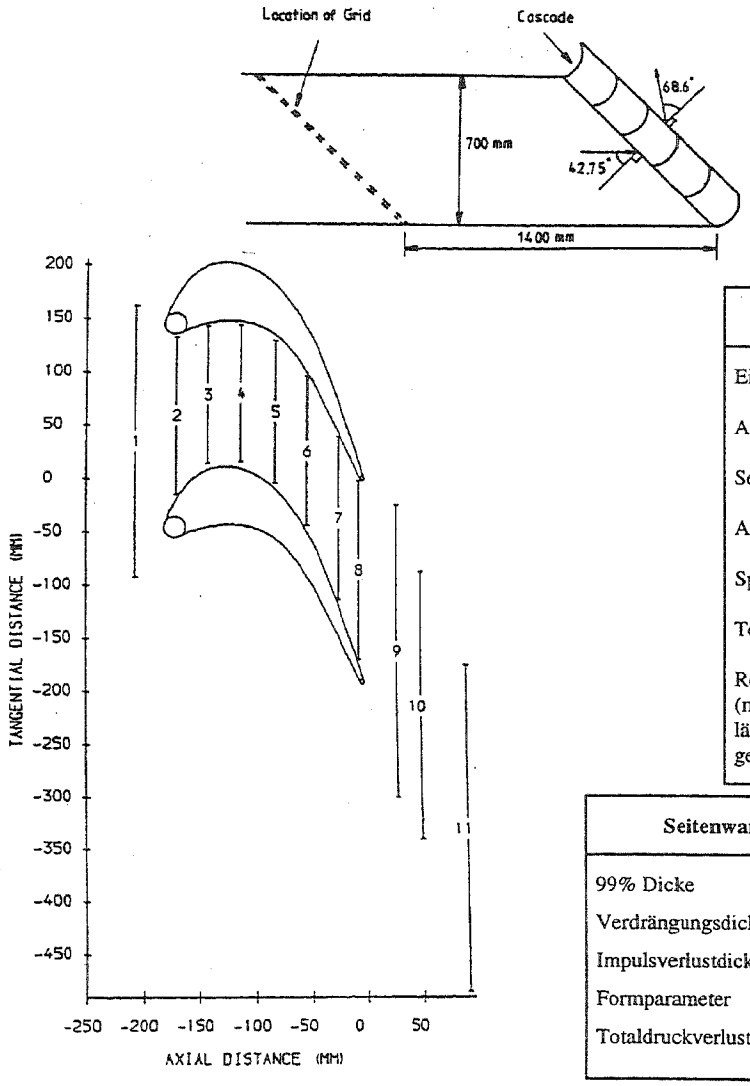

Gitterdaten	
Einströmwinkel	42.75°
Abströmwinkel	-68.60°
Sehnenlänge	224 mm
Axiale Sehnenlänge	181 mm
Spannweite	400 mm
Teilung	191 mm
Reynolds-Zahl (mit ax. Sehnenlänge und Abströmgeschwindigkeit)	4×10^5

Seitenwandgrenzschicht in der Einströmebene	
99% Dicke	43 mm
Verdrängungsdicke	3.7 mm
Impulsverlustdicke	3.1 mm
Formparameter	1.2
Totaldruckverlustbeiwert	0.027

Bild 25 Ebenes Turbinengitter von Cleak und Gregory Smith [29], Versuchsanordnung, Gitterdaten und Meßebenen

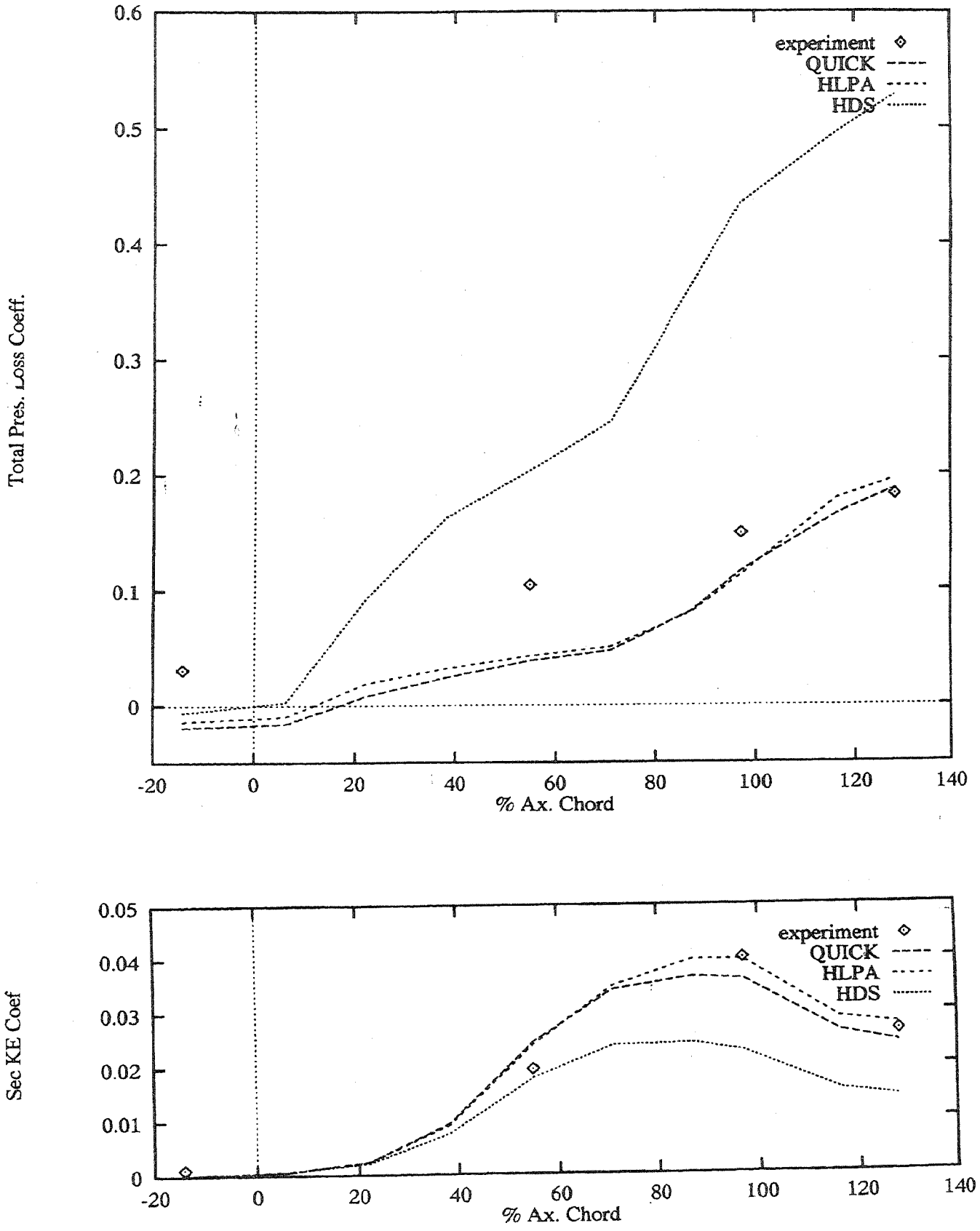

Bild 26 Axiale Verteilung von querschnittsgemitteltem Druckverlustbeiwert und Sekundärströmungsenergie für das ebene Turbinengitter von Cleak und Gregory Smith [29], Rechnungen mit einem 108 x 36 x 22 H-Gitter und Standard k-ε Modell

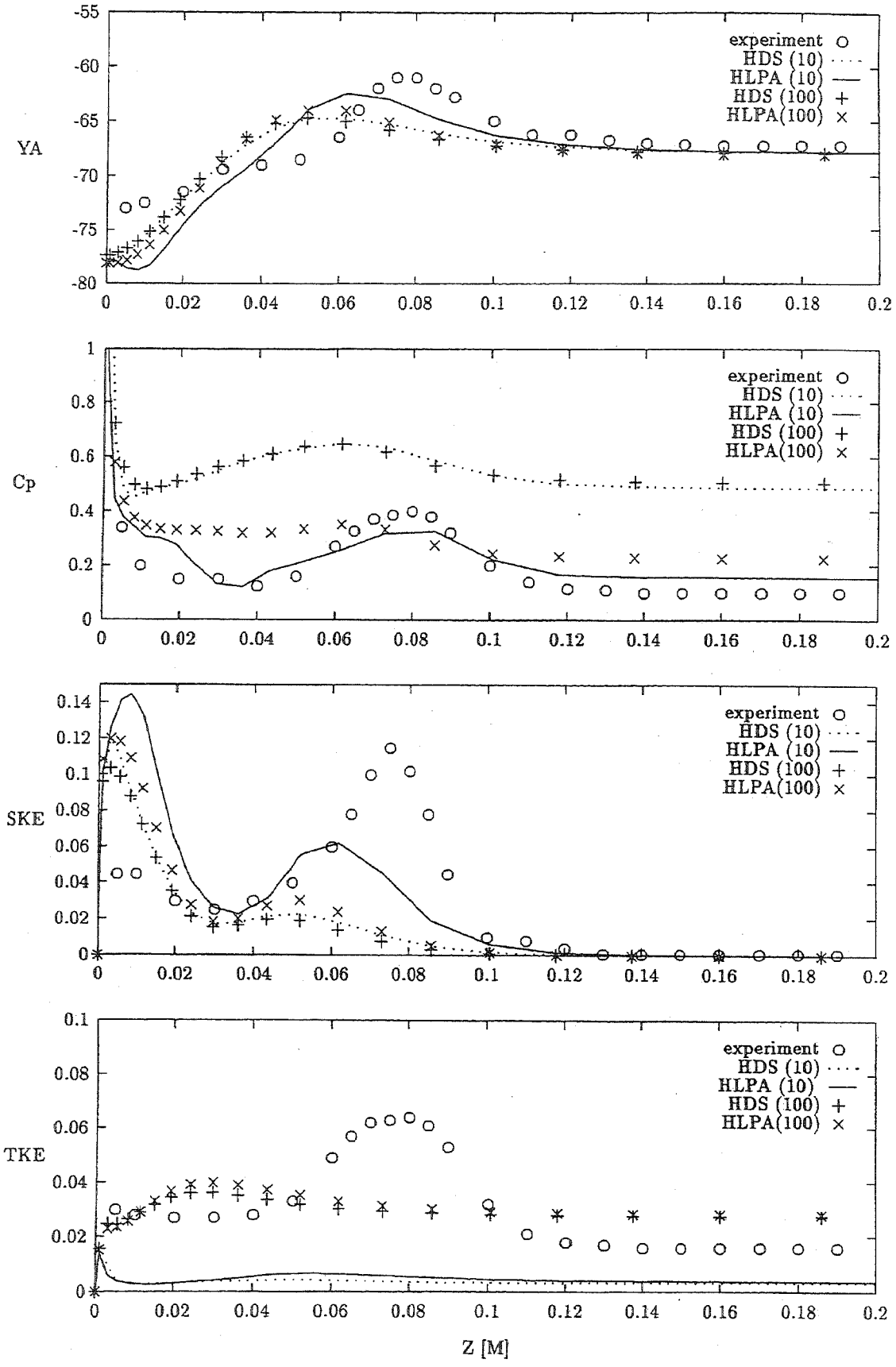

Bild 27 Über die Teilung gemittelter Abströmwinkel (y_a), Druckverlustbeiwert (c_p), Sekundärströmungsenergie (SKE) und Turbulenzenergie (TKE) bei Meßebene 10 des Turbinengitters von Cleak und Gregory Smith [29], Rechnungen mit dem108 x 36 x 22 H-Gitter bei Variation von μ_t/μ am Eintritt (10 und 100)

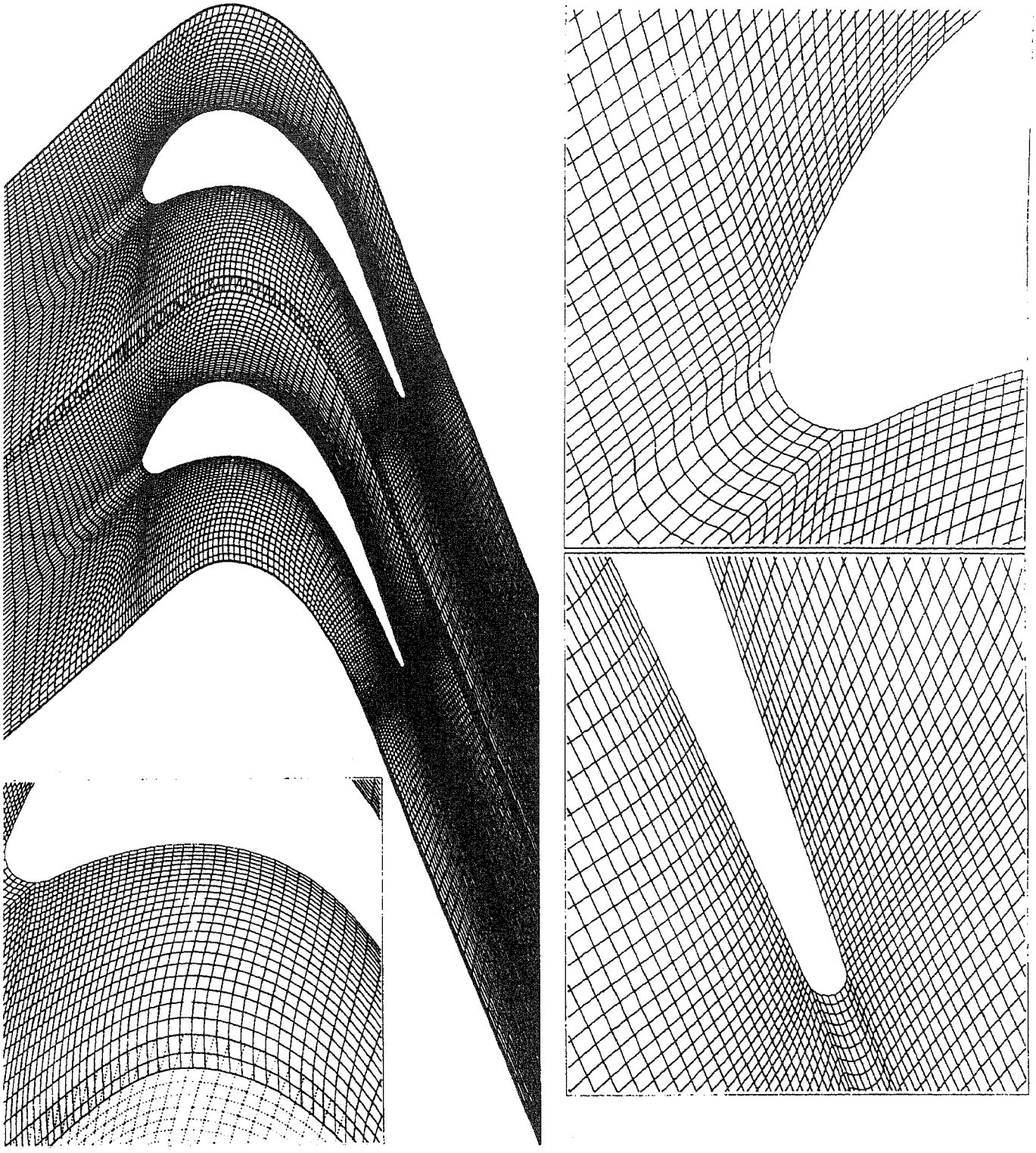

Bild 28 148 x 63 x 35 nicht-Punkt-zu-Punkt periodisches I-Gitter zur Berechnung der Strömung durch das ebene Turbinengitter von Cleak und Gregory Smith [29] bei Verwendung des k-ε Modells mit Wandfunktionen

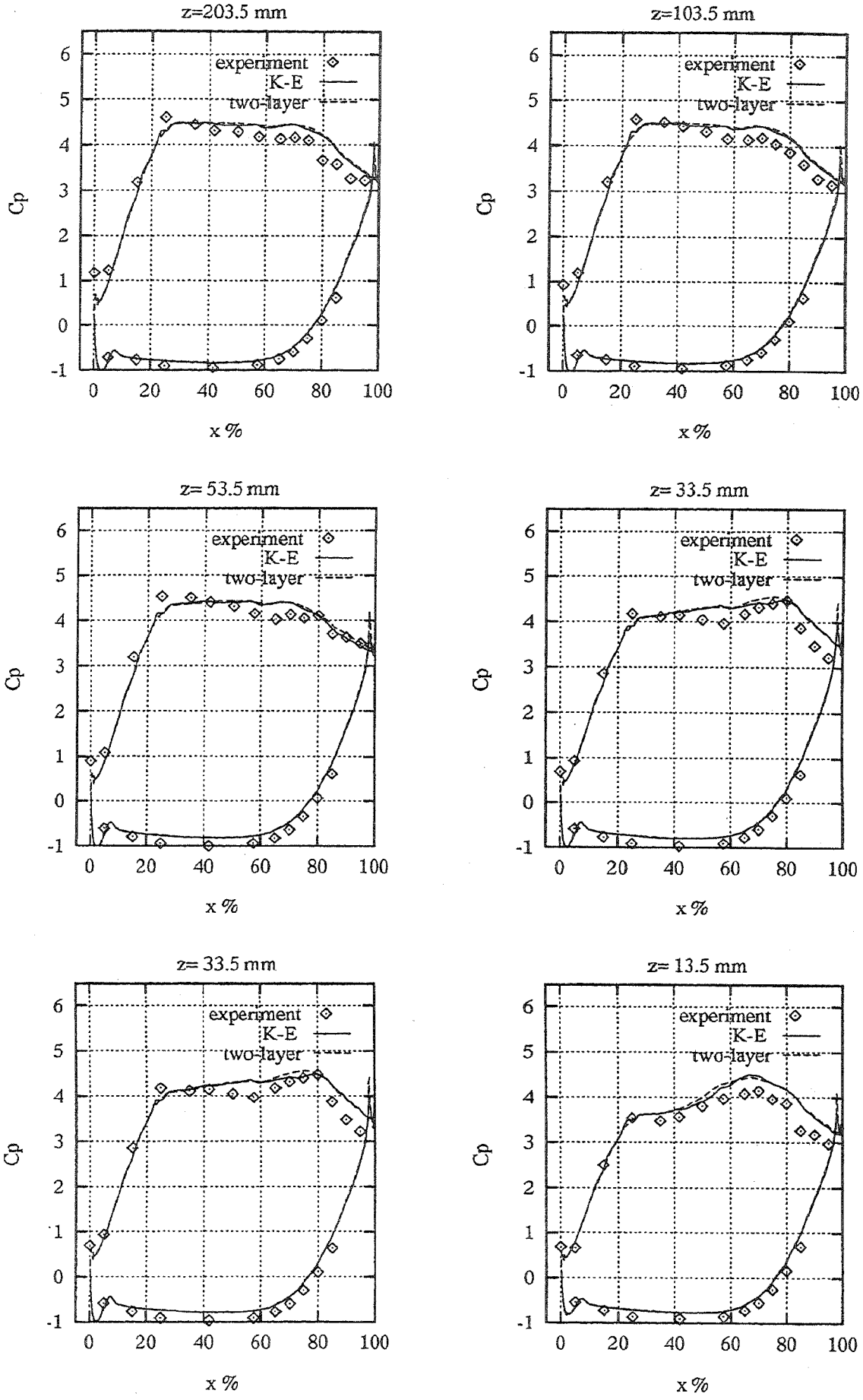

Bild 29 Druckverteilung für das ebene Turbinengitter von Cleak und Gregory Smith [29], Rechnungen mit dem 148 x 63 x 35 I-Gitter

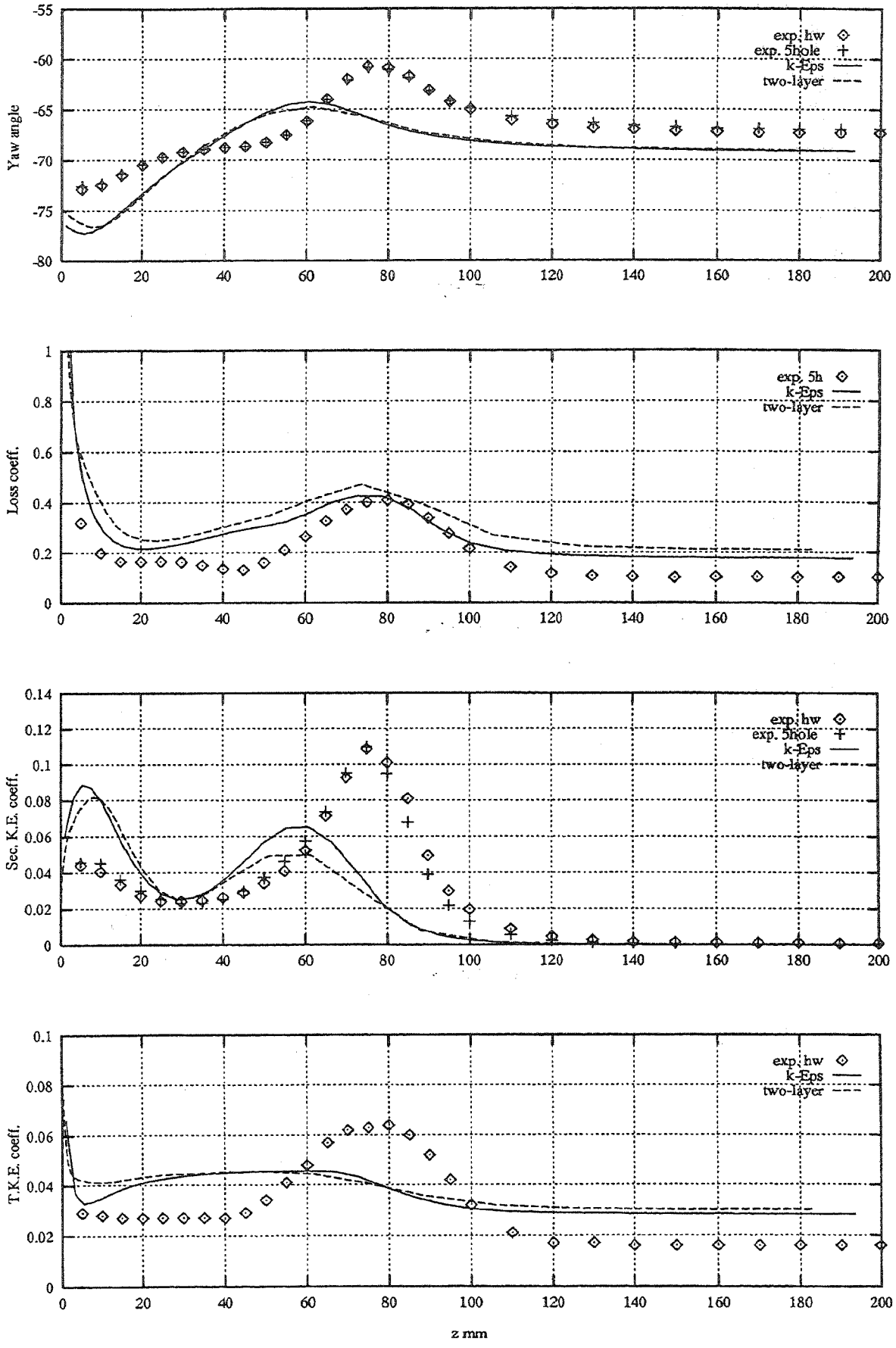

Bild 30: Über die Teilung gemittelter Abströmwinkel (y_a), Druckverlustbeiwert (loss coeff.), Sekundärströmungsenergie (SKE) und Turbulenzenergie (TKE) bei Meßebene 10 des Turbinengitters von Cleak und Gregory Smith [29], Rechnungen mit dem148 x 63 x 35 I-Gitter

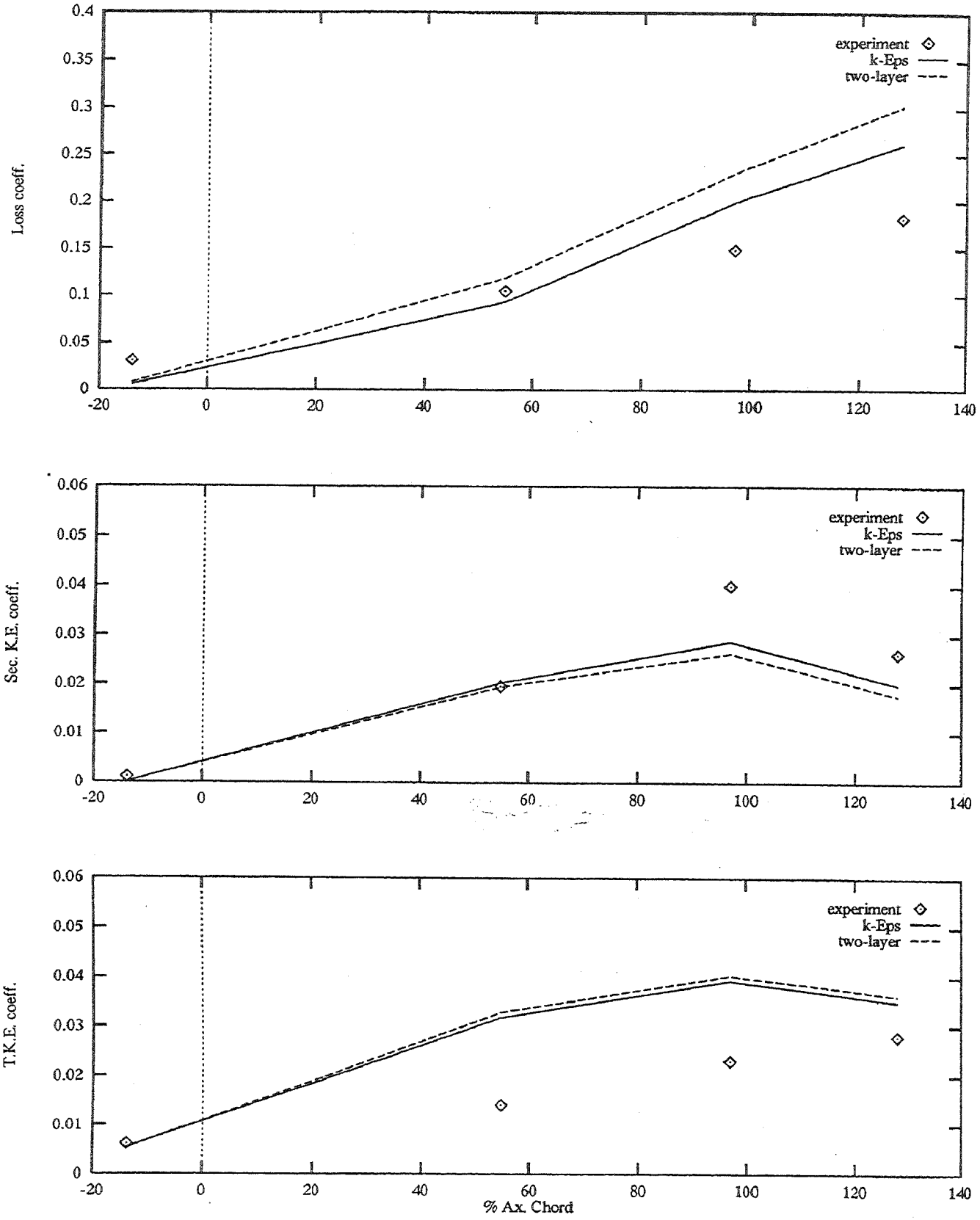

Bild 31 Axiale Verteilung des querschnittgemittelten Druckverlustbeiwerts, der Sekundärströmungsenergie und der Turbulenzenergie für das ebene Turbinengitter von Cleak und Gregory Smith [29], Rechnungen mit dem 148 x 36 x 35 I-Gitter

k-ε Modell-Rechnung

Experiment

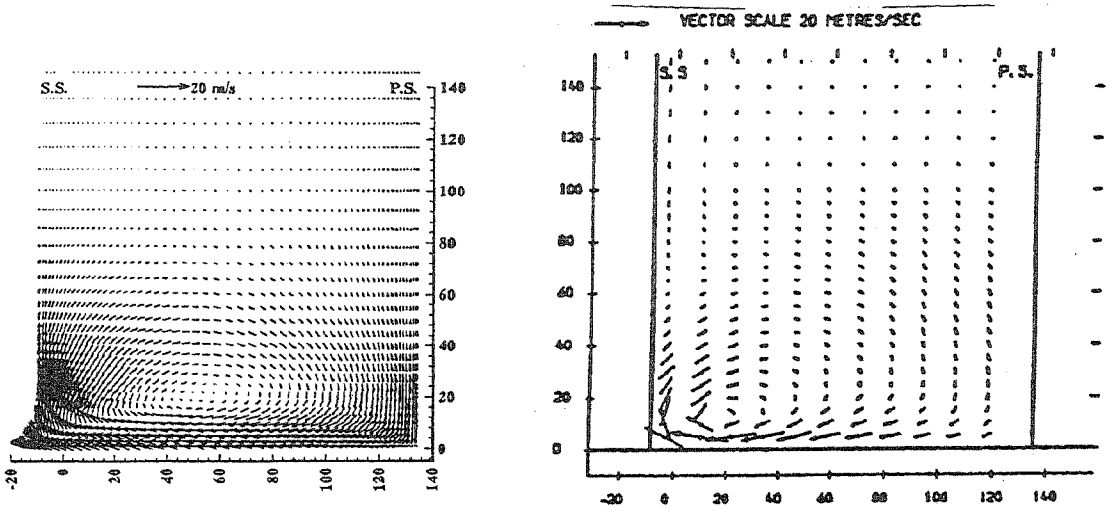

a) Meßebene 5

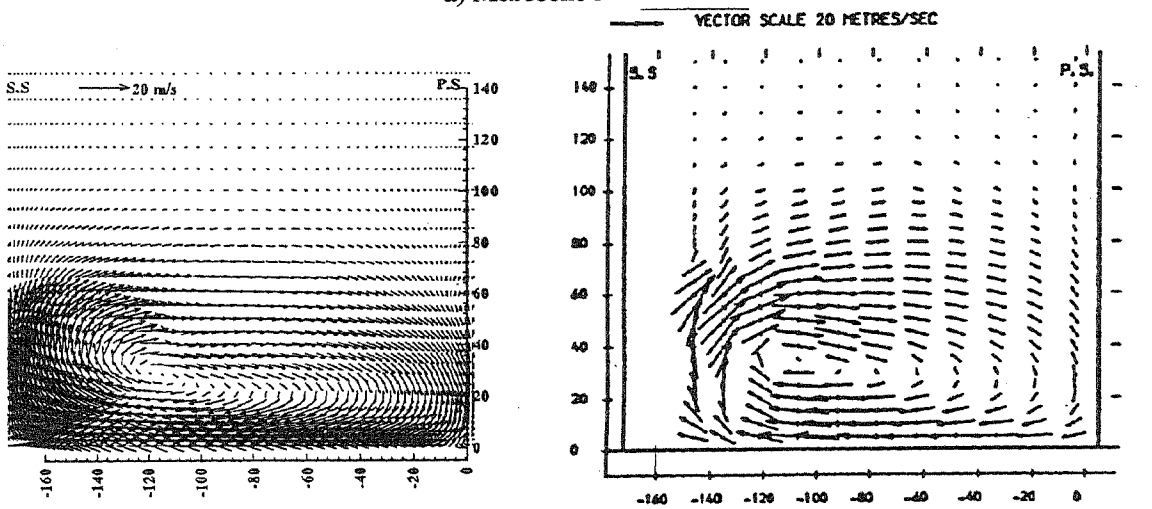

b) Meßebene 8

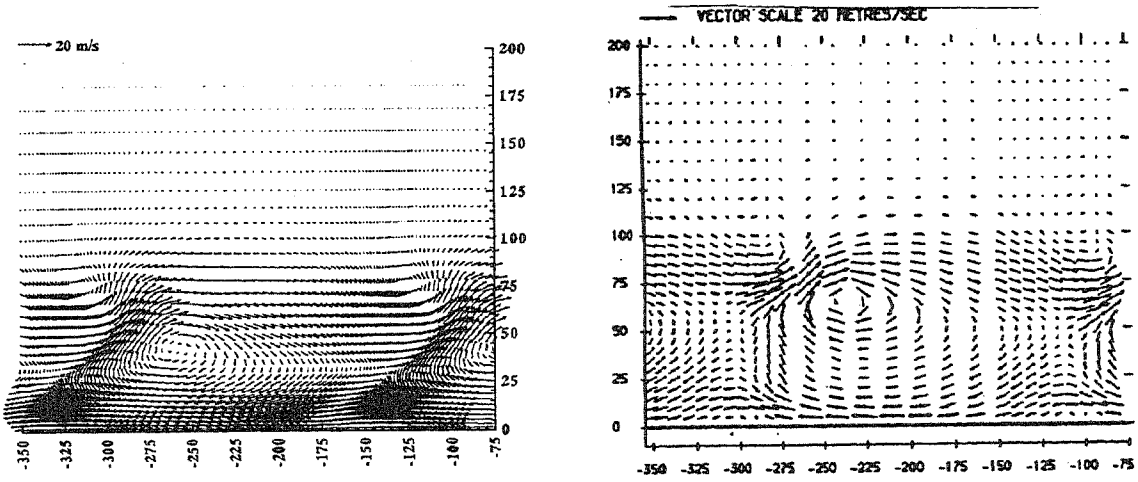

c) Meßebene 10

Bild 32 Vektoren der Sekundärströmungsgschwindigkeit im ebenen Turbinengitter von Cleak und Gregory Smith [29] an den Meßebenen 5, 8 und 10, Rechnung mit dem148 x 36 x 35 I-Gitter und dem Standard k-ε Modell

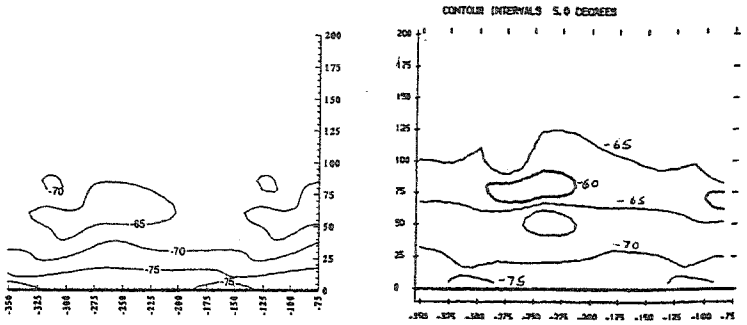

a) Strömungswinkel (yaw)

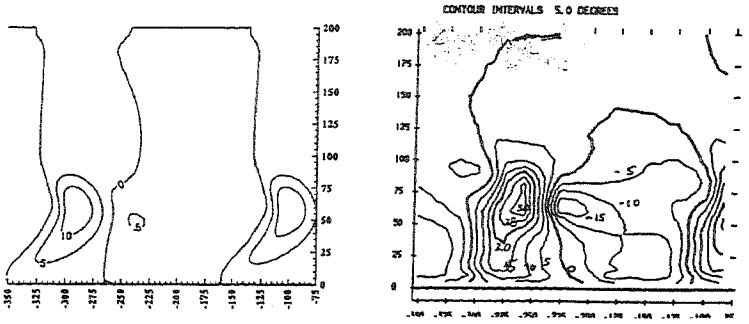

b) Strömungswinkel (pitch)

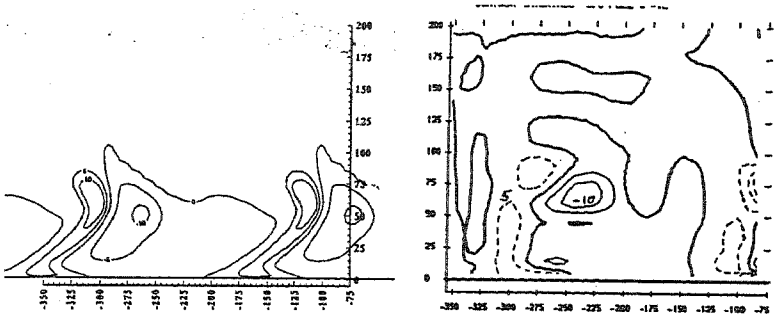

c) Wirbelstärke

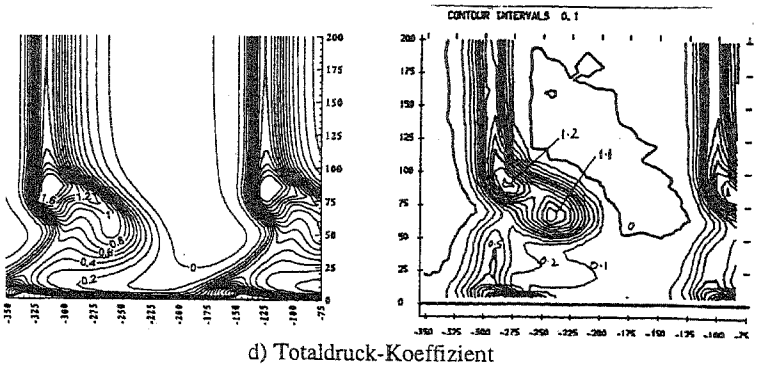

d) Totaldruck-Koeffizient

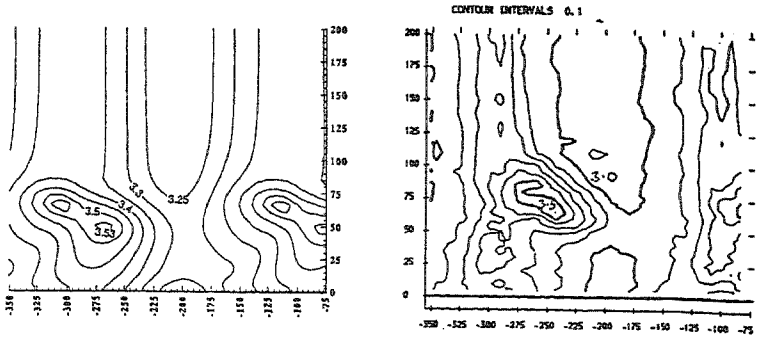

e) Statischer Druck-Koeffizient

Bild 33 Konturen von Strömungswinkel, Totaldruckverlustbeiwert, statischem Druck und Wirbelstärke bei Meßebene 10 für das ebene Turbinengitter von Cleak und Gregory Smith [29], Rechnung mit dem 148 x 63 x 35 I-Gitter und dem Standard k-ε Modell

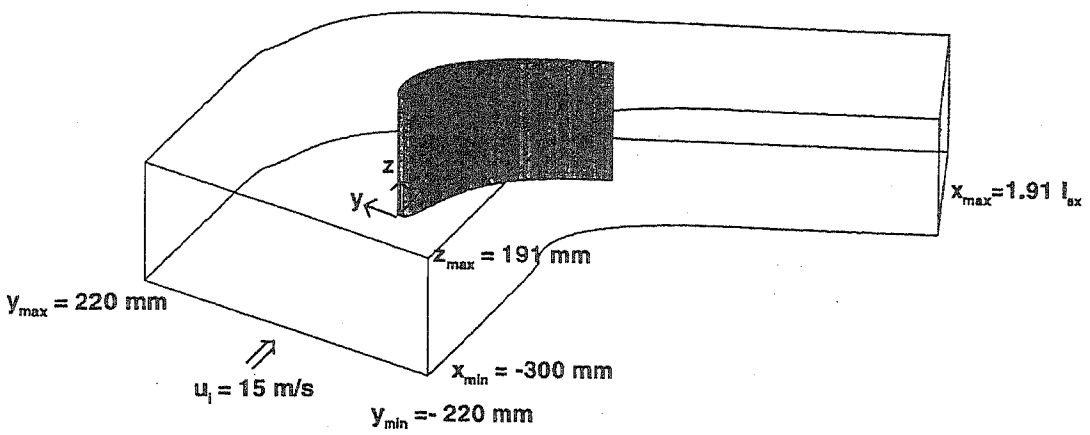

Bild 34 Beschaufelter Kanal (Aachen): Strömungskonfiguration und Rechengebiet

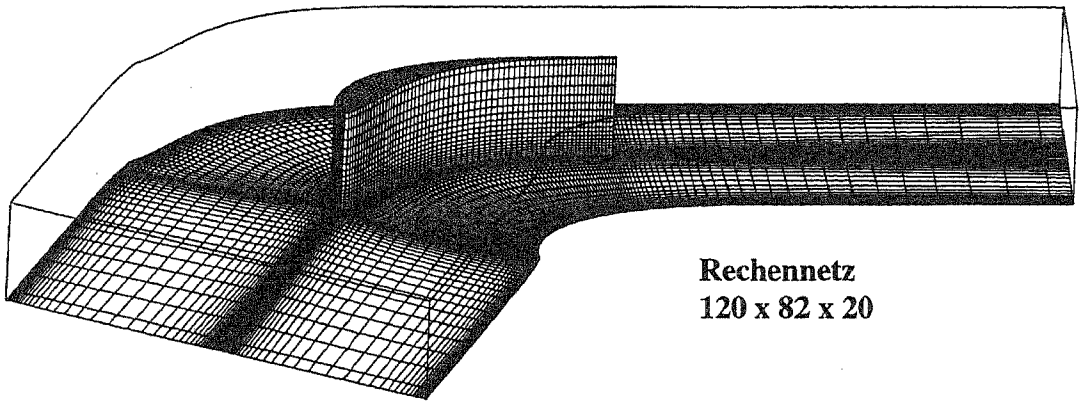

Bild 35 Beschaufelter Kanal (Aachen): Rechennetz

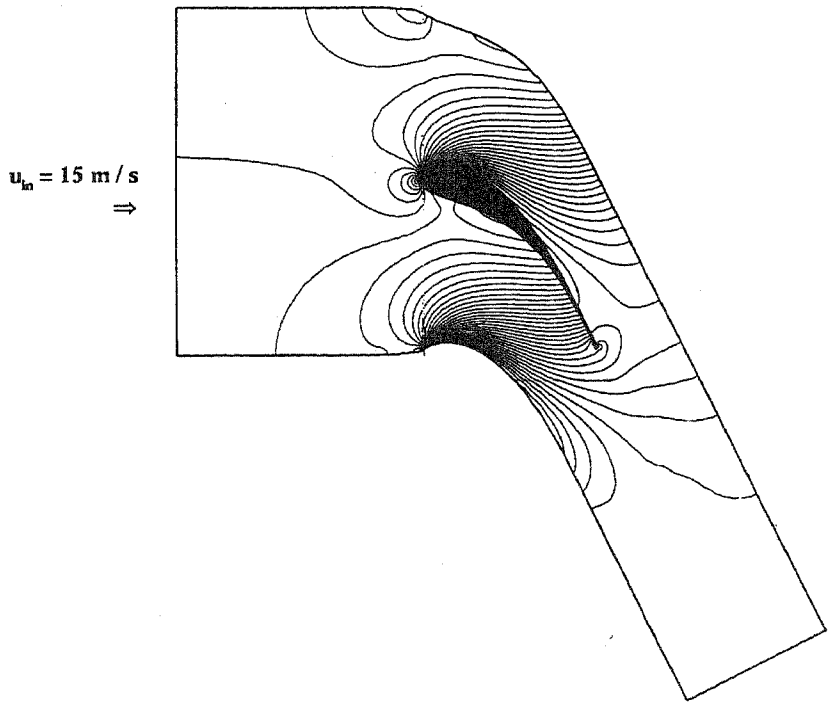

Bild 36 Beschaufelter Kanal (Aachen): Berechnete Druckkonturen im Mittelschnitt

a) z / h = 0.013

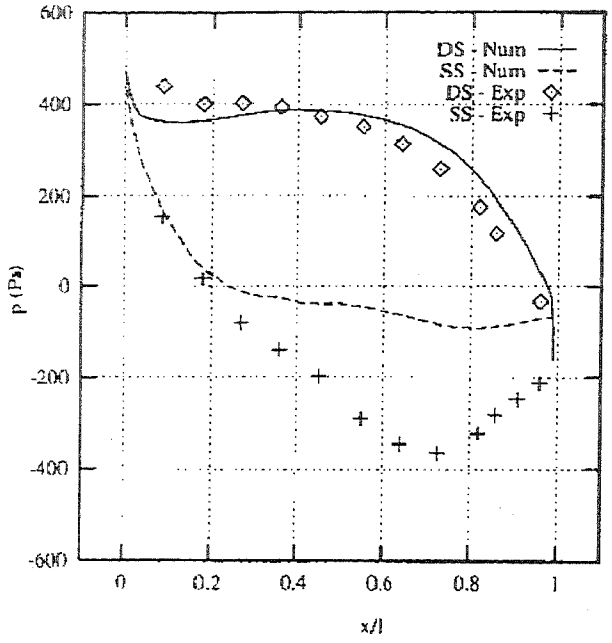

b) z / h = 0.078

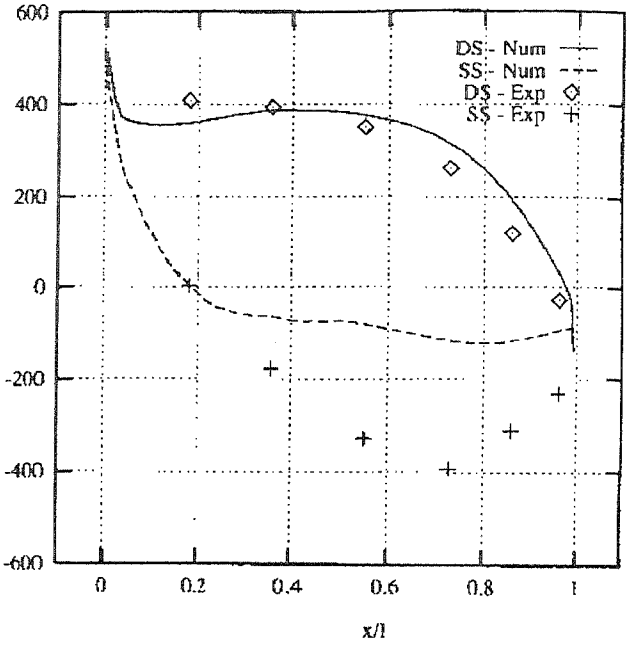

c) z / h = 0.314

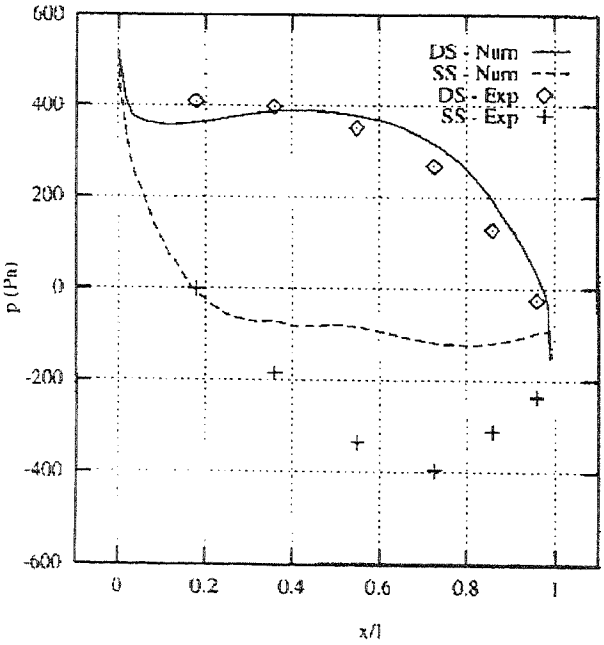

d) z / h = 0.5

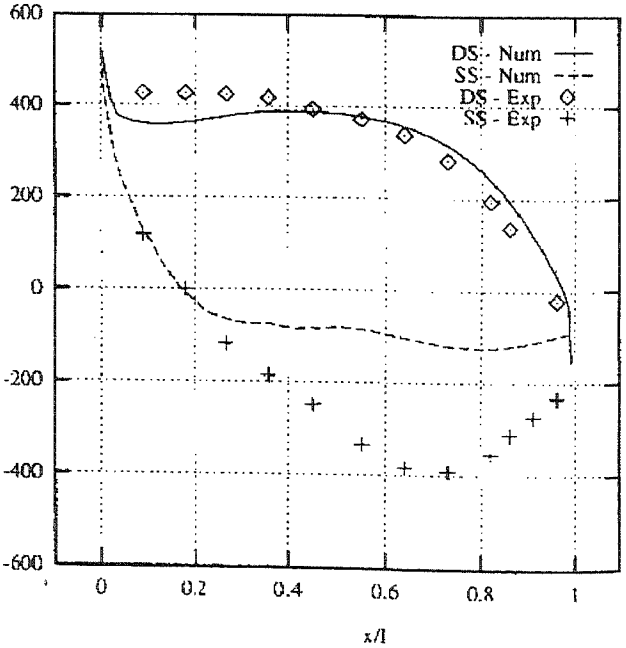

Bild 37 Beschaufelter Kanal (Aachen): Verlauf des statischen Drucks entlang der Schaufel (DS = Druckseite, SS = Saugseite)

a) $x/l_{ax} = 0.18$ b) $x/l_{ax} = 0.36$ c) $x/l_{ax} = 0.55$ d) $x/l_{ax} = 0.82$ e) $x/l_{ax} = 1.00$

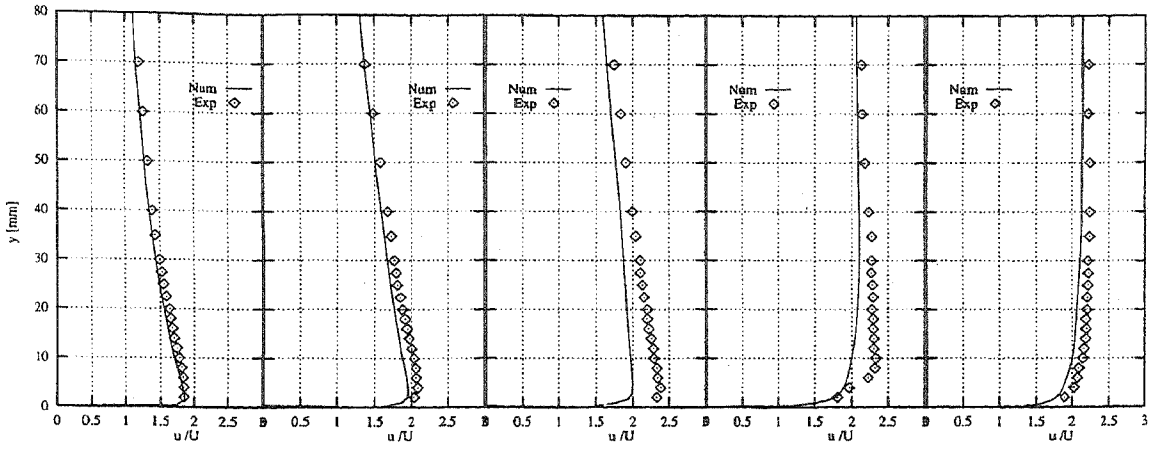

z / h = 0.05

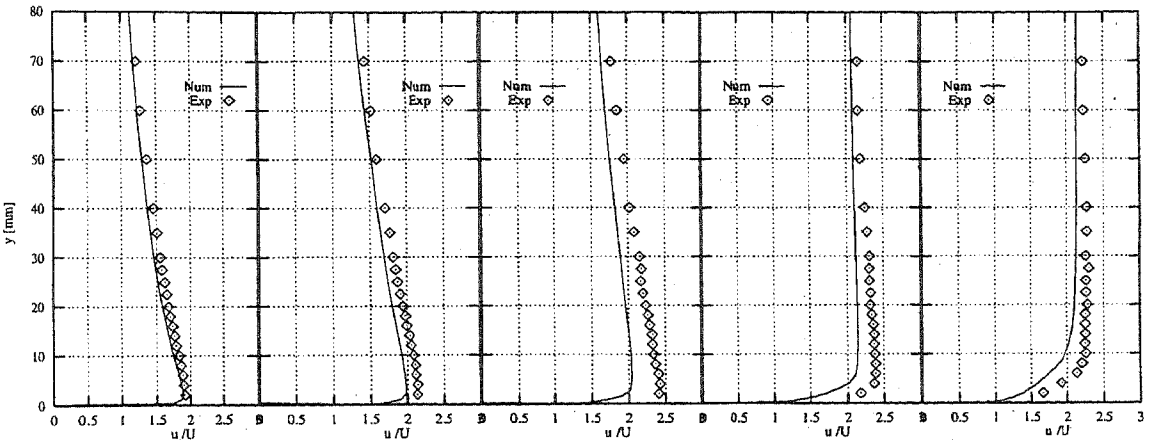

z / h = 0.131

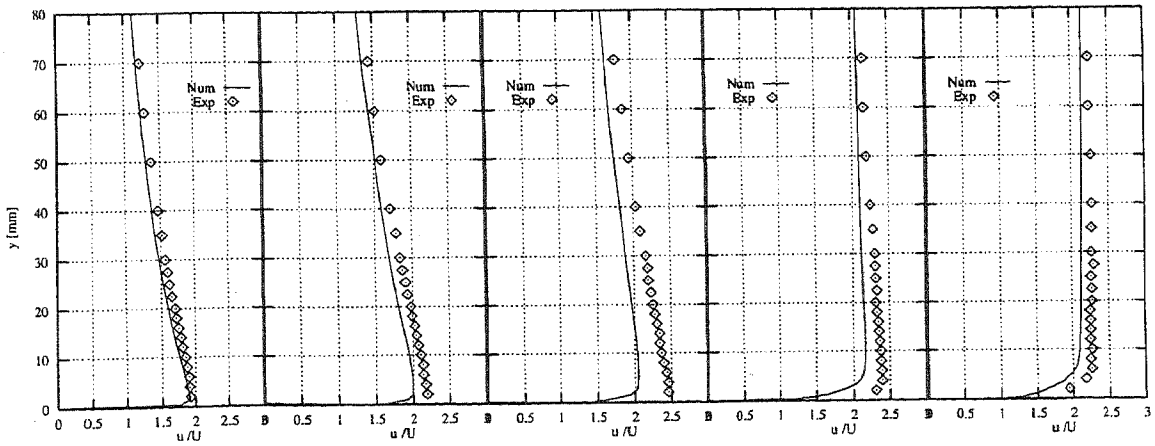

z / h = 0.234

Bild 38 Beschaufelter Kanal (Aachen): Profile der Längsgeschwindigkeit in Meßebenen senkrecht zur Saugseite

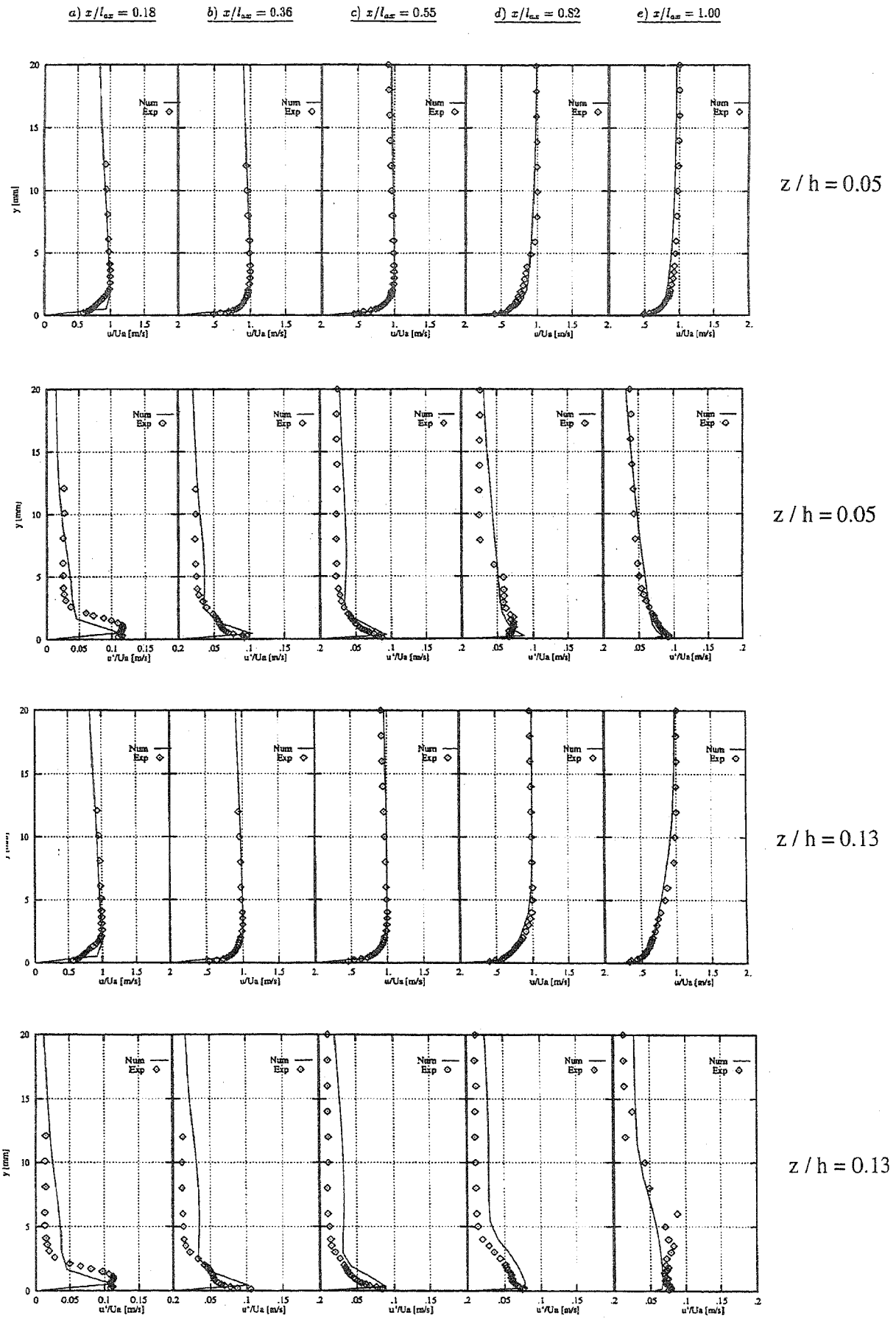

Bild 39 Beschaufelter Kanal (Aachen): Grenzschichtprofile der Geschwindigkeit (u/U_a) und der turbulenten Längsschwankungen $\sqrt{\overline{u'^2}}/U_a$ auf der Saugseite

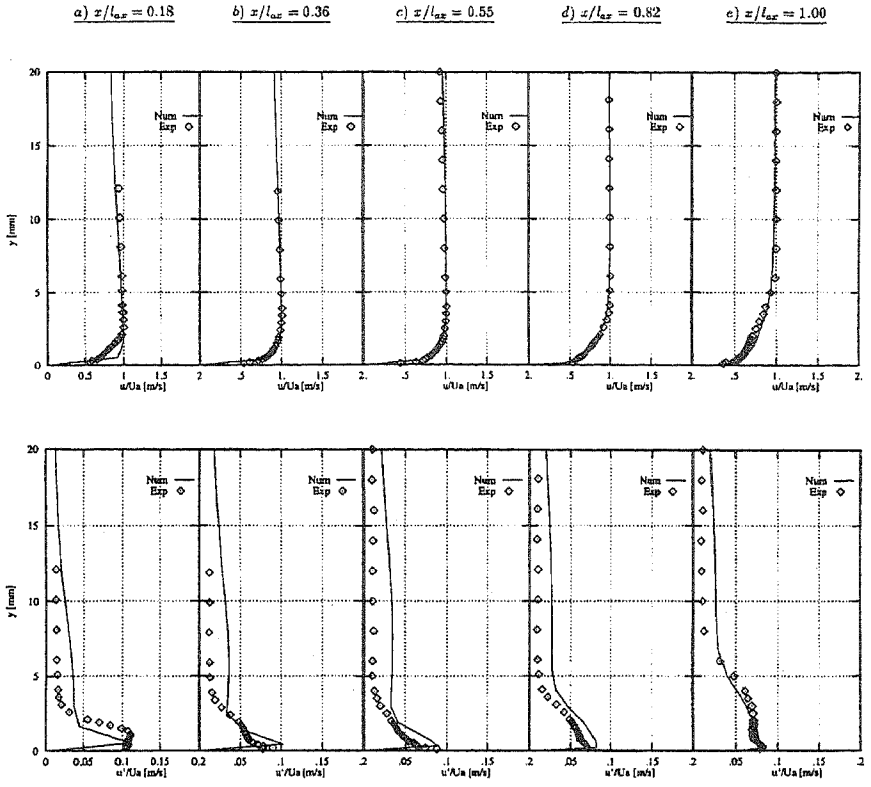

z / h = 0.50

z / h = 0.50

Bild 39 Fortsetzung

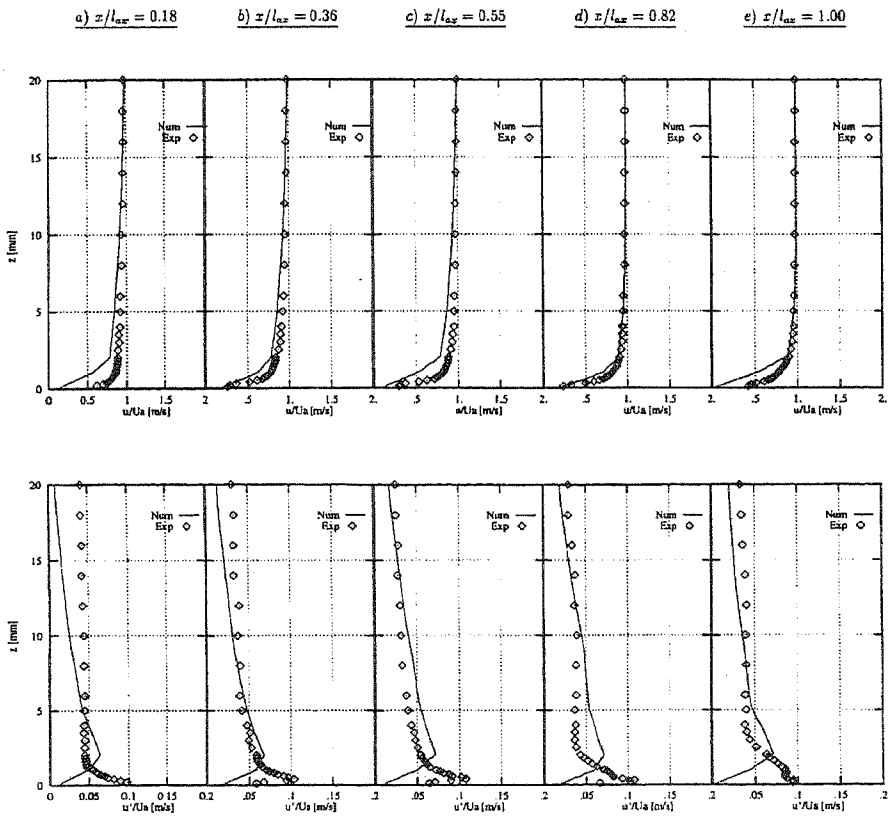

z / h = 0.14

z / h = 0.14

Bild 40 Beschaufelter Kanal (Aachen): Grenzschichtprofile der Geschwindigkeit (u/U_a) und der turbulenten Längsschwankungen $\sqrt{\overline{u'^2}}/U_a$ entlang des Bodens bei y/t = 0.14

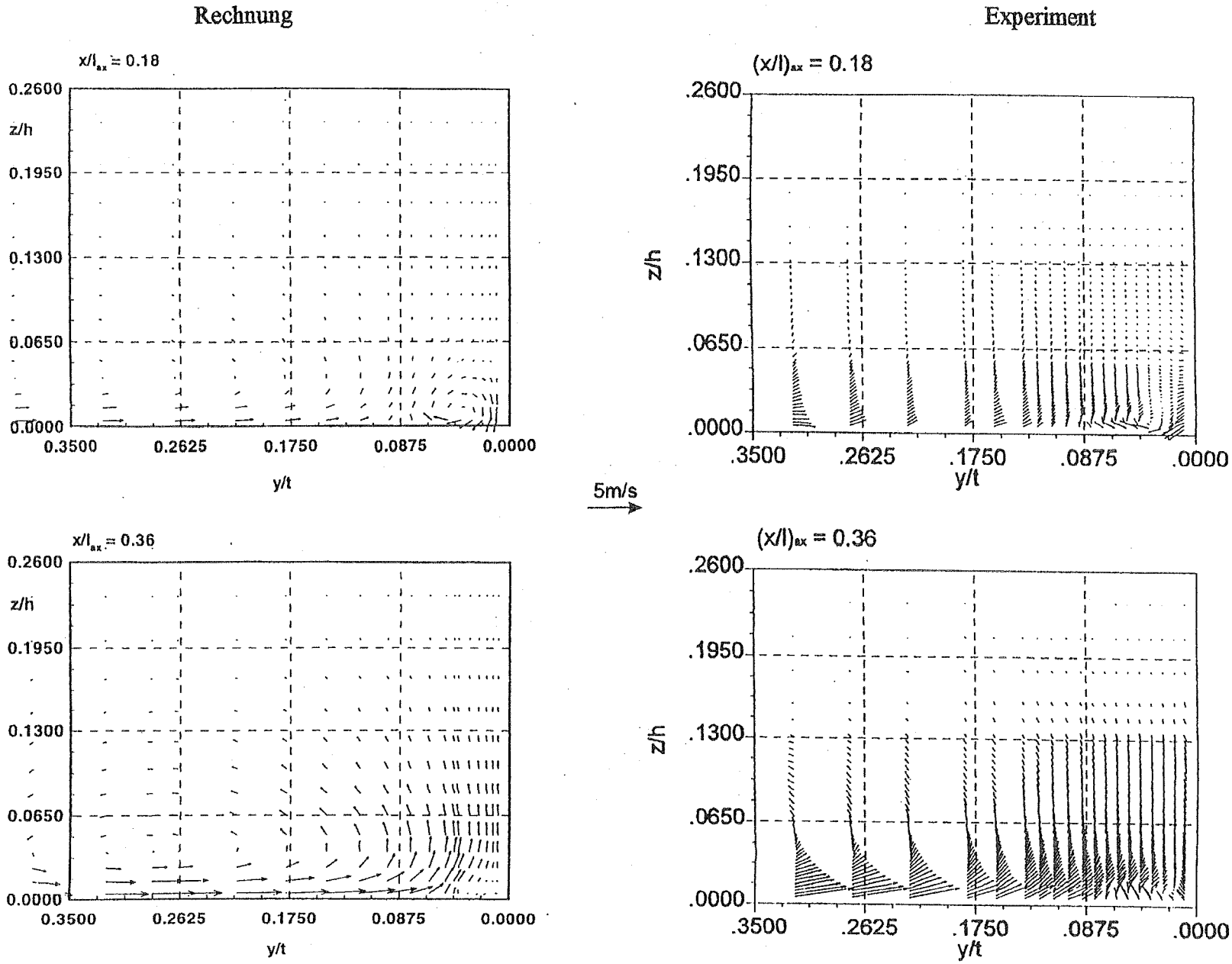

Bild 41 Beschaufelter Kanal (Aachen): Vektoren der Sekundärströmungsgeschwindigkeit (relativ zur entsprechenden Geschwindigkeit auf der Mittelebene) in verschiedenen Meßebenen senkrecht zur Saugseite

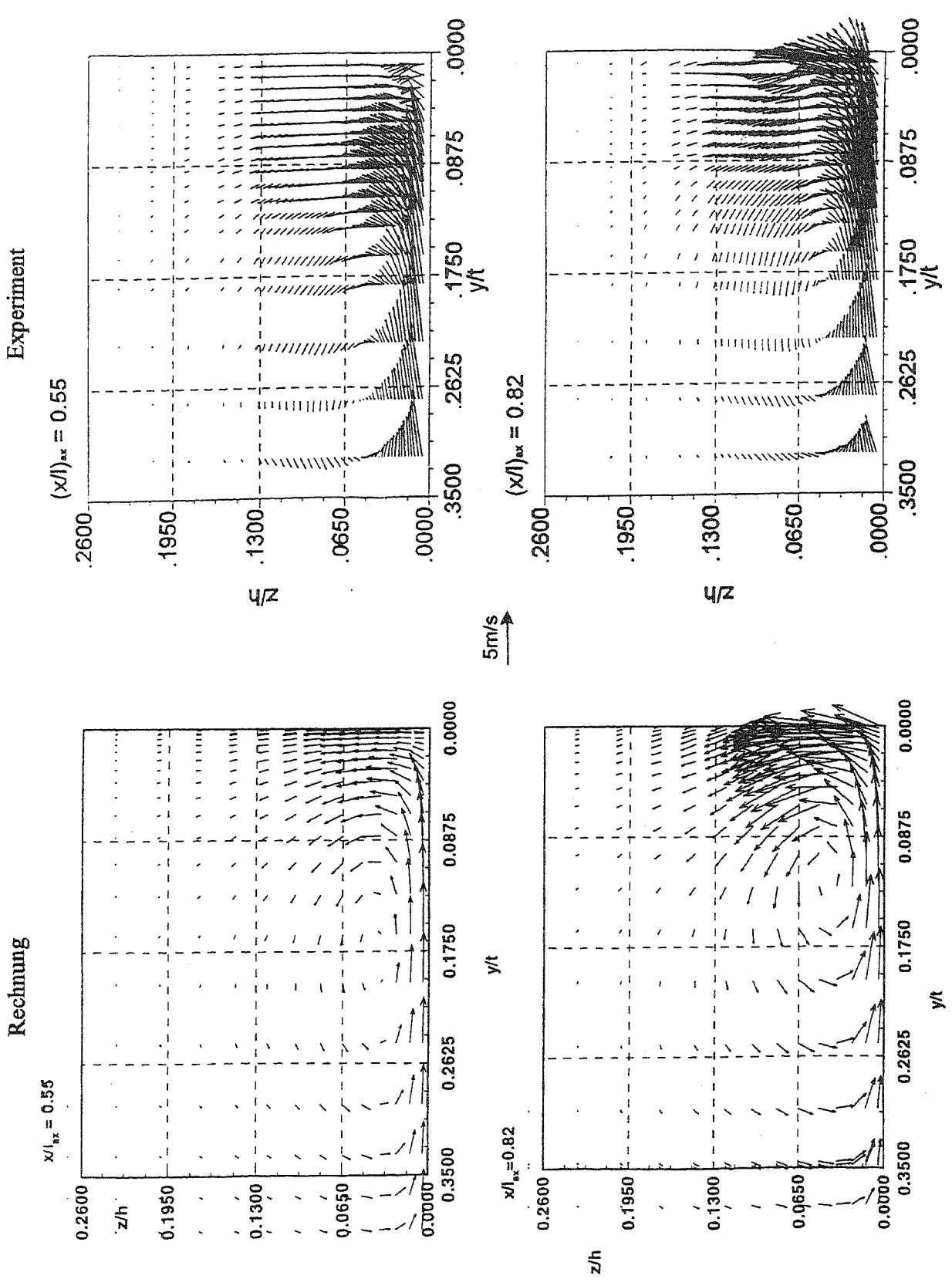

Bild 41 Fortsetzung

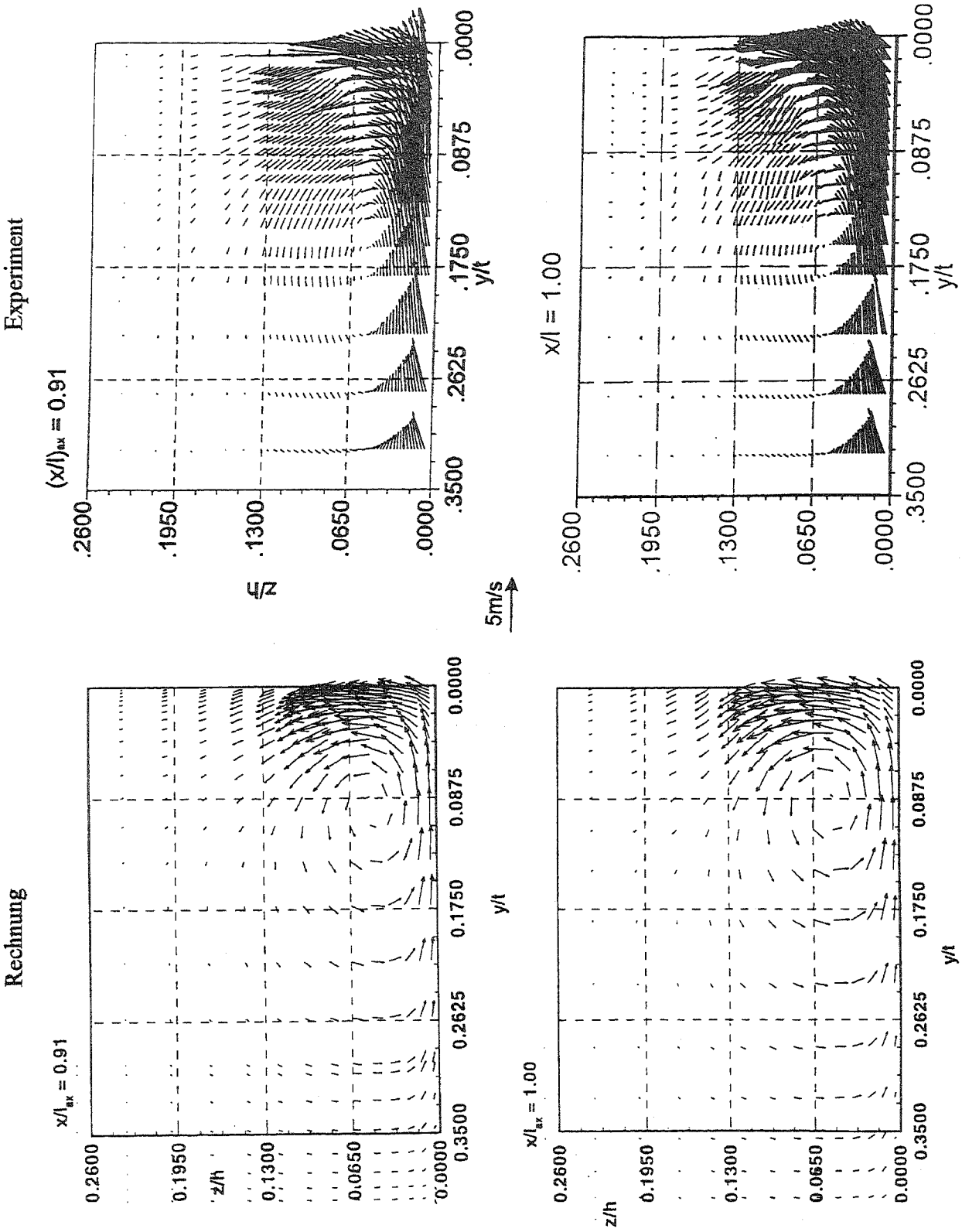

Bild 41 Fortsetzung

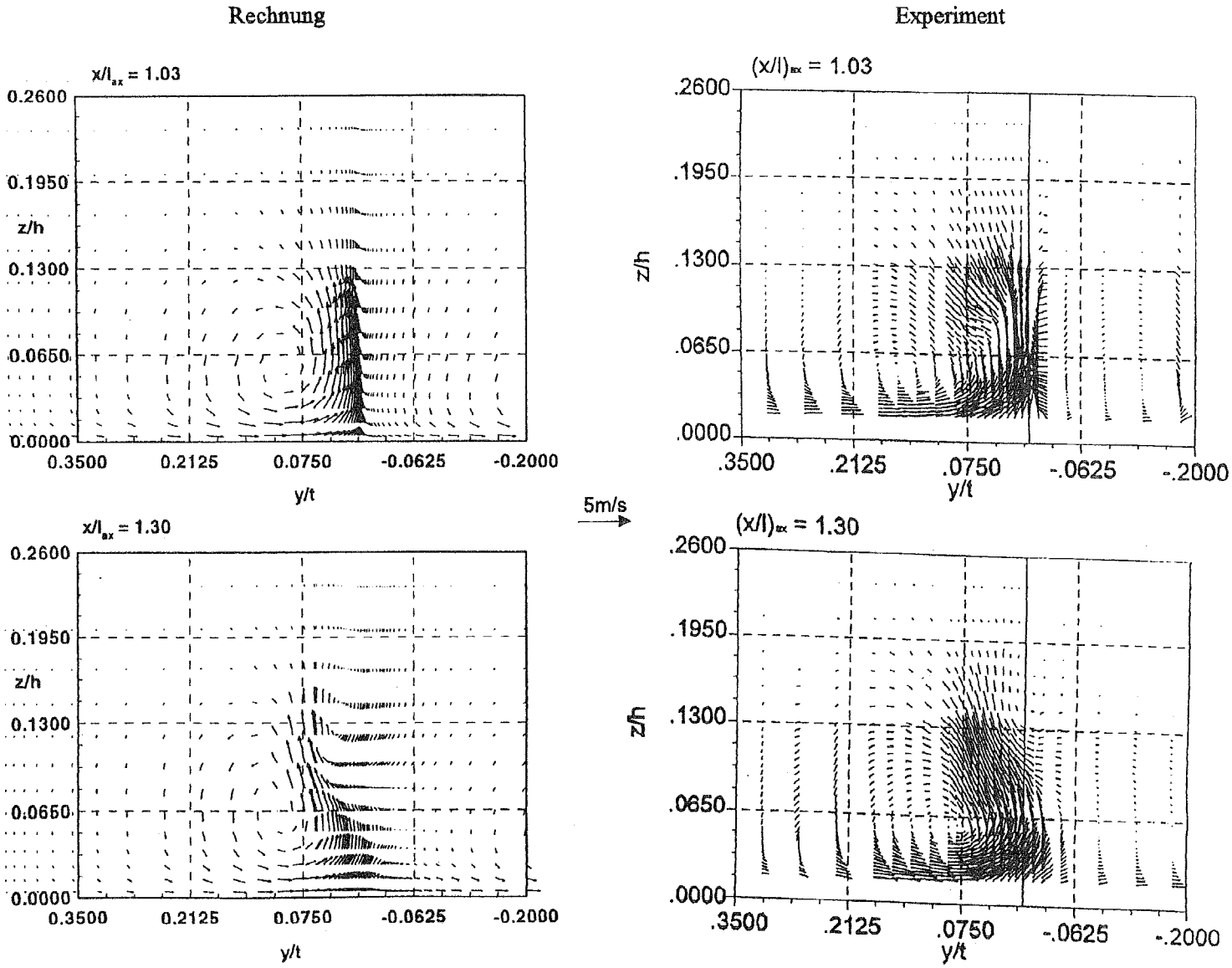

Bild 41 Fortsetzung

Anhang A

A Pressure-Correction Algorithm for All-Speed Flows

Institute for Hydromechanics
University of Karlsruhe

Report No. 718

A Pressure Correction Algorithm for All-Speed Flows

Vittorio Michelassi †

July 1994

† On leave from the University of Florence, Florence, Italy

Acknowledgements

The authors wishes to gratefully acknowledge Dr. Georgios Theodoridis and Dr. Elias Papanicolaou for the interesting and fruitful late night and weekend discussions about the incompressible and compressible pressure correction scheme.

The author also wishes to thank Prof. Wolfgang Rodi and Prof. Francesco Martelli for the support and guide granted during the preparation of his work.

The work was sponsored by the German Federal Ministry of Education, Science, Research and Technology through Programme TURBOTECH under contract no. 0326801G.

List of contents

1 INTRODUCTION

In the past decade the pressure correction scheme has been successfully applied to a wide variety of flows in complex geometries (Zhu et alt., 1992). Still, these applications were confined to flow regimes in which the Mach number did not exceed values around 0.3-0.4 so that compressibility effects could be neglected.

A different approach was often preferred in the literature in presence of compressibility effects. Namely, the most popular approach is the so called time-marching method in which the governing equations are solved by implicit procedures like, Beam and Warming(1982), Michelassi et alt. (1990, 1993). These algorithms use density as a main dependent variable, together with momentum and, generally, the total specific internal energy. The main drawback of such formulations lies in the strong link existing between the static pressure and density through the static temperature which becomes extremely weak at low Mach numbers. These methods can be accurately used for Mach number not below 0.1 (this value is in fact solver dependent) since the mass conservation and the solution quality rapidly deteriorate. Observe that in this class of algorithms the equations are generally solved in a coupled manner by constructing jacobian matrices which link together all the governing equations.

A valid alternative to these methods is represented by the generalization of the pressure correction algorithm to compressible flows. Several applications of the extented pressure correction scheme are available in the literature (Issa and Lockwood, 1977, Karki and Patankar, 1989, McGuirk and Page, 1990, Lien and Leschziner, 1993). These methods are all based on the SIMPLE or SIMPLEC (Patankar, 1980) algorithms for determining the static pressure field and correcting the mass fluxes. In this approach the continuity equation is transformed into the pressure correction equation by using the momentum conservation to establish a direct link between pressure and velocity. The system of governing equations is completed by an energy equation generally written in terms of static temperature, or static enthalpy. This choice, with respect to the introduction of a transport equation for the total specific internal energy, is often made to handle a quantity which can be readily measured in real flows. The introduction of the equation of state for a perfect gas establish the link between the computed pressure and temperature and the local density. The pressure correction algorithms solve the transport equation in a decoupled manner to gain in flexibility of the solution process.

The present work intends to briefly describe an existing pressure correction algorithm for incompressible flows which was modified for all speed flows. The current proposals to introduce compressibility effects are then outlined. A simple way to obtain an accurate all speed algorithm from an existing incompressible solver is then described. The new approch is compared with an existing time-marching implicit algorithm based on the scalar approximate factorization technique (Michelassi et al., 1990) which uses the non-linear artificial dissipation scheme proposed by Jameson et alt. (1981). The results of the two methods are then compared in a converging-diverging channel and for 10% and 4% bump flows.

2 PRESSURE CORRECTION FOR COMPRESSIBLE FLOWS

2.1 Existing compressible pressure correction algorithms

The pressure correction algorithm, originally developed for incompressible flows, has been extended to compressible flows by several authors. The first proposal is due to Issa and Lockwood (1977). Then Karki and Patankar (1989) modified the continuity equation to include density changes. In two dimensions the discretized continuty equation can be written as:

$$(\rho U)_e - (\rho U)_w + (\rho V)_n - (\rho V)_s = 0$$

in which U and V are the contravariant velocities. Karki and Patankar based their proposal on the SIMPLER algorithm and solved two pressure correction equations. The first pressure correction, usually named p', is used to update the existing pressure and density field, whereas the second correction, p'', is used to correct the velocity field to ensure mass conservation. The correction equation for p' includes the effect of density changes. The main drawback of the Karki-Patankar approach is that, following the suggestion of Issa and Lockwood (1977) who upwinded the pressure in supersonic flows, the density is first order upwinded in the pressure correction equation. The density upwinding does not produce any effect in low Mach number flows, but, as the Mach number increases and the hyperbolic nature of the flow is enhanced, the amount of artificial diffusion can rapidly become very large.

More recently Majumdar (1992), while keeping the SIMPLER algorithm, reformulated the Karki and Patankar algorithm to be able to solve for a single pressure correction by linking the density changes to the pressure changes via the perfect gas law. In his formulation Majumdar uses a collocated variable arrangement with momentum interpolation for the pressure correction equation, whereas Karki and Patankar utilize a staggered variable arrangement. The practice of a simple density upwinding in the pressure correction equation, often coupled with hybrid discretization schemes, produces very large shock smearing which makes the algorithms not attractive for supersonic flow calculations. In fact, one should observe that in compressible flows the continuity equation acts like a transport equation for the density the spatial changes of which are greatly smoothed by upwinding in both the results reported by Karki and Patankar, and Majumdar despite the differences in the discretization schemes. The practice of these authors produce flow patterns in which it is sometimes impossible to detect shocks.

In order to have sharper shocks McGuirk and Page (1990) proposed to solve for ρU and not for U and ρ separately. The SIMPLE algorithm is reformulated in a

staggered grid arrangement. The main improvement proposed by Mc Guirk and Page is the introduction of the so called "retarded pressure field" which replaces the "physical pressure field". The retarded density is introduced since the original pressure correction equation is essentially elliptic at any Mach number. When using a centered discretization scheme it is not possible to remedy this problem, which, conversely, can be cured by the density upwinding proposed by Karki and Patankar. The idea of a biased pressure is somewhat similar to the biased density proposed by Hafez et al. (1979) and is defined as:

$$\overline{p}_i = p_i + \mu_{i-1/2}(p_i - p_{i-1})$$

for a positive flow velocity. The biasing function μ is formulated as:

$$\mu_{i-1/2} = \max\left\{0, k\left[1-\left(M_{ref} / M_{i-1/2}\right)^2\right]\right\}$$

in which k and M_{ref} are constant of the order of one. The biasing function has no effect in subsonic flows, thereby not altering the accuracy of the discretization scheme. For supersonic flows the hyperbolic nature of the pressure is artificially achieved by upwinding the pressure. The amount of upwinding is not constant, like in Karki and Patankar, but is controlled by M_{ref} and k. The dramatic improvements obtained by Mc Guirk and Page with respect to the Karki and Patankar results in terms of shock capturing capabilities show that the practice of a pure density, or convective fluxes, upwinding must be avoided.

Following the work of McGuirk and Page, Lien and Leschziner (1993) recently presented a new algorithm which ensures good shock capturing capability. In place of the biased pressure field that should replace the physical pressure, Lien and Leschziner introduces the biased density which is directly used to compute mass fluxes. The biasing function μ has the same structure of that used for the biased pressure, but is generalized for two dimensional complex flow. This latest formulation proved competitive with all the existing time marching algorithms and was applied in complex flows in conjunction with turbulence models. Lien (1992) also provides a complete explanation of the links between the artificial damping scheme by Jameson and the biased density concept.

The scheme proposed by Mc Guirk and Page (and by Lien) solves for ρU. Conversly, the formulation proposed by Majumdar introduces only minor changes to existing incompressible pressure correction codes since it retains the original variable choice and simply add the compressibility effect to the pressure correction step usually carried out by using the SIMPLE or SIMPLEC algorithm. The changes required by the McGuirk and Page or the Lien and Leschziner schemes to an existing incompressible pressure correction scheme are somewhat deeper. This is due to the change of variables (ρU in place of U), and to the interpolation of the variables on the cell faces. The next section will describe an existing pressure correction code for incompressible flows and a simple and accurate

modification to ensure good shock capturing capabilities in presence of compressibility effects.

2.2 The pressure correction algorithm for incompressible fluid flows

The present investigation was carried out by starting from the standard version of the FAST-3D code by Zhu (1992). This code is designed for the simulation of internal complex incompressible flows. Since the incompressible formulation is largely left unaltered for compressible fluids, a brief description of the original solver is given. For the sake of simplicity, the equations will be given in their cartesian form, being the extension to curvilinear coordinate systems straightforward. The governing equations are written in tensor form as follows:

$$\textit{continuity} \qquad \frac{\partial \rho}{\partial t} + \frac{\partial \rho u_i}{\partial x_i} = 0 \tag{1}$$

$$\textit{momentum} \qquad \frac{\partial \rho u_i}{\partial t} + \frac{\partial}{\partial x_j}\left(\rho u_i u_j - \tau_{ij}\right) + \frac{\partial p}{\partial x_i} = 0 \tag{2}$$

in which t is time, x_i is the *i-th* coordinate vector, u_i the velocity component in the x_i direction, ρ is the fluid density, p is the static pressure, and τ is the viscous stress tensor. The equations are discretized by using finite volumes in three dimensions. The code uses a collocated variable arrangement, so that all the transported quantities are defined at the control volume centre. Convection can be treated by using the standard hybrid technique or the low-diffusive scheme, named HLPA, developed by Zhu (1991, 1992), which largely decreases the extra numerical diffusion brought by the hybrid scheme, but is more stable than other existing second order upwind schemes. This convection scheme is similar to the harmonic TVD scheme by Van Leer and for a positive velocity can be formulated as:

$$\phi_w = \phi_W + \gamma_w\left(\phi_p - \phi_W\right)\frac{\left(\phi_W - \phi_{WW}\right)}{\left(\phi_p - \phi_{WW}\right)} = \phi_W + \gamma_w\left(\phi_p - \phi_W\right)\hat{\phi}_W$$

in which

$$\gamma_w = \begin{cases} 1 \ \textit{if} \ \left|\hat{\phi}_W - 0.5\right| < 0.5 \\ 0 \ \textit{otherwise} \end{cases}$$

and the subscripts P, w, W, and WW are defined in figure 1.

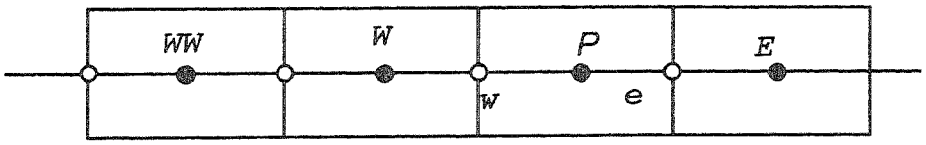

Figure 1. Collocated grid arrangement.

This scheme prevents from overshoots of the transported quantities. Further details on the code may be found in Zhu (1992).

Special attention is devoted to the continuity equation. In fact, the cell centre location of the transported variable implies the need to evaluate cell face values to discretize the mass conservation relation. While a simple linear interpolation is suited for the momentum and the energy equations, the same technique cannot be used for the continutiy equation since it results in the well known unphysical chequerboard pattern for the static pressure. To avoid this, equation (1) is first modified to get the pressure correction equation. This is done following the idea by Patankar(1980) for the SIMPLE family of algorithms according to which a link between cell centre pressure and cell face velocity is established by means of the momentum equation. The cell face velocities are not evaluated by linear interpolation of the cell centre velocities, but using the momentum interpolation technique by Rhie and Chow (1983) which introduces some extra diffusion in order to prevent pressure wiggles. For further details about the code see Zhu (1992).

2.3 The introduction of compressibility effects

The modification of an existing incompressible flow solver in order to make it able to cope with all speed flows may follow one of the basic guidelines proposed by Karki and Patankar (1989), or Mac Guirk and Page (1990), or Lien and Leschnizer (1993). Most of the incompressible flow solvers, like FAST-3D are designed to solve for the static pressure and the fluid velocity components. For compressible fluids it would be more convenient to solve for the static pressure and the directional momentums ρu_i, together with another quantity like static or total temperature, enthaply, or energy. The choice of solving for momentums is theoretically convenient since ρu_i is constant across a shock whereas u_i is not. This approach is followed by Mc Guirk and Page, and Lien and Leschziner. Unfortunately, the amount of modifications required to introduce this change in a existing 3D incompressible code is often excessive.

When retaining u_i as the unknown for the solution of the momentum equations, which remains substantially unaltered with respect to the incompressible fluid version, the pressure correction step requires some modifications. Karki and Patankar (1989) observe

that for compressible flows the continuity equation acts like a transport equation for density. Following the SIMPLE algorithm, the continuity equation is arranged in such a way that the static pressure comes out from an elliptic equation. Now, the elliptic nature cannot be retained for supersonic flows where the pressure correction equation must have an hyperbolic nature. Karki and Patankar solve this problem formulating the continuity equation in one dimension as follows:

$$\left(\rho_e^* + \rho_e'\right)\left(u_e^* + u_e'\right)l_e - \left(\rho_w^* + \rho_w'\right)\left(u_w^* + u_w'\right)l_w = 0 \tag{3}$$

in which the guessed density and velocity field are starred and the dashed variables are modification to the guessed field to ensure continuity, and l is the cell surface. Equation (3) is rewritten as:

$$\underbrace{\left(\rho_e^* u_e^* l_e - \rho_w^* u_w^* l_w\right)}_{T0} + \underbrace{\left(\rho_e^* u_e' l_e - \rho_w^* u_w' l_w\right)}_{T1} + \underbrace{\left(\rho_e' u_e^* l_e - \rho_w' u_w^* l_w\right)}_{T2} + \underbrace{\left(\rho_e' u_e' l_e - \rho_w' u_w' l_w\right)}_{T3} = 0 \tag{4}$$

The $T0+T1$ term is the usual incompressible contribution and the $T3$ term is normally neglected. The $T2$ term introduces the compressibility effects the discretization of which is a crucial task in solving compressible flows. In fact, while for subsonic flows $T2$ can be discretized by using a central scheme, this cannot be done in transonic or supersonic flows when this equation must have a dominat hyperbolic nature. Karki and Patankar propose to use a pure upwinding for the $T2$ term in order to introduce only the upstream influence on the pressure. The pressure density link may be computed by using the perfect gas relation to obtain:

$$\rho' = \frac{p'}{RT} = p'\frac{K}{T}$$

under the hypothesis of an isothermal transformation. Optionally, we can assume an isentropic transformation so that, via the definition of the speed of sound, we can write:

$$\frac{1}{a^2} = \left.\frac{d\rho}{dp}\right|_{S=\text{cost}} = \frac{1}{\gamma RT} = \frac{K}{T}$$

in which S is the fluid entropy. The two definitions give two different expressions for K, which weighs the influence of the density on the pressure field. By using the first expression

for K the density changes in the discretized $T2$ term may be expressed in terms of pressure changes as proposed by Karki and Patankar:

$$\rho_w' = \frac{1}{RT_W}\max\left(\frac{u_w}{|u_w|},0\right)p_W' + \frac{1}{RT_P}\max\left(\frac{-u_w}{|u_w|},0\right)p_P'$$

$$\rho_e' = \frac{1}{RT_P}\max\left(\frac{u_e}{|u_e|},0\right)p_P' + \frac{1}{RT_E}\max\left(\frac{-u_e}{|u_e|},0\right)p_E' \tag{5}$$

in which the density change is first order upwinded. This first order upwind is necessary only in transonic and supersonic flows. In fact Tamamidis (1990) used a simple linear interpolation for the density change in subsonic flows as follows:

$$\rho_w' = (1-f_x)\frac{1}{RT_W}p_W' + f_x\frac{1}{RT_P}p_P' \tag{6}$$

in which f_X is a linear interpolation function to get cell face values.

The practice proposed by Karki and Patankar, while able to introduce the necessary hyperbolic nature in the continuity equation, is generally regarded as the main source of inaccuracies in the wide number of applications and improvements to this method available in the literature. Moreover other authors (Majumdar, 1992) upwind the density change in the continuity equation and use an hybrid discretization scheme for all the convective terms. The results proposed by Majumdar are very much similar to those by Karki and Patankar, in which the position of the shocks can only be guessed. Mc Guirk and Page, and Lien and Leschziner indicate that using first order density upwinding is the main responsible for the poor quality of the results. Following the suggestion of Mc Guirk and Page a biasing function is introduced to weigh the upstream influence of the density change. The biasing function for a one dimensional positive velocity flow is defined as:

$$\mu = \max\left(0, k\left[1-\left(\frac{M_{ref}}{M}\right)^2\right]\right) \tag{7}$$

in which $k \approx 1$, $M_{ref} \approx 1$, and M is the local Mach number. Accordingly, a general quantity f is defined at each point P (see figure 1) as:

$$\tilde{f}_P = (1-\mu_w) f_P + \mu_w f_W$$

The biasing function decides when and the amount of density upwinding that should be brought inside the solution, depending on the local Mach number.

This simple biasing concept, retained by Lien and Leschziner (1993), may be directly applied to the original approach by Karki and Patankar with only minor changes. In place of the first order upwind, a blended linear-upwind interpolation is introduced. Additionaly, the direction sensor term appearing in equation (5) is replaced by a directional Mach number relation computed as:

$$M_P^+ = \frac{1+sgn(M_P)}{2}$$

$$M_P^- = \frac{1-sgn(M_P)}{2}$$

in which:

$$M_P = \frac{U_P}{a_P} = \frac{U_P}{\sqrt{\gamma R T}}$$

where Up is the local velocity module, and

$$sgn(f) = \begin{cases} 1 & for \quad f \geq 0 \\ 0 & for \quad f < 0 \end{cases}$$

So, for example, the density changes given in equation (5) are modified as follows:

$$\rho_w' = \frac{1}{R}\left\{ (1-\mu_w) \underbrace{\left[f_x \frac{p_P'}{T_P} + (1-f_x)\frac{p_W'}{T_W} \right]}_{\text{linear interpolation}} + \mu_w \underbrace{\left[M_P^+ \frac{p_W'}{T_W} + M_P^- \frac{p_P'}{T_P} \right]}_{\text{upwind}} \right\} \tag{8}$$

$$\varrho_e' = \frac{1}{R}\left\{(1-\mu_e)\underbrace{\left[f_x^+ \frac{p_E'}{T_E} + \left(1-f_x^+\right)\frac{1}{T_P}\right]}_{\text{linear interpolation}} + \mu_e \underbrace{\left[M_P^+ \frac{p_P'}{T_P} + M_p^- \frac{P_E'}{T_E}\right]}_{\text{upwind}}\right\}$$

in which f_x and f_x^+ are the linear interpolation functions for the *w-p* and *p-e* intervals respectively, and the velocities u on the cell faces are linearly interpolated from the cell centre values. In equation (8) the density is linearly interpolated on the cell face for low subsonic flow conditions, yielding to the elliptic nature of the pressure correction equation with $\mu_e = \mu_w = 0$, whereas it is upwinded for supersonic flows thereby increasing the hyperbolic nature of equation (4). Observe that while the biasing function μ is evaluated at the cell face by using the linear interpolated velocities, the function $M_p^{\pm}$ which is sensing the direction of the flow (i.e. positive or negative transport velocity) is evaluated only only at the centre P of the control volume. This choice was motivated by the need of reducing the computational overhead when extending the algorithm to three dimensional flows.

By selecting appropriate k and M_{ref} values it is possible to switch smoothly from the linear interpolation to the upwinding as the Mach number increases. So, after some algebra and keeping the equation stencil proposed by Patankar (1980), the discretized form of the continuty equation, Eq. (4), may be written as:

$$A_P p_P' = A_W p_W' + A_E p_E' + b \tag{9}$$

in which:

$$A_W = A_W^{T1} + A_W^{T2} = A_W^{T1} + \frac{l_w \mu_w}{R}\frac{1}{T_W}\left[(1-\mu_w)(1-f_x) + \mu_w M_P^+\right]$$

$$A_E = A_E^{T1} + A_E^{T2} = A_E^{T1} + \frac{l_e \mu_e}{R}\frac{1}{T_E}\left[(1-\mu_e) f_x^+ + \mu_e M_P^-\right]$$

$$A_P = A_P^{T1} + A_P^{T2} = A_P^{T1} + \frac{l_w}{T_P}\left\{\frac{u_w}{R}\left[(1-\mu_w)f_x + \mu_w M_P^-\right]\right\} + \frac{l_e}{T_P}\left\{\frac{u_e}{R}\left[(1-\mu_e)\left(1-f_x^+\right) + \mu_e M_P^+\right]\right\}$$

$$b = \varrho_w^* u_w^* l_w - \varrho_e^* u_e^* l_e$$

in which l_w and l_e are the cell face areas and u_w and u_e the cell face velocities obtained by momentum interpolation.

In FAST-3D the above modification to the coefficient A_p is written as:

$$\begin{aligned} A_P = A_P^{T1} + A_P^{T2} &= A_W^{T1} + A_E^{T1} + A_P^{T2} \\ &= \left(A_W - A_W^{T2}\right) + \left(A_E - A_E^{T2}\right) + A_P^{T2} \\ &= A_W + A_E - S_P \end{aligned}$$

where the source term S_P is defined in the following form:

$$S_P = A_W^{T2} + A_E^{T2} - A_P^{T2}$$

and the A_W, A_E are the total coefficients which include both the incompressible and compressible terms, as defined in Eq. (9). In other words, the compressible part of the matrix coefficient is lumped into the source term of the equation, S_P.

When osberving each term of equation (9) one might suspect that non positive contribution could arise to the A_P coefficient. This might have an important impact on the convergence of the algorithm insofar the resulting matrix can have a not-dominant main diagonal. If this happens, although only locally, the only cure lies in a reduction of the relaxation factor for the pressure corrector step. If α_p is the relaxation parameter of the pressure correction step, the matrix of a one-dimensional problem is diagonal dominant as long as:

$$\left(A_W + A_E - S_p\right) \cdot \frac{1}{\alpha_{p'}} > A_W + A_E$$

If this requirement is not fullfilled the obvious cure lies in a reduction of the relaxation parameter $\alpha_{p'}$. This reduction needs not be extended to the entire computational domain, but instead a local relaxation factor $\tilde{\alpha}_{p'}$ might be defined as:

$$\frac{1}{\tilde{\alpha}_{p'}} = S \cdot \frac{\left(A_W + A_E\right)}{\left(A_W + A_E - S_p\right)}$$

in which S is a security factor which ranges between 1.05 to 1.2.

The contribution A^{T1} to the pressure correction equation is the unaltered incompressible term in which the momentum interpolation is used for the velocity. So, the incompressible pressure correction step is modified to include the compressibility correction introduced by the *T2* term. The cell face mass fluxes must be computed with the same biased density adopted for the continuty equation (9) and maintaining the momentum interpolation for the velocity. This is accomplished by defining the biased densities as follows:

$$\tilde{\rho}_w = \rho_w^l \left(1 - \mu_w\right) + \mu_w \left(\rho_w M_p^+ + \rho_p M_p^-\right) \tag{10}$$

$$\tilde{\rho}_e = \rho_e^l \left(1 - \mu_e\right) + \mu_e \left(\rho_e M_p^- + \rho_p M_p^+\right)$$

in which ρ^l represents the density linearly interpolated on the cell face. The mass fluxes are then computed by the biased density given by equation (10) and accounting for the proper relaxation of the momentum interpolated fluxes, as proposed by Majumdar (1988), as:

$$c_w = \tilde{\rho}_w \cdot \tilde{U}_{contr} + \left(1 - \alpha_M\right) \cdot \left(c_w^{old} - c_w^l\right)$$

in which the $\tilde{U}_{contr}$ is the contravariant velocity on the cell face computed by using momentum interpolation, and α_M is the relaxation factor of the momentum equation.

The conservation of the static enthalpy is added to the momentum equations for which the HLPA convection scheme is retained. With respect to the Lien and Leschziner approach, which solves for ρu_i, here the basic unknowns are the static pressure, the three components of the velocity u_i and the static enthalpy (or temperature).

2.4 Extension to three dimensional flows

The aforedescribed algorithm can be easily extended to three dimensional flows by repeating to the other two directions the same considerations made for the west-central-east computational cell. The only differences are due to the non orthogonality of the three dimensional grid for which it is necessary to define the so-called unscaled form of the contravariant and covariant components of the velocity vector:

$$U_\xi^{contr} = c_x u + c_y v + c_z w$$

$$U_\xi^{cov} = \tilde{c}_x u + \tilde{c}_y v + \tilde{c}_z w$$

in which $c = \xi, \eta, \zeta$. The $c_{x,y,z}$ terms are the contravariant metrics and the $\tilde{c}_{x,y,z}$ are the covariant metrics. The contravariant velocity component is orthogonal to the cell faces, whereas the covariant component is aligned with the coordinate lines. These two velocity components are equivalent only in orthogonal coordinate systems. The contravariant component is used for the computation of fluxes and in the evaluation of the matrix coefficients.

Concerning the biasing formulas for the density (see equation (8)) it is necessary to observe that the density is upwinded along the curvilinear coordinate direction ξ, η, ζ. The amount of upwind is governed by the directional Mach number which, accordingly, has to be computed by using the covariant velocity component, thereby the component aligned with coordinate lines. This means that equation (7) is modified as follows:

$$\mu_\xi = \max\left(0, k\left[1 - \left(\frac{M_{ref}}{M_\xi^{cov}}\right)^2\right]\right) \tag{11}$$

in which the directional covariant Mach number is defined as:

$$M_{\xi}^{cov} = \frac{U_{\xi}^{cov}}{a \cdot \sqrt{\tilde{c}_x^2 + \tilde{c}_y^2 + \tilde{c}_z^2}} = \frac{\tilde{c}_x u + \tilde{c}_y v + \tilde{c}_z w}{\sqrt{\gamma RT} \cdot \sqrt{\tilde{c}_x^2 + \tilde{c}_y^2 + \tilde{c}_z^2}}$$

The covariant velocity components are linearly interpolated on the cell faces. The same expression can be easily modified to get the components in the other two spatial directions.

The directional sensor term, $M_P^{\pm}$, is computed by using the contravariant velocity components which are known already from the computation of the fluxes and does not require any additional computation with respect to the incompressible formulation.

With this implementation of the directional biasing, the density is upwinded along the coordinate lines in three dimensions. The amount of upwinding, if any, may vary along the three directions c, $c = \xi, \eta, \zeta$, depending on the component of the local Much number aligned with the local coordinate lines.

2.5 Boundary Conditions

The boundary condition procedure, which applies also to the time marching code, is developed for both subsonic or supersonic outlet.

- **Subsonic outlet Mach number**

  The isentropic outlet Mach number M_{ex} is fixed by the inlet total pressure to exit static pressure ratio. In case of a subsonic exit Mach number the inlet total pressure P_0^{in}, the exit static pressure P^{ex}, the inlet total temperature T_0^{in}, and the inlet flow angles α,β (in 3D flows two angles are needed) are fixed. This choice allows fixing directly the inlet total quantities that are very much often the only true data for compressible flow calculations. The inlet static pressure P^{in} is extrapolated at the inlet section from the interior points at every iteration, generally using a first order extrapolation, so that the local inlet Mach number is computed by the isentropic relation:

$$M_{in} = \sqrt{\frac{2}{\gamma - 1}\left[\left(\frac{P_0^{in}}{P^{in}}\right)^{\frac{\gamma-1}{\gamma}} - 1\right]}$$

in which γ is the specific heat ratio. Consequently the inlet static temperature is given as:

$$T^{in} = \frac{T_0^{in}}{1 + \frac{\gamma - 1}{2} M_{in}^2}$$

which allows computing the inlet sound speed a and the inlet density:

$$a_{in} = \sqrt{\frac{\gamma\, P^{in}}{\rho}} = \sqrt{\gamma\, R\, T^{in}}$$

$$\rho_{in} = \frac{P^{in}}{R\, T_{in}}$$

The inlet velocity module follows straightforward from the definition of the Mach number:

$$|U_{in}| = M^{in} \cdot a_{in}$$

The velocity module is then decomposed in the three components according to the inlet flow angles. Observe that in this case neither the inlet Mach number nor the outlet Mach number are known a priori. In fact both of them are influenced by the amount of entropy changes (or total pressure losses) inside the domain. Only in the case of isentropic flow can the exit Mach number be computed directly from the inlet total pressure P_0^{in} and the exit static pressure P^{ex}.

In the exit section the static pressure is fixed to P^{ex} and all the other variables are extrapolated.

- **Supersonic outlet Mach number**

  In case of supersonic exit the boundary condition specification is extremely simple. In fact no characteristic wave can enter the domain from the exit section so that all the variables are extrapolated at that section. At the inlet section the inlet total pressure P_0^{in}, the inlet static pressure P^{in}, the inlet total temperature T_0^{in}, and the inlet flow angles α,β (in 3D flows two angles are needed) are fixed.

3 THE TIME MARCHING CODE

3.1 The implicit solver

In order to compare the results computed by using the compressible pressure correction algorithm, the same test flows were also computed by using an implicit time marching code which solves for density, momentum, and total internal specific energy. In the implicit time marching code the transported and related quantities are made non dimensional with respect to the inlet total pressure P_0 and inlet total temperature T_0. Viscosities and diffusion coefficients are made non dimensional with respect to the inlet laminar viscosity. The equations can be written in a compact vector form as:

$$\frac{\partial Q}{\partial t}+\frac{\partial F_k}{\partial x_k}=\frac{\partial F_k^v}{\partial x_k} \quad , \qquad k=1,2,3 \tag{12}$$

The equations are discretized by centered finite differences in curvilinear non orthogonal coordinate systems.

The FLOS3D program is based on the scalar implicit algorithm proposed by Pulliam and Chaussée (1981). The program solves three-dimensional compressible flows with complex boundaries in inviscid, laminar and turbulent regime. In order to make the approximate factorization method by Beam and Warming (1982) less computational costly Pulliam and Chaussée proposed a scalar form, adopted for the present set of calculations, that retains the intrinsic robustness of the original algorithm for internal viscous flows (Michelassi et al., 1990, 1993), but decreases the number of operations per grid point. The introduction of a set of eigenvalues, Λ, and eigenvectors, T, allows writing:

$$T_\xi\left[I+\theta\Delta t\left(\delta_\xi\Lambda_\xi\right)\right]\cdot N\cdot\left[I+\theta\Delta t\left(\delta_\eta\Lambda_\eta\right)\right]\cdot P\cdot\left[I+\theta\Delta t\left(\delta_\zeta\Lambda_\zeta\right)\right]\cdot T_\zeta^{-1}\cdot\Delta Q=RHS \tag{13}$$

in which $\Delta Q=Q^{n+1}-Q^n$, the matrices $N=T_\xi^{-1}T_\eta$ and $P=T_\eta^{-1}T_\zeta$ are solution independent and Θ allows weighting of the explicit-implicit nature of the space operator in round brackets. This formulation, which drops the viscous contribution to the implicit space operator, was found weak in internal viscous flows because of the presence of boundary layers. Unfortunately the diffusive operators cannot be included in the left hand side of equation (13) since they have a totally different set of eigenvectors. Nevertheless, to render the algorithm more efficient in presence of viscous boundary layers the implicit side of equation (13) is modified to account for an approximate expression of the viscous eigenvalues. The modified algorithm reads:

$$T_\xi \cdot \left[I + \theta\Delta t\left(\delta_\xi \Lambda_\xi - \delta_\xi^2 \Lambda_\xi^\nu \right) \right] \cdot N \cdot \left[I + \theta\Delta t\left(\delta_\eta \Lambda_\eta - \delta_\eta^2 \Lambda_\eta^\nu \right) \right] \cdot P \cdot \left[I + \theta\Delta t\left(\delta_\zeta \Lambda_\zeta - \delta_\zeta^2 \Lambda_\zeta^\nu \right) \right] \cdot T_\zeta^{-1} \cdot \Delta Q = RHS \tag{14}$$

The eigenvalue vectors read:

$$\Lambda_l = \left(U_l, U_l, U_l, U_l + a\sqrt{l_{x_1}^2 + l_{x_2}^2 + l_{x_3}^2}, U_l - a\sqrt{l_{x_1}^2 + l_{x_2}^2 + l_{x_3}^2} \right)^t$$

$$\Lambda_l^\nu = \left(0, \frac{\rho\mu_{eff}\left(l_{x_1}^2 + l_{x_2}^2 + l_{x_3}^2 \right)}{\mathrm{Re}}, \frac{\rho\mu_{eff}\left(l_{x_1}^2 + l_{x_2}^2 + l_{x_3}^2 \right)}{\mathrm{Re}}, \frac{\rho\mu_{eff}\left(l_{x_1}^2 + l_{x_2}^2 + l_{x_2}^2 \right)}{\mathrm{Re}}, \frac{\gamma\rho\mu_{eff}\left(l_{x_1}^2 + l_{x_2}^2 + l_{x3}^2 \right)}{\mathrm{Re}} \right)^t$$

in which $l = \xi, \eta, \zeta$, and U_l is the unscaled contravariant velocity defined as:

$$U_l = l_{x_1} u_1 + l_{x_2} u_2 + l_{x_3} u_3$$

Further details about the eigenvector matrices may be found in Pulliam and Chausshée (1981) and in Michelassi et al. (1990).

3.2 Local time stepping and artificial damping

The implicit solver needs the solution of scalar tridiagonal matrices because of the centered space discretization. The approximate factorization technique may have stability and wiggles problems in presence of shocks or, in general, of sharp gradients yielding to non-diagonal-dominat matrices. These problems may be overcome by introducing the artificial damping terms as proposed by Jameson et al. (1981) on both the implicit and the explicit sides of the operator for equation (14). The non-linear artificial second plus fourth order damping formulation is the one by Jameson et al.. Equation (14) of the implicit solver is modified as follows:

$$T_\xi \left\{ I + \theta\Delta t \left[\delta_\xi \Lambda_\xi - \left(\delta_\xi^2 \Lambda_\xi^\nu + \delta_\xi\left(\Omega^\xi \ \omega_\xi^2 \ \delta_\xi(J) \right) \right) + \delta_\xi\left(\Omega^\xi \ \omega_\xi^4 \ \delta_\xi^3(J) \right) \right] \right\} \cdot$$

$$N\left\{I+\theta\Delta t\left[\delta_\eta\Lambda_\eta-\left(\delta_\eta^2\Lambda_\eta^v+\delta_\eta\left(\Omega^\eta\ \omega_\eta^2\ \delta_\eta(J)\right)\right)+\delta_\eta\left(\Omega^\eta\ \omega_\eta^4\ \delta_\eta^3(J)\right)\right]\right\}\cdot$$

$$P\cdot\left\{I+\theta\Delta t\left[\delta_\zeta\Lambda_\zeta-\left(\delta_\zeta^2\Lambda_\zeta^v+\delta_\zeta\left(\Omega^\zeta\ \omega_\zeta^2\ \delta_\zeta(J)\right)\right)+\delta_\zeta\left(\Omega^\zeta\ \omega_\zeta^4\ \delta_\zeta^3(J)\right)\right]\right\}\cdot T_\zeta^{-1}\cdot\Delta Q= \qquad (15)$$

$$=\Delta t\left(-\frac{\partial F_k}{\partial x_k}+\frac{\partial F_k^v}{\partial x_k}+D_k^2-D_k^4\right)^n$$

The terms D_k^2 and D_k^4 are second and fourth order differences of the transported quantities given by vector Q. In the i-direction these extra terms are discretized as follows:

$$D_i^2=\nabla_i\left(\Omega_{i,j,k}^\xi\,\omega_{i,j,k}^2\right)\Delta_i\left(J\,Q_{i,j,k}\right)$$

$$D_i^4=\nabla_i\left(\Omega_{i,j,k}^\xi\,\omega_{i,j,k}^4\right)\Delta_i\nabla_i\Delta_i\left(J\,Q_{i,j,k}\right)$$

in which Δ and ∇ are forward and backward difference operators respectively. The Ω terms represent a directional scaling dependent of the directional spectral radius which in three dimensions result:

$$\Omega^\xi=\lambda_\xi+\left(\lambda_\eta^\sigma+\lambda_\zeta^\sigma\right)\cdot\lambda_\xi^{(1-\sigma)}\ ;\ \Omega^\eta=\lambda_\eta+\left(\lambda_\xi^\sigma+\lambda_\zeta^\sigma\right)\cdot\lambda_\eta^{(1-\sigma)}\ ;\ \Omega^\zeta=\lambda_\zeta+\left(\lambda_\xi^\sigma+\lambda_\eta^\sigma\right)\cdot\lambda_\zeta^{(1-\sigma)}$$

The spectral radius is defined as:

$$\lambda_l=|U_l|+a\sqrt{l_{x_1}^2+l_{x_2}^2+l_{x_3}^2}$$

The ω^2 and ω^4 coefficients are the artificial terms weights (Jameson et al., 1981) which, for example, are computed in the i-direction as follows:

$$\omega^2=\varepsilon^2\max\left(\nu_{i-1,j,k},\nu_{i,j,k},\nu_{i+1,j,k}\right)$$

$$\nu_{i,j,k} = \left| \frac{p_{i-1,j,k} - 2\,p_{i,j,k} + p_{i+1,j,k}}{p_{i-1,j,k} + 2\,p_{i,j,k} + p_{i+1,j,k}} \right|$$

which represents the shock sensor term. The fourth order weight is defined as:

$$\omega^4 = \max\left(0, \varepsilon^4 - \omega^4\right)$$

The same procedure is used in the other directions.

The introduction of the extra terms in the implicit side of the scalar approximate factorization code needs the solution of pentadiagonal scalar matrices in place of the original tridiagonal ones because of the five-point molecule necessary to compute the fourth order differences and the relative linearization in time.

To balance the artificial spurious fluxes a third order difference D^3 and a first order difference D^1 are added on boundaries (Michelassi et al., 1990) so that, for example, the RHS for i=2 reads:

$$RHS_{i=2} = \Delta t \left(-\frac{\partial F_k}{\partial x_k} + \frac{\partial F_k^v}{\partial x_k} - D_k^1 + D_k^3 \right)_{i=2}^n$$

in which:

$$D_k^1 = -(Q_{i=2} - Q_{i=1}), \quad D_k^3 = +(-Q_{i=1} + 3Q_{i=2} - 3Q_{i=3} + Q_{i=4})$$

These extra terms bring some artificial damping that on solid boundaries they sort a positive effect in terms of stability. These extra terms allows the code to run at larger *CFL* numbers, provided that the first and third order differences are properly linearized on the left hand side.

For the local time step, a wide number of numerical tests showed that in case of turbulent viscosity fields with large spatial variations, the introduction of the viscous contribution into the time step formula gave the best convergence rates. The expression adopted in the code is:

$$\Delta t = \frac{CFL}{1/\Delta t_{conv} + 1/\Delta t_{diff}}$$

in which the convective and diffusive time steps, Δt_{conv} and Δt_{diff}, are defined as:

$$\Delta t_{conv} = \frac{1}{|U_\xi| + |U_\eta| + |U_\zeta| + a\sqrt{\xi_{x_1}^2 + \xi_{x_2}^2 + \xi_{x_3}^2 + \eta_{x_1}^2 + \eta_{x_2}^2 + \eta_{x_3}^2 + \zeta_{x_1}^2 + \zeta_{x_2}^2 + \zeta_{x_3}^2}}$$

$$\Delta t_{diff} = \frac{1}{C_d \frac{\mu_{eff}}{\mathrm{Re}}\left(\xi_{x_1}^2 + \xi_{x_2}^2 + \xi_{x_3}^2 + \eta_{x_1}^2 + \eta_{x_2}^2 + \eta_{x_3}^2 + \zeta_{x_1}^2 + \zeta_{x_2}^2 + \zeta_{x_3}^2\right)}$$

C_d allows weighting the viscous term contribution to the time step. Best results are obtained with C_d ranging between 1. and 2.5. The CFL number ranges between 7 to 15.

4 RESULTS

The predictions of both the pressure correction and the time marching codes are compared in three typical geometries, ranging from low speed subsonic to high speed supersonic flows in presence or not of weak and strong shocks. All the tests were run with the original three-dimensional version of both the codes, but specifying a symmetry condition in the third direction, so that the domain and the computed flow pattern are in fact two dimensional. All the test runs refer to the code version which uses a constant total enthalpy relation to compute the static temperature:

$$T = T_0 - \frac{1}{2C_P}U^2$$

in which C_P is specific heat coefficient at constant pressure, and T_0 is the total temperature which remains constant all over the computational domain under the hypothesis of adiabatic boundaries. All the runs are made by using the inviscid formulation.

Observe that, if not specified elsewhere, all the static pressure and density plots are nondimensionalized with respect to the inlet total pressure and temperature.

4.1 Convergent and convergent-divergent nozzle flow

This preliminary test is carried out to verify the capability of the compressible FAST-3D code to capture orthogonal shocks in a very simple geometry. The converging nozzle has an inlet to outlet area ratio of 3:1 and the grid has 30×14×3 nodes. This test was run for M_{ex}=0.5, and the results of the test run are given in figures 2a,b,c. The up-down shape of all the computed profiles is due to the presence of a short straight channel duct added at the end of the convergent. The plots are in good qualitative agreement with similar calculations (Majumdar, 1992). What is in fact most important to look at is the convergence history. This test case, while referring to a shock free flow pattern, does have compressibility effects which do not seem to affect the convergence of the algorithm which reduces the error down to machine accuracy (approximately $10^{-13} - 10^{-14}$) in less than 400 iterations (see figures 3a,b,c,d).

The same kind of test was repeated for M_{ex}=0.2 and 0.85 without noticing any difference in the slope of the convergence rate. Typical relaxtion factors are 1.0 for the pressure correction, 0.7 for momentums, 0.3 to 0.5 for temperature, 0.7 for static pressure and 1.0 for density. Observe that the relaxation factor for density was kept to 1.0 for all the tests because it is opinion of the author that the dependent variables, like the density, should not be relaxed. In this way, while the static pressure and the static temperature follow the solution of a differential equation, the static density always has the correct physical value

which corresponds to the computed pressure and density fields. Moreover a wide set of numerical experiments show that when the code diverges no improvement may be obtained by reducing the relaxation factor of the density. The results are obtained by using the HLPA discretization scheme for the convective terms.

The ability of the new approach to detect shocks is tested by computing a 2.035:1:2.035 area nozzle flow. Figures 4a,b,c show the computed velocity, static pressure and static density plots for the preliminary shock free M_{ex}=0.1 case. The computations are symmetric with respect to the throat indicating no entropy sources. When moving to the M_{ex}=0.37 case a shock is produced in the diverging part of the channel. Figure 5 shows the pressure profile computed by using a first order upwind for convection and a pure upwind of the density in the compressible pressure correction scheme (in the same way reported by Karki and Patankar and Majumdar). The 40-point grid together with the upwinding highly smears the shock. The situation does not improve when using an 80-point grid, as can be seen in figure 5.b. A considerable improvement is achieved when introducing the HLPA convection scheme as shown in figure 5.c in which the shock is captured in 5 points and the computed pressure profile is much closer to the theoretical profile. Here the density is purely upwinded in the compressible pressure correction equation. These tests prove that the use of a higher order convection scheme is by itself able to improve the results, although keeping the first order upwinding of density in equations (8) and (9). This must not be regarded as a general result since the shock pattern is very simple and the shock is aligned with the coordinate lines. For what concerns the convergence rate, approximately 500 iterations were needed to reach a residual of the order of $10^{-09}-10^{-10}$. The relaxation parameters are unaltered with respect to the low subsonic case. Figure 5.d shows the very good shock capturing of the time marching code FLOS3D. Clearly, when retaining the density upwind in equations (9) and (10) of FAST-3D the pressure profile is not as good as the one predictied by FLOS3D.

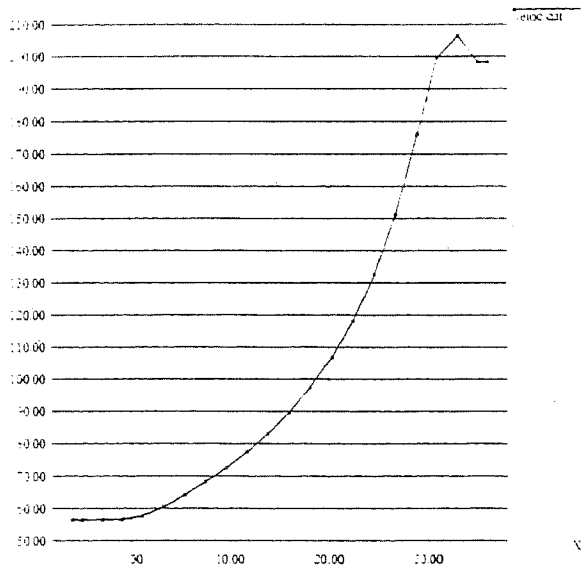

Figure 2.a Convergent 3:1 nozzle M_{ex}=0.5: velocity profile.

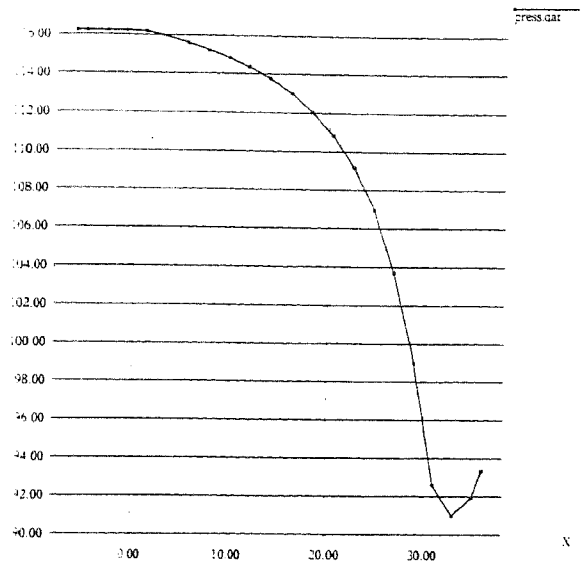

Figure 2.b Convergent 3:1 nozzle M_{ex}=0.5: static pressure profile.

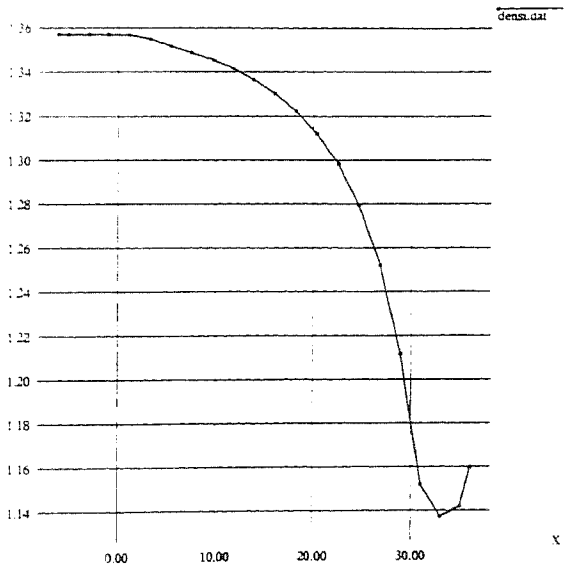

Figure 2.c Convergent 3:1 nozzle M_{ex}=0.5: static temperature profile.

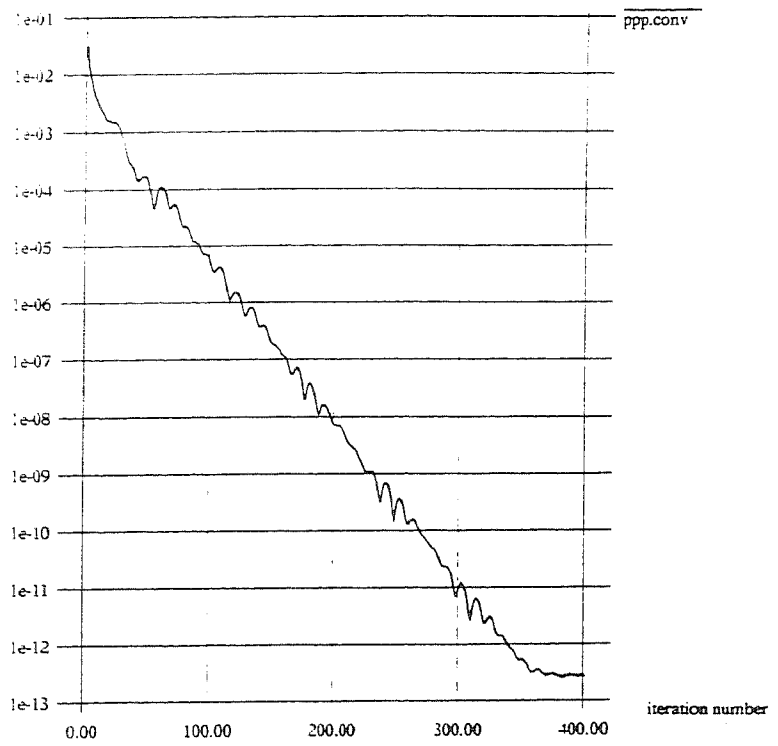

Figure 3.a Convergent 3:1 nozzle M_{ex}=0.5: convergence history of pressure.

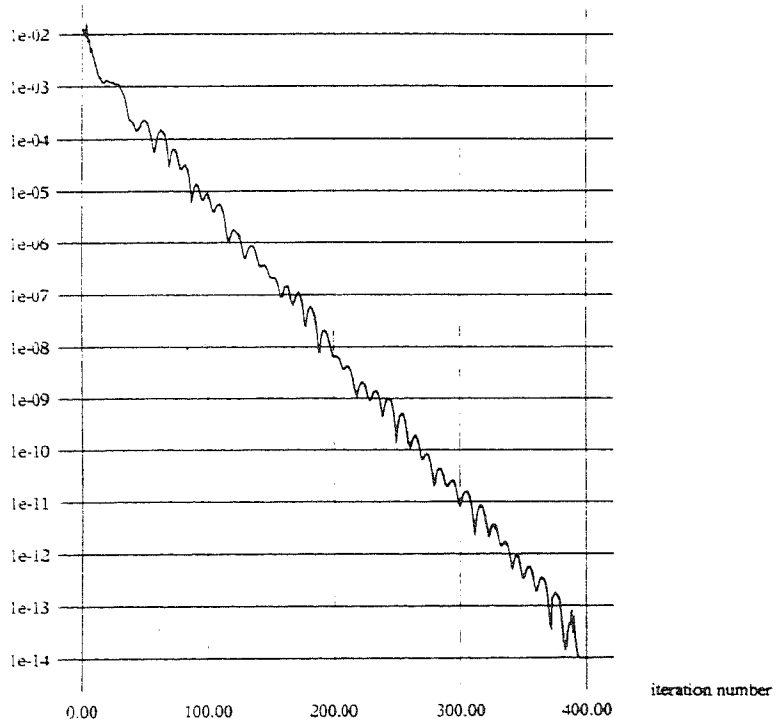

Figure 3.b Convergent 3:1 nozzle M_{ex}=0.5: convergence history of u-velocity.

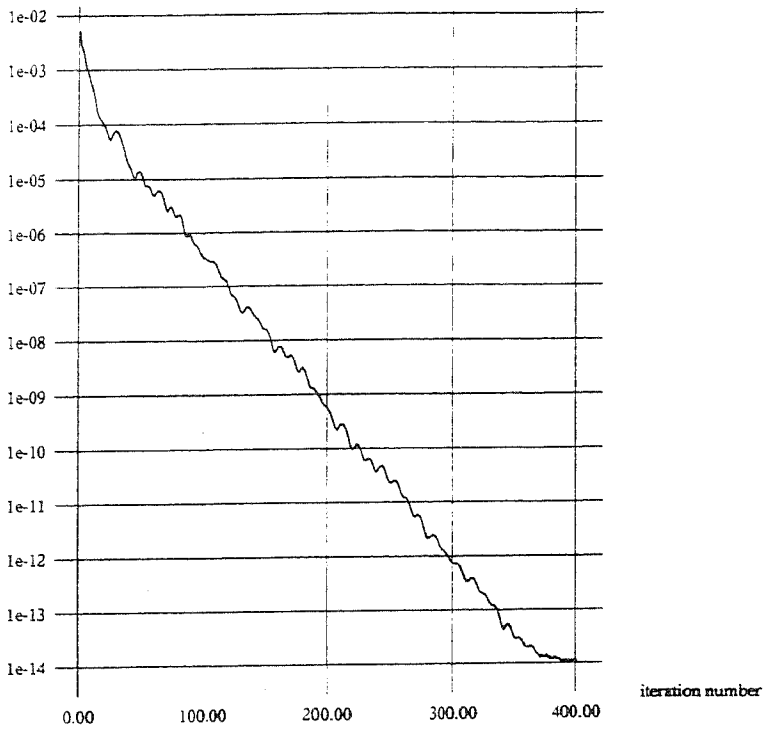

Figure 3.c Convergent 3:1 nozzle M_{ex}=0.5: convergence history of v-velocity.

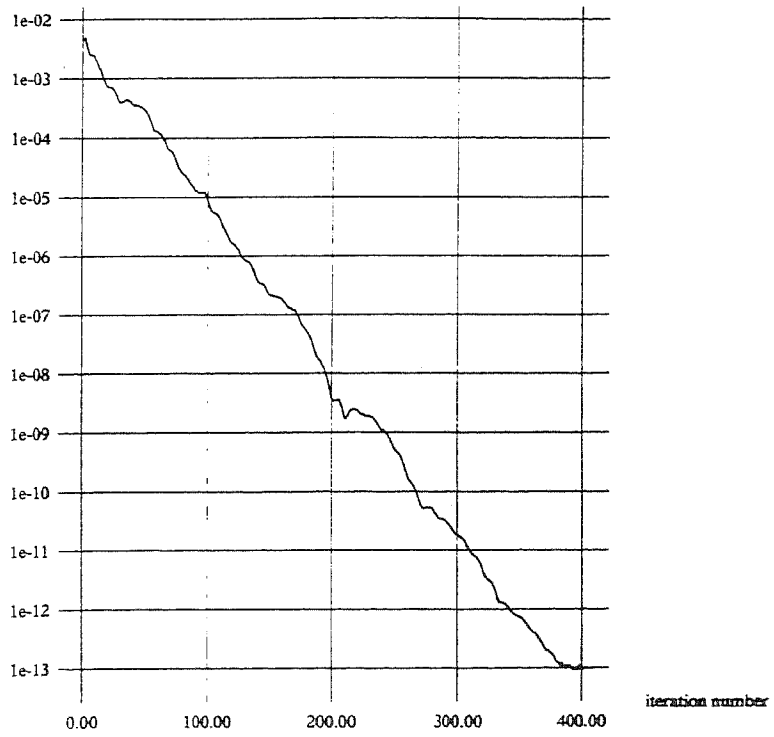

Figure 3.d Convergent 3:1 nozzle M_{ex}=0.5: convergence history of temperature.

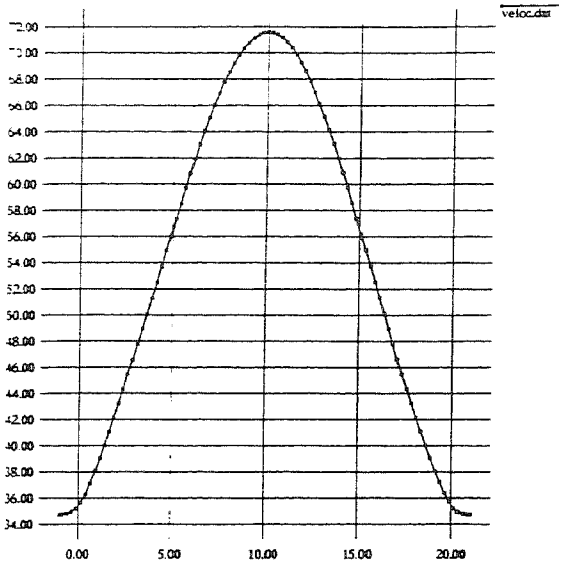

Figure 4.a Nozzle flow M_{ex}=0.1: velocity profile.

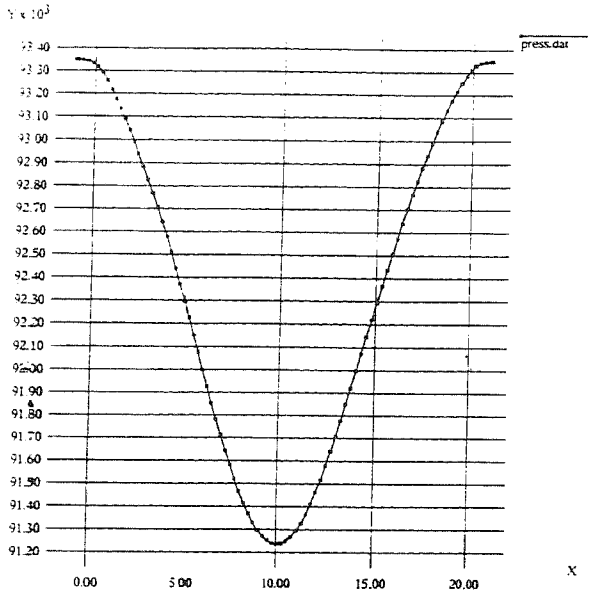

Figure 4.b Nozzle flow M_{ex}=0.1: static pressure profile.

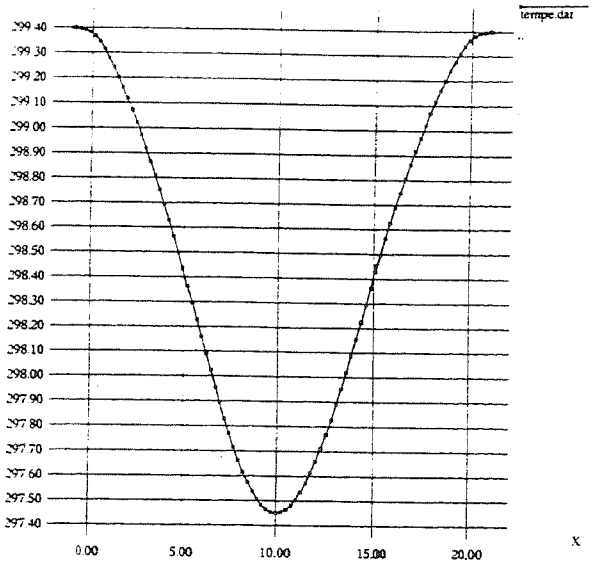

Figure 4.c Nozzle flow M_{ex}=0.1: static temperature profile.

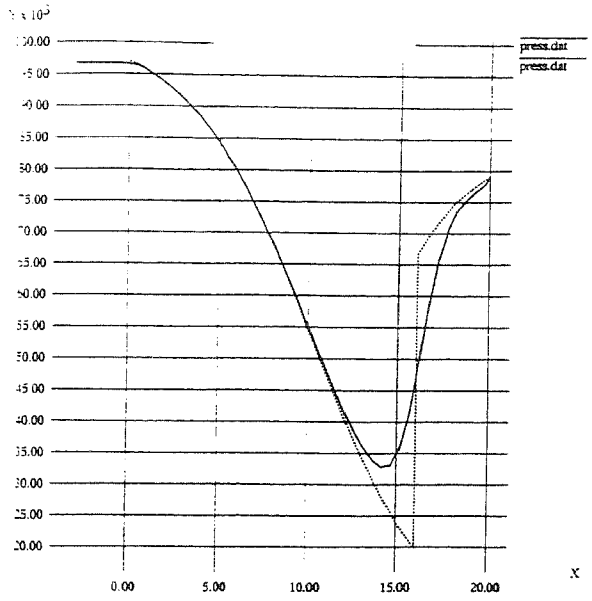

Figure 5.a Nozzle flow M_{ex}=0.37, 40 points mesh, convection and density upwind: static pressure profile.

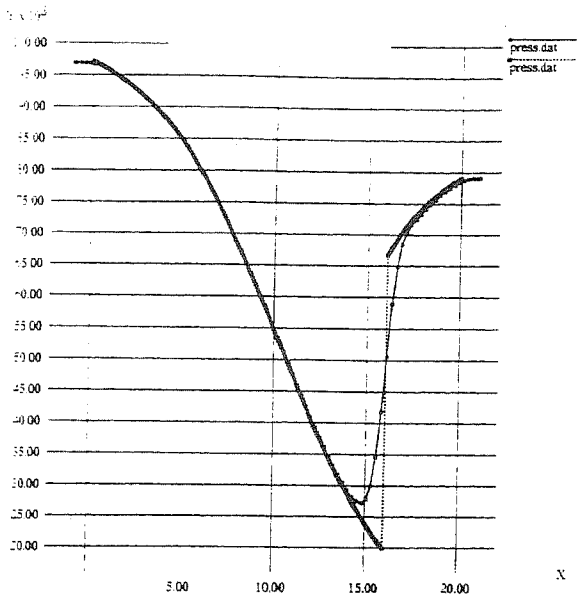

Figure 5.b Nozzle flow M_{ex}=0.37, 80 points mesh: convection and density upwind: static pressure profile.

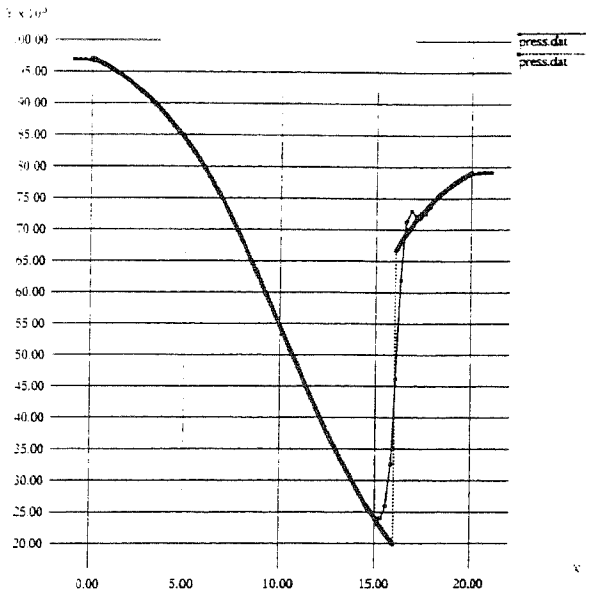

Figure 5.c Nozzle flow M_{ex}=0.37, 80 points mesh: HLPA for convection and density upwind: static pressure profile.

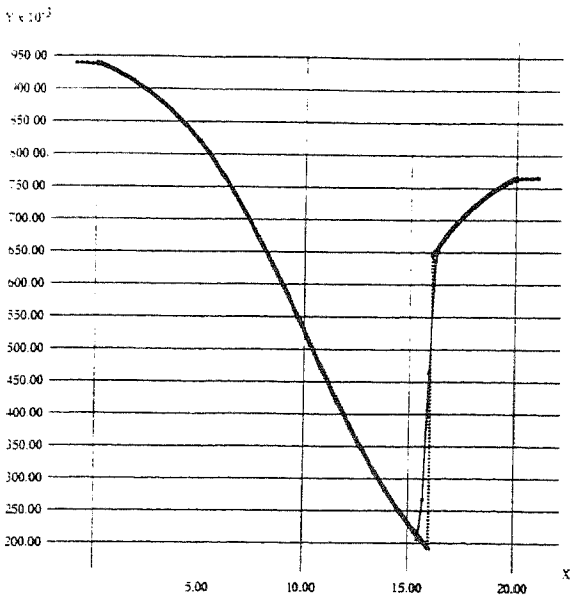

Figure 5.d Nozzle flow M_{ex}=0.37, 80 points mesh: FLOS3D: static pressure profile. (dashed→exact solution)

4.2 10% subsonic and transonic bump

A more complex flow pattern is encountered when solving for the flow over a 10% bump. At M_{ex}=0.675, a shock is known to develop downstream of the bump top. This is a storng shock which brings the stream from supersonic to subsonic. The shock remains attached to the lower boundary and does not travel to the upper boundary. The first test is made at M_{ex}=0.5, where the flow is computed using an 84×20×3 grid, shown in figure 6.a. The pressure isolines computed by using the HLPA convection scheme are given in figure 6.b. The pressure profile is highly symmetric thereby indicating that there are no entropy sources. Figure 5.c shows the pressure distribution on the lower and upper walls. Observe that at this Mach number no large differences are found if running the incompressible version of the FAST-3D code. The machine accuracy residual $10^{-09}-10^{-10}$ is reached in approximately 400 iterations.

In the M_{ex}=0.675 case, a shock is expected downstream of the top of bump. In this case the effect of the density biasing and the convection scheme are dramatic. Figure 7.a shows the pressure isolines computed by using the hybrid discretization scheme (which, for the grid under investigation, reduces in practice to a first order upwind) for the convection terms, and a first order upwind for the density in the pressure correction equation and for the evaluation of fluxes. This is the practice of Karki and Patankar, and Majumdar. Figure 7.a shows only a very slight increase in the density of the pressure isolines downstream of the top of the bump. The shock is very much smeared, but it is in fact questionable if this behaviour can be regarded as a shock. An evident improvement in the quality of the results can be obtained by introducing the HLPA convection scheme, while still retaining the first order upwind of density in equations (9) and (10) (see figure 7.b). The predictions obtained by using FLOS3D are given in figure 7.c, in which the shock can be easily located at x=0.20. The lower and upper wall pressures are compared in figure 7.d. The profile given by using the hybrid convection scheme and the upwinding of density produce an unacceptable shock smearing, which is only partially cured by the introduction of the HLPA convection scheme. Both the profiles computed by FAST-3D are still far from the one given by the time marching code.

After introducting the biased density, as specified in equations (9) and (10) the shock given by FAST-3D becomes sharper. Figure 8.a shows the effect of varying the values of k and M_{ref}. When going towards values of M_{ref} closer and closer to unity and small values of k, it is possible to increase the shock sharpness until a pressure undershoot appears at the foot of the shock. Figure 8.b shows the pressure isolines computed by using the blended density biasing approach. The shock can be easily detected and the predictions move toward the time marching code, as shown in figure 8.c. The dramatic improvement with respect to the formulation proposed by Karki and Patankar and retained by Majumdar is evident. Observe that M_{ref} is set to 0.8 and, in fact, the differences between FLOS3d and FAST-3D arise when the static to total pressure ratio reaches 0.65 in the accelerating part of the flow.

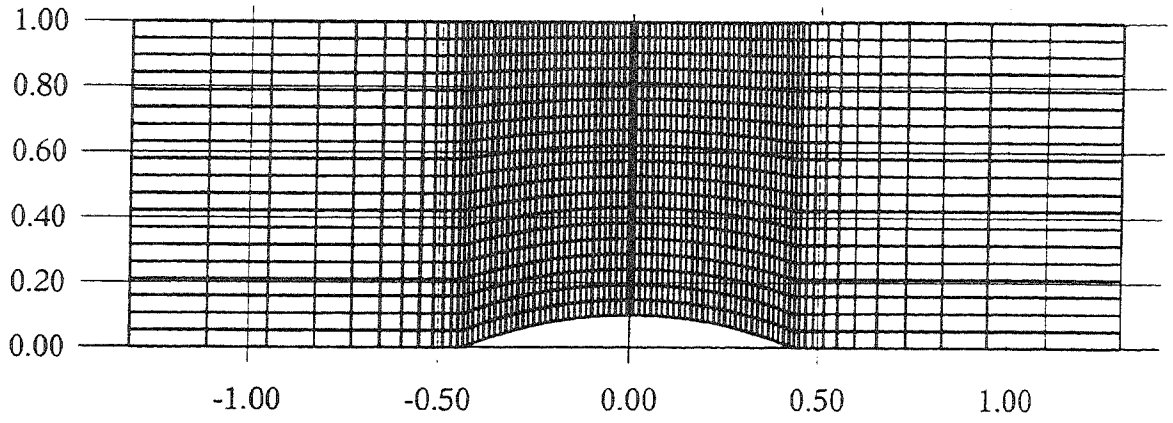

Figure 6.a 10% Bump: 84×20×3 grid.

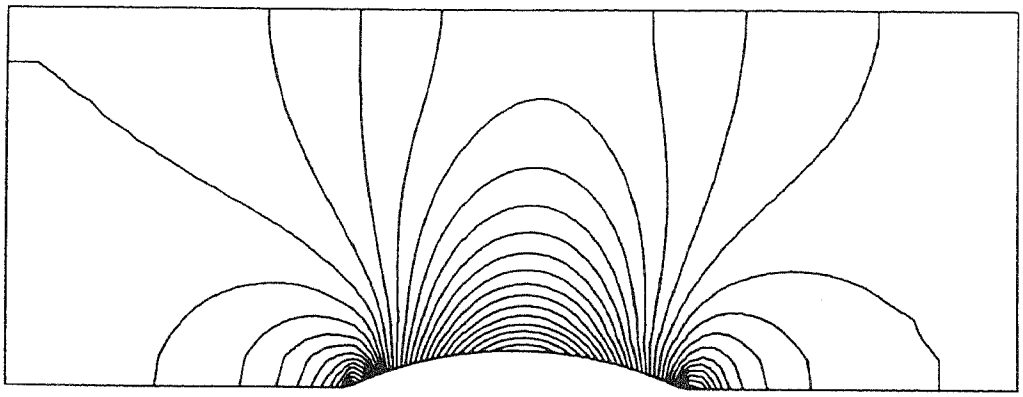

Figure 6.b 10% Bump: M_{ex}=0.5 pressure isolines.

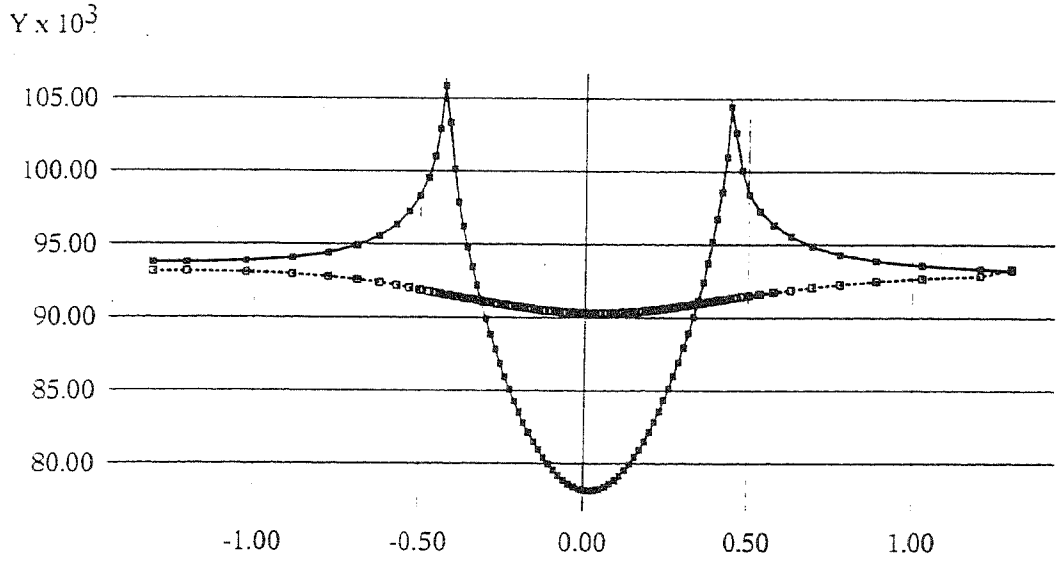

Figure 6.c 10% Bump: M_{ex}=0.5 wall pressure profile.

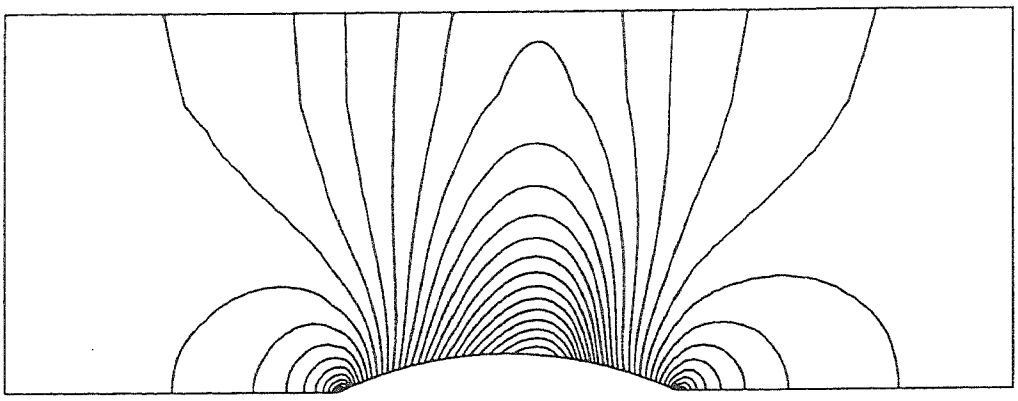

Figure 7.a 10% Bump: FAST-3D+hybrid+upwind of density, M_{ex}=0.675 pressure isolines.

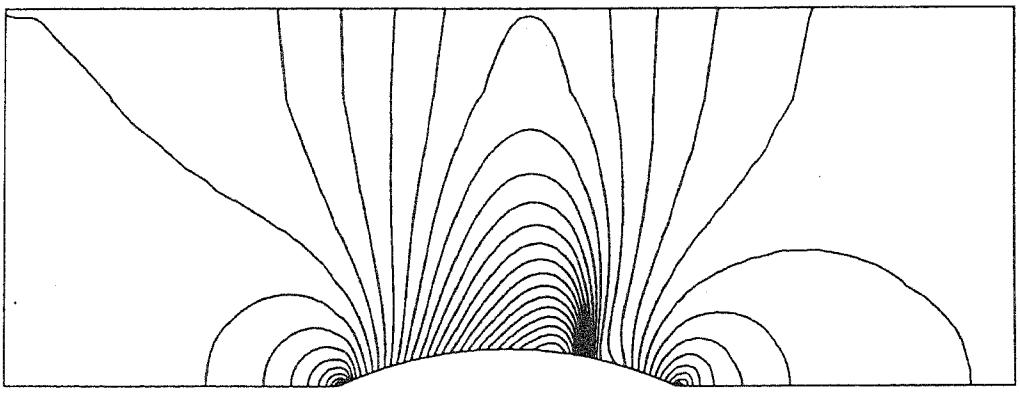

Figure 7.b 10% Bump: FAST-3D+HLPA+upwind of density, M_{ex}=0.675 pressure isolines.

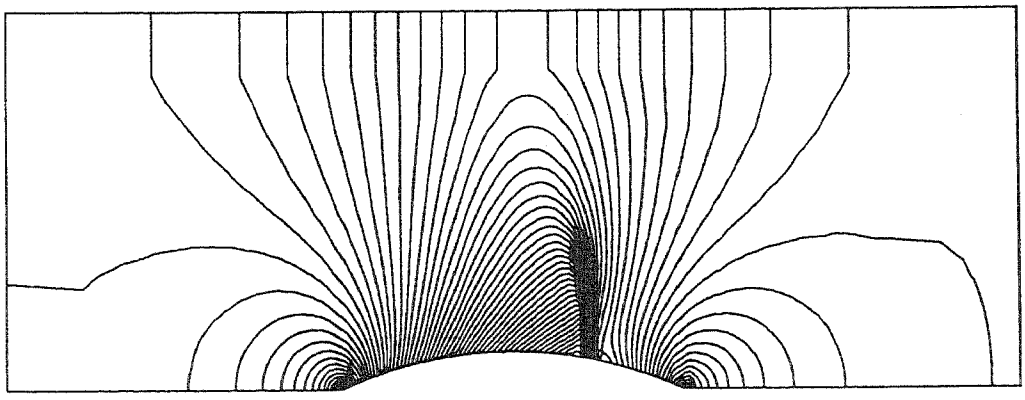

Figure 7.c 10% Bump: FLOS3D, M_{ex}=0.675 pressure isolines.

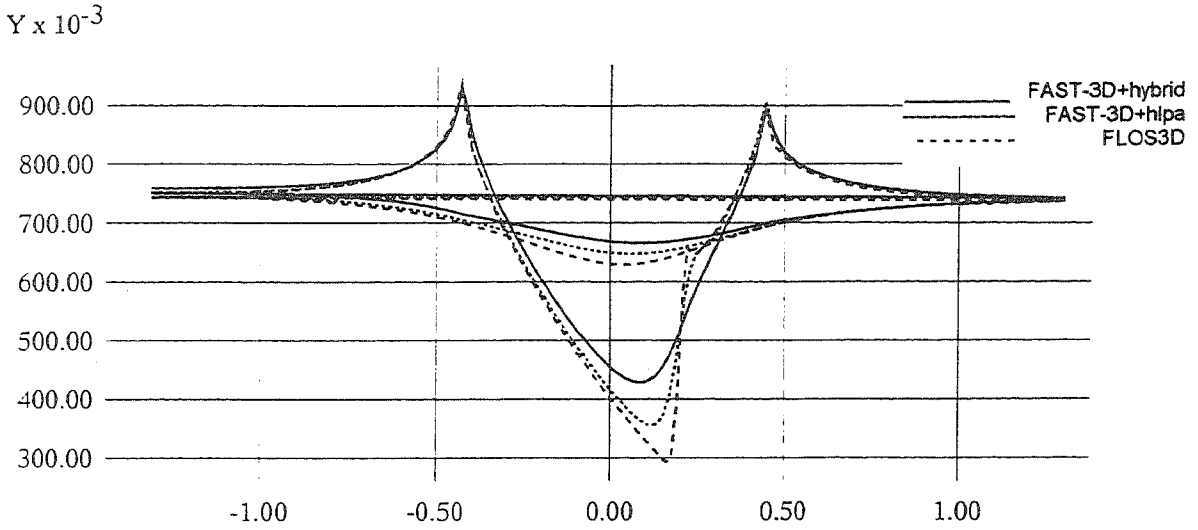

Figure 7.d 10% Bump: M_{ex}=0.675 wall pressure profiles.

M_{ref}=0.9 k=1.1 M_{ref}=0.975 k=0.6

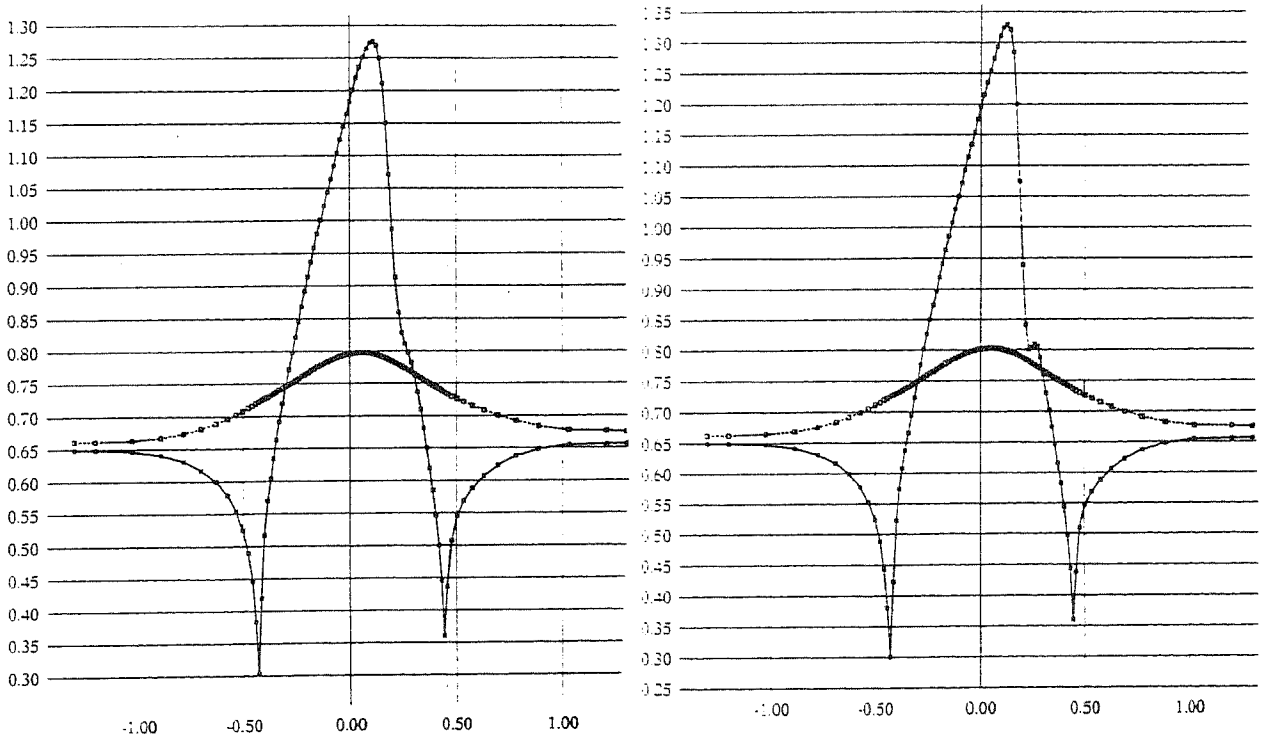

Figure 8.a 10% Bump: FAST-3D, HLPA+density biasing, M_{ex}=0.675 wall Mach number profiles for two different sets of the biasing parameters.

M_{ref}=0.9 k=0.5 M_{ref}=0.9 k=0.

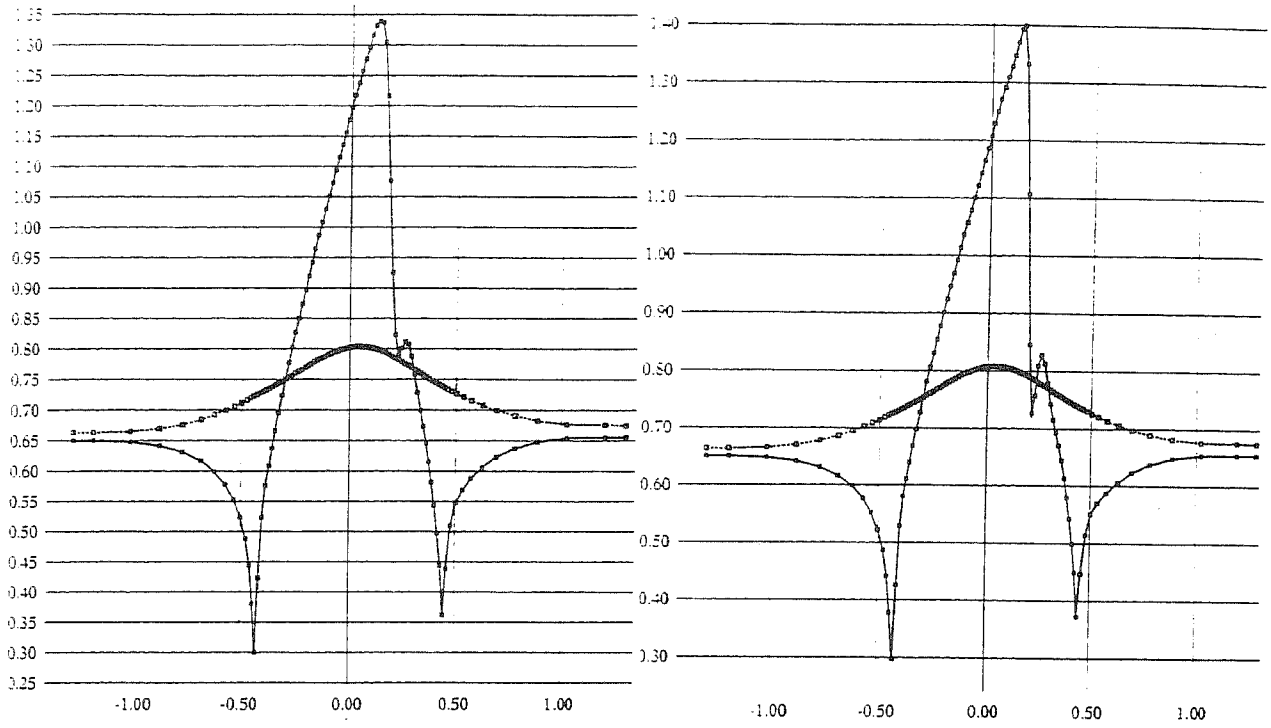

Figure 8.a (cont) 10% Bump: FAST-3D, HLPA+density biasing, M_{ex}=0.675 wall Mach number profiles.

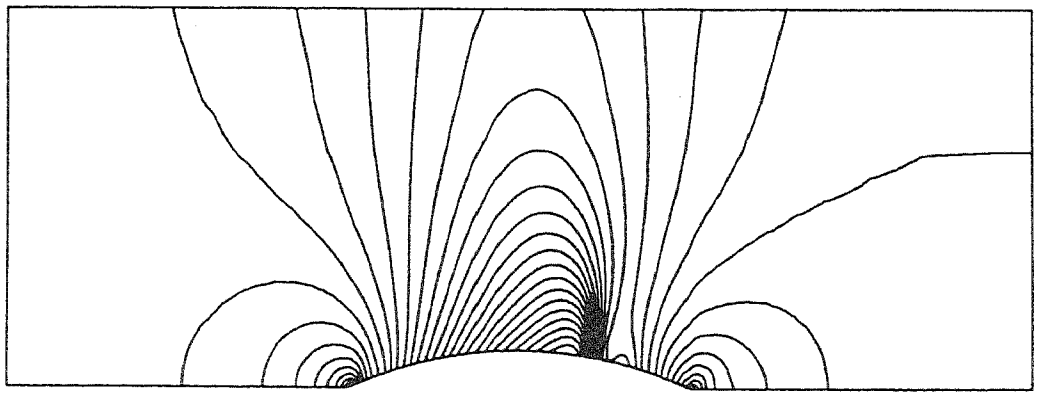

Figure 8.b 10% Bump: FAST-3D, HLPA+density biasing, M_{ex}=0.675, pressure isolines.

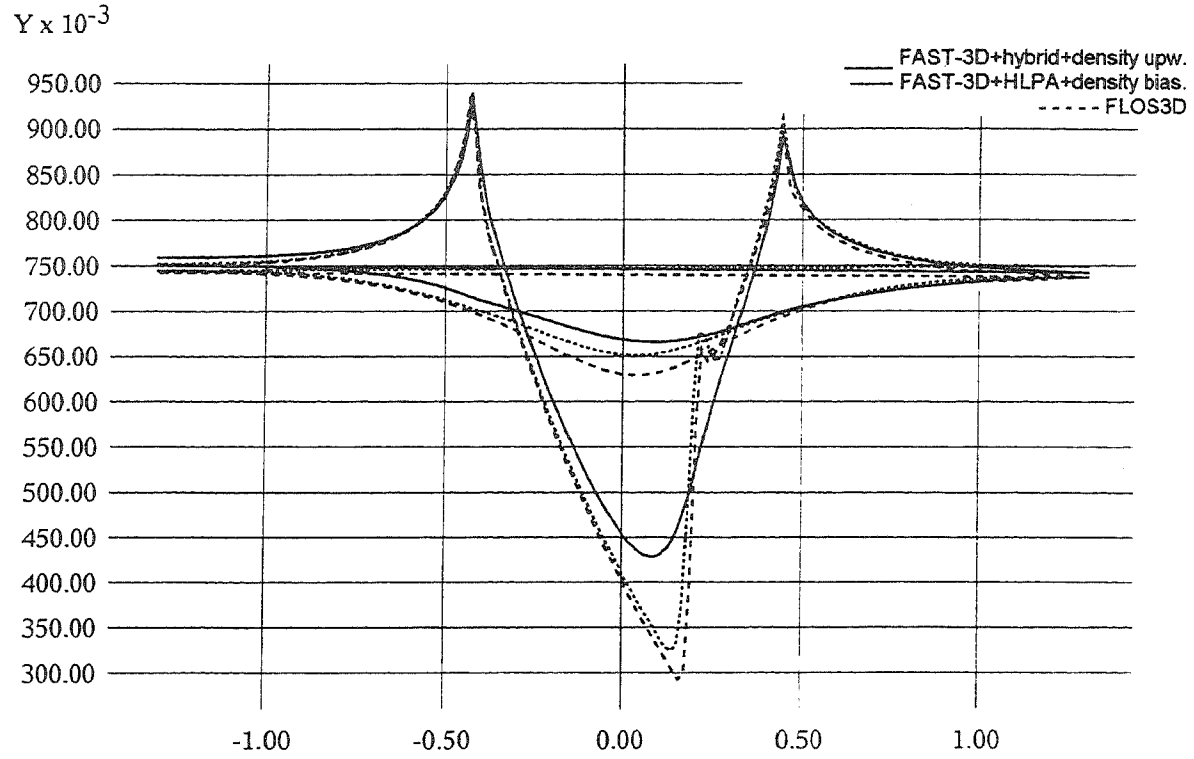

Figure 8.c 10% Bump: M_{ex}=0.675, wall pressure profiles.

4.3 4% supersonic bump

The flow over a 4% bump is studied with supersonic inlet and outlet Mach numbers. For M_{in}=1.4, a first shock travels from the leading edge of the bump up to the upper boundary where it reflects and interacts with the shock departing from the trailing edge. A typical "lambda" shaped shock is located downstream of the trailing edge. When increasing the inlet Mach number M_{in} to 1.65, the flow pattern is highly modified. In fact the trailing edge and the reflected shocks travel outside of the exit section without any considerable interaction.

The test runs are performed by using 116×30×3 and 116×40×3 grid points. Figure 9.a shows a typical 116×30×3 grid. For M_{in}=1.4 the pressure isolines computed by using the FLOS3D code are given in figure 9.b. The wall pressure profile is given in figure 9.c. Observe that the pressure exhibits a small overshoot in proximity to the shocks. The overshoots could be cured by increasing the weight of the second order damping in the artificial dissipation term used in the FLOS3D program. Still the two plots illustrate how the second plus fourth order damping scheme as developed by Jameson et al. (1981) succeed in controlling the instabilities generally induced by the sharp gradients in proximity to shocks.

When moving to the compressible FAST-3D code a deep investigation about the influence of k and M_{ref} is performed. Figure 10.a reports a set of wall pressure plots obtained by using the biased density approach described in equations (9) and (10). The

values of k and M_{ref} are reported in the following table and directly refer to the plots given in figure 10.a.

Table 1.
Test summary for the 4%bump, M_{in}=1.4.

Figure 10.a	M_{ref}	k	residual after 2000 it.
1	0.	0.2	10^{-6}-10^{-7}
2	0.	0.5	10^{-7}-10^{-8}
3	0.	0.9	10^{-8}-10^{-16}
4	0.	1.0	10^{-7}-10^{-16}
5	0.975	1.1	10^{-10}-10^{-15}
6	0.975	0.5	10^{-11}-10^{-16}
7	0.5	0.6	10^{-10}-10^{-16}

The number of tests done always retain the HLPA convection scheme and the density biasing. The plots given in figure 10.a make it evident that, as expected, at the foot of a shock some over- or undershoot of static pressure is expected. This phenomena is potentially very dangerous since the undershoot in pressure might produce negative values, whereas positive overshoots might yield the static pressure to exceed the total pressure. Increasing the value of k can clearly help in controlling this phenomena. The value of 0.5-0.6 should not be exceeded in order to maintain the shock as sharp as possible (see figure 10.a 1,2,3). At the same time, an increase in M_{ref}, from 0 to 0.975 sorts the effect of narrowing the range of application of the density upwinding. Moreover the increase in shock smoothing evidently improve convergence, like in the time marching code.

Figure 10.b shows a typical pressure isolines plot computed by using the compressible fluid version of FAST-3D. The shock and the shock reflection can be easily detected. Still when comparing with the time marching code, the shock appears slightly more smoothed, but still much better than what obtained by a pure pressure and density upwinding.

When moving to M_{in}=1.60 the flow pattern is highly changed. In fact the higher inlet speed bends both the leading edge and the trailing edge shocks which intersect at approximately 90-degrees dowstream of the bump trailing edge. Figure 11.a shows the pressure isolines computed by using the pressure correction approach. When comparing the flow pattern with the one given by the time marching code (see figure 11.b), one should consider that in figure 11.b the shock appears much sharper because of the larger number of isolines used with respect to figure 11.a. Although the time marching code always predicts sharper shocks, the difference with respect to the pressure correction algorithm is not very large.

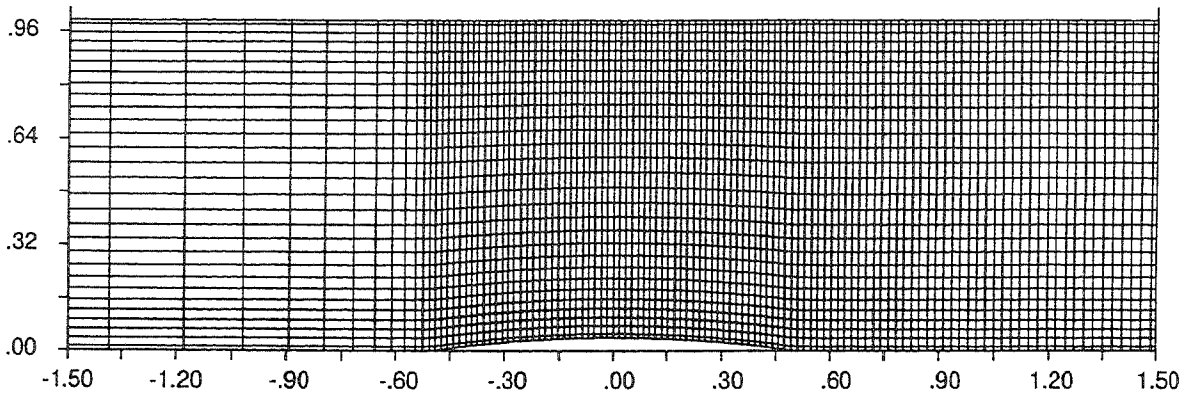

Figure 9.a 4% Bump: 116×30×3 grid.

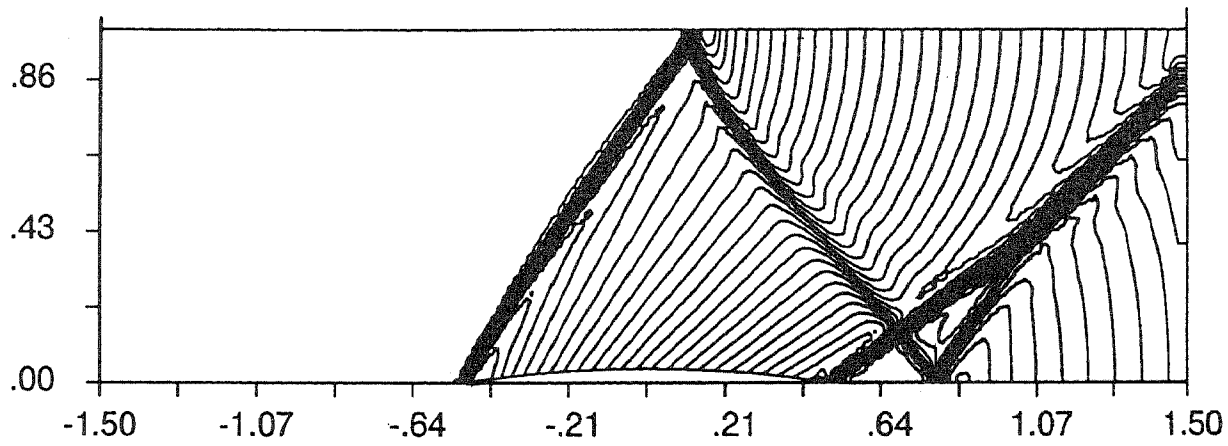

Figure 9.b 4% Bump: FLOS3D, M_{ex}=1.40: pressure isolines.

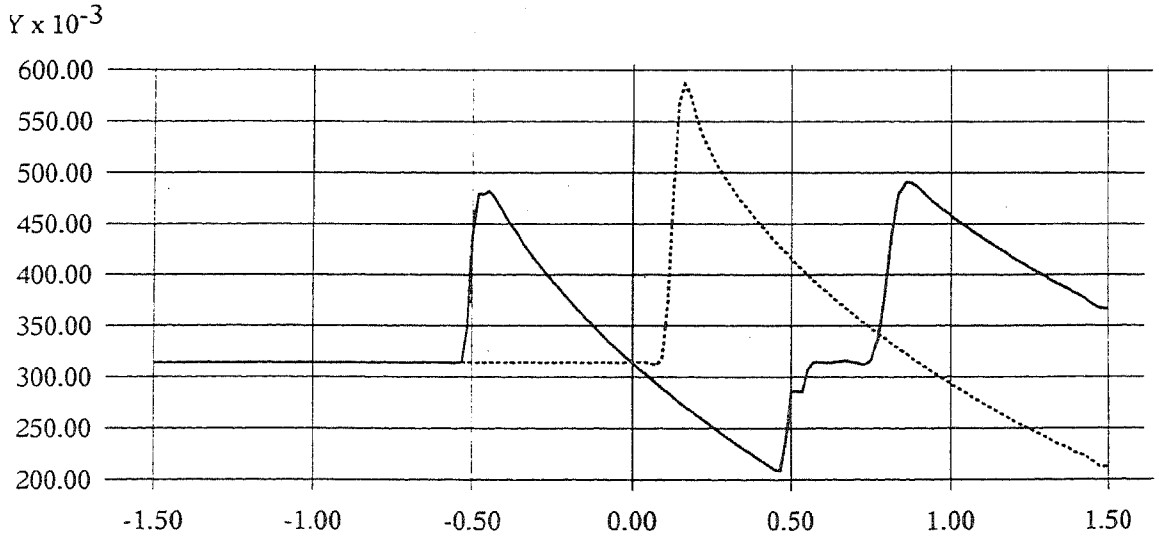

Figure 9.c 4% Bump: FLOS3D, M_{ex}=1.40: wall pressure profiles.

1

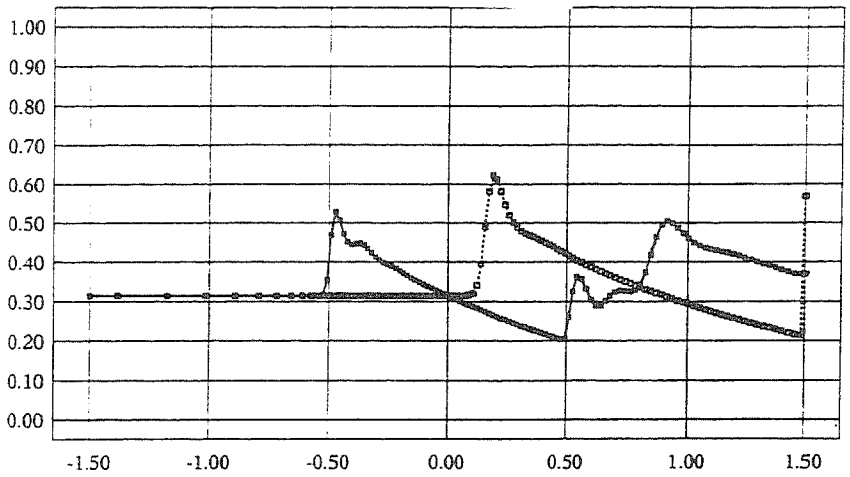

2

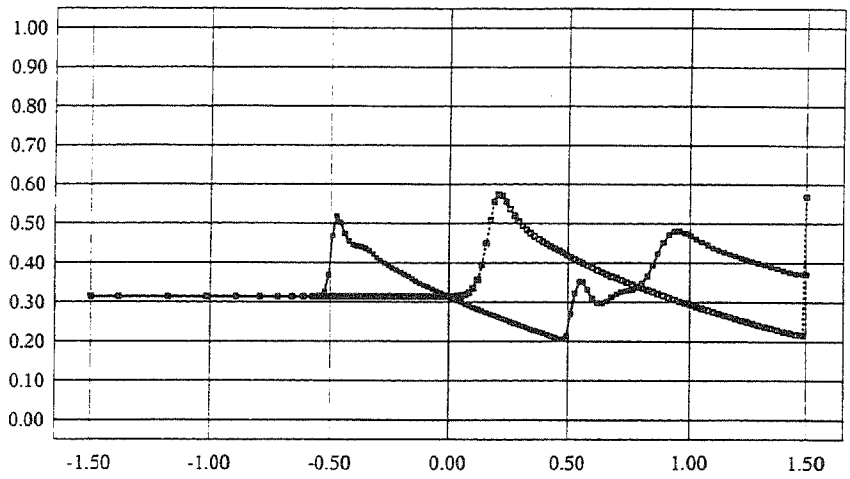

3

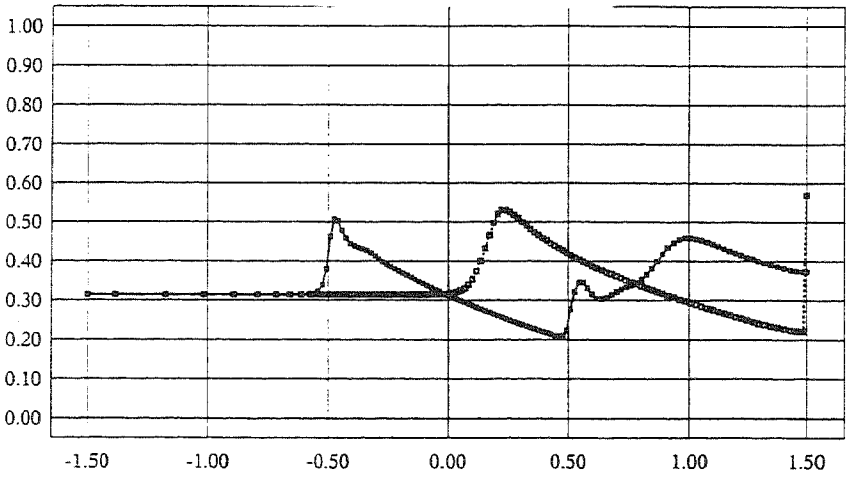

Figure 10.a 4% Bump: FAST-3D, M_{ex}=1.40: wall pressure profiles.

4

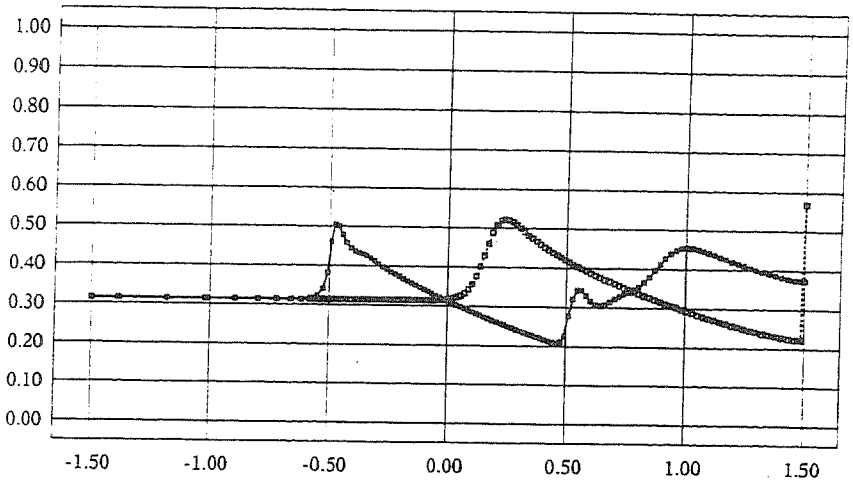

5

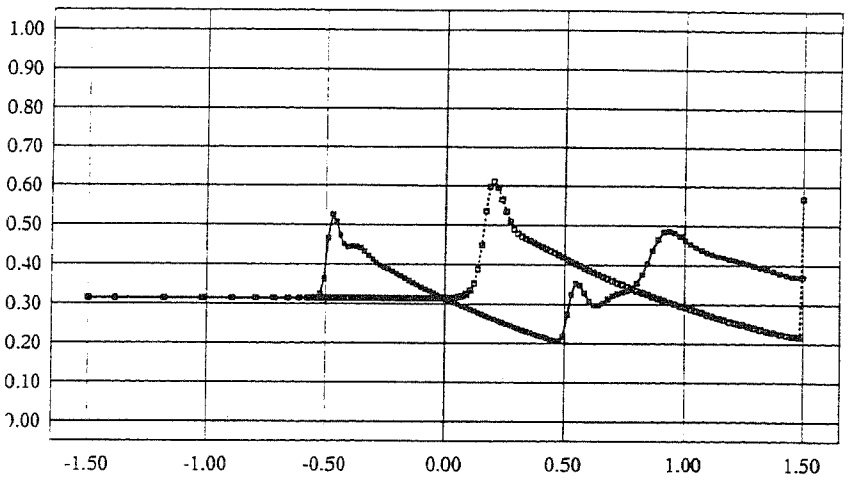

6

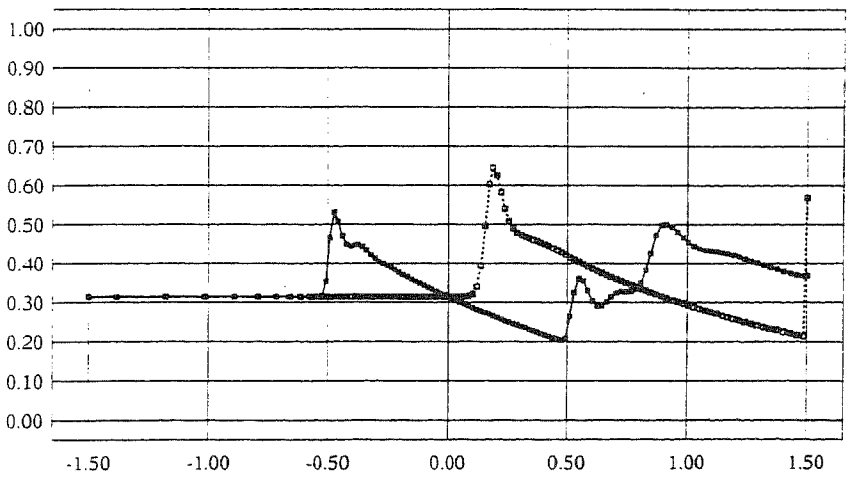

Figure 10.a(cont) 4% Bump: FAST-3D, M_{ex}=1.40: wall pressure profiles.

7

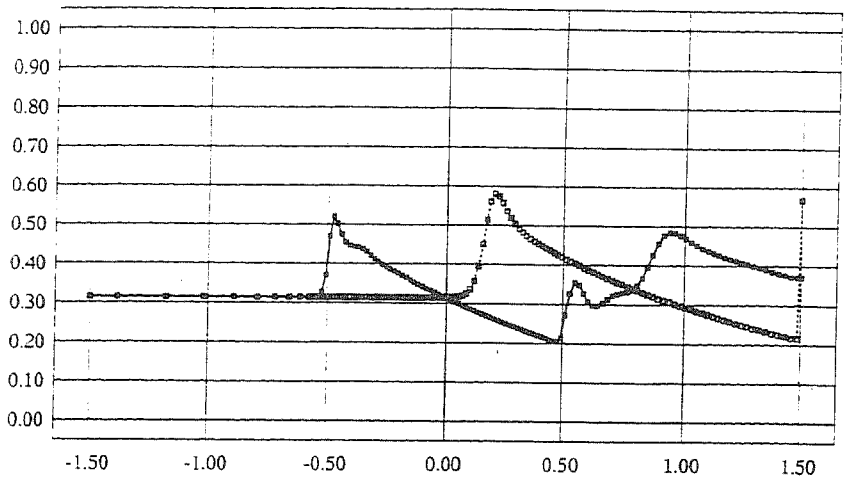

Figure 10.a(cont) 4% Bump: FAST-3D, M_{ex}=1.40: wall pressure profiles.

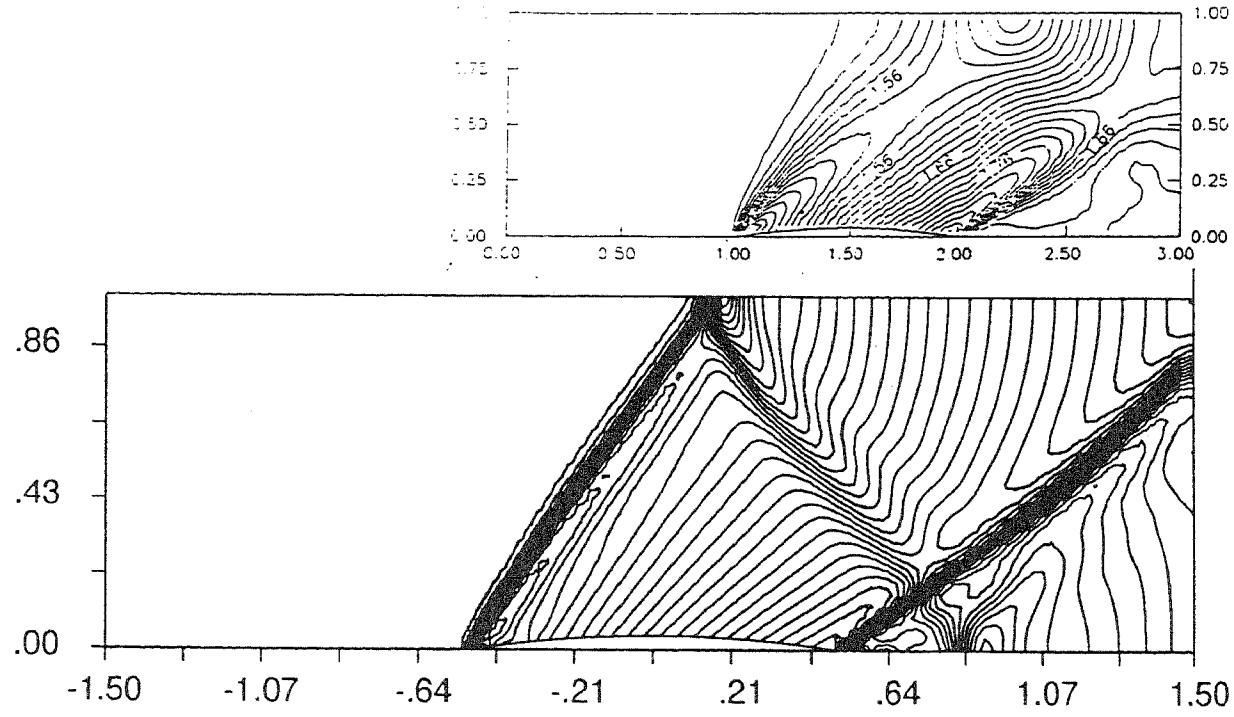

Figure 10.b 4% Bump: FAST-3D, M_{ex}=1.40: pressure isolines.
(small picture: from Majumdar, 1992).

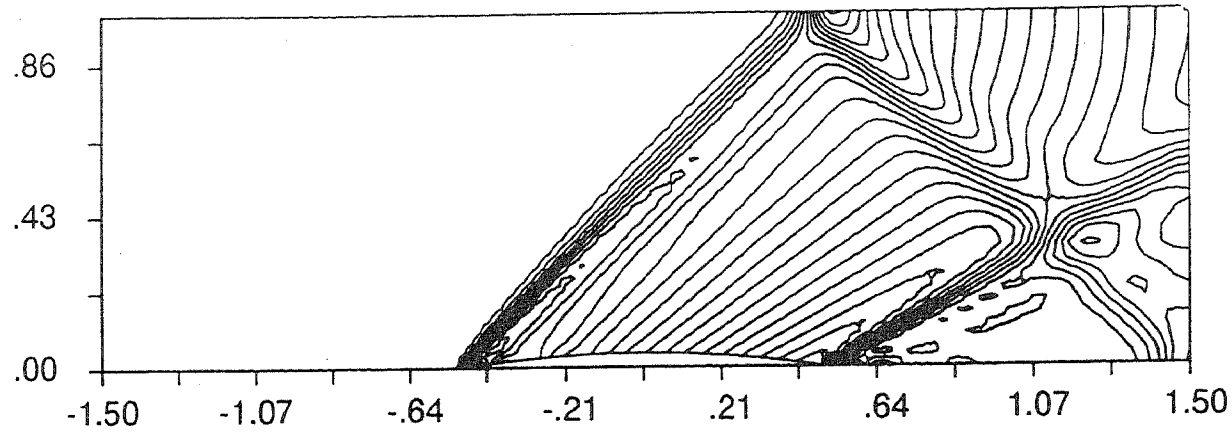

Figure 11.a 4% Bump: FAST-3D, M_{ex}=1.60: pressure isolines.

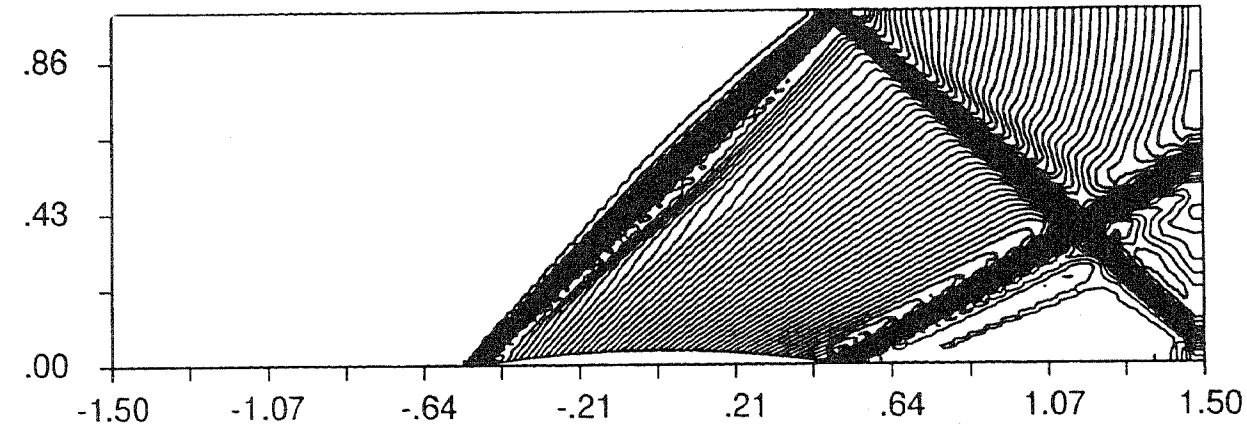

Figure 11.b 4% Bump: FLOS3D, M_{ex}=1.60: pressure isolines.

5 CONCLUSIONS

The present investigation was focused on inviscid flows in order to highlight the capabilities of the time marching and of the pressure correction codes to capture shocks, without the influence of the discretization of the diffusive terms.

The analysis proved that it is possible to include simple modifications into an existing incompressible pressure correction code retaining the original choice for the variables and still have a dramatic improvement with respect to the shock capturing capability of alternative approaches (Karki and Patankar, and Majumdar). The proposed approach allows an accuracy comparable with that granted by the McGuirk and Page, and by the Lien and Leschziner proposal, but with a considerable decrease in the amount of modifications to introduce in an existing incompressible pressure correction code.

The results also demonstrated the good shock capturing capability of the time marching code which adopts a spectral-radius-weighted version of the blended, second-plus-fourth order artificial damping, originally proposed by Jameson et al. (1981). Nevertheless, a carefull choice of the parameters controlling the amount of upwinding in the biasing formula allows very good shock capturing.

The time marching approach has a very well known limitation stemming from the weak link between pressure and density at low Mach number. Typically, the time marching code can be run with acceptable accuracy down to M_{ex}=0.2. For smaller values, although the code seems to converge, the converged solution often presents very poor mass conservation. This never happens with a pressure correction code. In fact, being the pressure, and not the density, that controls the mass conservation, the density can assume a constant value (i.e. very low Mach number flow) without any inconvenience. This problem alone limits the applicability range of the time marching method to flows in which the exit Mach number is never below 0.2-0.3. Although the time marching method is mainly limited by the overall exit Mach number, problems may arise also in low speed regions, for example in recirculation bubbles or in thick boundary layers, where the local Mach number can be very small. Theoretically, these problems should not arise when using a pressure correction code, the formulation of which is valid over a wider range of Mach numbers.

So far, the artificial damping scheme as proposed by Jameson et al. (1981) with the spectral radius weighting gives better shock resolution, but it is incorporated in codes which cannot be used for low Mach number flows. An attempt to improve the simple density biansing concept was done separately by both Mc Guirk and Page, and by Lien and Leschziner. The main role of the biasing function is to switch on the density upwinding. Now, although the criteria for upwinding or not must be related to the local directional Mach number, the simple first order upwinding of density could be replaced by a higher order upwinding. The implications of this choice in the stability and shock capturing ability of the resulting formulation are still totally unpredictable, but it is undeniably true that a higher order upwind will introduce less density diffusion, if we consider the continuity equation as the trasport equation for density.

6 REFERENCES

Beam, R.M., Warming, R.F., (1982), "Implicit Numerical Methods for the Compressible Navier-Stokes and Euler Equations", Lecture series on Computational Fluid Dynamics, VKI-LS-1982-04, Von Karman Institute for Fluid Dynamics.

Hafez, M., South, J., Murman, E., (1979), "Artificial Compressibility Methods for Numerical Solutions of Transonic Full Potential Equation", AIAA Journal, Vol.17, p. 838.

Karki, K.C., Patankar, S.V., (1989), "Pressure Based Calculation Procedure for Viscous Flows at All Speeds in Arbitrary Configurations", AIAA Journal, Vol. 27, No.9, September 1989, pp.1167,1174.

Jameson, A., Schmidt, W., Turkel, L., (1981), "Numerical Solutions of the Euler Equations by Finite Volume Methods Using Runge-Kutta Time-Stepping Schemes", AIAA Paper 81-1259.

Issa, R.I., Lockwood, F.C., (1977), "On the Prediction of Two-Dimensional Supersonic Visccous Interactions Near Walls", AIAA Journal, Vol.15, February 1977, pp. 182-188.

Lien, F.-S., (1992), "Computational Modelling of 3D Flow in Complex Ducts and Passages", Ph.D Thesis, UMIST.

Lien, F.-S., Leschziner, M.-A., (1993), "A Pressure-Velocity Solution Strategy for Compressible Flows and its Application to Shock/Boundary-Layer InteractionUsing Second-Moment Turbulence Closure", ASME Journal of Fluids Enginerring, December 1993.

Majumdar, S., (1988), "Role of Underrelaxation in Momentum Interpolation for Calculation of Flow with Nonstaggered Grids"., Numerical Heat Transfer, vol.13, pp.125-132.

Majumdar, S., (1992), "A Pressure Based Method for Numerical Computation of Compressible Flow", Project Document PD CF 9225, National Aeronautical Laboratory, July 1992, Bangalore, India.

McGuirk, J.J., Page, G.J., (1990), "Shock Capturing Using a Pressure-Correction Method", AIAA Journal, Vol.28, No.10, October 1990, pp.1751,1757.

Michelassi, V., Liou, M.-S., Povinelli, L.A., (1990), "Implicit Solution of Three-Dimensional Internal Turbulent Flows", NASA TM-103099, ICOMP-90-13, July.

Michelassi, V., Martelli, F., (1993), "3-D Implicit Navier-Stokes Solver for Internal Turbulent Compressible Flows", Journal de Phys. III, France 3, pp. 223-235.

Patankar, S.V., (1980), "Numerical Heat Transfer and Fluid Flow", Mc Graw-Hill Book Company.

Pulliam, T.-H., Chaussee, D.S., (1981), "A Diagonal Form of an Implicit Approximate-Factorization Algorithm", Journal of Computational Physics 39, pp.347-363.

Rhie, C.M., Chow, W.L., (1983), "Numerical Study of the Turbulent Flow Past an Airfoil with Trailing Edge Separation", AIAA Journal, No. 11, November 1983, pp. 1525-1532.

Tamamidis, P., (1990), "Numerical Prediction of Subsonic Turbulent Recirculating Flows Using Boundary Fitted Coordinates", Master Thesis, University of Illinois at Urbana-Champaign.

Zhu, J., (1991), "A Low-Diffusive and Oscillation-Free Convection Scheme", Communications in Applied Numerical Methods, Vol. 7.

Zhu, J., (1992), "An Introduction and Guide to the Computer Program FAST-3D", Report No. 691, Institute for Hydromechanik, University of Karlsruhe.

Anhang B

Low-Speed Turbine Computation by Pressure-Correction and Time-Marching Methods

Dieser Anhang wurde veröffentlicht in
AD-Vol. 49, Computational Fluid Dynamics in Aeropropulsion, ASME,
pp. 127-138, 1995

LOW-SPEED TURBINE COMPUTATION BY PRESSURE-CORRECTION AND TIME MARCHING METHODS

V. Michelassi
Energetics Department
University of Florence
Florence
Italy

G.S. Theodoridis and E.L. Papanicolaou
Institute of Hydromechanics
University of Karlsruhe
Karlsruhe
Germany

ABSTRACT

Two well-known approaches for computing various types of flows, both incompressible and compressible are compared in this study in turbine cascade configurations. A well established method for computing compressible flows by time marching and one based on the pressure-correction scheme are used, in both viscous and inviscid flow computations, for subsonic inlet and exit conditions. Two different turbine blades are used and results are compared with experimental data. The computational grid uses a non-poin-to-point periodic arrangement along the periodic boundaries of the cascade, allowing for improved grid quality near the blade surface. The results show good agreement between the codes and between computations and measurements except for low Mach number flow conditions (less than 0.3), where the time marching code suffers from a local mass conservation error which affects the pressure field. As far as convergence rates, the time marching code requires a much smaller number of iterations, which, although heavier computationally, make it a lot more efficient for inviscid flows than the pressure-correction method. In viscous flows however, this advantage is significantly diminished.

NOMENCLATURE

C_p	Specific heat under constant pressure
C_v	Specific heat under constant volume
e	Internal energy of the fluid
h	Enthalpy of the fluid $h = e + p/\rho$
J	Jacobian of the coordinate transformation matrix, defined as $J = \partial(x,y)/\partial(\xi,\eta)$
k	Turbulent kinetic energy
M	Mach number
Pr	Prandtl number of air $Pr = \mu\ C_p/\lambda$
Pr_t	Turbulent Prandtl number $Pr_t = \mu_t\ C_p/\lambda_t$
T	Local temperature
t	Time
u, v	Vertical and horizontal velocity components, respectively
$\vec{V}$	Velocity vector $\vec{V} = (u, v)$
x, y	Vertical and horizontal coordinate distance, respectively

Greek Symbols

γ	Specific heat ratio $\gamma = C_p/C_v$
ϵ	Rate of dissipation of turbulent kinetic energy
ζ	Total pressure loss coefficient : $\zeta = (p_{o1} - p_{o2})/p_{o1}$
ζ^*	Alternate total pressure loss coefficient : $\zeta^* = (p_{o1} - p_{o2})/(p_{o1} - p_2)$
λ	Thermal conductivity of air
λ_{eff}	Effective thermal conductivity $\lambda_{eff} = \lambda + \lambda_t$
μ	Viscosity of the fluid
μ_{eff}	Effective viscosity $\mu_{eff} = \mu_t + \mu$
$\xi,\ \eta$	Coordinates in the curvilinear (transformed) system
ρ	Density of the fluid
$\sigma_k, \sigma_\epsilon$	Prandtl number for the turbulent kinetic energy and its rate of dissipation respectively
τ	Shear stress
Φ	Dissipation function : $\Phi = \mu_{eff}\left[\left(\frac{\partial u_i}{\partial x_j} + \frac{\partial u_j}{\partial x_i}\right) - \frac{2}{3}\,\delta_{ij}(\nabla\cdot\vec{V})\right]\left(\frac{\partial u_j}{\partial x_i}\right)$

Subscripts

E, W, N, S	Neighbor grid point to the right, left, top and bottom of the control volume respectively
is	Isentropic
o	Total (stagnation) quantities
P	Grid point at the center of the control volume
t	Turbulent
1	Inlet cross-section
2	Exit cross-section

INTRODUCTION

The continuous and rapid developments in the field of Computational Fluid Dynamics (CFD) in recent years have resulted in a large variety of methods available today for the computation of the flow in a turbine cascade. Complete reviews of those methods have been presented by McNally and Sockol (1985) and Lakshminarayana (1991). In both reviews, classifications of the methods are proposed, on grounds of either physical approximations made or solution procedures and techniques employed. More specifically, one can distinguish between inviscid or viscous methods, boundary-layer or full Navier-Stokes solutions, incompressible or compressible-flow methods etc. The choice of a method is determined by the objectives of a particular investigation, and is the outcome of a compromise between the desired accuracy and the level of complexity allowed, when considering the time and computer resources that can be afforded.

One of the main objectives in CFD computations in turbomachinery is the estimation of losses that will lead to the optimal design of the blades. These losses are generally classified as profile losses, endwall losses and tip leakage losses (Denton, 1993). In two-dimensional cascades, the losses are mostly of the profile-type, and emanate from the boundary layers along the blade surface and the separation at the trailing edge. In compressible, high-Mach-number flows, there are additional losses due to shocks and the shock-boundary layer interactions. A complete estimate of the losses can be obtained by computing the flow field using the full compressible Navier-Stokes equations, with a suitable turbulence model.

For compressible flows, one of the most popular approaches is the use of time-marching methods, in which the governing equations are solved by implicit procedures such as those of Pulliam and Chaussée (1981) and Beam and Warming (1982). The former procedure was used for turbomachinery flows by Michelassi et al. (1990). These algorithms use the density as the main dependent variable, along with momentum and, in most cases, the total specific internal energy. The main drawback of these formulations lies in the fact that the strong link which exists between static pressure and density through the static temperature, becomes extremely weak at low Mach numbers. Therefore, their accuracy is reduced for Mach numbers below 0.2-0.3, where the mass conservation and the solution quality rapidly deteriorate. This cutoff value of the Mach number is nevertheless solver dependent. In general, the time marching methods are solved in a *coupled* manner, by constructing Jacobian matrices which link together all the governing equations.

A valid alternative to these methods is offered by the extension of the pressure-correction algorithm, most commonly associated with incompressible flows, to compressible flows. The most widely used pressure-correction algorithms are the SIMPLE and SIMPLER (Patankar,1980) and their variants, such as SIMPLEC (Van Doormaal and Raithby, 1984). In these algorithms, the continuity equation is transformed into the pressure-correction equation, by using the momentum conservation to establish a direct link between pressure and velocity. Besides, the computational domain is divided into a number of finite volumes (cells) over which the transport equations are integrated and thereby conservation of the transported properties is guaranteed. The latter is a very attractive feature, closely related to the pressure-correction methods. Several attempts have already been made to extend the pressure-correction scheme to compressible flow and the corresponding results are available in the literature. Among the earliest such works are those presented by Issa and Lockwood (1977), Van Doormaal et al. (1987) and Karki and Patankar (1989).

Karki and Patankar (1989) modified the continuity equation to include density changes in the SIMPLER algorithm, which solves for two pressure-correction equations, the first of which updates the pressure and density field, whereas the second one corrects the velocity field to ensure mass conservation. In their approach, the cell-face density appearing in the discretized pressure-correction equation is first-order upwinded, following the suggestion of Issa and Lockwood (1977) who upwinded the pressure in supersonic flows. The density upwinding was found to perform well in low-Mach-number flow conditions, but at high Mach numbers it seemed to introduce a large amount of artificial diffusion. More recently, Majumdar (1992) reformulated the Karki and Patankar (1989) method by using the SIMPLE algorithm along with a collocated variable arrangement and the momentum interpolation scheme of Rhie and Chow (1983) for the control-volume face velocities, whereas Karki and Patankar (1989) had utilized a staggered variable arrangement. Linear interpolation for the cell-face density in compressible pressure-correction schemes has also been used successfully for subsonic flows (Tamamidis, 1990).

In all cases, the system of governing equations is completed by the energy equation, most often written in terms of static temperature or static enthalpy as the transported variable. The computed pressure and temperature are then coupled with the local density through the equation of state for a perfect gas. The pressure-correction algorithms solve the transport equations in a *decoupled* (or *segregated*), sequential manner which gives more flexibility to the solution process and reduced computed storage.

In turbomachinery applications, pressure-correction methods including compressibility effects have been used by Hah (1984) and Hah and Leylek (1987), but generally have not as yet gained significant popularity. The present study attempts to contribute to this effort, while at the same time comparing two methods representing each of the two distinct classes discussed above, namely the coupled and uncoupled methods. The corresponding codes FLOS3D [1] and FAST-3D [2] are used for this purpose, which are capable, as their names indicate, to compute three-dimensional flow fields, even though the present study is considering only two-dimensional configurations. The procedure presented

[1] FLO-w S-olver 3 D-imensions, developed at the Dept. of Energetics, University Of Florence (Michelassi et al., 1990)

[2] F-low A-nalysis S-imulation T-ool of 3-Dimensions, developed at the Institute of Hydromechanics, University of Karlsruhe (Zhu, 1992)

here however is extendable to and implemented for three-dimensional studies, which will constitute the subject of a future work. The present comparison considers mainly viscous flows, although several inviscid test runs were also carried out in the early stages of the development. For the viscous cases, two different turbulence models were employed, one for each code, namely the $k-\epsilon$ (Launder and Spalding, 1974) and the $k-\omega$ (Wilcox, 1988) models.

To summarize, the objectives of the present study were to comparatively test the two codes mentioned above by particularly focusing on : 1) The lower Mach number limit for accurate solutions by the time marching method 2) The performance of the pressure-correction method when a density correction is introduced to allow for extension to compressible flows 3) The convergence rates of each method. Two different linear turbine cascades, with the corresponding blades designed by NuovoPignone (Bruzzi, 1992) and ATB (Beeck, 1992) respectively, are the geometries under consideration.

MATHEMATICAL FORMULATION

Model Equations

The governing equations for two-dimensional, viscous, compressible flow in a Cartesian coordinate system can be written in the following compact and conservative form :

$$\alpha \frac{\partial \mathbf{Q}}{\partial t} + \frac{\partial \mathbf{F}}{\partial x} + \frac{\partial \mathbf{G}}{\partial y} = \frac{\partial \mathbf{F_d}}{\partial x} + \frac{\partial \mathbf{G_d}}{\partial y} + \mathbf{S} \qquad (1)$$

where $\mathbf{Q}, \mathbf{F}, \mathbf{G}, \mathbf{F_d}, \mathbf{G_d}$ are vectors, defined as :

$$\mathbf{Q} = \begin{bmatrix} \rho \\ \rho u \\ \rho v \\ E_Q \\ \rho k \\ \rho d \end{bmatrix} , \mathbf{F} = \begin{bmatrix} \rho u \\ p + \rho u^2 \\ \rho uv \\ uE \\ \rho uk \\ \rho ud \end{bmatrix} , \mathbf{G} = \begin{bmatrix} \rho v \\ \rho uv \\ p + \rho v^2 \\ vE \\ \rho vk \\ \rho vd \end{bmatrix} \qquad (2)$$

and :

$$\mathbf{F_d} = \begin{bmatrix} 0 \\ \tau_{xx} \\ \tau_{yx} \\ \Gamma_E(\frac{\partial T}{\partial x}) \\ (\frac{\mu_{eff}}{\sigma_k})(\frac{\partial k}{\partial x}) \\ (\frac{\mu_{eff}}{\sigma_d})(\frac{\partial \epsilon}{\partial x}) \end{bmatrix} , \mathbf{G_d} = \begin{bmatrix} 0 \\ \tau_{yx} \\ \tau_{yy} \\ \Gamma_E(\frac{\partial T}{\partial y}) \\ (\frac{\mu_{eff}}{\sigma_k})(\frac{\partial k}{\partial y}) \\ (\frac{\mu_{eff}}{\sigma_d})(\frac{\partial \epsilon}{\partial y}) \end{bmatrix} , \mathbf{S} = \begin{bmatrix} 0 \\ 0 \\ 0 \\ S_E \\ S_k \\ S_d \end{bmatrix} \qquad (3)$$

Some of the variables, source terms and diffusion flux coefficients included in the vectors above are defined differently for each of the two codes used here. Therefore :

$$FLOS3D: \begin{cases} \alpha = 1 , \ \Gamma_E = \frac{\gamma}{\gamma-1}(\frac{\mu}{Pr} + \frac{\mu_t}{Pr_t}) \\ E_Q = e , \ E = e + p , \ d = \omega = \epsilon/k \\ S_E = \Phi , \ S_k = P_k - 0.09\,\rho\,\omega\,k \\ S_d = \frac{5}{9} P_k\,(\omega/k) - \frac{3}{40}\rho\omega^2 \\ \sigma_k = 2, \ \sigma_d = 2, \ \mu_t = \rho k/\omega \end{cases} \qquad (4)$$

$$FAST\text{-}3D: \begin{cases} \alpha = 0 , \ \Gamma_E = \gamma(\frac{\mu}{Pr} + \frac{\mu_t}{Pr_t}) \\ E = \rho T , \ d = \epsilon \\ S_E = -(\frac{1}{C_v})\,p\,(\nabla \cdot \vec{V}) , \ S_k = P_k - \rho\,\epsilon \\ S_d = -C_2\,(\epsilon^2/k) + C_1\,P_k\,(\epsilon/k) \\ \sigma_k = 1, \ \sigma_d = 1.3, \ \mu_t = C_\mu\,\rho\,(k^2/\epsilon) \end{cases} \qquad (5)$$

The constants of the $k-\epsilon$ model are assigned their standard values, i.e., $C_1 = 1.44, C_2 = 1.92, C_\mu = 1.0$, while the Prandtl numbers are equal to $Pr = 0.71$, $Pr_t = 1.0$ and $\gamma = 1.4$. The stresses τ_{ij} can be written as :

$$\tau_{ij} = \mu_{eff}\left[\left(\frac{\partial u_i}{\partial x_j} + \frac{\partial u_j}{\partial x_i}\right) - \frac{2}{3}\delta_{ij}(\nabla \cdot \vec{V})\right] \qquad (6)$$

while P_k is the production of turbulent kinetic energy, defined as :

$$P_k = \left\{\mu_t\left[\left(\frac{\partial u_i}{\partial x_j} + \frac{\partial u_j}{\partial x_i}\right) - \frac{2}{3}\delta_{ij}(\nabla \cdot \vec{V})\right] - \frac{2}{3}\delta_{ij}k\right\}\frac{\partial u_j}{\partial x_i} \qquad (7)$$

In the above, $i = 1, 2$, $j = 1, 2$ and δ_{ij} is the Kronecker delta. The energy equation for the FLOS3D code has been written with respect to the specific internal energy of the fluid : $e = p/(\gamma - 1) + (\rho/2)\,(u^2 + v^2)$, while for the FAST-3D code with respect to the temperature T as the transported variable. The latter form is obtained by suitable manipulation of the original form of the energy equation in terms of e, by using the caloric equation of state $e = C_v T$. For inviscid flow computations, the turbulence model equations and the diffusion flux terms are omitted.

In a non-orthogonal coordinate system (ξ, η) which is needed for turbine blade geometries, the vectors involved in Eq. 1 need to be transformed. $\mathbf{F}$ and $\mathbf{G}$ for instance, are transformed as follows :

$$\overline{\mathbf{F}}(\xi,\eta) \equiv \left(\mathbf{F}\frac{\partial y}{\partial \eta} - \mathbf{G}\frac{\partial x}{\partial \eta}\right) , \ \overline{\mathbf{G}}(\xi,\eta) \equiv \left(-\mathbf{F}\frac{\partial y}{\partial \xi} + \mathbf{G}\frac{\partial x}{\partial \xi}\right) \qquad (8)$$

The unsteady term vector $\mathbf{Q}$ and the vectors on the right-hand side of Eq. (1), i.e. $\mathbf{F_d}$, $\mathbf{G_d}$ and $\mathbf{S}$, are treated similarly. Thus, one can write the transformed form of Eq. (1) as :

$$\alpha\frac{\partial \overline{\mathbf{Q}}}{\partial t} + \frac{\partial \overline{\mathbf{F}}}{\partial \xi} + \frac{\partial \overline{\mathbf{G}}}{\partial \eta} = \frac{\partial \overline{\mathbf{F}}_d}{\partial \xi} + \frac{\partial \overline{\mathbf{G}}_d}{\partial \eta} + \mathbf{J}\,\overline{\mathbf{S}} \qquad (9)$$

THE NUMERICAL SCHEMES

The Pressure-Correction Solver

Discretization - Boundary Conditions. The computer code FAST-3D has been originally developed for the calculation of three-dimensional, incompressible, elliptic flows with complex boundaries. The numerical method is described in detail in Majumdar et al. (1989) and Zhu (1992) and only a brief description of the original solver is given here.

The governing differential equations are integrated over arbitrary three-dimensional control volumes with the aid of the Gauss theorem. The conservative form of the resulting discretization equations is further enhanced by adopting the

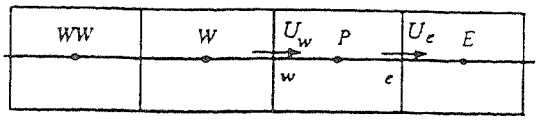

Figure 1: COLLOCATED GRID ARRANGEMENT

cartesian velocity components as the principal unknowns for the momentum equations. All variables are stored at the control volume centers, necessitating thus the implementation of the momentum interpolation procedure of Rhie and Chow (1983), to avoid the checker-board splitting of the pressure field. The convective fluxes can be handled by various schemes among which the Hybrid scheme of Spalding (1972), the second order QUICK scheme of Leonard (1979) and the second order bounded HLPA scheme of Zhu (1991). HLPA is a good compromise between numerical stability and accuracy and is considered as the standard numerical scheme of the code.

The discretized momentum and continuity equations are combined to form a pressure-correction equation following the SIMPLE algorithm of Patankar and Spalding (1972). The resulting system of the algebraic difference equations is solved in an uncoupled manner by the Strongly Implicit Procedure (SIP) of Stone (1968). A high lever of vectorization is accomplished, allowing for fast results on fine grids.

The original version of FAST-3D is designed for a generalized coordinate system with a flexible boundary condition algorithm. Four most commonly used boundary conditions - inflow plane, outflow plane, symmetry plane and solid wall are implemented. For turbulent flow computations, the standard wall-function approach (Launder and Spalding, 1974) is adopted.

Compressibility Effects. The pressure-correction method has been originally developed for incompressible flows. In order to allow for compressibility effects, the density corrections are introduced into the discretized continuity equation as proposed by Karki and Patankar (1989). The mass conservation equation for the one-dimensional situation of Fig. 1 is then written as:

$$(\rho_e^* + \rho_e')(U_e^* + U_e')l_e - (\rho_w^* + \rho_w')(U_w^* + U_w')l_w = 0, \quad (10)$$

where U is the contravariant velocity component in the ξ direction and l_e, l_w the east and west cell-face areas (see Fig. 1). The starred variables denote the guessed values from the previous iteration and the primed variables stand for the corrections to the guessed values to ensure mass conservation. The density corrections ρ' are related to the pressure corrections p' via the state equation:

$$\rho' = \left.\frac{\partial \rho}{\partial p}\right|_s p' = \frac{1}{\gamma R T} p' \quad (11)$$

under the assumption of an isentropic process. Eq. (10) is rewritten as:

$$\underbrace{(\rho_e^* U_e^* l_e - \rho_w^* U_w^* l_w)}_{T0} + \underbrace{(\rho_e^* U_e' l_e - \rho_w^* U_w' l_w)}_{T1} +$$

$$\underbrace{(\rho_e' U_e^* l_e - \rho_w' U_w^* l_w)}_{T2} + \underbrace{(\rho_e' U_e' l_e - \rho_w' U_w' l_w)}_{T3} = 0 \quad (12)$$

In the above equation, the second order term T3 is usually neglected for linearization and terms T0, T1 are the standard incompressible contributions. The T2 term introduces a correction due to compressibility effects. This term involves the density corrections on the e and w cell faces and a decision needs to be made for the density profiles between any two neighboring nodes. For subsonic flows the usual practice is to adopt a linear profile for ρ (Tamamidis , 1990). According to Karki and Patankar (1989) however, the density should always be upwinded, in order to avoid numerical instabilities observed especially in regions were the local Mach number is close to unity. Since this study is focused on subsonic and transonic shock-free turbomachinery flows, both linear and pure upwinding practices for density have been implemented in FAST-3D.

Using Eq. (11) the cell-face density corrections ρ_w', ρ_e' in the T2 term of Eq. (12) are written as:

$$\begin{aligned} \rho_w' &= \frac{1}{\gamma R}\left[f_x \frac{p_P'}{T_P} + (1-f_x)\frac{p_W'}{T_W}\right] \\ \rho_e' &= \frac{1}{\gamma R}\left[f_x^+ \frac{p_E'}{T_E} + (1-f_x^+)\frac{p_P'}{T_P}\right] \end{aligned} \quad (13)$$

for linear interpolation or

$$\begin{aligned} \rho_w' &= \frac{1}{\gamma R}\left[g_w^+ \frac{p_W'}{T_W} + (1-g_w^+)\frac{p_P'}{T_P}\right] \\ \rho_e' &= \frac{1}{\gamma R}\left[g_e^+ \frac{p_P'}{T_P} + (1-g_e^+)\frac{p_E'}{T_E}\right] \end{aligned} \quad (14)$$

for pure upwinding. In the above equations f_x , f_x^+ are the linear interpolation factors for the W-P and P-E intervals respectively (see Fig. 1) and g_e^+, g_w^+ are defined as

$$g_e^+ = \frac{1+sgn(U_e)}{2}, \quad g_w^+ = \frac{1+sgn(U_w)}{2}$$

$$sgn(a) = \begin{cases} 1 & a \geq 0 \\ -1 & a < 0 \end{cases}$$

Introducing Eqs. (13) or (14) in Eq. (12) the final discretized form of the continuity equation may be written as:

$$A_P p_P' = A_W p_W' + A_E p_E' + b \quad (15)$$

where:

$$\begin{aligned} A_W &= A_W^{T1} + A_W^{T2} \quad , \quad A_E = A_E^{T1} + A_E^{T2} \\ A_P &= A_P^{T1} + A_P^{T2} \quad , \quad b = \rho_w^* U_w^* l_w - \rho_e^* U_e^* l_e \end{aligned}$$

$$A_W^{T2} = \frac{l_w U_w}{\gamma R T_W} \times \begin{cases} (1-f_x) & \text{for linear interp.} \\ g_w^+ & \text{for upwinding} \end{cases}$$

$$A_E^{T2} = -\frac{l_e U_e}{\gamma R T_E} \times \begin{cases} f_x^+ & \text{linear} \\ (1-g_e^+) & \text{upwinding} \end{cases}$$

$$A_P^{T2} = -\frac{l_w U_w}{\gamma R T_P} \times \begin{cases} f_x & \text{linear} \\ (1-g_w^+) & \text{upwinding} \end{cases} + \frac{l_e U_e}{\gamma R T_P} \times \begin{cases} (1-f_x^+) & \text{linear} \\ g_e^+ & \text{upwinding} \end{cases}$$

and A_W^{T1}, A_E^{T1}, A_P^{T1} are the usual incompressible coefficients.

The effect of the divergence of the velocity field $\nabla \cdot \vec{V}$ on the normal stresses τ_{xx}, τ_{yy} (Eq. (6)) is assumed to be insignificant for the range of the Mach numbers studied in the present work and is not taken into account. Likewise the dissipation function Φ, normally appearing in the source term S_E of the transport equation for the internal energy E, has been neglected and only the reversible source term $-p(\nabla \cdot \vec{V})$ is introduced in the pressure-correction solver.

The Time Marching Solver

The FLOS3D code (Michelassi et al. 1990) is based on the scalar form of the approximate factorization method which was introduced by Pulliam and Chaussée (1981) to render the implicit approximate factorization method by Beam and Warming (1982) less computational costly. The code solves two and three-dimensional problems in inviscid, laminar and turbulent flow regime. The governing equations are discretized by using centered finite volumes for the convective terms, and centered finite differences for the diffusion terms. The algorithm is implemented in its one step version so that the accuracy in time is first order. The approximate factorization method requires the solution of block tridiagonal of pentadiagonal matrices. In three dimensions the implicit solution procedure is often excessively heavy so that the original algorithm has been rendered scalar by substituting the original convective Jacobian, A, with a set of eigenvalues, Λ, and eigenvector, T:

$$\mathbf{A} = \mathbf{T}^{-1} \cdot \Lambda \cdot \mathbf{T} \qquad (16)$$

This choice allows solving for a scalar, and not block, tridiagonal or pentadiagonal matrix, which is extremely easier to solve than the original implicit operator. The intrinsic robustness of the algorithm may be disrupted by the explicit treatment of the diffusive terms. This weakness of the code, which may be evident in internal flows, is overcome by the implicit treatment of a set of approximate diffusive eigenvalues (Michelassi et al., 1990), which proved to bring about the necessary degree of robustness in presence of viscous effects.

In order to take full advantage of the implicit time marching procedure the code utilizes a local time step formula which was optimized for the present applications. Stability is enhanced by using a spectral radius weighted version of the artificial damping scheme by Jameson et al. (1981) which proved adequate for the solution of two and three-dimensional turbomachinery flows. Particular care is devoted to the conservative treatment of the artificial damping terms, which may introduce some inaccuracies especially close to solid boundaries. Details about the code may be found in Michelassi et al. (1990).

The Grid Generation Program MESHHO

The MESHHO program (Michelassi, 1994) is an interactive tool for grid generation. The algorithm produces I-type grids which represent a compromise between the C and the H-type grids. The I grid allows having a very good resolution in the wake of the profile, together with a good grid refinement in both the leading and trailing edges. The code allows identifying several zones in the computational domain in which it is possible to fix the slope of the coordinate lines. A set of guide lines in the computational domain, constructed as Bezier curves, are set and the grid is finally generated by isoparametric transformations. These operations are done interactively and can be easily controlled by the user.

Observe that the code allows for defining the grid inside the blade as well. While this feature is a computational overhead for standard calculations, it might be of great help when studying aerodynamic and blade heat transfer problems. In particular this approach is very useful in the presence of coolant injection holes, or cooled blades.

Fig. 2a shows a typical I grid generated by using MESHHO. The grid has a non-point-to-point periodic distribution on the periodic boundaries. Although a point-to-point distribution will be the simplest option, the resulting grid would be excessively distorted expecially in the wake for high turning angle blades. To decrease the grid skewness in the blade passage and the wake, the point-to-point periodicity is therefore abandoned. The non-point-to-point periodic arrangement requires a special interpolation technique of the solution which is described below. Fig. 2a shows clearly the advantage of the non periodic structure, as the grid is only marginally distorted, and much more regular than a standard periodic grid.

Numerical Treatment of the Non-Point-to-Point Periodic Grid

Since the two solvers originally did not make provision for a non-point-to-point periodic boundary treatment, which was found necessary in the present turbine cascade flow computations, the standard solution algorithms have been modified accordingly. From the original computational grid with $i = 1, m$ grid lines in the streamwise direction and $j = 1, no$ grid lines in the cross flow direction the line $j = 2$ is shifted at a tangential distance of $y = +pitch$, while the line $j = no - 1$ is shifted at a distance $y = -pitch$ (see Figs. 2, 3). The $j = n = no + 2$ grid line of the extended computational grid is formed by linear extrapolation of the north end of the original $i = 1, m$ grid lines to the aforementioned shifted line of $j = 2$, while the extended $j = 1$ grid line is formed in a similar way. For each iteration the implicit solution is performed for $i = 2, ni - 1$ and $j = 3, nj - 2$, i.e. for all control volumes that lie inside the original periodic domain (see Fig. 2c). After each internal iteration the values of ϕ at $j = 2$ are updated by linear interpolations from the appropriate points at $j = nj - 2$. The values of variable ϕ at all points $j = 2$, $i = 1, ni$ are updated by

$$\phi(i,2) = w_2(i)\,\phi(i_2(i), nj-2) + (1-w_2(i))\,\phi(i_2(i)-1, nj-2) \qquad (17)$$

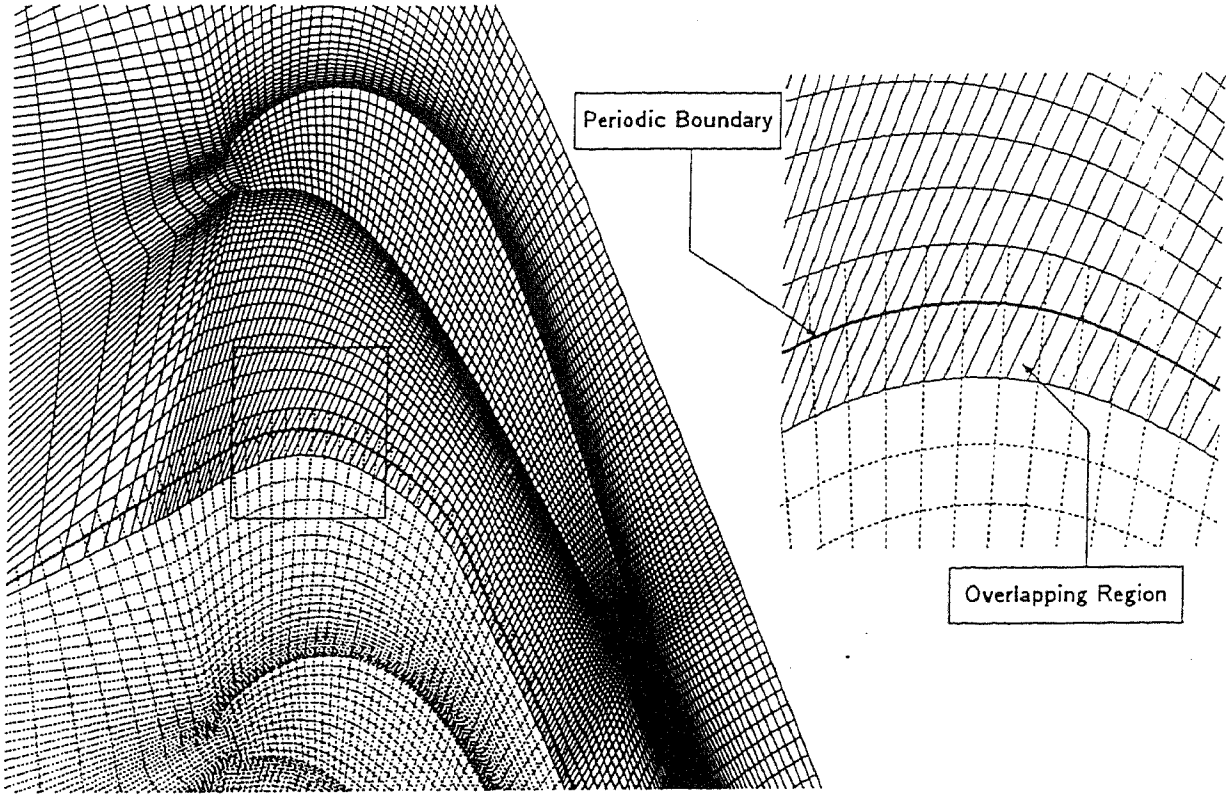

(a) PARTIAL VIEW INCLUDING OVERLAPPING REGION (b) DETAIL NEAR PERIODIC BOUNDARY

Figure 2: PERIODIC GRID ARRANGEMENT.

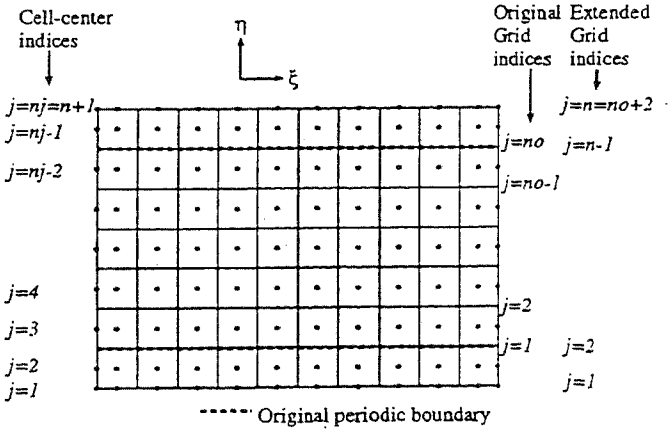

Figure 3: PERIODIC GRID ARRANGEMENT, COMPUTATIONAL SPACE (ξ, η).

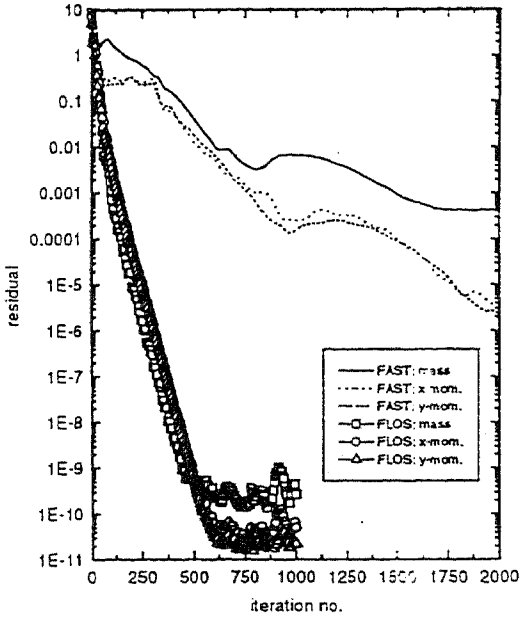

Figure 4: TYPICAL CONVERGENCE HISTORIES

where $i_2(i)$, $i = 1, ni$ is the periodicity-mapping array for j=2 and $w_2(i)$, $i = 1, ni$ the proper weights of the linear interpolation at constant η. In a similar manner the values of ϕ at all points $j = nj - 1$, $i = 1, ni$ are updated by

$$\begin{aligned}\phi(i, nj-1) &= w_{nj-1}(i)\ \phi(i_{nj-1}(i), 3) \\ &+ (1 - w_{nj-1}(i))\ \phi(i_{nj-1}(i) - 1, 3) \quad (18)\end{aligned}$$

The ϕ's at $j = 1$ are updated by linear interpolations between the corresponding values at lines $j = nj - 2$ and $j = nj - 3$, and at $j = nj$ by linear interpolation from lines $j = 3$ and $j = 4$, in a similar sense to Eqs. (17) and (18).

Specifying the values at the two rows of control volumes on the north and south extended periodic boundaries with the above procedure guarantees that not only the ϕ values but also the spatial derivatives of ϕ's are made periodic, resulting in higher-order periodicity. Regarding the structure of the FAST-3D code it is the momentum interpolation technique combined with the non-point-to-point periodic grid arrangement that dictated the use of the extended periodic control volumes. The existence of the row of control volumes at $j = nj - 1$ and $j = 2$ ensures the proper computation of the pressure-correction coefficients $A_N(i, nj - 2)$ and $A_S(i, 3)$ respectively. Since the pressure correction on the extended grid points is updated for every internal iteration, this results in a semi-implicit periodic scheme for the pressure-correction equation. The FLOS code needs in fact a double grid line extension on each periodic boundary. This allows for a correct implementation of the artificial damping scheme which requires a five-point computational molecule, while still maintaining the high vectorization of the solver.

RESULTS AND DISCUSSION

The NuovoPignone Linear Turbine Cascade

The turbine rotor blade was designed by NuovoPignone to operate under a wide range of pressure ratios. The measurement data used in this paper has been obtained at the University of Florence and at the CNPM research center, Milan, Italy. The experiments were run on two different experimental pieces of apparatus in order to have a sort of a comparison between two completely different test sections. In fact, the low speed wind tunnel of the University of Florence has a $500 \times 200mm$ test section and the exit Mach number is approximately 0.3, depending on the final contraction ratio. The large test section allows testing the blade with a 1:2 scale, whereas in the CNPM wind tunnel the scale reduces to 4:1, while the exit Mach number can go up to 1.6. For the low speed cases the results on both wind tunnels are almost collapsing, as described by Bruzzi (1992).

The wide set of measurements include the isentropic Mach number distribution on the blade at various pressure ratios, the mass-averaged exit flow angle, the total pressure losses, and a wide set of secondary flow visualization which is intended for the validation of three-dimensional Navier-Stokes solvers.

The computations were performed at M_2=0.2, 0.3, 0.5, 0.7 covering the subsonic and transonic shock-free range of the experimental data. At $M_2 = 0.7$ the flow shows a sonic line located at approximately 25% of the cord, but no shock has been detected in either the computations or the experiments. Some preliminary tests on the behavior of FAST were performed first, in order to investigate the influence of the linear and upwind schemes for density on the results. The upwind scheme was found to be more stable than the linear scheme. Since there was no significant difference in the results of the two schemes the upwind scheme was adopted for all FAST computations in the present study. The higher stability of the upwind scheme has no physical justification, since the density is almost constant in this range of Mach numbers, and it is probably related to the lack of articial damping in high speed regions. Moreover, in case of the development of supersonic regions during the iterative numerical procedure, the linear scheme is not able to ensure the stability.

Inviscid computations were performed first on a highly refined grid of 200x63 points in order to concentrate on the numerical schemes and avoid the influence of the turbulence models on the results. Fig. 4 shows the convergence histories for mass and momentum conservation of the time marching and pressure-correction solvers. The plot refers to the inviscid calculation of the NP blade at $M_2 = 0.3$. Although the plot shows a large difference between the performances of the two codes, the reader should remember that FLOS solves all the equations in a coupled manner, whereas FAST solves the same equations sequentially. While one iteration of the time marching solver is definitely heavier from a computational point of view, it evidently brings about a higher degree of coupling between the N-S and the energy equations. This clearly sorts a positive effect in terms of convergence rates for compressible fluid flows. Nevertheless, the coupled procedure is less flexible than the sequential approach. Additionally, the periodic inviscid compressible nature of the flow under investigation makes this test particularly suited for FLOS, which is probably at its maximum speed. The main reason for this is the absence of viscous terms which are treated in an approximate implicit way by FLOS. Although it would have been desirable, a comparison on a turbulent flow was not possible because of the totally different grid requirements of the two codes due to the different nature of the turbulence models implemented. Still, the differences tend to reduce by a factor of 2 when considering the overall computational time, especially in the turbulent flow regime. Accordingly, Fig. 4 does not allow to draw any general conclusion, but it mainly stresses the high performances of the scalar approximate factorization for inviscid compressible flows.

A first comparison of the computed isentropic Mach number contours at $M_2 = 0.3$ is shown in Fig. 5. The overall agreement between the two codes is excellent in regions where the M_{is} number exceeds the value of 0.2. This region of agreement is roughly bounded between the contour line A departing from the suction-side leading edge and the outflow plane. Some significant differences can be seen in the low speed region, especially near the stagnation point. This point is clearly marked by the minimum $M_{is} = 0.02$ contour

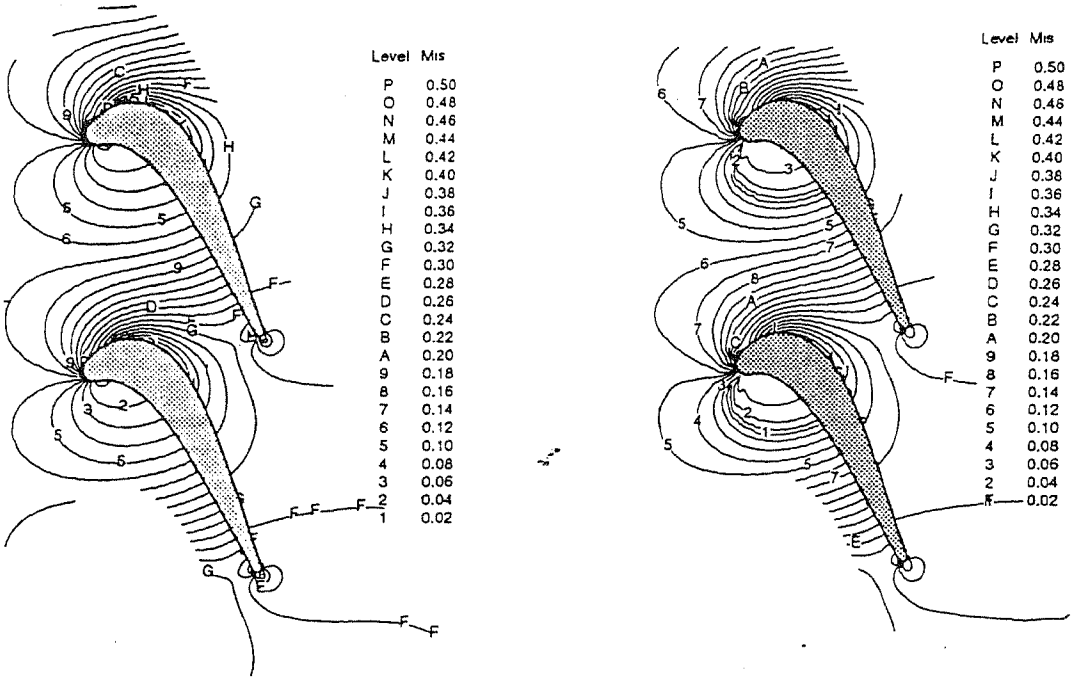

(a) FAST - INVISCID

(b) FLOS - INVISCID

Figure 5: NP BLADE: CONTOUR PLOTS OF M_{is} COMPUTED BY THE TWO CODES AT $M_2 = 0.3$.

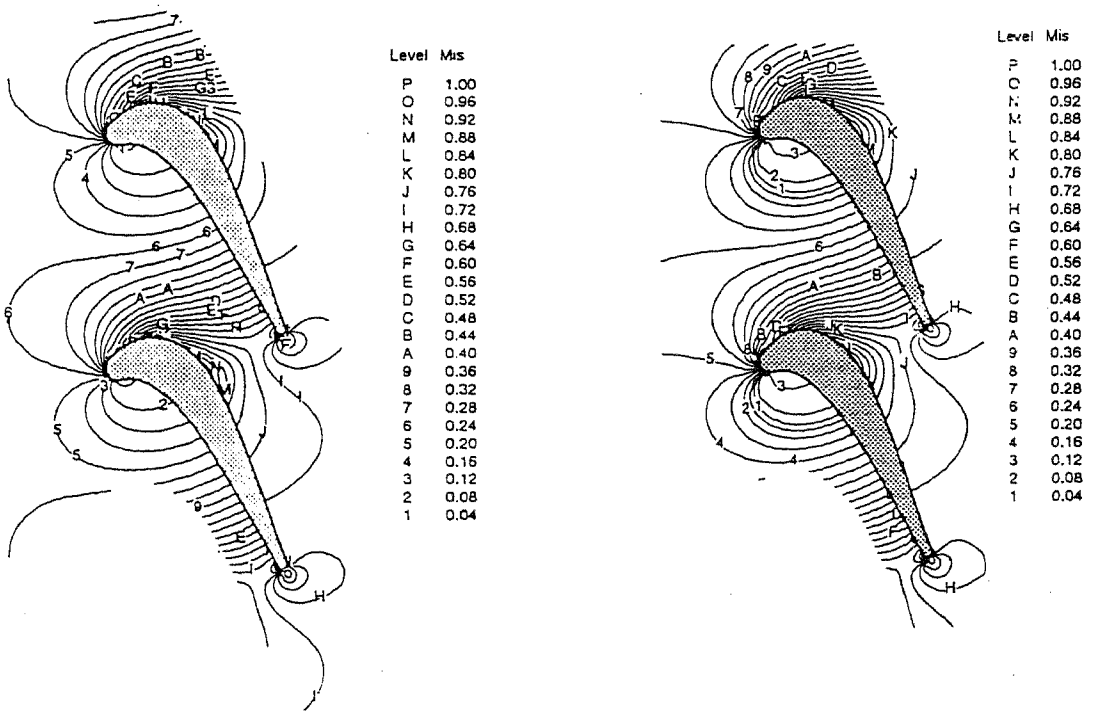

(a) FAST - INVISCID

(b) FLOS - INVISCID

Figure 6: NP BLADE: CONTOUR PLOTS OF M_{is} COMPUTED BY THE TWO CODES AT $M_2 = 0.7$.

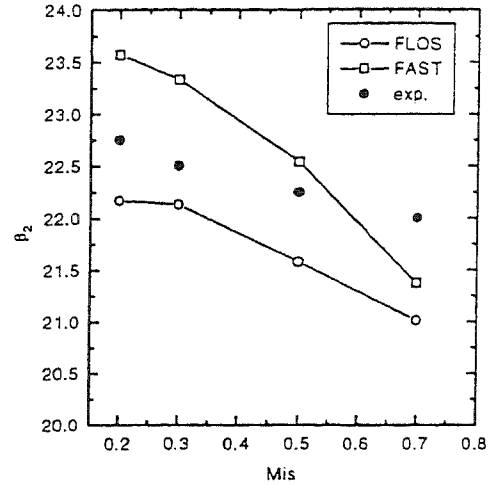

Figure 8: NP BLADE: MASS-AVERAGED EXIT FLOW ANGLE β_2 FOR VISCOUS FLOW.

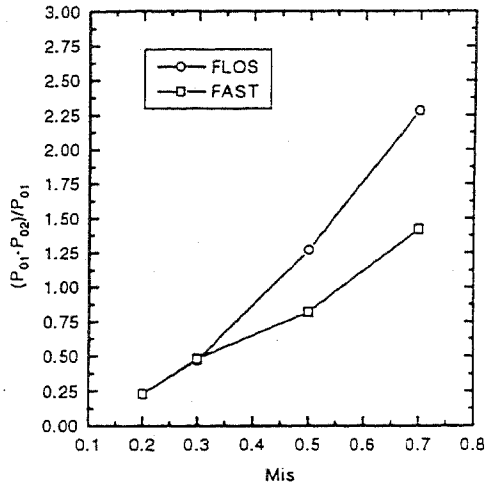

Figure 9: NP BLADE: MASS AVERAGED-TOTAL PRESSURE LOSS COEFFICIENT ζ_2.

in highly accelerating flows. All the plots confirm that the predictions of FLOS tend to those given by FAST as the exit Mach number increases up to $M_2 = 0.7$.

In Figs. 8 and 9, two mass-averaged quantities are plotted, namely the exit flow angle β_2 and the total pressure loss coefficient ζ_2 respectively. These are computed using the expression :

$$\phi = \frac{\int_0^1 \rho_2(y^*)u_2(y^*)\phi(y^*)\,dy^*}{\int_0^1 \rho_2(y^*)u_2(y^*)\,dy^*} \qquad (19)$$

where ϕ is either one of β_2 and ζ_2 and y^* is the vertical coordinate y along the exit cross section non-dimensionalized with the pitch of the cascade. The plots show the variation with the exit Mach number M_2. Both codes seem to predict the angle β_2 within 1° or less. The angle, which is defined here with respect to the vertical, seems to decrease with the exit Mach number, but both codes predict a faster rate of decrease than the experiments. The loss coefficient ζ increases with M_2 at a rate which is code dependent. The

Table 1: COMPARISON OF MASS ERROR $\left(\frac{m_{in}-m_{out}}{m_{in}}\right)(\%)$

$M_2 \Longrightarrow$	0.2	0.3	0.5	0.7
FAST	0.025	0.041	0.046	0.031
FLOS	0.200	0.150	0.480	0.520

$k-\omega$ turbulence model associated with the FLOS3D code appears to yield a larger amount of losses than the $k-\epsilon$ model used by the FAST-3D code, although the two codes agree for $M_2 \leq 0.3$. Table 1 shows a comparison of the % mass error defined as $100 \times (m_{in} - m_{out})\, m_{in}$ for both codes. It is obvious that the pressure-correction solver experiences a much smaller error than the time marching solver. This means that a method solving for pressure is more conservative than a method which solves for density when solving low speed flows. On the other hand the maximum error for FLOS is always less than 0.6% which gives marginal effects on the pressure field, and can be neglected.

The ATB Linear Turbine Cascade

The ATB linear turbine cascade was designed for a two-dimensional turning of 104.7° at an isentropic Mach number of 0.95 . The experiments were performed at the high speed cascade wind tunnel of the University of the Armed forces Munich (Beeck , 1992). A turbulence grid upstream of the cascade produced a turbulence level of 5%. The experiment was carried out at an exit isentropic Mach number of $M_{is} = 0.716$, an exit Reynolds number of $Re_2 = 5.94 \times 10^5$ an inlet total pressure of 19880 Pa and an inlet total temperature of 313K. A wedge probe was used for wake traverse measurements at an axial position of 32% of the cord downstream of the trailing edge plane.

Only viscous computations have been performed for this test case. Again two different grids (182×110 for FAST and 292×149 for FLOS) had to be used because of the different turbulence modes used in the codes. An excellent agreement between the computed results of both methods and experiments can be seen in Fig. 10 for the surface M_{is}. Both computational results have captured the local minimum of the static pressure on the pressure side near stagnation, as implied by the local minimum of the isentropic Mach number. A sonic line can be seen at approximately 50% of the cord for this test case. Figure 11 shows the comparison between the computed and measured exit flow angle β_2, local exit Mach number M, and total pressure loss coefficient ζ^* at an axial plane located at x=80mm downstream of the blade trailing edge. Both codes produce a similar shape of the β_2 profiles with an overall difference of no more than 0.8 degrees. FLOS is in excellent agreement with the experimental data for β_2, which were given at a limited number of points. This result is reflected in the M_2 and ζ_2 profiles

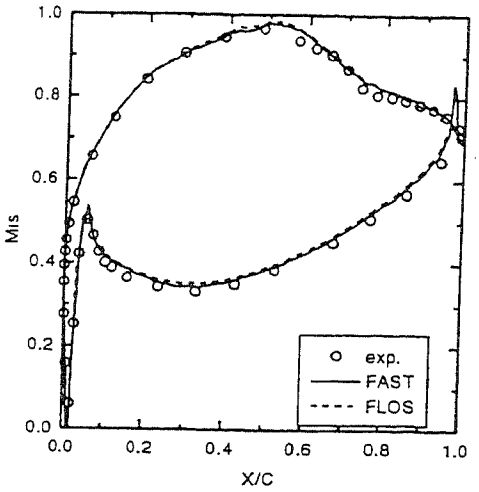

Figure 10: ATB BLADE: COMPARISON OF COMPUTED AND MEASURED SURFACE M_{is} DISTRIBUTION FOR VISCOUS FLOW.

(Figs. 11b-c) where FLOS captures the exact position of the wake center. Both codes over-predict the local minimum in the M_2 profiles of Fig. 11b. This over-prediction, which is more pronounced in the case of FLOS, results in an overall overestimation of ζ_2^* as compared with the experimental values. The predictions of the two codes are in very good agreement for the total pressure losses.

CONCLUSIONS

A comparison of computations obtained by two different computer codes, implementing a time marching and a pressure-correction method respectively, was conducted for two different turbine cascades at low-Mach-number compressible flow. The study has demonstrated the ability of a pressure-correction scheme, arising as an extension of its previously existing incompressible form, to predict results of comparable accuracy as a well established compressible flow solver. Differences were observed locally in the flow field, mostly due to the turbulence models which were inherent to each code and were maintained in order to minimize the necessary modifications to the original codes. The time marching code, which uses an artificial damping approach seemed to lose in accuracy in low Mach number regions (less than 0.3), accompanied by weaker mass conservation, unlike the pressure-correction code, whose corresponding properties are not affected. For inviscid flows, the time marching code was found the most efficient of the two by far, but this advantage is largely reduced for turbulent flows. Generally, both codes were in good agreement with the experimental data as far as isentropic Mach number distribution on the blade and exit flow angles, which were predicted within less than 1°. The prediction of the total pressure losses was however less succesfully predicted, although the codes agreed with one another, mostly due to the inability of the turbulence models used to adequately resolve the boundary layers or capture transition phenomena.

ACKNOWLEDGMENTS

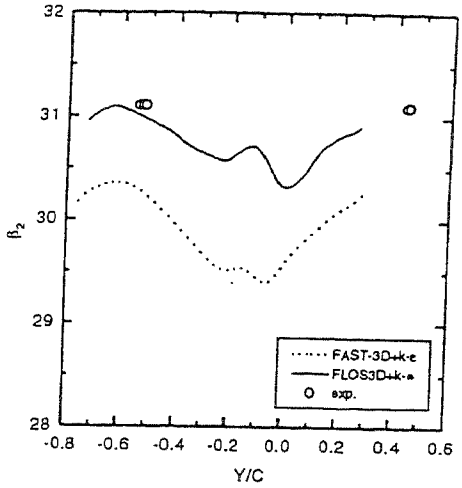

(a) EXIT FLOW ANGLE β_2.

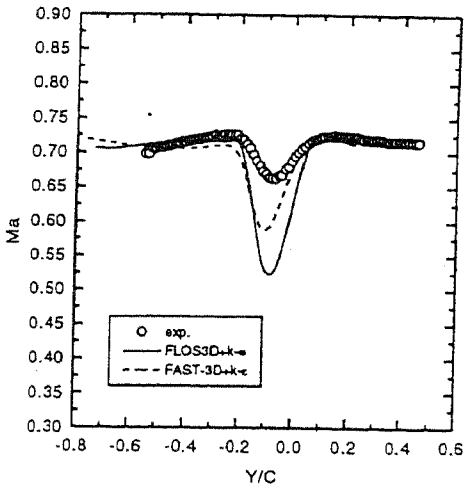

(b) MACH NUMBER M_2.

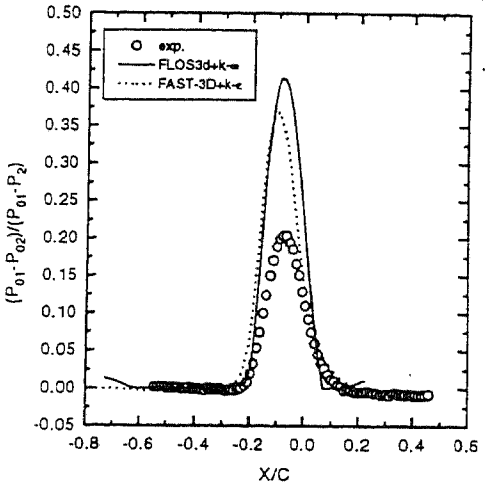

(c) TOTAL PRESSURE LOSS COEFFICIENT ζ_2^*.

Figure 11: ATB BLADE: COMPARISON OF COMPUTED AND MEASURED WAKE FLOW PARAMETERS.

This work was partly sponsored by the German Federal Ministry of Research and Technology through program TURBOTECH under contract No. 0326801G and through program TURBOTHERM under contract No. 0326760D. The authors would like to gratefully acknowledge Prof. W. Rodi and Prof. F. Martelli for their support granted during the preparation of this work. The authors should like to thank Dipl.-Ing. S. Ardey for kindly providing the ATB measurement data in machine readable form. The first author would also like to thank CINECA, MURST and CNR for providing the necessary computer time.

REFERENCES

Beam, R.M. and Warming, R.F., 1982, "Implicit Numerical Methods for the Compressible Navier-Stokes and Euler Equations", Lecture Series on Computational Fluid Dynamics, VKI-LS-1982-04, Von Karman Institute for Fluid Dynamics.

Beeck, A., 1992, "Strömungsfelduntersuchungen zum aerodynamischen Verhalten eines hochbelasteten Turbinengitters mit Kühlluftausblasung an der Vorderkante", Dissertation, Universität der Bundeswehr München, Institut für Strahlantriebe.

Bruzzi, M., 1992, "Analisi dei Flussi Secondari a Valle di una Schiera di Turbina", Phd thesis, Energetics Dept., University of Florence, Italy.

Denton, J.D., 1993, "Loss Mechanisms in Turbomachines", *ASME J. of Turbomachinery*, Vol. 115, pp. 621-656.

Hah, C., 1984, "A Navier-Stokes Analysis of Three-Dimensional Turbulent Flows Inside Turbine Blade Rows at Design and Off-Design Conditions", *ASME J. of Engng. for Gas Turbines and Power*, Vol. 106, pp. 421-429.

Hah, C. and Leylek, J.H., 1987, "Numerical Solution of Three-Dimensional Turbulent Flows for Modern Gas Turbine Components", ASME Paper 87-GT-84, pp. 1-8.

Issa, R.I. and Lockwood, F.C., 1977, "On the Prediction of Two-dimensional Supersonic Viscous Interactions Near Walls", *AIAA Journal*, Vol. 15, No.2, pp. 182-188.

Jameson, A., Schmidt, W., Turkel, E., 1981 : "Numerical Solutions of the Euler Equations by Finite Volume Methods Using Runge-Kutta Time-Stepping Scheme", AIAA 81-1259.

Karki, K.C. and Patankar, S.V., 1989, "Pressure Based Calculation Procedure for Viscous Flows at All Speeds in Arbitrary Configurations" *AIAA Journal*, Vol.27, No.9, pp. 1167-1174.

Lakshminarayana, B., 1991, "An Assessment of Computational Fluid Dynamic Techniques in the Analysis and Design of Turbomachinery - The 1990 Freeman Scholar Lecture", *ASME J. of Fluids Engng.*, Vol. 113, pp. 315-352.

Launder, B.E. and Spalding, D.B., 1974, "The Numerical Computation of Turbulent Flows" *Comp. Meth. Appl. Mech. Eng.*, Vol. 3, pp. 269-289.

Leonard, B.P., 1979, "A Stable and Accurate Convective Modeling Procedure Based on Quadratic Upstream Interpolation", *Comp. Meth. in Appl. Mech. and Eng.*, Vol. 19, 1979, pp. 59-98.

Majumdar, S., Rodi, W. and Zhu. J. 1989, "Three Dimensional Finite-Volume Method for Incompressibl Flows With Complex Boundaries", *ASME J. Fluids Engng* Vol. 114, pp. 496-503.

Majumdar, S., 1992, "A Pressure Based Method for Numerical Computation of Compressible Flow", Project Document PD CF 9225, Nat. Aeron. Lab., Bangalore, India July 1992.

McNally, W. and Sockol, P.M., 1985."REVIEW: Computational Methods for Internal Flows With Emphasis on Turbomachinery", *ASME J. of Fluids Engng.*, Vol. 107 pp. 6-22.

Michelassi, V., Liou, M.-S., Povinelli, L.A. and Martelli, F., 1990, "Implicit Solution of Three-Dimensional Internal Turbulent Flows", NASA CP-10045.

Michelassi, V., 1994, "The Meshho program 1.06", Rept no. 1- 1994, Dept. of Energetics, University of Florence, Italy.

Spalding, D.B., 1972, " A Novel Finite-Difference Formulation for Differential Expressions Involving Both First and Second Derivatives" Int. J. Num. Meth. Eng., Vol. 4, pp. 551-559.

Patankar, S.V. and Spalding, D.B., 1972, "A calculation Procedure for Heat, Mass and Momentum Tranfer in Three-Dimensional Parabolic Flows", *Int. J. of Heat and Mass Tranfer*, Vol.15, pp.1778-1806.

Pulliam, T.-H. and Chausée, D.S., 1981, "A Diagonal Form of an Implicit Approximate Factorization Algorithm", *J. Comput Physics*, Vol. 39, pp. 347-363.

Rhie, C.M. and Chow, W.L. 1983, "Numerical Study of the Turbulent Flow Past an Airfoil with Trailing Edge Separation", *AIAA Journal*, Vol. 21, No. 11, pp. 1525-1532.

Stone, H.L., 1968, "Iterative Solution of Implicit Approximation of Multidimensional Partial Differential Equations", *SIAM J. on Num. Analysis*, Vol.5, pp.530-558.

Tamamidis, P., 1990, "Numerical Prediction of Subsonic Turbulent Recirculating Flows Using Boundary-Fitted Coordinates", MS Thesis, Univ. of Illinois at Urbana-Champaign, Urbana, Illinois.

Van Doormaal, J.P. and Raithby, G.D., 1984, "Enhancements of the SIMPLE Method for Predicting Incompressible Fluid Flows", *Num. Heat Transfer*, Vol. 7, pp. 147-163.

Van Doormaal, J.P., Raithby, G.D. and McDonald, B.H., 1987, "The Segregated Approach to Predicting Viscous Compressible Fluid Flows", *ASME J. of Turbomachinery*, Vol. 109, pp. 268-277.

Wilcox, D.C., 1988, "Reassessment of the Scale-Determining Equation for Advanced Turbulence Models", AIAA Journal, Vol. 26, No. 11, pp. 1299-1310.

Zhu, J., 1991, "A Low-Diffusion and Oscillation-Free Convection Scheme", *Comm. in Applied Num. Methods*, Vol. 7, pp. 225-232.

Zhu, J., 1992, "An Introduction Guide to the Computer Program FAST-3D", Report No. 691, Institute for Hydromechanics, University of Karlsruhe, Germany.

Anhang C

A Comparison of Time-Marching and Pressure-Correction Algorithms for Transonic Turbine Blades

Dieser Anhang wurde veröffentlicht in
AD-Vol. 49, Computational Fluid Dynamics in Aeropropulsion, ASME,
pp. 115-126, 1995

AD-Vol. 49, Computational Fluid Dynamics in Aeropropulsion
ASME 1995

A COMPARISON OF TIME MARCHING AND PRESSURE-CORRECTION ALGORITHMS FOR TRANSONIC TURBINE BLADES

V. Michelassi
Energetics Department
University of Florence
Florence
Italy

E.L. Papanicolaou, G.S. Theodoridis
Institute for Hydromechanics
University of Karlsruhe
Karlsruhe
Germany

ABSTRACT

The paper describes the comparison of a classical time marching algorithm with a pressure-correction method reformulated for compressible flows. The comparison is carried out for inlet guide vanes in the presence or not of shocks. The time marching code is based on the scalar approximate factorization algorithm. The pressure-correction solver uses a modified SIMPLE algorithm to enforce mass conservation for compressible fluids. The equations are discretized by means of centered finite volumes. The two solvers use different artificial damping schemes which end up in very similar results for the invisid flow over a 4% bump. The comparison for subsonic, transonic, and supersonic turbine blades yielded some differences in the shock resolution, although losses and exit flow angles predictions are very much similar.

NOMENCLATURE

a	speed of sound
C_p	specific heat at constant pressure
C_v	specific heat at constant volume
e	specific total energy
F,G	convective flux vectors
F_d,G_d	diffusive fluxes
h	static enthalpy
h_0	total enthalpy
k	turbulent kinetic energy
J	coordinate transformation Jacobian
M	mach number
p	static pressure
Pr	laminar Prandtl number
Q	vector of unknowns in the time marching method
R	universal gas constant
Re	Reynolds number
S	source term vector
T	static temperature
u,v	velocity components in the x,y directions (vector $\bar{v}$)
x,y,z	Cartesian coordinates

subscripts

eff	effective
ex	exit
is	isentropic
t	turbulent

greek symbols

γ	specific heat ratio ($=C_p/C_v$)
ε	turbulent dissipation rate
Λ	convective eigenvector
Λ^v	viscous eigenvector
μ	dynamic viscosity
ρ	density
τ	shear stresses
Φ	dissipation function ($=\mu_{eff}\left[\left(\frac{\partial u_i}{\partial x_j}+\frac{\partial u_j}{\partial x_i}\right)-\frac{2}{3}\delta_{ij}\nabla\cdot\bar{v}\right]\frac{\partial u_i}{\partial x_j}$)
ω	specific turbulent dissipation rate

INTRODUCTION

It is very common for multi-stage turbines to operate in transonic flow conditions, so that a high stage pressure ratio is obtained and the number of stages is reduced (Hourmouziadis, 1989). However, under these circumstances shock waves develop and the losses are increased. Computational Fluid Dynamics (CFD) methods can be used to estimate those losses, by computing the flow field using the full compressible Navier-Stokes (N-S) equations, with a suitable turbulence model. In

many occasions, the solution of the Euler equations may suffice for the needs of the design, if the pressure distribution on the blade is of interest, or the capturing of shocks in the flow field. Therefore, both N-S and Euler equation solvers are still very widely used in the turbomachinery design process, along with their approximate forms.

Complete reviews of the various methods that are available today for CFD (Computational Fluid Dynamics) computations in turbomachinery have been presented by McNally and Sockol (1985) and Lakshminarayana (1991). For transonic and supersonic flows, the most commonly used are the *time marching* methods whereby an unsteady term is added to the equations, whether Euler or Navier-Stokes are to be solved, so that their nature is always guaranteed to be hyperbolic. Typical implicit methods are those presented by Pulliam and Chaussèe (1981) and Beam and Warming (1982) and used in turbomachinery applications by Michelassi et al., (1990). Although the range of applicability of these methods is high, from low subsonic to hypersonic flows, their performance deteriorates at very low Mach numbers and incompressible flows (Lakshminarayana, 1991).

In recent years pressure-correction methods (Patankar, 1980) have been adopted in the solution of compressible flows as well (Issa and Lockwood (1977), Van Doormaal et al. (1987), Karki and Patankar (1989)). A density correction was introduced in the continuity equation and a linearized, discretized form of the pressure-correction equation for compressible flow was derived. The main concerns in this formulation were how to approximate the cell face density in the discretized equations and how to simulate the necessary *hyperbolic character* of the governing equations for high-Mach-number flows. Issa and Lockwood (1977) proposed the hybrid differencing scheme along with backward differences for pressure gradients and the use of upstream values of density for the cell-face mass-fluxes. Such a first-order density-upwinding approach was also followed by Van Doormaal et al. (1987) and Karki and Patankar (1989). The results were successfull at low Mach numbers, but at higher Mach numbers the shocks were significantly smeared by the numerical diffusion associated with first-order upwinding. This drawback made the algorithms not very attractive for supersonic flow calculations.

In subsequent studies, effort was directed towards improving the shock-capturing capabilities of the compressible pressure-correction based schemes. In order to have sharper shocks McGuirk and Page (1990) recommended solving for ρu (momentum per unit volume) instead of u and ρ separately, and reformulated the SIMPLE algorithm, using a staggered grid. Since the standard pressure-correction equation is still elliptic for supersonic flows (when using a centered discretization scheme), McGuirk and Page (1990) also introduced the so called *retarded pressure field* which replaces the "physical pressure field". The retarded pressure concept introduces a locally adjusted amount of upwinding, based on the value of a suitably chosen function defined on the upstream cell face. The discretization scheme is not altered in subsonic regions, whereas in supersonic regions the hyperbolic nature of the pressure-correction equation is artificially achieved by upwinding the pressure. The amount of upwinding, unlike the previous pressure-correction schemes, is not constant. The dramatic improvements obtained by McGuirk and Page (1990) with respect to the Karki and Patankar (1989) results in terms of shock capturing capabilities show that the practice of a pure density upwinding must be avoided in high-Mach-number flows, together with the upwind or hybrid discretization of the convective terms. Following the work of McGuirk and Page (1990), Lien and Leschziner (1993) recently presented a new algorithm by introducing the *biased density* which is directly used to compute mass fluxes. The biasing function has the same structure of that for the biased pressure, but is generalized for two dimensional complex flow. This latest formulation was applied in complex flows in conjunction with turbulence models.

More recently, Michelassi (1994b) presented a simple way to include compressibility effects in a pressure correction algorithm by using a blended density biasing which allows retaining u, and not ρu, as the main variable. This was done starting from an existing computer code FAST-3D (F-low A-nalysis S-imulation T-ool of 3-D) developed at the Institute of Hydromechanics, University of Karlsruhe (Zhu, 1992), which had been previously used to compute a variety of incompressible flows in complex geometries. The performance of this modified pressure-correction scheme is evaluated by comparison with a time marching method FLOS3D (FLO-w S-olver in 3-D) developed at the Energetics Department, University of Florence. Both FLOS3D and FAST-3D are capable of computing three-dimensional flow fields, eventhough the present study is considering only two-dimensional configurations. The compressible modification to the pressure-correction method presented here however, is extendable to and already implemented for three-dimensional computations.

The present study considers both inviscid and viscous flows, with the latter case being treated by two different turbulence models, one for each code, namely the k-ε (Launder and Spalding, 1974) and the k-ω (Wilcox, 1988) models.

MATHEMATICAL FORMULATION

Although both FLOS3D and FAST-3D are 3D codes, herein they will be used for solving 2D flows. The codes differ in the choice of the transport equation for energy. For inviscid flows FAST-3D replaces the energy equation with a simple constant total enthalpy relation ($h_0 = \overline{h_0}$), whereas FLOS3D maintains the inviscid version of the transport equation for the total specific energy e. Accordingly, the governing equations for steady two-dimensional, compressible flows in a Cartesian coordinate system are written in the following conservative form.

Inviscid Flow

$$\alpha \cdot \frac{\partial Q}{\partial t} + \frac{\partial F}{\partial x} + \frac{\partial G}{\partial y} = 0 \qquad (1)$$

in which α=1 for FLOS, α=0 in FAST, and

$$Q = \begin{bmatrix} \rho \\ \rho u \\ \rho v \\ e \end{bmatrix}, \; F = \begin{bmatrix} \rho u \\ p + \rho u^2 \\ \rho uv \\ u(e+p) \end{bmatrix}, \; G = \begin{bmatrix} \rho v \\ \rho vu \\ p + \rho v^2 \\ v(e+p) \end{bmatrix} \qquad (2)$$

The fourth equation in FAST-3D is replaced by $\widetilde{h_0} = C_p T + \frac{u^2}{2}$, while in FLOS3D the quantity "e" is the specific total energy defined as $e = \frac{p}{\gamma - 1} + \frac{\rho}{2}\left(u^2 + v^2\right)$.

Viscous Flow

In viscous flows FAST-3D cannot retain the costant total enthalpy relation, which is replaced by a transport equation for the internal energy written directly in terms of static temperature. This choice allows for better coupling with the pressure correction step. The viscous transport equation reads:

$$\alpha \cdot \frac{\partial Q}{\partial t} + \frac{\partial F^v}{\partial x} + \frac{\partial G^v}{\partial y} = \frac{\partial F_d^v}{\partial x} + \frac{\partial G_d^v}{\partial y} + S \qquad (3)$$

in which:

$$Q = \begin{bmatrix} \rho \\ \rho u \\ \rho v \\ E_Q \\ \rho k \\ \rho d \end{bmatrix}, \quad F = \begin{bmatrix} \rho u \\ p + \rho u^2 \\ \rho uv \\ uE \\ \rho uk \\ \rho ud \end{bmatrix}, \quad G = \begin{bmatrix} \rho v \\ \rho uv \\ p + \rho v^2 \\ vE \\ \rho vk \\ \rho vd \end{bmatrix} \qquad (4)$$

$$F_d = \begin{bmatrix} 0 \\ \tau_{xx} \\ \tau_{xy} \\ C_{en}(\partial T/\partial x) \\ \left(\frac{\mu_{eff}}{\sigma_k}\right)(\partial k/\partial x) \\ \left(\frac{\mu_{eff}}{\sigma_d}\right)(\partial d/\partial x) \end{bmatrix}, \quad G_d = \begin{bmatrix} 0 \\ \tau_{yx} \\ \tau_{yy} \\ C_{en}(\partial T/\partial y) \\ \left(\frac{\mu_{eff}}{\sigma_k}\right)(\partial k/\partial y) \\ \left(\frac{\mu_{eff}}{\sigma_d}\right)(\partial d/\partial y) \end{bmatrix}, \quad S = \begin{bmatrix} 0 \\ 0 \\ 0 \\ S_E \\ S_k \\ S_d \end{bmatrix} \qquad (5)$$

For turbulent flows FAST-3D solves for the standard high-Reynolds number version of the k-ε model (Launder and Spalding, 1974), and FLOS3D implements the high-Reynolds number version of the k-ω model by Wilcox (1988), so that the terms in equations (4) and (5) are:

$$\text{FLOS:} \begin{cases} C_{en} = \frac{\gamma}{\gamma - 1} \cdot \left(\frac{\mu}{Pr} + \frac{\mu_t}{Pr_t}\right), \; E_Q = e, \; E = (e + p), \\ S_E = \Phi, \; S_k = P_k - 0.09\rho\omega k, \; S_d = \frac{5}{9} P_k \frac{\omega}{k} - \frac{3}{40}\rho\omega^2 \\ d = \omega = (\varepsilon/k), \; \alpha = 1, \; \sigma_k = 2, \; \sigma_d = 2, \; \mu_t = \frac{\rho k}{\omega} \end{cases}$$

$$\text{FAST:} \begin{cases} C_{en} = \gamma \cdot \left(\frac{\mu}{Pr} + \frac{\mu_t}{Pr_t}\right), \; E = \rho T, \; d = \varepsilon, \; S_k = P_k - \rho\varepsilon \\ S_d = \frac{1}{C_v}\left(p(\nabla \cdot \bar{v}) + \Phi\right), \; S_\varepsilon = 1.44 \cdot P_k(\varepsilon/k) - 1.92 \cdot \left(\varepsilon^2/k\right) \\ \alpha = 0, \; \sigma_k = 1, \; \sigma_d = 1.3, \; \mu_t = 0.09\frac{\rho k^2}{\varepsilon} \end{cases}$$

The viscous stresses are written as:

$$\tau_{ij} = \mu_{eff}\left[\left(\frac{\partial u_i}{\partial x_j} + \frac{\partial u_j}{\partial x_i}\right) - \frac{2}{3}\delta_{ij}(\nabla \cdot \bar{v})\right], \quad \mu_{eff} = \mu + \mu_t$$

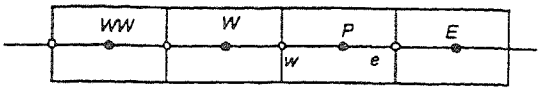

FIGURE 1. COLLOCATED GRID ARRANGEMENT

in which i=1,2, j=1,2, and δ_{ij} is the Kronecker delta, while P_k is the production of turbulent kinetic energy defined as:

$$P_k = \left\{\mu_t\left[\left(\frac{\partial u_i}{\partial x_j} + \frac{\partial u_j}{\partial x_i}\right) - \frac{2}{3}\delta_{ij}\left(\nabla \cdot \bar{V}\right)\right] - \frac{2}{3}\delta_{ij}k\right\}\frac{\partial u_j}{\partial x_i} \qquad (7)$$

The Cartesian equations are further transformed to a curvilinear system by the usual chain rule expansion.

THE NUMERICAL SCHEMES

The pressure correction solver

As previously mentioned, the compressible pressure-correction solver is developed based on the FAST-3D code by Zhu (1992). This code is designed for the simulation of internal complex incompressible flows. Since the incompressible formulation is largely left unaltered for compressible fluids, a brief description of the original solver is given.

The equations are discretized by using finite volumes in three dimensions. The code uses a collocated variable arrangement, so that all the transported quantities are defined at the control volume centre. Convection can be treated by using the standard hybrid technique or the low-diffusive scheme, named HLPA, developed by Zhu (1991), which largely decreases the extra numerical diffusion brought by the hybrid scheme, but is more stable than other existing second order upwind schemes. This convection scheme for a generic quantity ϕ is similar to the harmonic TVD scheme by Van Leer and for a positive velocity can be formulated as:

$$\phi_w = \phi_W + \gamma_w\left(\phi_p - \phi_W\right)\frac{\left(\phi_W - \phi_{WW}\right)}{\left(\phi_p - \phi_{WW}\right)} = \phi_W + \gamma_w\left(\phi_p - \phi_W\right)\hat{\phi}_W$$

in which

$$\gamma_w = \begin{cases} 1 \text{ if } \left|\hat{\phi}_W - 0.5\right| < 0.5 \\ 0 \text{ otherwise} \end{cases}$$

and the subscripts P, w, W, and WW are defined in figure 1.

This scheme prevents from overshoots of the transported quantities for momentum and scalar transport. The cell centre location of the transported variable would require a linear interpolation to get the cell face values for the discretization of the mass conservation equation. This practice produces the well known unphysical chequerboard pattern for the static pressure and cannot be retained in the pressure-correction equation. Accordingly, equation (2) is first modified to get the pressure-correction equation following the idea by Patankar(1980) for the SIMPLE family of algorithms. The staggered grid approach,

which was found capable of removing the pressure chequerboard pattern, is here replaced by the central scheme in which the cell face velocities are computed by the momentum interpolation technique of Rhie and Chow (1983). For further details about the incompressible fluid code see Zhu (1992).

Compressibility Correction. The modification of the incompressible flow solver is done following the proposal of Michelassi (1994b) who follows the basic guideline highlighted by Karki and Patankar (1989) by writing 1-D the mass conservation in one-dimensional flow as follows:

$$\left(\rho_e^* + \rho_e'\right)\left(u_e^* + u_e'\right)\Gamma_e - \left(\rho_w^* + \rho_w'\right)\left(u_w^* + u_w'\right)\Gamma_w = 0 \qquad (8)$$

in which the guessed density and velocity fields are starred and the primed variables are introduced as corrections to the guessed field to ensure continuity, and Γ is the cell surface. Equation (8) is rewritten as:

$$\underbrace{\left(\rho_e^* u_e^* \Gamma_e - \rho_w^* u_w^* \Gamma_w\right)}_{T0} + \underbrace{\left(\rho_e^* u_e' \Gamma_e - \rho_w^* u_w' \Gamma_w\right)}_{T1} + \underbrace{\left(\rho_e' u_e^* \Gamma_e - \rho_w' u_w^* \Gamma_w\right)}_{T2} + \underbrace{\left(\rho_e' u_e' \Gamma_e - \rho_w' u_w' \Gamma_w\right)}_{T3} = 0 \qquad (9)$$

in which the pressure density link is given by the perfect gas relation:

$$\rho' = \frac{p'}{RT}$$

under the hypothesis of an isothermal transformation.

The T0+T1 term is the usual incompressible contribution and the T3 term is normally neglected (linearization). The T2 term introduces the compressibility effects. While for subsonic flows T2 can be discretized by using a central scheme, this cannot be done in transonic or supersonic flows when this elliptic equation should have a dominat hyperbolic nature.

Karki and Patankar (1989) propose to use a pure upwinding for the density in the T2 term in order to introduce only the upstream influence on the pressure. Mc Guirk and Page (1990), and Lien and Leschziner (1993) indicate that using first order density upwinding is mainly responsible for the poor shock capturing ability. Following the suggestion of Mc Guirk and Page, Michelassi (1994b) introduces a biasing function to weigh the upstream influence of the density change. The biasing function for a one dimensional positive velocity flow is defined as:

$$\mu = \max\left(0, k\left[1 - \left(\frac{M_{ref}}{M}\right)^2\right]\right) \qquad (10)$$

in which k= 1, $M_{ref} \approx 1$, and M is the local Mach number. Accordingly, one can define the biased value of a generic quantity φ on a face upstream of a node P (see figure 1) as:

$$\tilde{\varphi}_w = (1-\mu_w)\varphi_P + \mu_w \varphi_W$$

The biasing function determines the amount of density upwinding, if any, that should be brought inside the solution, depending on the local Mach number. This simple biasing concept, retained by Lien and Leschziner (1993), may be directly applied to the original approach by Karki and Patankar (1989) with only minor changes. In place of the first order upwind, a blended linear-upwind interpolation is introduced. The corrected scheme for the computation of the cell face density changes in the T2 term of equation (9) reads:

$$\rho_w' = \frac{1}{R}\left\{ (1-\mu_w)\underbrace{\left[f_x \frac{p_P'}{T_P} + (1-f_x)\frac{p_W'}{T_W}\right]}_{\text{linear interpolation}} + \mu_w \underbrace{\left[M_P^+ \frac{p_W'}{T_W} + M_P^- \frac{p_P'}{T_P}\right]}_{\text{upwind}} \right\}$$

$$\rho_e' = \frac{1}{R}\left\{ (1-\mu_e)\underbrace{\left[f_x^+ \frac{p_E'}{T_E} + (1-f_x^+)\frac{p_P'}{T_P}\right]}_{\text{linear interpolation}} + \mu_e \underbrace{\left[M_P^+ \frac{p_P'}{T_P} + M_P^- \frac{p_E'}{T_E}\right]}_{\text{upwind}} \right\} \qquad (11)$$

in which:

$$M_P^+ = \frac{1+\mathrm{sgn}(M_P)}{2}, \qquad M_P^- = \frac{1-\mathrm{sgn}(M_P)}{2}$$

and

$$M_P = \frac{U_P}{a_P} = \frac{U_P}{\sqrt{\gamma R T}}$$

U_P is the local velocity module, and

$$\mathrm{sgn}(\varphi) = \begin{cases} +1 & \text{for } \varphi \geq 0 \\ -1 & \text{for } \varphi < 0 \end{cases}$$

The terms f_x and f_x^+ are the linear interpolation factors for the w-p and p-e intervals respectively, and the velocities u on the cell faces are linearly interpolated using the cell centre values. In equation (11), a linearly interpolated density on the cell face is obtained for subsonic flow conditions when $\mu_e = \mu_w = 0$, yielding an elliptic pressure correction equation. For supersonic flows the density is upwinded, thereby increasing the hyperbolic nature of equation (9). By selecting appropriate k and M_{ref} values in equation (10) it is possible to switch smoothly from the linear interpolation to the upwinding as the Mach number increases. So, after some algebra and keeping the equation stencil proposed by Patankar (1980), the discretized form of the continuty equation (9) may be written as:

$$A_P p_P' = A_W p_W' + A_E p_E' + b \qquad (12)$$

in which:

$$A_W = A_W^{T1} + A_W^{T2} = A_W^{T1} + \frac{\Gamma_w u_w}{R}\frac{1}{T_W}\left[(1-\mu_w)(1-f_x) + \mu_w M_P^+\right]$$

$$A_E = A_E^{T1} + A_E^{T2} = A_E^{T1} - \frac{\Gamma_e u_e}{R}\frac{1}{T_E}\left[(1-\mu_e)f_x^+ + \mu_e M_P^-\right]$$

$$A_P = A_P^{T1} + A_P^{T2} = A_P^{T1} - \frac{\Gamma_w}{T_P}\left\{\frac{u_w}{R}\left[(1-\mu_w)f_x + \mu_w M_P^-\right]\right\} + \frac{\Gamma_e}{T_P}\left\{\frac{u_e}{R}\left[(1-\mu_e)(1-f_x^+) + \mu_e M_P^+\right]\right\}$$

$$b = \rho_w^* u_w^* \Gamma_w - \rho_e^* u_e^* \Gamma_e$$

and Γ_w and Γ_e are the cell face areas, u_W and u_e the cell face velocities obtained by momentum interpolation.

Observe that the contribution A^{T1} to the pressure-correction equation is the unaltered incompressible term in which the momentum interpolation is used for the velocity.

The cell face mass fluxes must be computed with the same biased density adopted for the continuty equation (9) and maintaining the momentum interpolation for the velocity. This is accomplished by defining the biased densities as follows:

$$\tilde{\rho}_w = \rho_w^l(1-\mu_w) + \mu_w\left(\rho_W M_P^+ + \rho_P M_P^-\right)$$

$$\tilde{\rho}_e = \rho_e^l(1-\mu_e) + \mu_e\left(\rho_E M_P^- + \rho_P M_P^+\right)$$

in which ρ^l represents the density linearly interpolated on the cell face. Further details about the compressible pressure-correction solver may be found in Michelassi (1994b).

The Time Marching Solver

The FLOS3D program is based on the scalar implicit approximate factorization proposed by Pulliam and Chaussée (1981). The program solves three-dimensional compressible flows with complex boundaries in inviscid, laminar and turbulent regime. This algorithm is less computational costly than the standard approximate factorization (Beam and Warming, 1982) and it retains the intrinsic robustness of the original algorithm for internal viscous flows (Michelassi et al., 1990, 1993), but decreases the number of operations per grid point. The original formulation by Pulliam and Chaussee drops the viscous contribution to the implicit space operator, which renders the solver weak for internal viscous flows. To render the algorithm more efficient in the presence of viscous boundary layers the implicit side of equation (13) is assembled to account for an approximate expression of the viscous eigenvalues. The modified algorithm reads:

$$T_\xi\cdot\left[I+\theta\Delta t\left(\delta_\xi\Lambda_\xi - \delta_\xi^2\Lambda_\xi^v\right)\right]\cdot N\cdot\left[I+\theta\Delta t\left(\delta_\eta\Lambda_\eta - \delta_\eta^2\Lambda_\eta^v\right)\right]\cdot P\cdot \left[I+\theta\Delta t\left(\delta_\zeta\Lambda_\zeta - \delta_\zeta^2\Lambda_\zeta^v\right)\right]\cdot T_\zeta^{-1}\cdot\Delta Q = RHS \qquad (13)$$

in which $\Delta Q = Q^{n+1} - Q^n$, the matrices $N = T_\xi^{-1}T_\eta$ and $P = T_\eta^{-1}T_\zeta$ are solution independent, δ is the central difference operator, and Θ allows weighting of the explicit-implicit nature of the space operator in round brackets. The eigenvalue vectors read:

$$\Lambda_{x,y,z} = \begin{bmatrix} U_{x,y,z} \\ U_{x,y,z} \\ U_{x,y,z} \\ U_{x,y,z} + a\sqrt{m_{x,y,z}^2} \\ U_{x,y,z} - a\sqrt{m_{x,y,z}^2} \end{bmatrix} \qquad \Lambda_{x,y,z}^v = \begin{bmatrix} 0 \\ \rho\mu_{eff}\left(m_{x,y,z}^2\right) \\ \rho\mu_{eff}\left(m_{x,y,z}^2\right) \\ \rho\mu_{eff}\left(m_{x,y,z}^2\right) \\ \gamma\rho\mu_{eff}\left(m_{x,y,z}^2\right) \end{bmatrix}$$

in which $U_{x,y,z}$ are the unscaled contravariant velocity, and m are metric terms. Further details about the eigenvector matrices may be found in Pulliam and Chaussbée (1981) and in Michelassi et al. (1990).

Local time stepping and artificial damping. The implicit solver requires the solution of scalar tridiagonal matrices because of the centered space discretization. The approximate factorization technique may have stability and wiggles problems in presence of shocks or, in general, of sharp gradients yielding to non-diagonal-dominat matrices. These problems may be overcome by introducing the artificial damping terms as proposed by Jameson et al. (1981) on both the implicit and the explicit sides of the operator for equation (13). The non-linear artificial second plus fourth order damping formulation is the one by Jameson et al.(1981). Equation (13) of the implicit solver is modified as follows:

$$T_\xi\left\{I+\theta\Delta t\left[\delta_\xi\Lambda_\xi - \left(\delta_\xi^2\Lambda_\xi^v + \delta_\xi\left(\Omega^\xi\,\omega_\xi^2\,\delta_\xi(J)\right)\right) + \delta_\xi\left(\Omega^\xi\,\omega_\xi^4\,\delta_\xi^3(J)\right)\right]\right\}\cdot N\left\{I+\theta\Delta t\left[\delta_\eta\Lambda_\eta - \left(\delta_\eta^2\Lambda_\eta^v + \delta_\eta\left(\Omega^\eta\,\omega_\eta^2\,\delta_\eta(J)\right)\right) + \delta_\eta\left(\Omega^\eta\,\omega_\eta^4\,\delta_\eta^3(J)\right)\right]\right\}\cdot P\left\{I+\theta\Delta t\left[\delta_\zeta\Lambda_\zeta - \left(\delta_\zeta^2\Lambda_\zeta^v + \delta_\zeta\left(\Omega^\zeta\,\omega_\zeta^2\,\delta_\zeta(J)\right)\right) + \delta_\zeta\left(\Omega^\zeta\,\omega_\zeta^4\,\delta_\zeta^3(J)\right)\right]\right\}\cdot T_\zeta^{-1}\cdot\Delta Q = \Delta t\left(-\frac{\partial F_k}{\partial x_k} + \frac{\partial F_k^v}{\partial x_k} + D_k^2 - D_k^4\right)^n \qquad (14)$$

The terms D_k^2 and D_k^4 are second and fourth order differences of the transported quantities given by vector Q. In the i-direction these extra terms are discretized as follows:

$$D_i^2 = \nabla_i\left(\Omega_{i,j,k}^\xi\,\omega_{i,j,k}^2\right)\Delta_i\left(J\,Q_{i,j,k}\right)$$

$$D_i^4 = \nabla_i\left(\Omega_{i,j,k}^\xi\,\omega_{i,j,k}^4\right)\Delta_i\nabla_i\Delta_i\left(J\,Q_{i,j,k}\right)$$

in which Δ and ∇ are forward and backward difference operators respectively. The Ω terms represent a directional scaling dependent of the directional spectral radius which in three dimensions is:

$$\Omega^\xi = \lambda_\xi + \left(\lambda_\eta^\sigma + \lambda_\zeta^\sigma\right)\cdot\lambda_\xi^{(1-\sigma)} \qquad \Omega^\eta = \lambda_\eta + \left(\lambda_\xi^\sigma + \lambda_\zeta^\sigma\right)\cdot\lambda_\eta^{(1-\sigma)}$$

$$\Omega^\zeta = \lambda_\zeta + \left(\lambda_\xi^\sigma + \lambda_\eta^\sigma\right)\cdot\lambda_\zeta^{(1-\sigma)}$$

The spectral radius is defined as:

$$\lambda_{x,y,z} = \left|U_{x,y,z}\right| + a\sqrt{m_{x,y,z}^2}$$

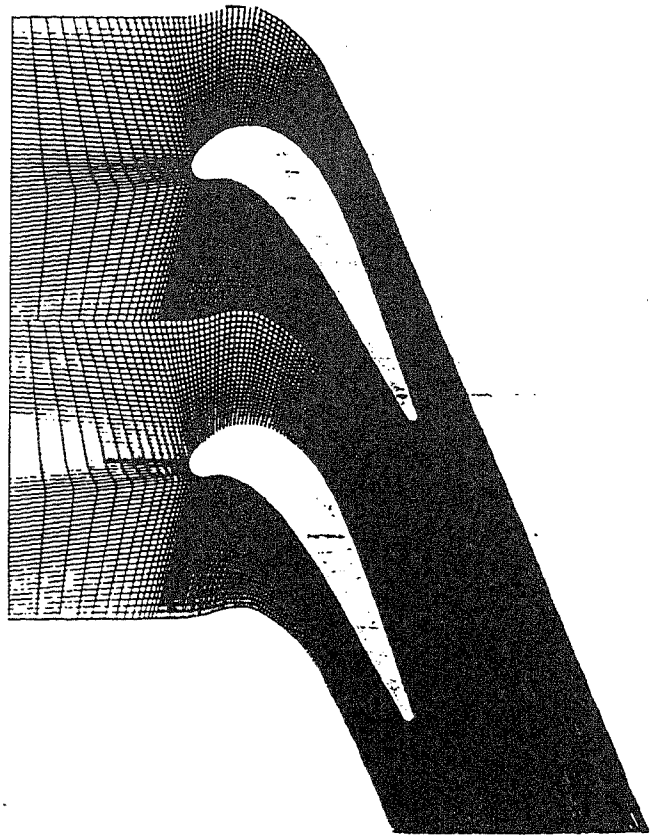

FIGURE 2. TYPICAL I-TYPE GRID FOR THE NUOVOPIGNONE TURBINE BLADE.

The ω^2 and ω^4 coefficients are the artificial terms weights which are computed according to Jameson et al., (1981). Details about the boundary treatment of the artificial damping may be found in Michelassi et. al. (1994b).

The local time step formula includes the viscous contribution. After intense numerical testing the following expression was found to ensure the best convergence rates:

$$\Delta t = \frac{CFL}{1/\Delta t_{conv} + 1/\Delta t_{diff}}$$

in which the convective and diffusive time steps are defined as:

$$\Delta t_{conv} = \frac{1}{|U_\xi| + |U_\eta| + |U_\zeta| + a\sqrt{\xi_x^2+\xi_y^2+\xi_z^2+\eta_x^2+\eta_y^2+\eta_z^2+\zeta_x^2+\zeta_y^2+\zeta_z^2}}$$

$$\Delta t_{diff} = \frac{1}{C_d \frac{\mu_{eff}}{Re}\left(\xi_x^2+\xi_y^2+\xi_z^2+\eta_x^2+\eta_y^2+\eta_z^2+\zeta_x^2+\zeta_y^2+\zeta_z^2\right)}$$

C_d allows weighting the viscous term contribution. Best results are obtained with C_d ranging between 1. and 2.5, and $10 \leq CFL \leq 20$.

Grid Generation and Periodic Boundaries.

When retaining the structured grid approach, the discretization of the flow domain around a turbine blade is usually done by using H, C, or O-type grids. The H-type grid is probably better suited for compressor blades because of the poor grid resolution normally obtained in the presence of a thick leading and trailing edges. The leading edge can be conveniently discretized by using a C grid, which, conversely, has the same poor resolution close to the trailing edge than that given by a standard H grid. The O-grid is the best approach as long as a good discretization of the leading and trailing edges is concerned, but generally requires a patched grid approach to allow a proper discretization of the wake region. A good compromise between the three is the so called I-type grid in which the blade is placed inside the computational grid by blocking a number of grid nodes. Figure 1 shows the typical structure of the grid utilized for the present set of calculations which is generated by using the program MESHHO (Michelassi, 1994a). Observe that the blade is placed inside the domain and that the grid is defined inside the blade as well. Althouhg the blocked grid nodes represent a computational overhead, one must observe that this grid structure is potentially able to cope with coolant injection or blade cooling problems.

The periodic boundaries show a non-periodic point distribution. This choice allows having nearly orthogonal grids in the wake region, but requires a special treament of the periodic boundaries. In order not to spoil the high vectorization of both FLOS and FAST, the first code adds two control volumes on both the periodic boundaries, whereas the second adds only one on each side, and solve for the interior domain only. This practice does not have any computational overhead. The solution is then interpolated to have a periodic flow field. Details about the method can be found in Michelassi and Bruzzi (199[illegible]).

RESULTS AND DISCUSSION

Flow over a 4% circular bump M_{ex}=1.4

A wide set of preliminary tests included the transonic flow in a nozzle, and the flow past 10% and 4% bumps. For brevity only the latter will be discussed here. The flow past a 4% bump with M_{ex}=1.4 is computed by using a 80×21 points grid. The test is particularly significative because it allows for verifying the shock capturing ability of the time marching and pressure-correction schemes, in the presence of shock reflection and intersection. The two codes in this simple geometry exhibited similar convergence rates. For what concerns the artificial damping terms one should remember that for the time marching code the only source of smoothing is the non-linear second-plus-fourth order terms described in equation (14). Conversely, the pressure-correction solver has multiple sources of artificial damping, namely the TVD scheme for the convective terms, the momentum interpolation for the discretization of the pressure-correction equation, and the density biasing in the compressible terms. The non-linear damping scheme by Jameson shows a larger flexibility in the presence of shocks. In fact the relative

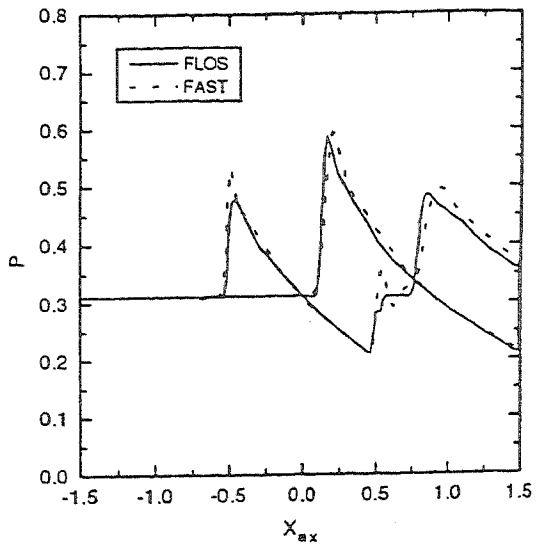

FIGURE 3. 4% BUMP MEX=1.4.

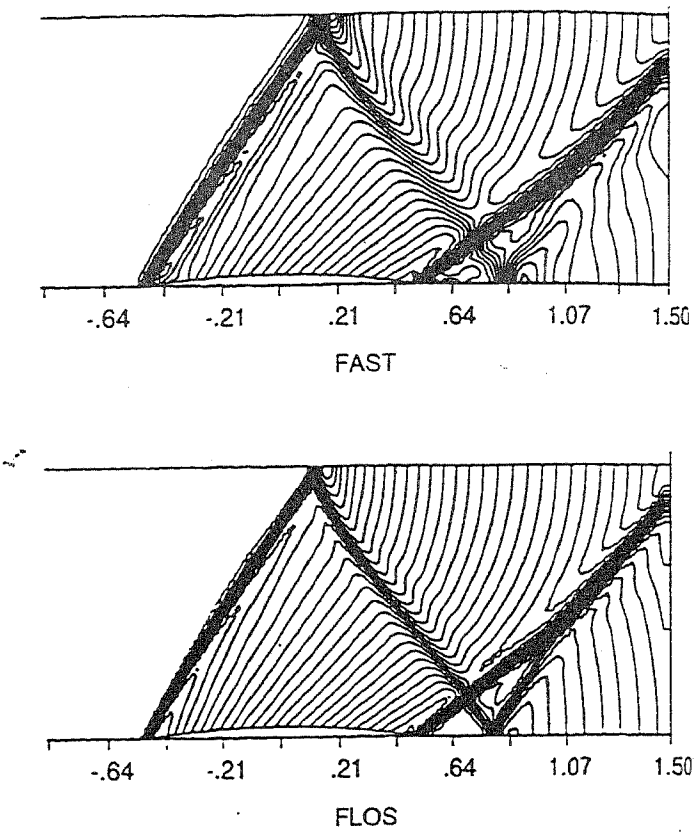

FIGURE 4. 4% BUMP M_{EX}=1.4: PRESSURE ISOLINES.

importance of the second and fourth order damping can be easily adjusted to ensure the proper damping expecially at the foot of the shock.

Figure 3 shows the computed pressure profiles on the walls of a straight channel with a 4% circular arc bump. The plot shows that the Jameson's scheme allows for controlling the pressure jumps across the shocks, without producing any significant shock smearing. Conversely, the density biasing as implemented in the pressure-correction solver, together with the HLPA convection scheme, still exhibits some oscillations which are more evident at x_{ax}=0.5. These pressure instabilities are not properly filtered by the biasing function, although the problem remains local and does not introduce any stability limitation. In particular, it was not possible to find values of M_{ref} and k in equation (10) which removed the pressure jumps at the shock foot. When using a first order upwind discretization scheme these jumps disappear, but the large amout of momentum diffusion smears the shock out.

Figure 4 shows that, although there are no differences in the overall shock pattern, FLOS gives somewhat sharper shocks, and cleaner reflections, especially in the region downstream of the bump, where the departing and reflected shock waves merge together.

Flow in a Transonic Turbine Rotor Blade

The transonic flow in the turbine guide vane designed by NuovoPignone (NP) represents a much more interesting test case. In fact the presence of stagnation points and of shocks departing from the trailing edge of the blade make this computation particularly suited for comparing two completely different approaches. The blade profile was designed by NuovoPignone for the PGT2 power turbine and tested to work under a wide range of exit Mach numbers, which are varying between 0.3 to 1.6. In this range the blade does not exhibit any appreciable stall and the profile losses are below 6-7%. The blade has a thin trailing edge, but the profile in the accelerating part of the flow shows a marked thickening of the boundary layer on the suction side. The measurements where performed both at the University of Florence for the low speed cases and at CNPM-Milan for the high speed cases and are reported in Bruzzi (1992). Figure 2 shows a typical I-grid used for inviscid calculations. The grid has 200×63 points with both the leading and trailing edge regions discretized by a nearly orthogonal grid. The grid is approximately aligned with the inlet and outlet flow angles which are 33-deg and 69-deg respectively.

The simulations were carried out at M_{ex}=0.7,0.9,1.07,1.3,1.6 to cover a significative operational range. At M=0.7 the flow already shows a sonic line located approximately at 25% of the chord, but the flow remains shock free. At M_{ex}=0.9 a shock is detected at approximately 30% of the chord with a strong recompression which terminates at 55% of the chord. In supersonic flow regime (M_{ex}=1.3,1.6), the shock is clearly located further downstream. The measurments show that the static pressure remains substantially constant downstream of the shock till the trailing edge. The experiments also show that the M_{ex}=1.6 case is very close to the limit loading since the shock reaches the suction side in proximity to the trailing edge.

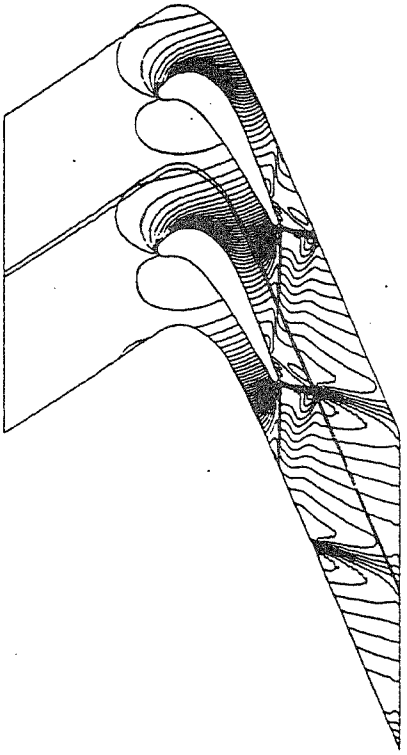

a) FAST - Inviscid, M_{ex}=1.6 (grid 200x63)

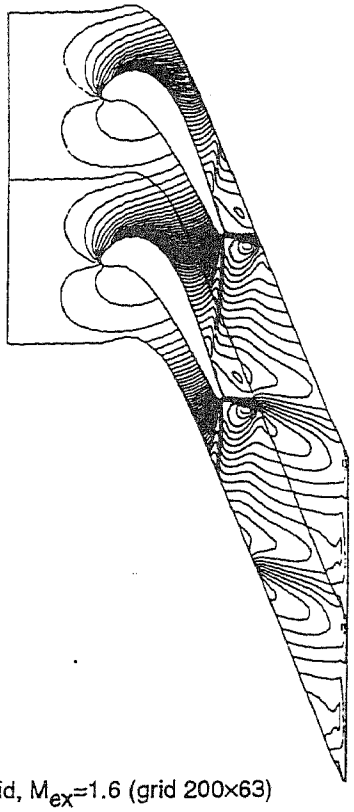

b) FLOS - Inviscid, M_{ex}=1.6 (grid 200x63)

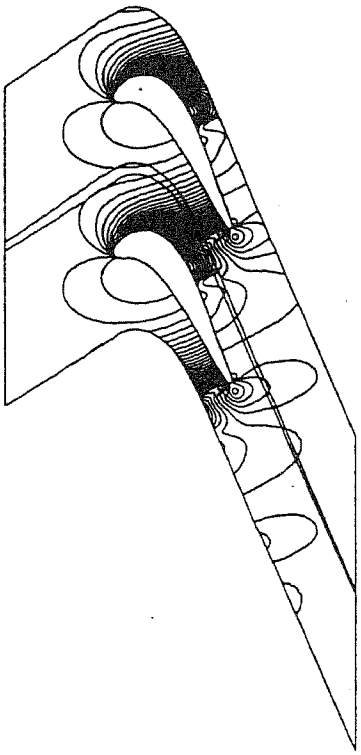

c) FAST - Turbulent, M_{ex}=0.9 (grid 200x75)

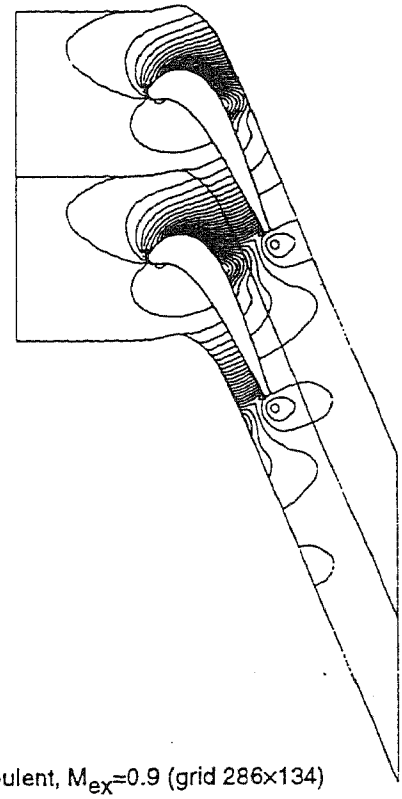

d) FLOS - Turbulent, M_{ex}=0.9 (grid 286x134)

FIGURE 5 NP BLADE: PRESSURE ISOLINES

A first set of tests were performed using the inviscid formulation so as to avoid the influence of the turbulence model on the results. In these tests the time marching code was run with CFL=15-20, with ω_2=1/8 and ω_4=1/64 for the artificial damping terms (see equation (14)), while ω_2=1 was used for the M_{ex}=1.3 and 1.6 cases. The pressure-correction code was run using the HLPA convection scheme and selecting M_{ref}=0.9, k=1 in the density biasing function (see equation (10)).

Figure 5 shows a first qualitative comparison between the pressure isolines predicted by the two codes. The plots 5a and 5b compare the inviscid M_{ex}=1.6 case. The shock pattern is very similar for the two codes, although the shock reflection on the suction side appear a bit more defined in the pressure-correction algorithm. This is due to the high second order damping weight necessary to ensure the stability of the time marching code. While a reduction of ω_2 could probably increase the sharpness of the shock, it would produce large pressure spikes at the thin trailing edge. The two codes suffer from a consistent shock smearing across the periodic boundary which is due to the sudden change in grid spacing while approaching the exit section. Observe that in FAST the shocks are departing a bit downstream of the t.e. due to a small t.e. recirculation bubble, which is absent in the predictions by FLOS.

Figures 5c and 5d compare the computed pressure isolines at M_{ex}=0.9 in turbulent flow regime. The weak shock can be hardly detected in both the plots, but the pattern is very similar although, again, the shock reflection is neater in the pressure-correction solver.

The qualitative impressions gathered looking at figure 5 can be verified by observing figure 6 which compares the computed isentropic Mach number profiles on the blade with the measurements along the chord C. On the pressure side both the time marching and the pressure-correction codes closely follow the measurements. On the suction side for M_{ex}=0.7 the computed profiles overlap with the measurements. Some differences arise at M_{ex}=0.9 where the two codes give somewhat different shocks. In fact, although the position of the shock is the same for both the codes, FLOS tends to smoothen the shock especially in the recompression region. In this complex pattern it is interesting to observe the presence of a small pressure undershoot at the foot of the shock for both the codes, which is also evident in figure 8. This indicates that there are no large overall differences between the two damping schemes. The shock strength is overestimated by both codes, but this is consistent with the inviscid formulation in which the absence of the viscous terms removes the only physical source of smoothing.

In the supersonic flow regime (figure 7), the differences become more evident. At M_{ex}=1.3 the time marching code predicts the correct base pressure dowstream of the shock, but misses the M_{is} peak located at X/C=0.6, while the pressure-correction solver gives the right acceleration, but fails to reproduce the correct base pressure level. This behavior is clearly caused by the density biasing function, as in the 4% bump case, where the density biasing method predicts large pressure changes across the shock with respect to the profiles obtained by using the scheme proposed by Jameson. In this turbine blade case FAST also locates the shock downstream of the position indicated by FLOS. This tendency is repeated for M_{ex}=1.6, where the differences are not so evident like in the M_{ex}=1.3 case. It is important to observe that the intensity of the shock smearing can be controlled in FLOS by selecting appropriate values of ω_2. A wide set of tests performed by Michelassi (1994b) indicated that the density biasing method does not have the flexibility granted by the mixed second-plus-fourth order damping, insofar as the shock pattern is not very much sensitive to the changes in M_{ref} and k.

In the turbulent flow regime FAST implements the standard high Reynolds number version of the k-ε method, whereas FLOS introduces the k-ω model by Wilcox (1988). The totally different nature of the turbulence models require different grids. In fact FAST bridges the viscous and buffer layers around the blade by using standard wall functions, whereas FLOS requires a strong mesh point clustering in proximity of the wall. Thereby the grid utilized by FAST has 200×75 points, while FLOS uses a 286×134 point grid which allows placing the first grid away from the wall at approximately y^+=1.

Figure 8 shows the Mis profiles predicted by the two solvers for M_{ex}=0.7 and 0.9. For the lower Mach number the time marching code shows a weaker throat acceleration with respect to FAST which is in better agreement with experiments. This behavior is induced by the k-ω model which seems to give higher losses with respect to the k-ε model. When moving to the M_{ex}=0.9 case the computations show large changes with respect to the inviscid flow. FLOS predicts a smooth recompression downstream of the shock which is in qualitative good agreement with experiments. FAST gives a sharper shock, and the peak in Mis in good agreement with experiments, although the recompression downstream is too sharp. Observe that the shock strength is largely controlled by the size of the recirculation bubbles downstream of the trailing edge. The difference in the grid side and turbulence model in this crucial region may well explain the different shock strengths. Despite the differences in the shock capturing, the two codes predict identical pressure levels after the recompression. In the supersonic regime, the pressure-correction algorithm exhibited some stability problems because of the early development of large supersonic bubbles. The FAST code could be run up to M_{ex}=1.07, while FLOS showed no limitations in the exit Mach number. Figure 9 shows the comparison of the predictions and experiments at M_{ex}=1.07 and 1.3. The profile computed by FAST at M_{ex}=1.07 is not in good agreement with experiments which indeed are not very much reliable for this transonic flow case, as can be concluded by the fluctuations in the measured base pressure values (Bruzzi, 1992). At M_{ex}=1.3 the predictions by FLOS are in excellent agreement with experiments, although the flat pressure region downstream of the shock, which indicates a growth of the boundary layer, is not properly reproduced. Figure 10 shows the mass averaged exit flow angles for the turbulent flow regime computations. The plot shows that the exit flow angle is predicted with the accuracy of approximately 0.5-deg. FLOS predictions fit remarkably well with the experiments, especially for the transonic and supersonic exit Mach numbers. Observe that the presence of shocks does not affect the accuracy of the predictions. A closer view of the code predictions is given by figure 11 in which the flow angle profiles are compared at the exit of the computational domain. For M_{ex}=0.7 the differences stay in the range of approximately 0.25-deg indicating the coincidence of the flow patterns predicted by the two codes. The same remarks apply to the M_{ex}=0.9 case shown in the same

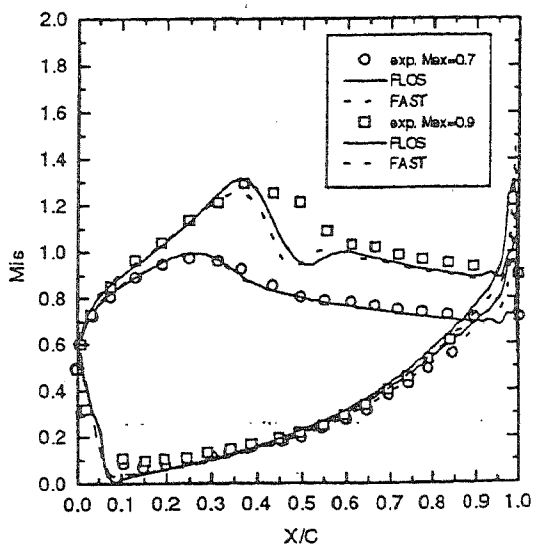

FIGURE 6. NP BLADE: ISENTROPIC MACH NUMBER DISTRIBUTION - SUBSONIC INVISCID FLOW.

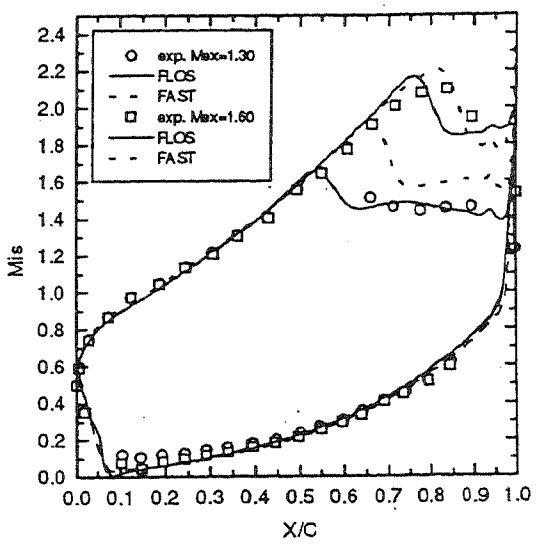

FIGURE 7. NP BLADE: ISENTROPIC MACH NUMBER DISTRIBUTION - SUPERSONIC INVISCID FLOW.

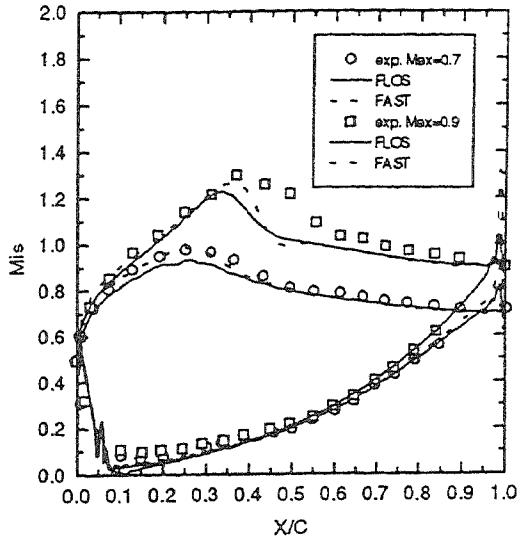

FIGURE 8. NP BLADE: ISENTROPIC MACH NUMBER DISTRIBUTION - SUBSONIC TURBULENT FLOW.

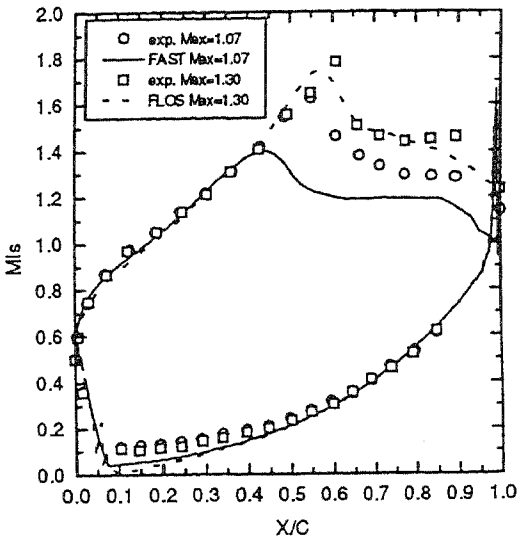

FIGURE 9. NP BLADE: ISENTROPIC MACH NUMBER DISTRIBUTION - SUPERSONIC TURBULENT FLOW.

figure. The predicted total pressure losses are compared with the experimental values in figure 12. The measured losses are a two-dimensional estimate, considering that the two-dimensionality of the flow at the midspan section was checked. Since the total pressure losses may be altered by mass conservation errors, both the codes were run until the overall mass error dropped by five orders of magnitude with respect to the inital guess. The predictions by FLOS are in good agreement with experiments for M_{ex}=0.7,0.9, while the total pressure loss is overestimated by approximately 2% at M_{ex}=1.3. A careful investigation of the results revealed the presence of a recirculation bubble downstream of the shock. The size of this bubble, which extends approximately from 0.6 to 0.7 X/C is probably excessive and is mainly responsible for the overestimation of the losses in the supersonic case. The presence of a separation bubble can also explain the convergence

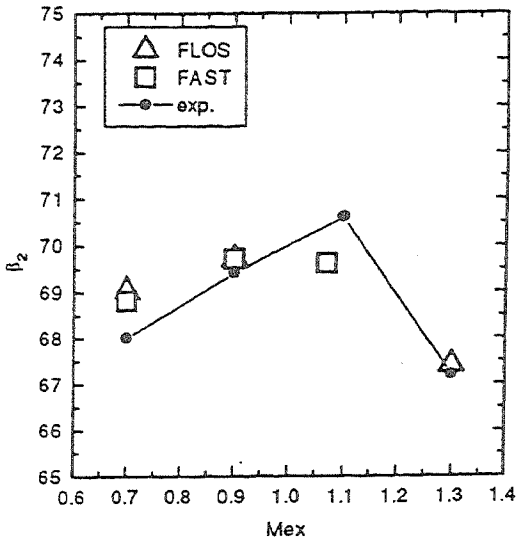

FIGURE 10. NP BLADE: COMPUTED AND MEASURED EXIT FLOW ANGLES FOR TURBULENT FLOW REGIME

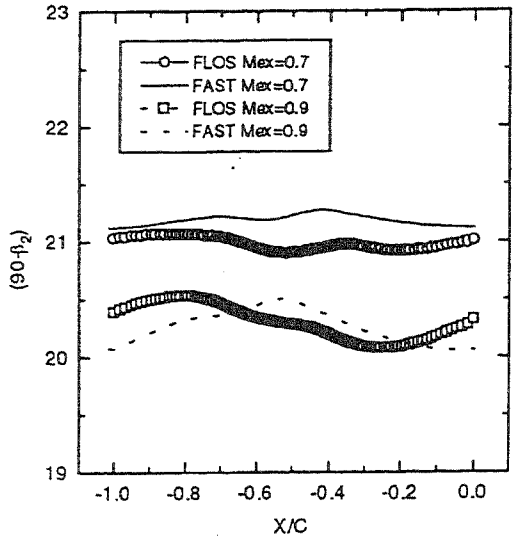

FIGURE 11. NP BLADE: COMPUTED EXIT FLOW ANGLE PROFILES FOR TURBULENT FLOW REGIME

problems of FAST which uses the wall function approach.

The pressure-correction solver showed an opposite trend. The losses are in fact always underestimated by approximately 0.5%. This behavior is largely caused by the turbulence model which can not achieve adequate resolution of the boundary layer (since it uses the standard set of wall functions). Still, the differences between the two codes are always of the order of 1%, while both the codes differ by less than 0.5% from the experiments.

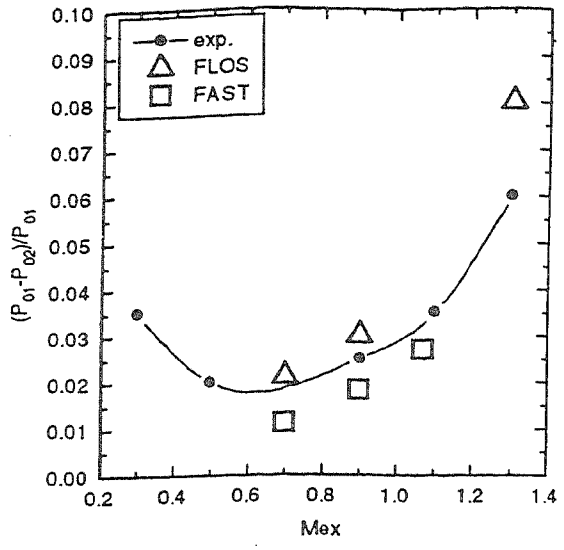

FIGURE 12. NP BLADE: COMPUTED AND MEASURED TOTAL PRESSURE LOSSES FOR TURBULENT FLOW

CONCLUSIONS

The time marching and the pressure-correction algorithms give a satisfactory shock resolution for both the supersonic flow past a 4% bump, and the transonic flow in a turbine. Both approaches require a certain amount of artificial damping to have a stable solution and a good covergence rate. While the time marching code relies only on a spectral-radius scaled version of the artificial damping scheme by Jameson, the pressure-correction method has several sources of damping. These sources are the momentum interpolation for the pressure-correction step, the HLPA convection scheme for the transport equations, and the density biasing in the compressible term. All these sources, although they basically introduce a second order damping, seem to perform well in complex flows such as a turbine flow, where the shock resolution and reflection seems better than that given by the time marching code. Observe that the time marching code uses a centred discretization scheme in conjunction with the artificial damping, whereas the pressure-correction method relies on a TVD scheme which seems more efficient in controlling the amount of artificial damping for complex flows. In fact, the flow past the 4% bump showed a marked superiority of the time marching code in terms of shock capturing capabilities, but when moving to a complex geometry, this superiority fades out. This might be due to the grid which, for the bump flow, is regular and nearly othogonal, whereas for the turbine blade is non othogonal and distorted. The computations proved that the artificial damping as implemented in the time marching code suffers more from grid quality than the density biasing method. The reader should also not forget that the algorithm used by the time marching code is unconditionally unstable unless the artificial damping terms are introduced. These terms are linearized in the implicit operator, but their impact on the solution might be

relevant in order to ensure the stability of the iterative procedure. The lack of space prevented from reporting the full set of tests performed with the two codes by varying the density biasing constants and the weights of the artificial damping terms for the pressure-correction and the time marching code respectively. The main conclusion drawn from all these tests is that the time marching method is more flexible and, at the present stage, more stable at least for high speed turbulent flow regimes, where the compressible pressure-correction solver still suffers some stability limitations.

In terms of overall accuracy, the two approaches give similar results. In fact both the mass averaged exit flow angle and the total pressure losses are in good agreement with experiments. The differences between the two predictions are largely due to the different turbulence models adopted.

The blended linear-biasing function approach proved able to compute supersonic turbine blades in turbulent flow regime. The method is clearly competitive with the more established time marching algorithm, although the biasing function form still lacks some optimization. and tuning in order to be solve the stability limitations found for high speed turbulent flows.

ACKNOWLEDGEMENTS

The authors would like to gratefully acknowledge Prof. F. Martelli and Prof. W. Rodi for the support granted during the preparation of this work. The authors would also like to thank CINECA, MURST, and CNR, for providing the necessary computer time. This work was partly sponsored by the German Federal Ministry of Research and Technology through program TURBOTECH under contract No. 0326801G, and through program TURBOTERM under.contract No. 0326760D.

REFERENCES

Beam, R.M., Warming, R.F., 1982. "Implicit Numerical Methods for the Compressible Navier-Stokes and Euler Equations", Lecture series on Computational Fluid Dynamics, VKI-LS-1982-04, Von Karman Institute for Fluid Dynamics.

Bruzzi, M., 1992, "Analisi dei Flussi Secondari a Valle di una Schiera di Turbina", Phd thesis, Energetics Dept., University of Florence, Italy.

Denton J.D., 1993, "Loss Mechanisms in Turbomachines", ASME J. of Turbomachinery, Vol. 115, pp. 621-656.

Hourmouziadis (1989), "Aerodynamic Design of Low Pressure Turbines", in Blading Design for Axial Turbomachines, AGARD Lecture Series No. 167.

Issa, R.I., Lockwood, F.C, 1977, "On the Prediction of Two-Dimensional Supersonic Viscous Interactions Near Walls", AIAA Journal, Vol. 15, No. 2, pp.182-188.

Jameson, A., Schmidt, W., Turkel, E., 1981 : "Numerical Solutions of the Euler Equations by Finite Volume Methods Using Runge-Kutta Time-Stepping Schemes", AIAA 81-1259.

Karki, K.C., Patankar, S.V., (1989), "Pressure Based Calculation Procedure for Viscous Flows at All Speeds in Arbitrary Configurations", AIAA Journal, Vol. 27, No.9, September 1989, pp.1167,1174.

Lakshminarayana B., 1991, "An Assessment of Computational Fluid Dynamic Techniques in the Analysis and Design of Turbomachinery - The 1990 Freeman Scholar Lecture", ASME J. of Fluids Engng., Vol. 113, pp. 315-352.

Launder B.E. and Spalding D.B., 1974, "The Numerical Computation of Turbulent Flows" Comp. Meth. Appl. Mech. Eng., Vol. 3, pp. 269-289.

Lien, F.-S., Leschziner, M.-A., 1993, "A Pressure-Velocity Solution Strategy for Compressible Flows and its Application to Shock/Boundary-Layer InteractionUsing Second-Moment Turbulence Closure", ASME Journal of Fluids Engineering, December 1993.

McGuirk, J.J., Page, G.J., 1990, "Shock Capturing Using a Pressure-Correction Method", AIAA Journal, Vol.28, No.10, October 1990, pp.1751,1757.

McNally W. and Sockol P.M., 1985, "REVIEW-Computational Methods for Internal Flows With Emphasis on Turbomachinery", ASME J. of Fluids Engng., Vol. 107, pp. 6-22.

Michelassi, V., 1994a, "The Meshho program 1.06", Rept no. 1-1994, Dept. of Energetics, University of Florence, Italy.

Michelassi, V., 1994b, "A Pressure-Correction Algorithm for All-Speed Flows", Report No.718, Institute for Hydromechanik, University of Karlsruhe, Germany.

Michelassi, V., Liou, M.-S., Povinelli, L.A., Martelli, F., 1990, "Implicit Solution of Three-Dimensional Internal Turbulent Flows", NASA CP-10045.

Michelassi, V., Martelli, F., 1993, "3-D Implicit Navier-Stokes Solver for Internal Turbulent Compressible Flows", Journal de Phys. III, France 3, pp. 223-235.

Michelassi, V., Bruzzi, M., 1992, "Experimental and Numerical Investigation of Turbine Cascade Flow", ASME PD-Vol.47-1, General Design Analysis, Considerations, and Applications, Book No. G0685A-1992.

Patankar, S.V., 1980, "Numerical Heat Transfer and Fluid Flow", Mc Graw-Hill Book Company.

Pulliam,T.H., Chaussee, D.S., 1981, "A Diagonal Form of an Implicit Approximate-Factorization Algorithm". Journal of Computational Physics, N. 39.

Rhie, C.M., Chow, W.L., 1983, "Numerical Study of the Turbulent Flow Past an Airfoil with Trailing Edge Separation", AIAA Journal, No. 11, November 1983, pp. 1525-1532.

Van Doormaal J.P. and Raithby G.D., 1984, "Enhancements of the SIMPLE Method for Predicting Incompressible Fluid Flows", Num. Heat Transfer, Vol. 7, pp. 147-163.

Van Doormaal J.P., Raithby G.D. and McDonald B.H., 1987, "The Segregated Approach to Predicting Viscous Compressible Fluid Flows", ASME J. of Turbomachinery, Vol. 109, pp. 268-277.

Wilcox, D.C., 1988, "Reassessment of the Scale-Determining Equation for Advanced Turbulence Models", AIAA Journal, Vol. 26, No. 11, pp. 1299-1310.

Zhu, J., 1991, "A Low-Diffusive and Oscillation-Free Convection Scheme", Communications in Applied Numerical Methods, Vol. 7.

Zhu, J., 1992, "An Introduction and Guide to the Computer Program FAST-3D", Report No. 691, Institute for Hydromechanik, University of Karlsruhe.

Anhang D

Computation of Separated Flow Transition Using a Two-Layer Model of Turbulence

Institut für Hydromechanik
Universität Karlsrhue

Report No. 733

Computation of Separated-Flow Transition Using a Two-Layer Model of Turbulence

E. Papanicolaou

June 1996

Abstract

A model for predicting transition in flows with separation is presented in this study. The two-layer model of turbulence is employed, along with a suitably defined intermittency function, which takes appropriate values in each of the laminar-, transitional- and turbulent-flow regions. Correlations derived from experimental measurements are used for this purpose. Two test cases were selected : the flow over a long horizontal body with semi-circular leading edge and the flow over the backward-facing step of small height (expansion ratio fo 1:1.01). In the former, oncoming flows with freestream turbulence of an order of magnitude typically encountered in practical applications was considered (0.2 % - 5.5 %), whereas in the latter the corresponding level was much lower, 1×10^{-2} %. The Reynolds numbers, based on a respective characteristic length (diameter in the first case and step height in the second) lie in the range of 1600-6600 for both cases, a range in which limited numerical investigations were previously available and were laminar separation bubbles, leading to turbulent reattachment are expected.

The predictions were found to compare well with the corresponding experimental measurements, both in terms of the lengths of the separation and the transition regions, as well as in terms of velocity and turbulence intensity profiles at various streamwise locations. The results showed that in all cases transition is completed downstream of the reattachment point and the rate at which the process is completed increases with the freestream turbulence level.

Contents

List of tables

List of figures

Nomenclature

C_f	=	Skin friction coefficient $= \tau_w/(\rho\ U_\infty^2)$
C_p	=	Pressure coefficient $= \Delta p/(\rho\ U_\infty^2)$
D	=	Leading-edge diameter of the body in testcase 1
H	=	Height of the backward-facing step (testcase 2)
H_{12}	=	Shape factor $H_{12} = \delta_1/\delta_2$
$\mathbf{J}$	=	Jacobian of the coordinate transformation matrix, defined as $\mathbf{J} = \partial(x,y)/\partial(\xi,\eta)$
k	=	Turbulent kinetic energy, non-dimensionalized by ${U_i}^2$
L	=	Length scale of turbulence (dimensionless)
p	=	Pressure
P	=	Dimensionless pressure $\mathrm{P} = p/(\rho\ {U_i}^2)$
Re	=	Reynolds number based on a characteristic length for each testcase (D or H), e.g., $Re = (U_i D \rho)/\mu$
Re_x	=	Local Reynolds number based on the streamwise coordinate x
Re_2	=	Local Reynolds number based on momentum thickness δ_2
Tu	=	Freestream turbulence (%)
u, v	=	Vertical and horizontal cartesian velocity components, respectively
U, V	=	Dimensionless cartesian velocity components $U = u/U_i,\ V = v/U_i$
x, y	=	Vertical and horizontal cartesian coordinate distance, respectively
X, Y	=	Dimensionless cartesian coordinate distances, e.g., $X = x/D,\ Y = y/D$ (or $X = x/H,\ Y = y/H$ for case 2)

Greek Symbols

γ	=	Intermittency function
δ	=	Boundary Layer Thickness
δ_1	=	Displacement Thickness
δ_2	=	Momentum Thickness
ϵ	=	Rate of dissipation of turbulent kinetic energy, non-dimensionalized by ${U_i}^3/D$ or ${U_i}^3/H$
$\xi,\ \eta$	=	Coordinates in the curvilinear (transformed) system
μ	=	Molecular viscosity of air
μ_t	=	Turbulent viscosity
μ_t^*	=	Viscosity ratio $\mu_t^* = \mu_t/\mu$

ρ	=	Density of the fluid
$\sigma_k, \sigma_\epsilon$	=	Prandtl number for the turbulent kinetic energy and its rate of dissipation respectively
τ_w	=	Wall shear stress

Subscripts

i	=	Inlet
r	=	Reattachment point
s (or sep)	=	Separation point
t (or tr)	=	Start of transition
T	=	End of transition
∞	=	Local freestream conditions
$\infty, 6$	=	Freestream conditions 6 mm from the leading edge (reference point for case 1)

1 Introduction

The successful numerical prediction of the flow around surfaces or bodies such as, for instance, airfoils, turbine or compressor blades, depends to a great extent on the ability of the particular computational code to account for and adequately simulate the transition from laminar to turbulent flow. Although a large number of experimental observations and quantitative data are available to characterize such transitions in various flows of practical interest, the numerical predictions are still lagging behind and are mostly limited to simple geometries. Due to the complexity of the general problem, it is common practice to classify the various types of flows and the associated mechanisms of transition, so that a theoretical investigation or the development of a numerical model can be more focused in its attempt to represent the physics. Therefore, as far as transition mechanisms are concerned, one can distinguish between *natural transition* and *bypass transition*, while more recently a third type, the *separated-flow transition* has received increasingly wide attention. The first two apply to boundary layers attached to a surface, while the third one rather refers to a separated shear layer transition.

The different features of each transition type have been described by Mayle (1991). The natural transition is closely related to the development of Tollmien-Schlichting waves in a laminar boundary layer, which is a well known problem in fluid mechanics and has been treated by linear stability analysis (Schlichting, 1979). It is normally associated to flows with low freestream turbulence. Bypass transition is due to the entrainment and subsequent growth of turbulent spots in the laminar boundary layer and occurs at high freestream turbulence levels. Its analytical treatment is based on the turbulent spot theory of Emmons (1951). Separated-flow transition occurs when a laminar boundary layer separates from a surface and a separation bubble is formed. Then a free-shear layer develops, along which the transition takes place. In most cases, the separation bubble is laminar and the flow is turbulent at or soon after the reattachment point, in which case the flow situation can be described as laminar separation -turbulent reattachment.

A large number of computational studies has been presented over the past decades on boundary-layer transition, the large majority of which considered attached flow configurations. Most of them were naturally based on modifications of previously existing turbulence models and as research in the area of turbulence modelling itself was advancing, so was transition modelling. An extensive account of the recent modelling efforts in transition, particularly those made by European researchers, has been presented by Savill (1995). This reflects the activities of the Special Interest Group (SIG) on Transition formed within ERCOFTAC [1]. The most

[1] European Research Community On Flow Turbulence And Combustion

popular approach seems to be the low Reynolds $k - \epsilon$ model, both in a parabolic and an elliptic form, but also integral methods, non-isotropic $k - \epsilon$ models, Reynolds stress models, models including transport equations for intermittency and large eddy simulation have been used among others. All these have been used for computations under a variety of external flow conditions, such as level of freestream turbulence and pressure gradient, the latter of which can have zero or non-zero values and can be of favorable or adverse nature.

In the study of separated-flow transition, the most common configuration has been the leading edge separation bubbles on airfoils. The various methods that have been adopted for this purpose have been classified by Walker et al. (1988) as : a) *Semi-empirical methods*, b) *Viscous-inviscid interaction methods* and c) *Navier-Stokes solutions*, of which the first two classes are the most widely encountered in the literature. An example of semiempirical methods and correlations was offered by the work of Roberts (1980), which aimed at analysing the phenomena associated with leading-edge separation bubbles on airfoils. He discussed in detail the features of the two main types of separation bubbles, namely *short* and *long* bubbles. The short ones have a local effect on the flow and only slightly affect the inviscid flow outside the bubble. Long bubbles on the other hand exhibit a significant interaction with the external flow, so that the pressure distribution is significantly modified compared to the inviscid case. He defined four flow regimes based on very low, low, medium and high chord Reynolds numbers which give complete separation, long bubbles, short bubbles and no separation respectively.

Some of the earliest attempts to investigate transition in separation bubbles were based however on analytical methods which distinguished between an inviscid region outside the bubble, where potential-flow theory could be employed, and a viscous region inside the bubble where boundary-layer analysis could be used. Thus each region was treated independently and an iterative procedure was followed, during which an attempt was made to match the two results at the interface between the two regions. Among the most representative studies in this area are those by Crimi and Reeves (1976) and Kwon and Pletcher (1979). Both were interested in leading-edge separation bubbles on airfoils and the prediction of the phenomenon of 'bursting', which could lead to stall at a given angle of attack.

A constant-thickness airfoil with a cylindrical nose was the configuration used by Arena and Mueller (1980) for low-speed wind tunnel measurements in an attempt to study leading-edge separation bubbles. Different chord Reynolds numbers, angles of attack and flap angles were investigated. The reattachment location was determined as the point where the pressure attains the value of the inviscid-flow solution. The chord Reynolds numbers where varied in the range 150,000-460,000. The separation point in all cases was found to lie between 9 % and 11 % of the chord length. An increased angle of attack led to longer bubbles and reattachment points

which shifted towards the trailing edge of the airfoil. Accordingly, for a constant angle of attack and by increasing the Reynolds number the bubble lengths were shorter and the reattachment points moved towards the leading edge. Unsteady and three-dimensional phenomena in the bubble were also observed.

In this study, some of the ideas described above and previously used to model separation bubbles are employed in conjunction with a full, elliptic simulation of the flow over a body with a semi-circular leading edge and a backward facing step of small height. The two geometries are shown in Fig. 1. These were proposed in the course of the activities of the ERCOFTAC SIG on Transition mentioned earlier (Savill, 1992). The first testcase has not been very extensively investigated in the past and only the experimental studies of Arena and Muller (1980) and Malkiel (1994) resemble very closely to it, even though they considered higher Reynolds numbers and mostly non-zero angles of attack.

The second testcase, the backward-facing step, is much more familiar and has been one of the most commonly used benchmark cases for assessing the performance of various computer codes. Numerous relevant studies on the subject and various aspects of it can be found in the literature, using both numerical and experimental techniques. Generally, the numerical investigations for laminar flow extended up to a Reynolds number $Re = 800$, based on the step height, while for turbulent flow the values considered were $Re = 5000$ or higher. In the intermediate region (transitional regime) very few attempts have been made to simulate the flow, such as for instance the studies of Karniadakis et al. (1990) and Kaiktsis et al. (1991), the second of which reported bifurcations to three-dimensional and oscillatory flow patterns at the early stages of transition. The expansion ratios (outlet height/inlet height) associated with the step were in most cases 1.5 or larger. The present value is very close to unity, due to the very small step height, namely 1.012, while the step-hight Reynolds number is equal to 4095.

Here, both testcases described above are simulated numerically in the transitional regime. In both of them laminar separation is expected, with a separation point whose location is either not known in advance (case 1) or is fixed (case 2, step corner). Eventually a fully-turbulent reattached flow is expected. The full elliptic flow equations are solved, along with a two-layer model of turbulence, where the viscosity is adjusted through an intermittency function in each of the laminar, transitional and turbulent flow regions. This function is defined in such a manner that previous findings on separated flows can be incorporated into the transition model, thus allowing some elements of the physics of these particular flows to be accounted for. Experimental data for testcase 1 were obtained at the Rolls-Royce Applied Science Laboratory (RRASL), Derby, UK (Coupland, 1995) and for testcase 2 at the Engineering Department of Cambridge University, Cambridge, UK (Savill, 1992).

2 Mathematical Model

2.1 Model Equations

In a two-dimensional, Cartesian coordinate system, the steady equations of incompressible, turbulent flow, using the mean velocities as the main flow variables, can be written in the following dimensionless and compact form :

$$\frac{\partial \mathbf{F}}{\partial X} + \frac{\partial \mathbf{G}}{\partial Y} = \frac{\partial \mathbf{F_d}}{\partial X} + \frac{\partial \mathbf{G_d}}{\partial Y} + \mathbf{S} \tag{1}$$

where $\mathbf{F}$ and $\mathbf{G}$ are the convective flux vectors, defined as :

$$\mathbf{F} = \begin{bmatrix} \overline{U} \\ \overline{U}\,\overline{U} + \mathrm{P} \\ \overline{U}\,\overline{V} \\ \overline{U}k \\ \overline{U}\epsilon \end{bmatrix} \quad , \quad \mathbf{G} = \begin{bmatrix} \overline{V} \\ \overline{V}\,\overline{U} \\ \mathrm{P} + \overline{V}\,\overline{V} \\ \overline{V}k \\ \overline{V}\epsilon \end{bmatrix} \quad , \tag{2}$$

$\mathbf{F_d}, \mathbf{G_d}$ are the diffusive flux vectors and $\mathbf{S}$ a source term vector defined as :

$$\mathbf{F_d} = \frac{1}{Re} \begin{bmatrix} 0 \\ (1+\gamma\mu_t^*)\left(2\frac{\partial \overline{U}}{\partial X}\right) \\ (1+\gamma\mu_t^*)\left(\frac{\partial \overline{U}}{\partial Y} + \frac{\partial \overline{V}}{\partial X}\right) \\ \left(1+\frac{\gamma\mu_t^*}{\sigma_k}\right)\left(\frac{\partial k}{\partial X}\right) \\ \left(1+\frac{\gamma\mu_t^*}{\sigma_\epsilon}\right)\left(\frac{\partial \epsilon}{\partial X}\right) \end{bmatrix} \quad , \quad \mathbf{G_d} = \frac{1}{Re} \begin{bmatrix} 0 \\ (1+\gamma\mu_t^*)\left(\frac{\partial \overline{U}}{\partial Y} + \frac{\partial \overline{V}}{\partial X}\right) \\ (1+\gamma\mu_t^*)\left(2\frac{\partial \overline{V}}{\partial Y}\right) \\ \left(1+\frac{\gamma\mu_t^*}{\sigma_k}\right)\left(\frac{\partial k}{\partial Y}\right) \\ \left(1+\frac{\gamma\mu_t^*}{\sigma_\epsilon}\right)\left(\frac{\partial \epsilon}{\partial Y}\right) \end{bmatrix} \quad , \quad \mathbf{S} = \begin{bmatrix} 0 \\ 0 \\ 0 \\ S_k \\ S_\epsilon \end{bmatrix} \tag{3}$$

where :

$$S_k = \gamma P_k - \epsilon \quad , \quad S_\epsilon = C_1\,\gamma P_k \left(\frac{\epsilon}{k}\right) - C_2 \left(\frac{\epsilon^2}{k}\right) \tag{4}$$

$$P_k \equiv \frac{1}{Re}\,\mu_t^* \left(\frac{\partial \overline{U}_i}{\partial X_j} + \frac{\partial \overline{U}_j}{\partial X_i}\right) \frac{\partial \overline{U}_i}{\partial X_j} \quad , \quad \mu_t^* = C_\mu \frac{k^2}{\epsilon} Re \tag{5}$$

The values of the turbulent Prandtl numbers are : $\sigma_k = 1$, $\sigma_\epsilon = 1.3$. and those of the constants : $C_1 = 1.44$, $C_2 = 1.92$, $C_\mu = 0.09$. Since here a two-layer model is employed, the $k-\epsilon$ model is used only in the outer region. In the near-wall region a one equation model is used as explained below, whereby the ϵ equation is not solved. For computational domains of non-rectangular shape, such as the one in testcase 1, a curvilinear coordinate system (ξ, η) is

more appropriate. The chain rule is used for the transformation of the derivatives from the cartesian to the curvilinear system and Eq. 1 can be written as :

$$\frac{\partial \overline{\mathbf{F}}}{\partial \xi} + \frac{\partial \overline{\mathbf{G}}}{\partial \eta} = \frac{\partial \overline{\mathbf{F}}_d}{\partial \xi} + \frac{\partial \overline{\mathbf{G}}_d}{\partial \eta} + \mathbf{J}\,\overline{\mathbf{S}} \tag{6}$$

where the transformed vectors, for instance $\overline{\mathbf{F}}$ and $\overline{\mathbf{G}}$, have the following form :

$$\overline{\mathbf{F}}(\xi,\eta) = \left(\mathbf{F}\frac{\partial Y}{\partial \eta} - \mathbf{G}\frac{\partial X}{\partial \eta}\right) \;,\; \overline{\mathbf{G}}(\xi,\eta) = \left(-\mathbf{F}\frac{\partial Y}{\partial \xi} + \mathbf{G}\frac{\partial X}{\partial \xi}\right) \tag{7}$$

2.2 Boundary Conditions

In both cases an inlet velocity and an inlet freestream turbulence level are specified. At the outflow, all streamwise gradients are taken as zero (provided that the outflow location is carefully selected for this to be accurate, as was done here). On the solid surfaces the no-slip conditions are applied. In testcase 1, the computations extend all the way to the opposite wall, were again no-slip conditions are specified, with the wall functions of the standard $k-\epsilon$ model, i.e., the viscous sublayer along this wall is not resolved. Due to the symmetry of the geometry, only the upper half of the body is modelled and a symmetry condition is imposed at the bottom boundary upstream of the body. In testcase 2, due to the large extent of the actual configuration in the crossflow direction, the upper boundary is taken midway across the channel height, where symmetry conditions are imposed.

However, of utmost importance in transition modelling, are the inlet conditions for the turbulence quantities. For testcase 1, it is given that the freestream turbulence Tu, under the prevailing zero-pressure-gradient conditions, decays in a power-law fashion, while the dissipation length scale L_ϵ increases with the square-root of the streamwise distance (Savill, 1992). Depending on the properties of the turbulence-generating grids used in each subcase, suitable constants of the power-law expression were computed, using measured values of freestream turbulence above the body surface that were provided. Once the expressions for Tu and L_ϵ are fully determined, their corresponding inlet values can be determined by upstream extrapolation. The value of dissipation rate at the inlet is in turn obtained from the relationship $L_\epsilon = k^{3/2}/\epsilon$, while the turbulent viscosity at inlet from Eq. 5. In testcase 2, Blasius conditions at the inlet are proposed, along with a measured, given profile for the turbulence intensity, while for the dissipation length scale a profile obtained from the relationship : $L_\epsilon = min[\kappa\, y, 0.085\, \delta]/{C_\mu}^{3/4}$ was recommended (Savill, 1994), where $\kappa = 0.41$ (Karman's constant) and y is the distance from the bottom surface of the inlet channel.

2.3 Two-layer model

The two-layer model as described in the paper by Rodi (1991) is used in the present computations. It is a combination of the standard $k-\epsilon$ model, used in the outer region and the Norris-Reynolds, one-equation model which applies in the near-wall region. Since the computations here are carried out in non-dimensional variables, the various realtionships are presented in a non-dimensionless form. Therefore, in the Norris-Reynolds approach, the turbulent viscosity is given by the following expression :

$$\mu_t^* = Re\ f_\mu\ C'_\mu\ \sqrt{k}\ L \tag{8}$$

$$\text{where} \ : \ C'_\mu = 0.084\ , \quad f_\mu \ = \ 1 - exp\left(-\frac{Re_y}{A_\mu}\ \frac{25}{A^+}\right)\ , \quad A_\mu \ = \ 50.5\ ,$$
$$Re_y \ = \ Re\ \sqrt{k}\ Y_n \ , \ L = C_D\ \kappa\ Y_n \ , \quad C_D = 6.41 \ , \quad \kappa = 0.41 \tag{9}$$

Y_n is the dimensionless distance normal to the wall. Only the k equation is solved in the near-wall region, with the source term S_k of Eq. 4 using the following value of ϵ :

$$\epsilon \ = \ \frac{k^{3/2}}{L}\ \left(1 + \frac{1}{Re}\ \frac{C_\epsilon}{\sqrt{k}\ L}\right) \ , \quad C_\epsilon = 13.2 \tag{10}$$

The criterion for switching between inner and outer region modelling is determined by the value : $f_\mu \ \approx \ 0.95$ (Rodi, 1991) or the boundary layer edge, whichever is attained first as one moves away from the wall. This model has been previously used to compute transitional, attached flows in turbine cascades (Cho et al., 1993), along with the empirical formulas of Abu-Ghannam and Shaw (1980) and suitable modification of the A^+ parameter in each of the laminar, transition and turbulent regions (Rodi, 1991). Here A^+ is kept constant at $A^+ = 25$ (turbulent flow) and the transition process is controlled instead through the intermittency function, as shown in Eqs. 3 and 4 and as will be described below. In both testcases, the streamwise pressure gradients in the external flow were almost zero, therefore no special treatment for variable pressure gradient had to be introduced into the model.

2.4 Transition Model Parameters

The intermittency function γ, appearing in Eqs. 3- 4 above as a multiplication factor for the eddy viscosity, is a measure of the level of turbulence that is present at a specific point in a flow field and more strictly, it represents the fraction of time during which a flow at the given location is turbulent (Mayle, 1991). The values of γ range from 0, corresponding to laminar flow, to 1, which indicates a fully-turbulent flow. Values between 0 and 1 represent a state of

transition from laminar to turbulent flow at a particular point. The rate at which the values of γ increase from 0 to 1 during transition is determined by the rate of the turbulent spot production (Emmons, 1951) and is generally of exponential nature. Different investigators have proposed different parameters that control this exponential growth and presented γ as a one-dimensional function of the streamwise coordinate, corresponding to values near the wall (near-wall intermittency) (Mayle, 1991). Such expressions, accompanied by correlations for the onset of transition and the extent of the transition region may then be used for modelling the flow in the transition region.

Here, the following expression is used for intermittency :

$$\gamma(x) = 1 - exp\left[-G(x - x_{tr}) \int_{x_{tr}}^{x} \frac{dx}{U_\infty}\right] \tag{11}$$

$$\text{where : } G = \frac{exp(0.99\ Tu)}{100} \frac{{U_\infty}^3}{\nu^2} {Re_{2,tr}}^{-8/3} \tag{12}$$

proposed by Rodi and Schönung (1987) as an extended version of the work by Chen and Thyson (1971). This expression involves the value of the Reynolds number $Re_{2,tr}$ based on the momentum thickness at the transition point and the coordinate of the transition point x_{tr}. $Re_{2,tr}$ is obtained at each streamwise location from the following correlation :

$$Re^2_{2,tr} = \left(1 + \frac{0.05}{exp(0.365\ Tu)}\right) Re^2_{2,sep} + \frac{17000}{exp(0.509\ Tu)} \tag{13}$$

The coordinate at the start of transition x_{tr} is taken as the location at which the local value of Re_2 exceeds the value of $Re_{2,tr}$ computed from Eq. 13. The above expression was also proposed by Rodi and Schönung (1987) and the various coefficients involved were obtained by optimization, based on the experimental data of Gotthardt (1983) and Haas et al. (1986). As can be observed, this correlation involves the Reynolds number at the separation point and therefore it is particularly suited for separated flows. The good prediction of the separation point and the accurate estimation of the various boundary layer thicknesses are essential to the successful use of this model.

3 Computational Scheme

3.1 Main Features

The code **FAST-2D** [2] (Zhu, 1991a) was used for the present computations. This was developed at the Institute for Hydromechanics, at the University of Karlsruhe, Germany over the past decade by various researchers. A detailed description of it, or more strictly its three-dimensional version, is given in the paper by Majumdar et al. (1992). Its main features consist of a control-volume approach, discretization of Eq. 6 in a generalized, non-orthogonal coordinate system, where the cartesian velocity components are used to describe the flow field. The code is based on the pressure-correction algorithm SIMPLE (Patankar, 1980) and its variant SIMPLEC (Van Doormal and Raithby, 1984) in a non-staggered grid arrangement and the momentum interpolation procedure of Rhie and Chow (1983) is used to avoid the checkerboard splitting. The convective terms are discretized using the HLPA scheme (**H**ybrid **L**inear / **P**arabolic **A**pproximation) described by Zhu (1991b). This is a higher-order, bounded scheme, with good stability properties.

3.2 Computational Grid

The grids used in the computations for the two testcases are shown in Fig. 2 For the first testcase, the computational domain extends up to 100.5 diameters from the leading edge (thus making the horizontal surface equal to exactly 100 diameters), while vertically the domain is extended up to the wind tunnel wall, as specified by the experimental setup (21.8 diameters from the leading edge). The inlet location is taken at 21.3 diameters upstream of the leading edge. After several attempts, the final grid dimensions which were considered necessary for a good resolution of the body surface were 142×102, with 142 points in the streamwise direction. The grid spacings were stretched in the streamwise direction towards the curved surface of the body.

In the second testcase, a similar number of points was used. Here the emphasis in the stretching of the grid was towards the shear layer expected to develop as the flow separates at the corner. Therefore stretching in both the upward and downward direction was used towards the approximate vertical location of the shear layer. Downstream of the step, the domain extended to a distance of 80 step heights, while vertically up to the mid-height of the test channel (42.8H), where a symmetry condition was employed. Those distances were eventually found to be sufficient to avoid any undesirable boundary influence on the solution, after several

[2] **F**-low **A**-nalysis **S**-imulation **T**-ool of **2-D**

alternatives were tested. In both cases, the grid dimensions and stretching factors used yielded values of Y^+ at the first grid point from the wall of the order of 1 or less, therefore ensuring a fair amount of grid points inside the boundary layers.

3.3 Procedure and stability considerations

The velocity components and the pressure were initialized with the laminar flow solution obtained on the same configuration for a sufficiently lower Reynolds number. The computations proceeded until the root-mean square residuals of all variables were reduced to the order of 10^{-5} or less. During the early attempts, it became evident that the numerical procedure tended to become unstable, especially in testcase 2 where the level of freestream turbulence is very low, and multiple separation bubbles were developing. It was soon realized that this was due to setting $\gamma = 0$ in the laminar-flow regions. It was therefore found necessary to avoid letting the turbulent viscosity go to zero in the diffusion terms shown in Eq. 3 in those regions. The intermittency was instead set to 1 in the diffusion terms in the laminar region in the free stream and a small amount of diffusion was also allowed in the laminar boundary layer, by setting γ to a small value, in the range 0.1-0.2, again in the diffusion terms only. Such values were found to be adequate for numerical stability without affecting the overall results, after experimentation in several cases with various flow conditions, and they were maintained in that range in all subsequent calculations. This practice was also directed by physical reasoning, since otherwise the diffusion of freestream turbulence into the laminar boundary layer would not have been properly accounted for and since it was also known from the measurements that the oncoming flow carried some amount of turbulence with it, both in the free stream and within the laminar boundary layer before transition.

4 Results and Discussion

4.1 Testcase 1

4.1.1 Results for $U_i = 5$ m/s, Re = 3293

The flow conditions which were specified for the body with the semi-circular leading edge are shown in Table 1. Each subcase is characterized by a letter 'a-f'. In Fig. 3 a typical streamline plot is shown. A quite sizeable separation bubble is present, whose size varies from case to case, as will be demonstrated below. The bubble in case 1b, for instance, had a length roughly equal to 2.4 diameters. The separation point is located slightly upstream of the beginning of the

horizontal surface of the body. On the same figure, the streamwise intermittency distribution $\gamma(x)$ is also shown. The predicted transition point is located at $X_t = 2.41$ diameters from the leading edge. This corresponds to a distance equal to 80% of the bubble length. The transition ends at a streamwise coordinate of $X_T = 3.34$, yielding a total length of transition equal to 0.93 diameters. It is interesting to note that the predicted transition behavior is more in accord with the findings of Walker (1992), than those of Mayle (1991), as far as the end-of-transition point is concerned. More specifically, here the transition process seems to be completed downstream of the reattachment point, i.e., the flow is not fully-turbulent at reattachment.

In Fig. 4 several quantities of interest are plotted against the corresponding experimental values of case 1b, namely, boundary-layer thickness δ, maximum velocity of the external flow U_{max} and the shape factor in terms of the local Reynolds number Re_x. δ is determined as the distance where the velocity is 0.99 of the maximum value. The comparison with the experimental results can be seen to be good, both in terms of δ and maximum velocity. As one may observe in Fig. 4b, the effect of the bubble extends up to about ten body diameters downstream of the leading edge. The shape factor plot in Fig. 4c exhibits a sharp peak typical of a separation bubble, more so the numerical than the experimental values, before an asymptotic value of 1.44 is attained. This is very close to the value reported by Schlichting (1979) for turbulent boundary layer on a flat plate. The comparison with the measurements appears fairly good.

In Fig. 5 additional comparisons with measured values are made, this time for the skin friction coefficient C_f and the Reynolds number Re_2 based on the momentum thickness, both plotted against the local Reynolds number. The bubble location in the plot of C_f is indicated by zero values in the measurement data and by negative values in the computations. It can be readily observed that the predicted length and location for the separation bubble agrees very well with the measurements. The analytical result for the variation of C_f in a turbulent boundary layer over a flat plate, given by a ${Re_x}^{-0.2}$ relationship (Schlichting, 1979), is also plotted and the similarities with the numerical result in the fully turbulent region are clearly shown. The flow behavior in the laminar region is very different from that of a boundary layer over a flat plate, both due to the curvature and the separated region, therefore it would be meaningless to include the analytical result for C_f in the laminar region. Fig. 5b is a graphical representation of the relationship between Re_2 and Re_x as predicted numerically in comparison with the analytical result for a flat plate. This can be obtained using the corresponding expression for δ_2 (Schlichting, 1979) and indicates a $Re_x^{0.8}$ dependence. In the laminar region the corresponding result is $Re_x^{0.5}$ but, for the same reasons as discussed for C_f, the laminar-flow correlation is not shown as not applicable. However, in Fig. 5b it is clearly

shown that as the turbulent regime establishes, the analytical curve is being asymptotically approached by the numerical results.

Fig. 6 compares predicted velocity profiles for case 1b with the corresponding measured values, at several streamwise distances, measured from the leading edge of the body and indicated in *'mm'*. The agreement seems to be fairly good, in both the separation and the reattached flow regions. The reattachment point also seems to have been predicted within good accuracy. Fig. 7 compares predicted turbulence intensity profiles for case 1b with the corresponding measured values, at the same streamwise locations as for the velocity profiles. The comparison is reasonably good for most profiles, even though in part of the laminar region ($x \leq 17$ mm) the intensity is over-predicted. This is probably due to allowing larger amounts of turbulence than the actual one to diffuse into the laminar boundary layer for stability purposes in the numerical model, as discussed earlier.

In Fig. 8 the streamline plot for case 1c, corresponding to the same freestream velocity as case 1b (5 m/s) but a higher level of freestream turbulence, i.e., 2.3 %, is shown. The size of the bubble is now somewhat reduced (2.1 diameters compared to 2.4 before) and the separation point moves slightly downstream. The transition point X_t moves somewhat upstream and the total length of the transition region is reduced by 28%. Fig. 9 shows the comparisons with measured values in terms of boundary-layer thickness, maximum velocity and the shape factor in terms of the local Reynolds number Re_x for case 1c. The comparison is generally good, except for some under-prediction of the maximum velocity in the separation region (Fig. 9b).

In Fig. 10 the skin friction coefficient and the momentum-thickness Reynolds number are plotted against the corresponding experimental values for case 1c. As before, analytical results for flat-plate boundary layers are comparatively shown, where applicable. Again, zero values of C_f in the experimental data indicate a separation bubble. The location of the transition point is again reasonably well predicted as Fig. 10a shows. In both Fig. 10a and 10b the numerical predicitions approach closely the flat plate correlations as a fully-turbulent boundary layer establishes along the horizontal surface of the body. In Fig. 11 the computed velocity profiles for case 1c are compared against the corresponding measured values, at several streamwise distances, measured from the leading edge of the body and specified in *'mm'*. The comparison is generally good, except for some indication of delayed reattachment. The corresponding turbulence intensity profile comparisons in Fig. 12 are also satisfactory.

In the following figures, Figs. 13- 17 results are presented for a higher level of freestream turbulence (5.56 %). The transition is found to be very abrupt in Fig. 13 and the length of the bubble smaller than before (roughly 1.5 diameters). The boundary-layer thickness surprisingly appears not to be in agreement with the experimental results in this case (Fig. 14a), although

agreement for the maximum velocities is still good (Fig. 14b). This is also the case with the shape factor values (Fig. 14c). The skin-friction coefficient in Fig. 15a, even though not as good as in previous cases, is still well predicted and shows a sharper negative peak in the separation region than before. The predictions of the velocity profiles and of the turbulent intensities were also in this case shown to be satisfactory in Figs. 16 and 17 respectively.

4.1.2 Results for $U_i = 10$ m/s, Re = 6586

The results that follow are for a testcase with a similar value of freestream turbulence as in case 1c (2.5 %), always taken 6 mm from the leading edge, but a higher velocity, namely 10 m/s. The corresponding streamline plot for this case (1f) is shown in Fig. 18. It is clearly observed that the length of the bubble is much smaller than for cases 1a and 1b and more specifically equal to only 1.1 diameters. Transition starts therefore much closer to the leading edge, but the total length of the transition region (approximately 0.7 diameters) is not significantly different than in case b, indicating that this is mostly dependent on the value of the freestream turbulence rather than the Reynolds number of the oncoming flow.

Figs. 19 and 20 are plots of various boundary layer quantities similar to the ones previously presented for cases 1b, 1c and 1d. Again, overall good agreement may be observed. In particular the plot of C_f shows a very good prediction of the reattachment point. The Re_2 vs. Re_x plot shows again the attainement of turbulent flow conditions at increasing Re_x when compared with the analytical result. The velocity profiles and turbulent intensities for case 1f are presented in Figs. 21 and Fig. 22 respectively. Fig. 21 verifies one more time the good prediction of the reattachment point, along with good overall agreement, which is also the case in Fig. 22.

Equally good comparisons with the measured values were obtained for the remaining sets of flow conditions shown on Table 1. Some discrepancies were only observed in the prediction of turbulence intensities for the smalest value of the freestream turbulence, $Tu_\infty = 0.17$ % (case 1a), and for the smallest value of the inlet velocity, $U_i = 2.5$ m/s (case 1e). Clearly, some experimentation with alternative values of the parameters involved in Eqs. 12 and 13 would be necessary to produce a more universal model, but this was considered outside the scope of the present work.

4.1.3 Comparisons with experimental correlations

The main results of all six computed cases 1a-1f are summarized in Table 2. By using the distances X_s, X_t and X_T presented on this table, one can calculate and plot three suitably defined Reynolds numbers Re_{sT}, Re_{st} and Re_{LT} , often used to characterize transition, vs. the momentum-thickness Reynolds number at the separation point $Re_{2,s}$. For instance, Re_{sT} is

computed as :

$$Re_{sT} = \frac{u_s\,(x_t - x_s)\,\rho}{\mu} = Re\,U_s\,(X_t - X_s) \tag{14}$$

and similarly the other two numbers. In this manner, plots similar to those presented by Mayle (1991) can be constructed. The correlations proposed by Mayle (1991) and Walker (1992) are also graphically depicted on the same figure, Fig. 23. The values of $Re_{2,s}$ appearing here represent a relatively narrow band compared to the results plotted by Mayle (1991) and therefore a new correlation can not be derived based on the present data. However, one can see that, although not significantly apart, the computed values of Re_{sT}(Fig. 23a) are higher than what the correlation of Mayle predicts and this relates to what has already previously been discussed, namely that here the transition is completed after reattachment, while Mayle's findings suggest otherwise. There is however one data point which falls exactly on the correlating line and this corresponds to the highest freestream turbulence level used (5.56 %) and for this value the transition is completed shortly after reattachment. Fig. 23b is somewhat more conclusive, showing the data points more closer to the correlating line proposed by Mayle (1991) for $Re_{st}$and specifically the one for long bubbles. The short bubble correlation is also plotted. Both correlations have a ${Re_{2,s}}^{0.7}$ dependence, but are multiplied by a different factor. In Fig. 23c, the values of $Re_{LT}$are plotted against two different correlations, one proposed by Mayle (1991) and suggesting a $Re_{2,s}^{0.7}$ dependence and another one by Walker (1992) where the dependence is ${Re_{2,s}}^{1.5}$. Interestingly enough, although qualitatively this study agrees more with the findings of Walker (1992) as far as the end-of-transition is concerned, the present results seem to agree quantitatively better with the correlation of Mayle (1991) for Re_{LT}, except for one data point, corresponding to the highest freestream turbulence level (5.56 %). If one takes into account that the correlations of Mayle (1991) where derived from experimental data corresponding to freestream turbulence levels of 0.2-0.5 %, such an observation may not be unreasonable.

4.2 Testcase 2

Here, although experimental data were available for three different inlet velocities (inlet Reynolds numbers $Re = 1830, 2535$ and 4095) (Savill, 1994) and essentially the same freestream turbulence level Tu, of the order 10^{-2} %, the numerical instabilities that were encountered, exactly due to these low values of Tu, only allowed the computation of one subcase and more specifically the one corresponding to the highest value of the Reynolds number, $Re = 4095$. In Fig. 24 the streamline plot for this case, along with the corresponding streamwise distribution of the intermittency function, is shown over the same horizontal scale. The computed flowfield is

characterized by a relatively long separation bubble (9.54 step heights) immediately donwstream of the step, with a small secondary eddy at the foot of the step. The transition process appears to be relatively slow, a fact that was to be expected considering the very low freestream turbulence level of the oncoming flow. It starts at about 4.8 step heights downstream of the step and is completed at a distance of about 18.4 step heights.

The experimental data available for this testcase were in terms of streamwise varying values of the momentum thickness, the maximum velocity of the external flow and the shape factor. In Fig. 25 these are compared with the present, numerically predicted values along a non-dimensional streamwise distance x/H. The agreement is very good for all three quantities and the extent of the separated region is well predicted. Fig. 26 shows the skin friction coefficient and the Reynolds number based on the momentum thickness vs. the local Reynolds number. No experimental data were provided for these two quantities and the results are only compared with the analytical flat-plate boundary layer correlations. What can be observed is that the reattached shear layer in this particular testcase deviate somewhat from the results of turbulent flow over a flat plate.

In Fig. 27 velocity profiles are compared at several streamwise locations downstream of the step with the experimental values. Generally the agreement is good, except for some indication of early reattachment in the numerical results. Fig. 28 the corresponding turbulence intensities, both numerical and experimental are shown, at the same streamwise locations as the velocities. It can be observed that there is some overprediction of the intensity values at the first station but gradually the numerical values approach the experimental ones. The transition process appears to be very rapid at its early stages in the numerical predictions.

5 Conclusions

A computational approach based on the two-layer model of turbulence and an intermittency function was presented for transition in separated flows. Two flow testcases were investigated, one involving flow separation due to curvature and the other one separation due to sudden expansion (step). The transition process was modelled by means of an intermittency function defined through empirical correlations, based on experimental data. Those allowed for the effect of separation to be included in the modelling. The results appear promising in the sense that for a relatively wide range of external flow conditions, such as freestream velocity and level of turbulence, corresponding to values of practical interest in areas such as turbomachinery flows, good comparisons with experimental values were obtained. This can be said both about global quantities such as length of separated region, location of transition point, as well as about local

quantities, such as velocity and turbulent intensity profiles.

The model behaved better in freestream turbulence levels from 0.6 %-5.6 %, but has been also tested at levels one order of magnitude lower, where it produced reasonably good results. This study has proven that the intermittency function can be used in several ways in transition modelling, such as for instance in combination with the two-layer model used here, and can lead to successful predictions, but it is necessary to handle the laminar regions of flow where this function vanishes, with care, for numerically stable computations and more physical results.

Available correlations for separated flows based on experimental data such as the ones used here can provide good inputs to transitional modelling. However, further experimentation with the various parameters involved in such correlations is needed, in order to improve the universality of the models.

6 Acknowledgments

This work was sponsored by the German Federal Ministry of Research and Technology through program TURBOTECH, under contract No. 0326801G. The author would like to thank Prof. Rodi for his guidance and for offering him the opportunity to work in this exciting area. Many thanks also to Dr. Mark Savill of Cambridge University, Cambridge UK for his valuable work in the ERCOFTAC Transition SIG and for providing the experimemtal results for testcase 2. Also to Dr. John Coupland from the Rolls-Royce Applied Sciences Laboratory, Derby, UK, for providing us with the experimental data for testcase 1.

7 References

Abu-Ghannam, B.J. and Shaw, R., 1980, "Natural transition of Boundary Layers- The effects of turbulence, pressure gradient, and flow history", *J. of Mech. Engg. Science*, Vol. 22, No. 5, pp. 213-228.

Arena, A.V., and Mueller, T.J., 1980, "Laminar separation, transition and turbulent reattachment near the leading edge of airfoils", *AIAA J.*, Vol. 18, No. 7, pp. 747-753.

Chen, K.K., and Thyson, N.A., 1971, "Extension of Emmons' spot theory to flows on blunt bodies", *AIAA J.*, Vol. 9, No. 5, pp. 821-825.

Cho, N.-H., Liu, X., Rodi, W., and Schönung, B., 1993, "Calculation of wake-induced unsteady flow in a turbine cascade", *ASME J. of Turbomachinery*, Vol. 115, pp. 675-686.

Coupland, J., 1995, "Transition modelling for tubromachinery flows", ERCOFTAC Bulletin, No. 24, pp. 5-8, 1995.

Crimi, P., and Reeves, B.L., 1976, "Analysis of leading-edge separation bubbles on airfoils", *AIAA J.*, Vol. 14, No. 11, pp. 1548-1555.

Emmons, H.W., 1951, "The laminar-turbulent transition in a boundary layer-Part I", *J. of the Aeronautical Sciences*, Vol. 18, pp. 490-498.

Gotthardt, H., 1983, Theoretische und experimentele Untersuchungen an ebenen Turbinengittern mit Pfeilung und V-Stellung. Dissertation, Universität Braunschweig.

Haas, W., Rodi, W., Schönung, B., Swamy, N.V.C., 1987, "Experimentelle Untersuchung von lokalen Ablöseblasen an Gasturbinenschaufeln", *Z. Flugwiss. Weltraumforschung*, Vol. 11, pp. 261-270.

Karniadakis, G.E., Orszag, S.A., and Yakhot V., 1990, "Large-Eddy/RNG simulation of flow over a backward-facing step ", in *Engineering Turbulence Modelling and Experiments*, W. Rodi and E.N. Ganić (eds.), pp. 269-278, Elsevier, New York.

Kaiktsis, L., Karniadakis, E.M. and Orszag, S.A., 1991, "Onset of three-dimensionality, equilibria, and early transition in flow over a backward-facing step", *J. of Fluid Mech.*, Vol.

231, pp. 501-528.

Kwon, O.K., and Pletcher, R.H., 1979, "Prediction of incompressible separated boundary layers including viscous-inviscid interaction", *ASME J. of Fluids Engg.*, Vol. 101, pp. 466-472.

Majumdar, S., Rodi, W. and Zhu, J., 1992, "Three-dimensional finite-volume methods for incompressible flows with complex boundaries", *ASME J. of Fluids Engg.*, Vol. 114, pp. 496-503.

Malkiel, E., 1994, "An experimental investigation of a separation bubble", Ph.D. Dissertation, Rensselaer Polytechnic Institute, Troy, New York.

Mayle, R.E., 1991, "The role of laminar-turbulent transition in gas turbine engines", *ASME J. of Turbomachinery*, Vol. 113, pp. 509-537.

Patankar S.V., 1980, *"Numerical Heat Transfer and Fluid Flow"*, Hemisphere, Washington D.C.

Roberts, W.B., 1980, "Calculation of laminar separation bubbles and their effect on airfoil performance", *AIAA J.*, Vol. 18, No. 1, pp. 25-825.

Rhie, C.M., and Chow, W.L., 1983, "Numerical study of the turbulent flow past an airfoil trailing edge separation", *AIAA J.*, Vol. 21, No. 11, pp. 1525-1532.

Rodi, W. and Schönung, B., 1987, "Interaktives-Inverses Grenzschichtverfahren zur Berechnung von lokalen Ablöseblasen an Turbinenschaufeln", *Z. Flugwiss. Weltraumforschung*, Vol. 11, pp. 271-280.

Rodi, W., 1991, "Experience with two-layer models combining the $k-\epsilon$ model with a one-equation model near the wall", AIAA Paper No. 91-0216, presented at the 29th Aerospace Sciences Meeting, Reno, Nevada.

Savill, A.M., 1992, "A T3 Test Case Project Report - Predicting Transition Induced by Free-Stream Turbulence", presented at the IAHR/ERCOFTAC Turbulence Modelling SIG Seminar, Delft, The Netherlands.

Savill, A.M., 1994, T3D Test Case Problem Specification (private communication).

Savill, A.M., 1995, "A Summary report on the COST ERCOFTAC Transition SIG project evaluating turbulence models for predicting transition", ERCOFTAC Bulletin No. 24, pp. 57-61.

Schlichting, H., 1979, "Boundary Layer Theory", McGraw-Hill, New York.

Van Doormal, J.P. and Raithby, G.D., 1984, "Enhancements of the SIMPLE Method for Predicting Incompressible Fluid Flows", *Num. Heat Transfer*, Vol. 7, pp. 147-163.

Walker, G. J., Subroto, P.H., and Platzer, M.F., 1988, "Transition modeling effects on viscous/inviscid interaction of low Reynolds number airfoil flows involving laminar separation bubbles", ASME Paper No. 88-GT-32, presented at the Gas Turbine and Aeroengine Congress, Amsterdam, The Netherlands.

Walker, G. J., 1992, "The role of laminar-turbulent transition in gas turbine engines : a discussion", ASME Paper No. 92-GT-301, presented at the Int. Gas Turbine and Aeroengine Congress and Exposition, Cologne, Germany.

Zhu, J., 1991a, "FAST-2D : A computer program for numerical simulation of two-dimensional incompressible flwos with complex boundaries", Rep. No. 690, Institute for Hydromechanics, Univeristy of Karlsruhe, Germany.

Zhu, J., 1991b, "A low-diffusive and oscillation-free convection scheme", *Comm. in Applied Num. Methods*, Vo. 7, pp. 225-232.

Tables and Figures

Table 1: Flow Conditions for Testcase 1

Case $\Downarrow$	U_i (m/s)	Re	Tu (%)
a	5	3293	0.17
b	5	3293	0.63
c	5	3293	2.31
d	5	3293	5.56
e	2.5	1646.5	2.30
f	10	6586	2.50

Table 2: Length of Separation Bubble and Transition Regions for Testcase 1

Testcase $\Longrightarrow$	**1a**	**1b**	**1c**	**1d**	**1e**	**1f**
U_i (m/s)	5	5	5	5	2.5	10
Tu %	0.17	0.63	2.3	5.6	2.3	2.5
X_s	0.448	0.466	0.485	0.466	0.500	0.448
X_t	3.159	2.412	2.169	1.854	4.158	1.181
X_T	6.695	3.336	2.834	2.058	5.495	1.953
X_r	3.247	2.913	2.759	2.005	3.829	1.550
$Re_{2,s}$	24.5	24.8	21.8	26.9	21.2	36.5
Re_{st}	11257	7792	6449	5837	7450	6526
Re_{LT}	11644	3700	2547	858	2723	6589
Re_{sT}	25940	11492	8996	6695	10173	12846

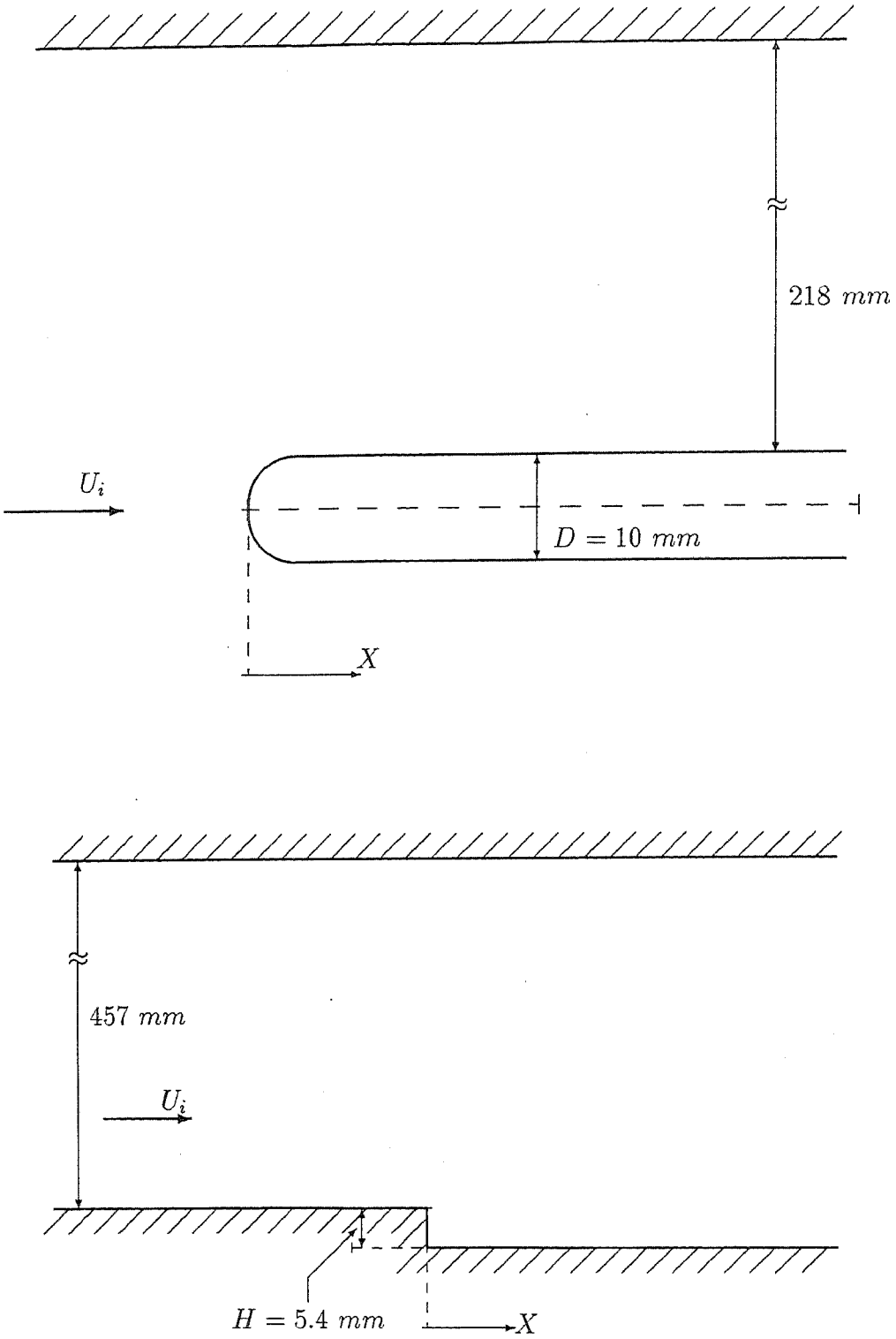

Fig. 1: Schematic of the two testcases and the corresponding significant dimensions.
Case 1 : Long horizontal body with semi-circular leading edge (top).
Case 2 : Backward-facing-step of small height (bottom).

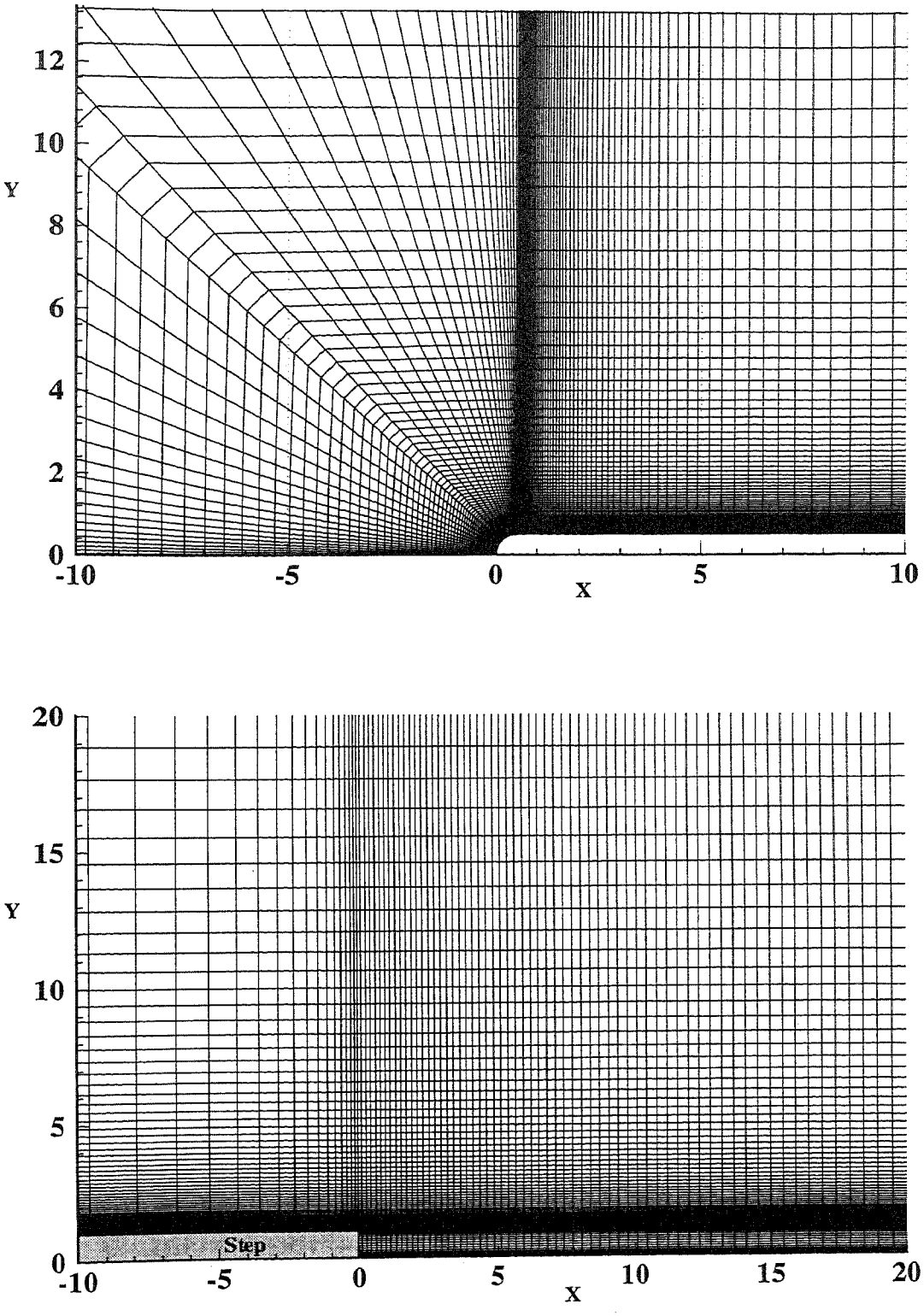

Fig. 2: Section of the computational grid for the two testcases
Top : Horizontal body with semi-circular leading edge (testcase 1)
Bottom : Backward-facing step (testcase 2)

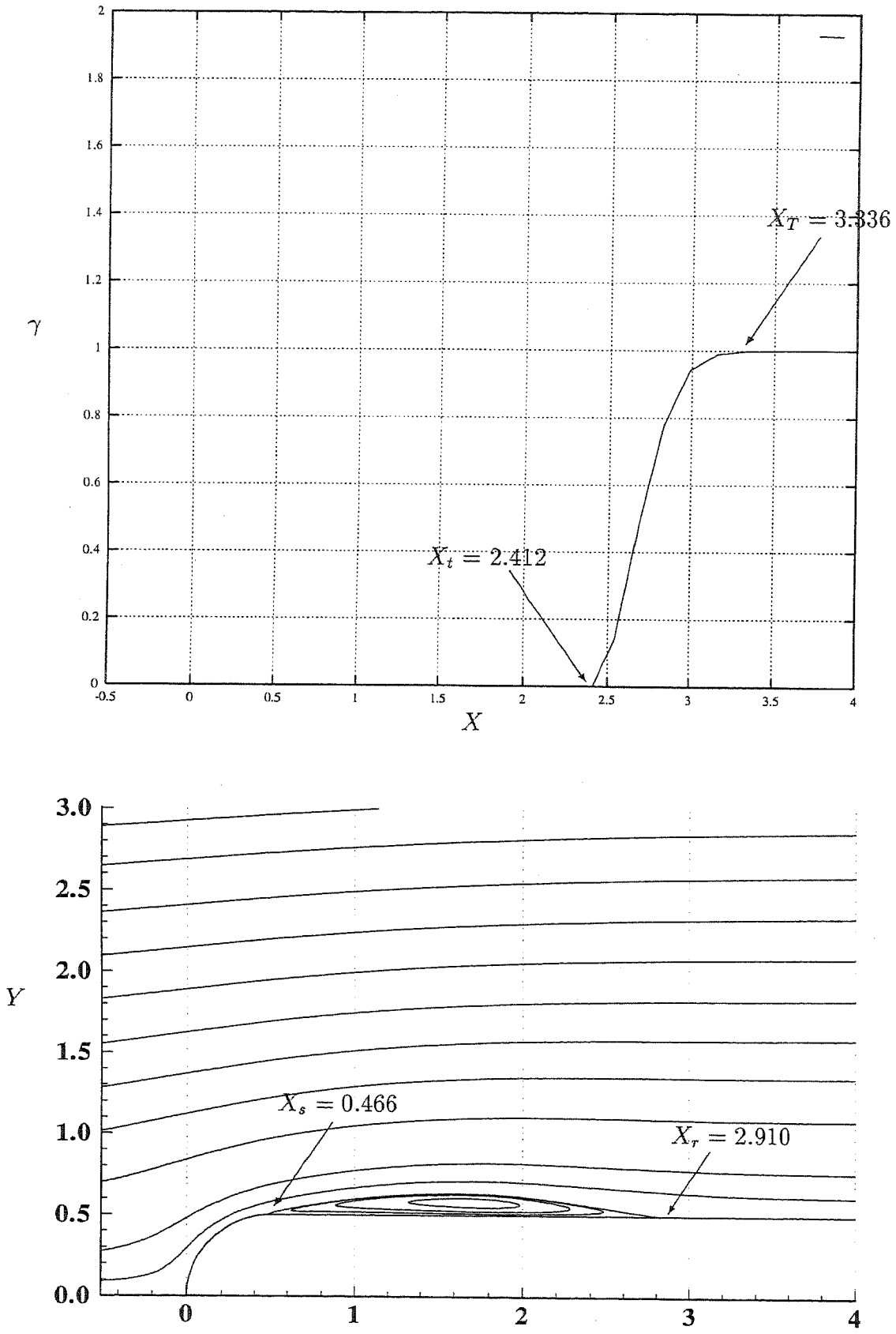

Fig. 3: Results for testcase 1b, $U_o = 5\ m/s$, $Tu_{\infty,6} = 0.63\ \%$.
Top : Intermittency - Bottom : Streamlines

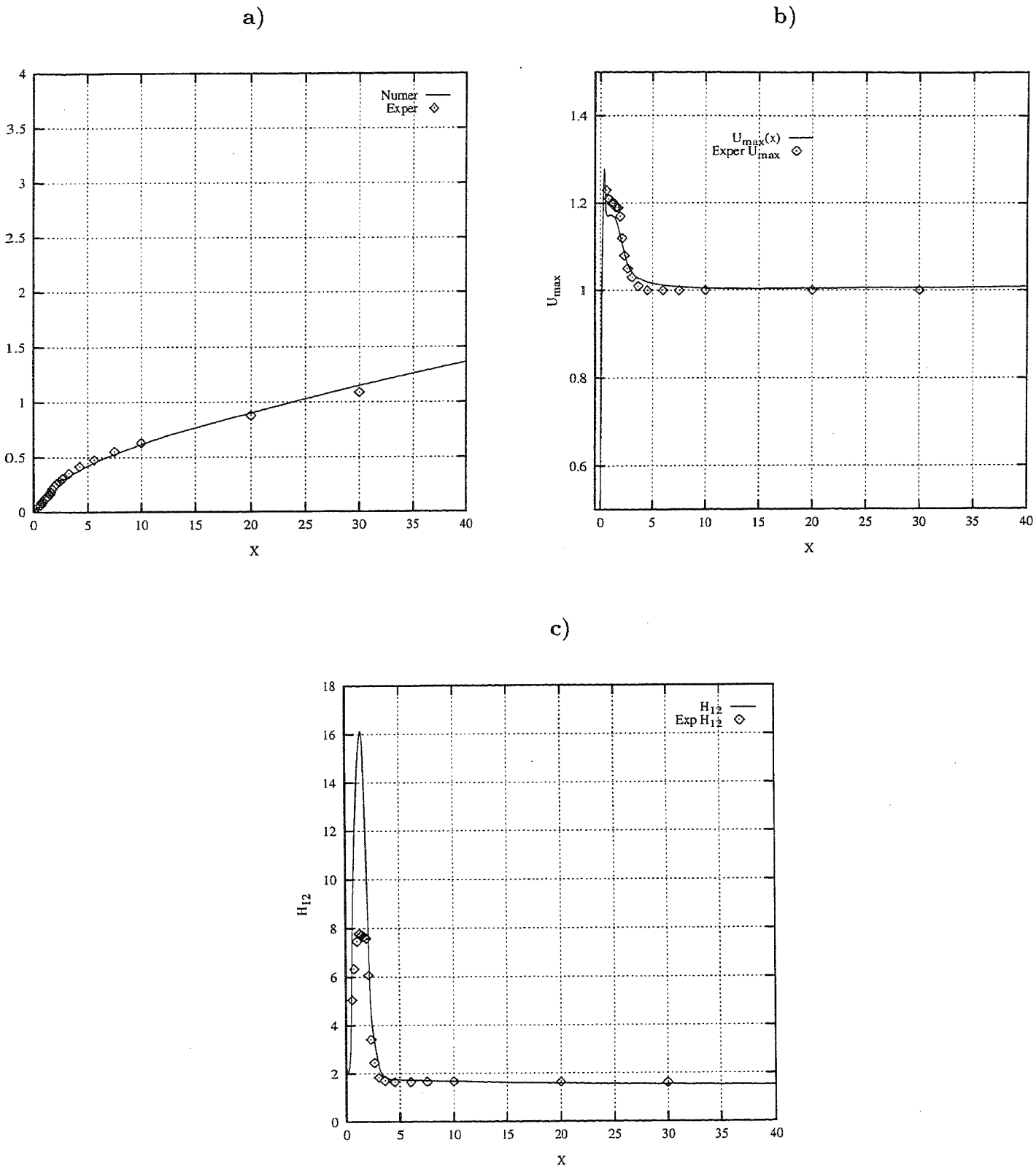

Fig. 4: Comparison between numerical (solid line) and experimental results (points) for case 1b, with $U_o = 5\ m/s$, $Tu_{\infty,6} = 0.63\ \%$.
a) Boundary-layer thickness vs. X b) Maximum velocity vs. X
c) Shape Factor H_{12} vs. X

a)

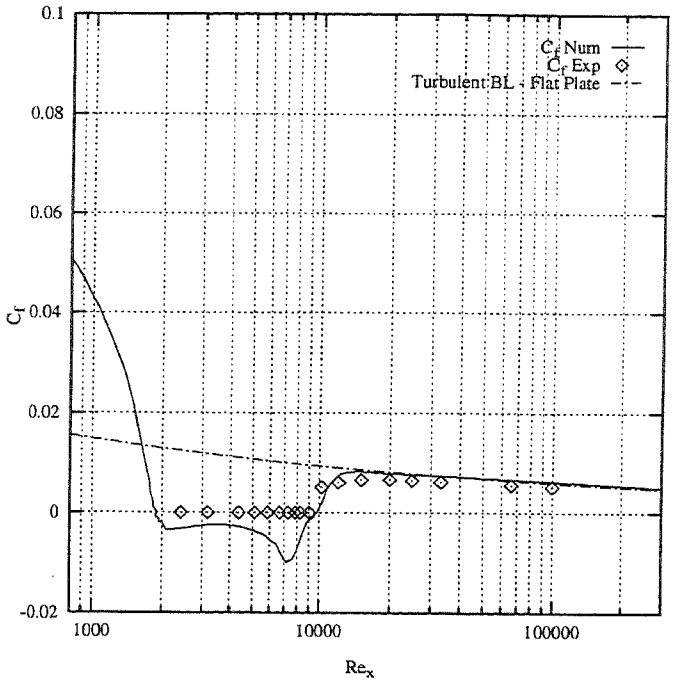

b)

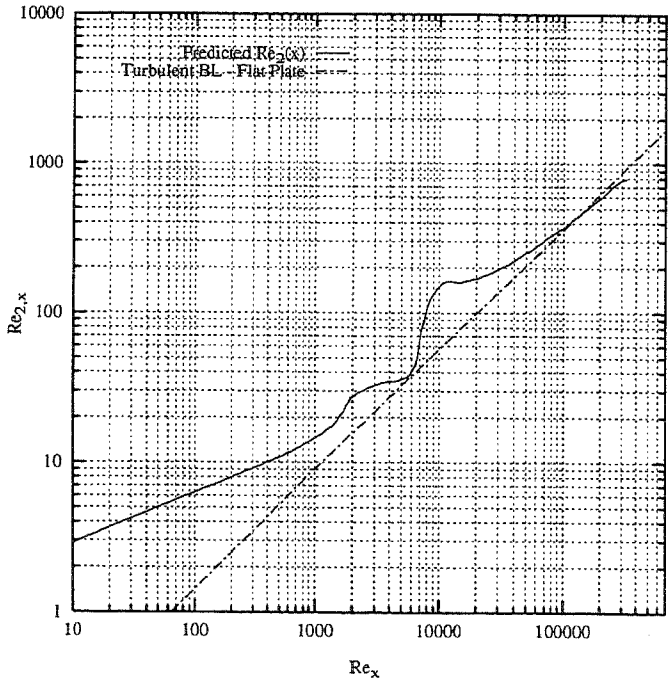

Fig. 5: Comparison between numerical (solid line), experimental results (points) and flat plate correlations (dashed lines) for case 1b, with $U_o = 5\ m/s$, $Tu_{\infty,6} = 0.63\ \%$.

a) Skin-friction coefficient C_f vs. Re_x

b) Momentum thickness Reynolds number $Re_{2,x}$ vs. Re_x

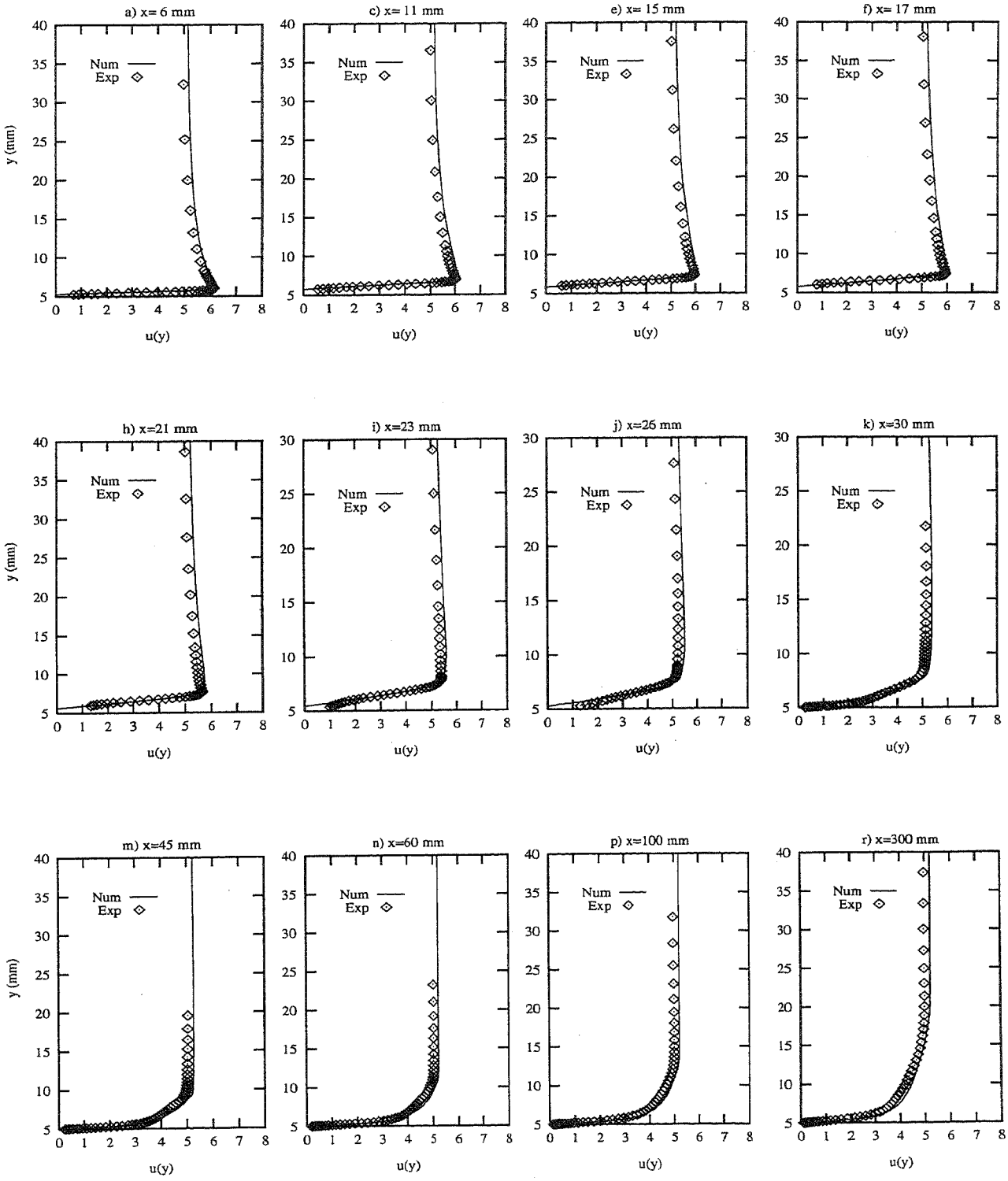

Fig. 6: Velocity $u(y)$ profiles (m/s) for case 1b with $U_o = 5\ m/s$, $Tu_{\infty,6} = 0.63\ \%$

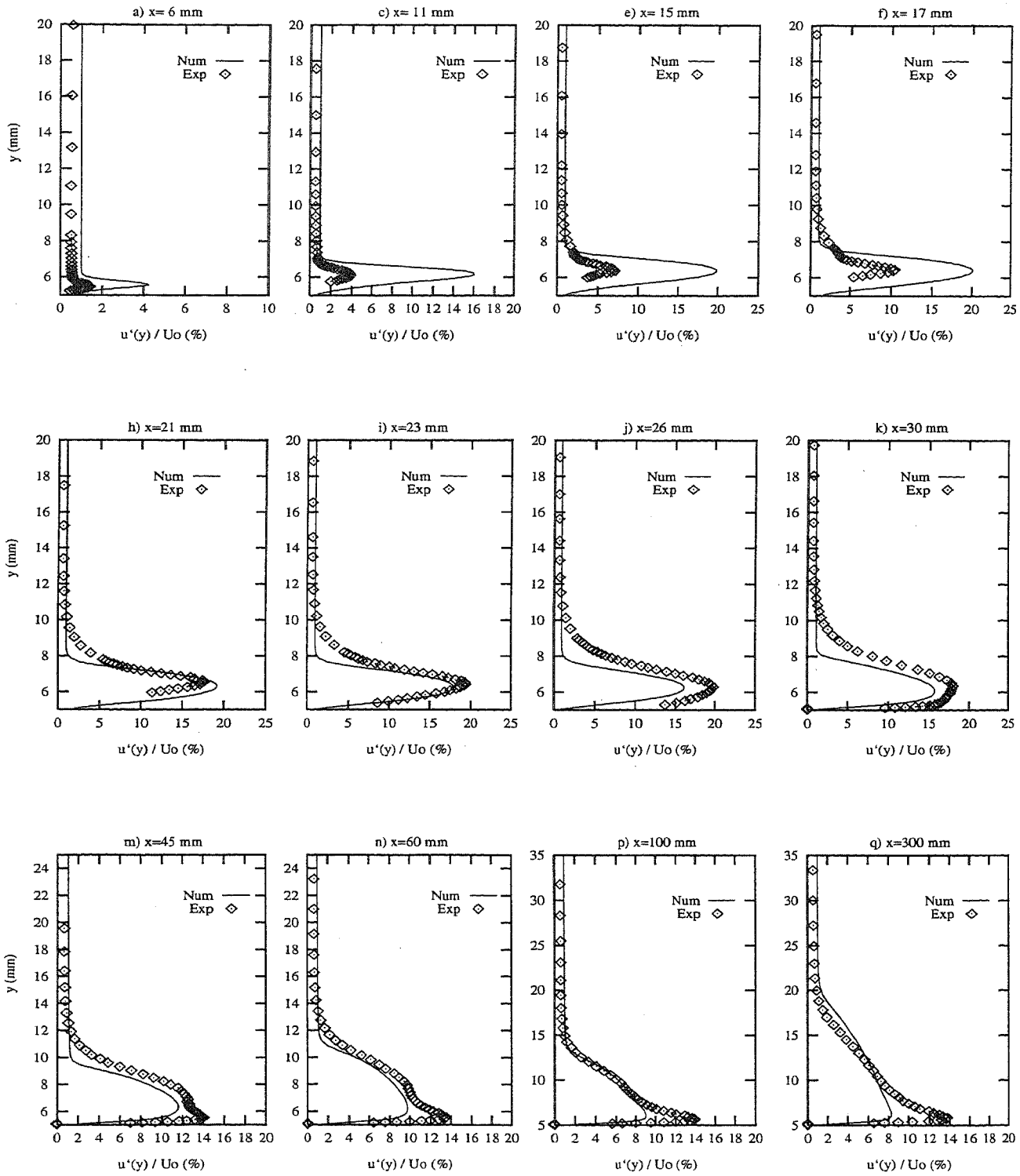

Fig. 7: Turbulence intensity $\sqrt{\overline{u'^2}}/U_i$ profiles (%) for case 1b, with $U_o = 5\ m/s$, $Tu_{\infty,6} = 0.63\ \%$

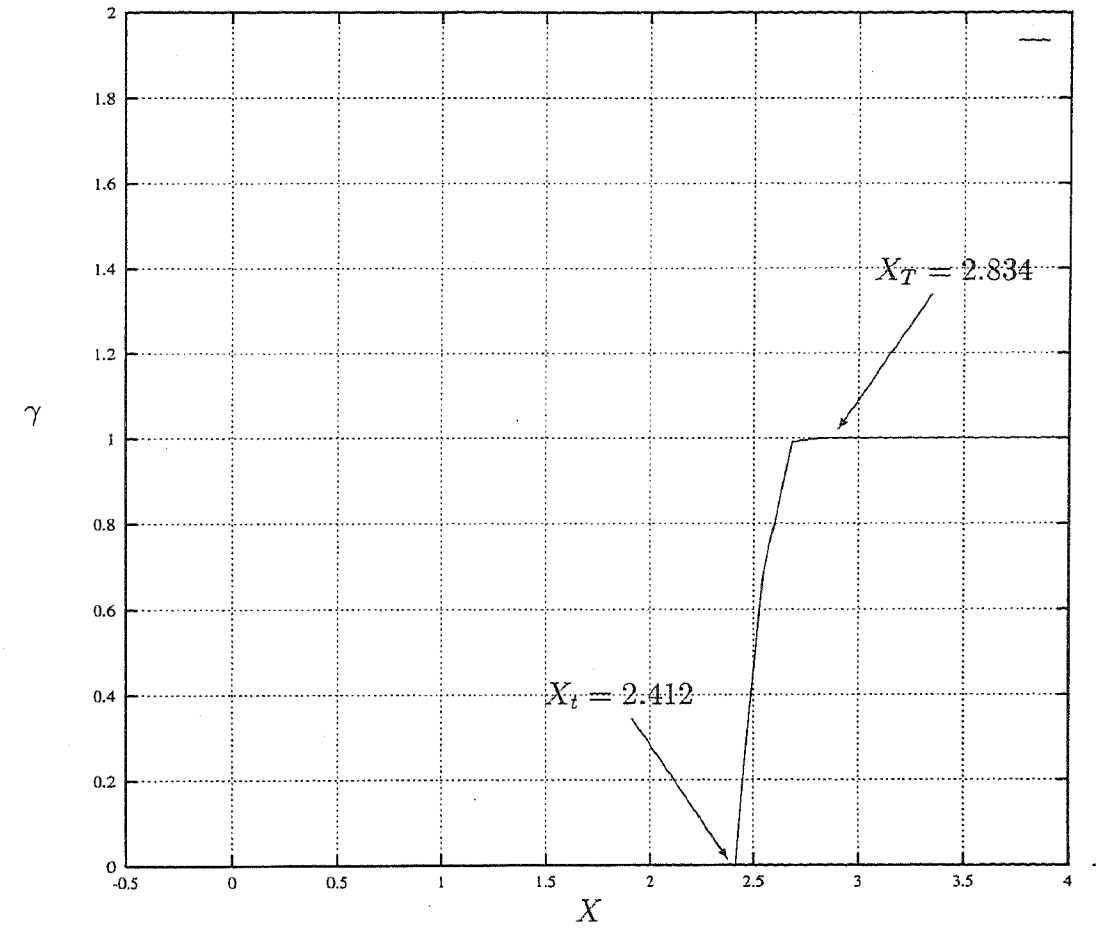

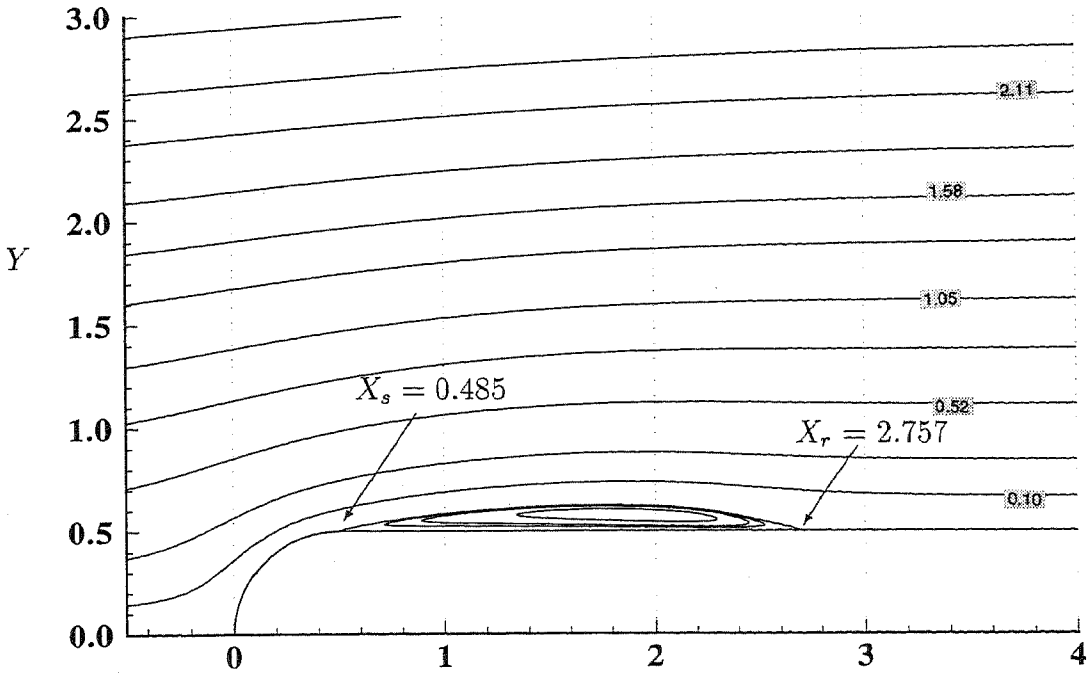

Fig. 8: Results for case 1c with $U_o = 5\ m/s$, $Tu_{\infty,6} = 2.31\ \%$.
Top : Intermittency $\gamma(x)$ - Bottom : Streamlines

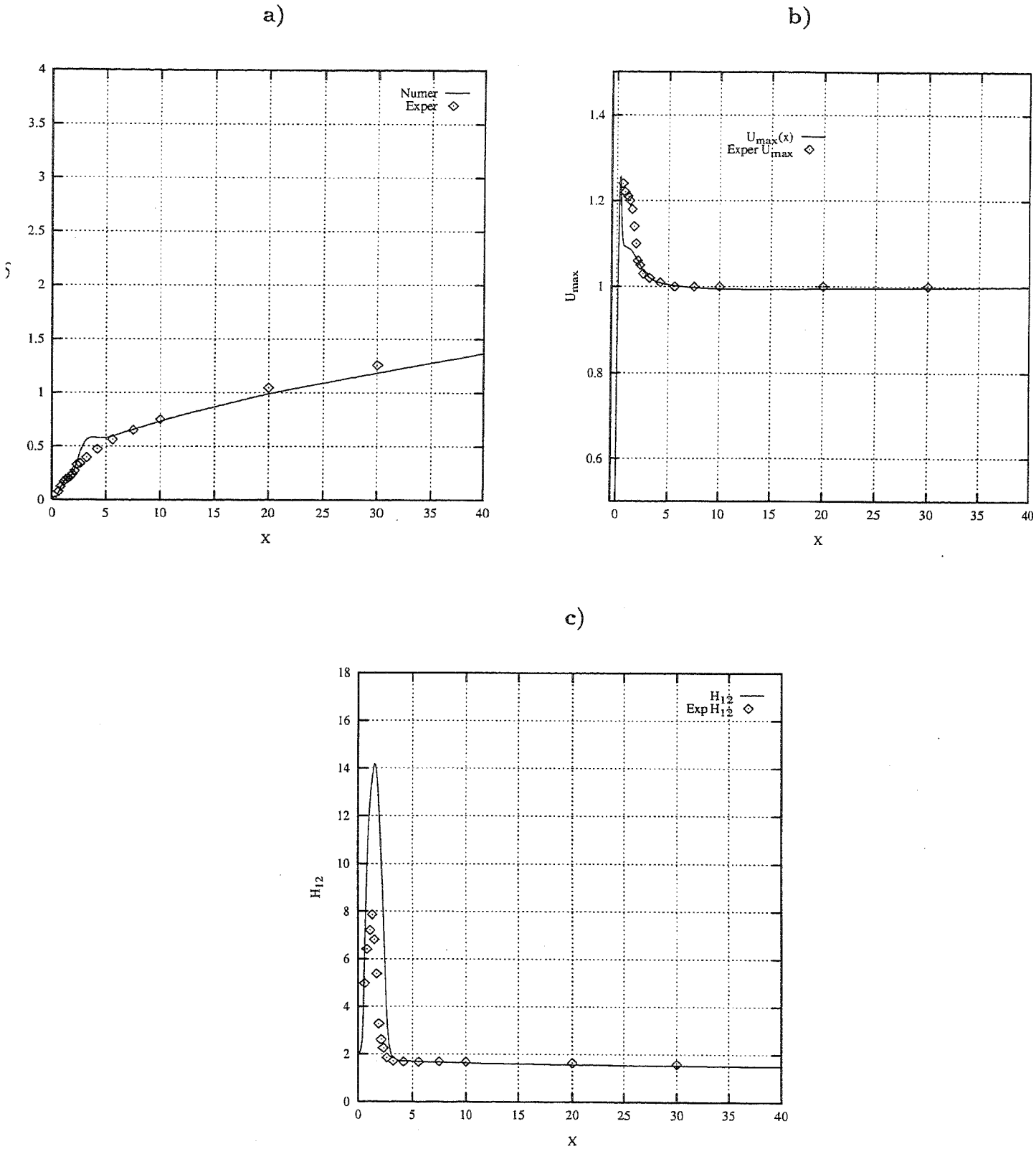

Fig. 9: Comparison between numerical (solid line) and experimental results (points) for case 1c, with $U_o = 5\ m/s$, $Tu_{\infty,6} = 2.31\ \%$.
a) Boundary-layer thickness vs. X b) Maximum velocity vs. X
c) Shape Factor H_{12} vs. X

a)

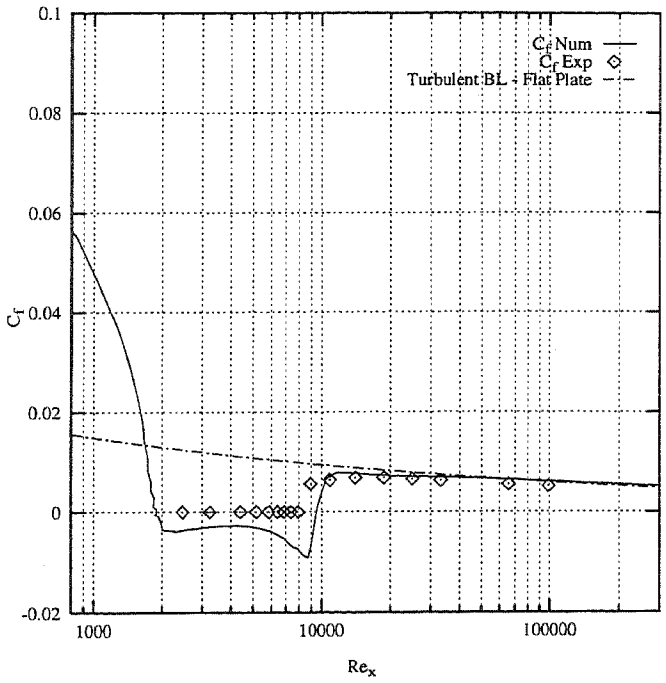

b)

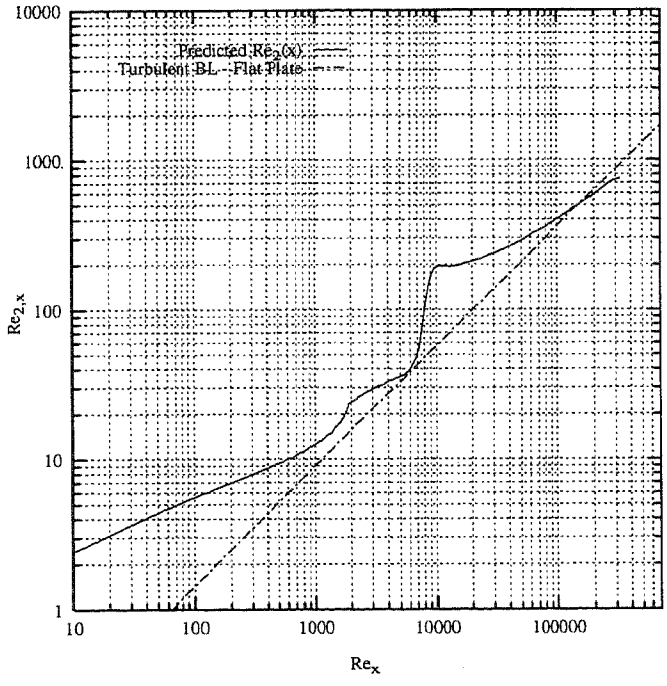

Fig. 10: Comparison between numerical (solid line), experimental results (points) and flat-plate correlations (dashed lines) for case 1c, with $U_o = 5\ m/s$, $Tu_{\infty,6} = 2.31\ \%$.

a) Skin friction coefficient C_f vs. Re_x

b) Momentum-thickness Reynolds number $Re_{2,x}$ vs. Re_x

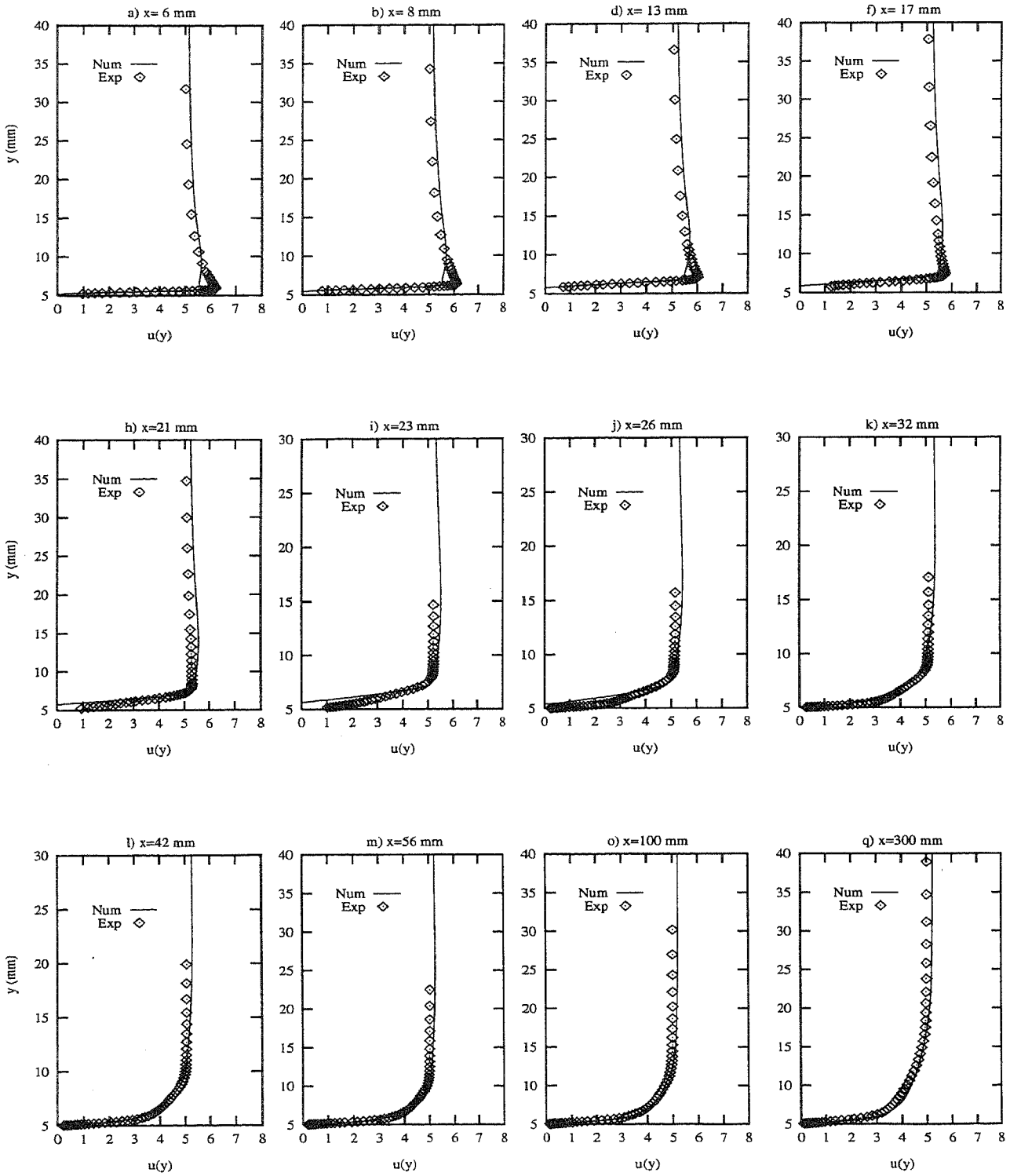

Fig. 11: Velocity $u(y)$ profiles (m/s) for case 1c with $U_o = 5\ m/s$, $Tu_{\infty,6} = 2.31\ \%$

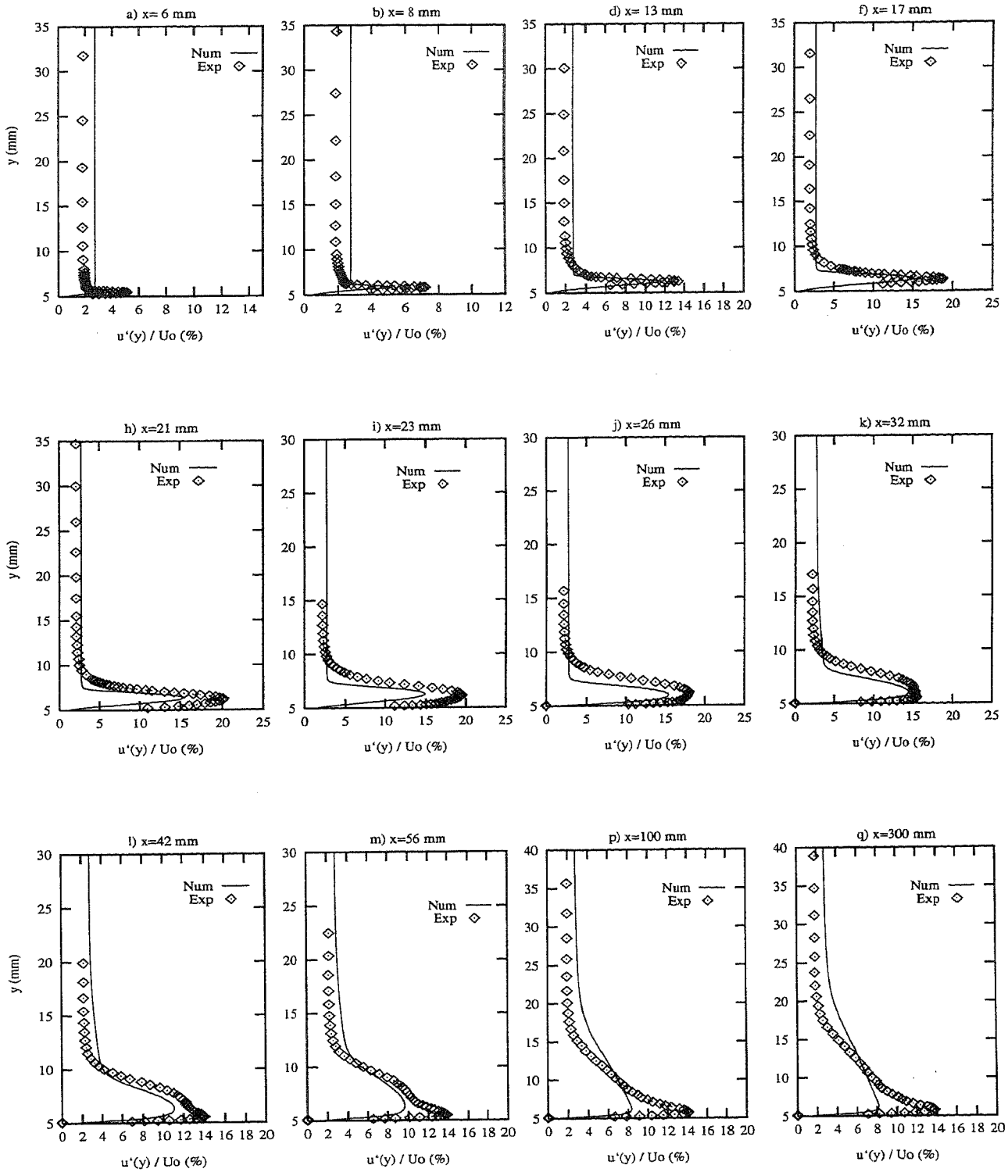

Fig. 12: Turbulence Intensity $\sqrt{\overline{u'^2}}/U_i$ profiles (%) for case 1c, with $U_o = 5\ m/s$, $Tu_{\infty,6} = 2.31\ \%$

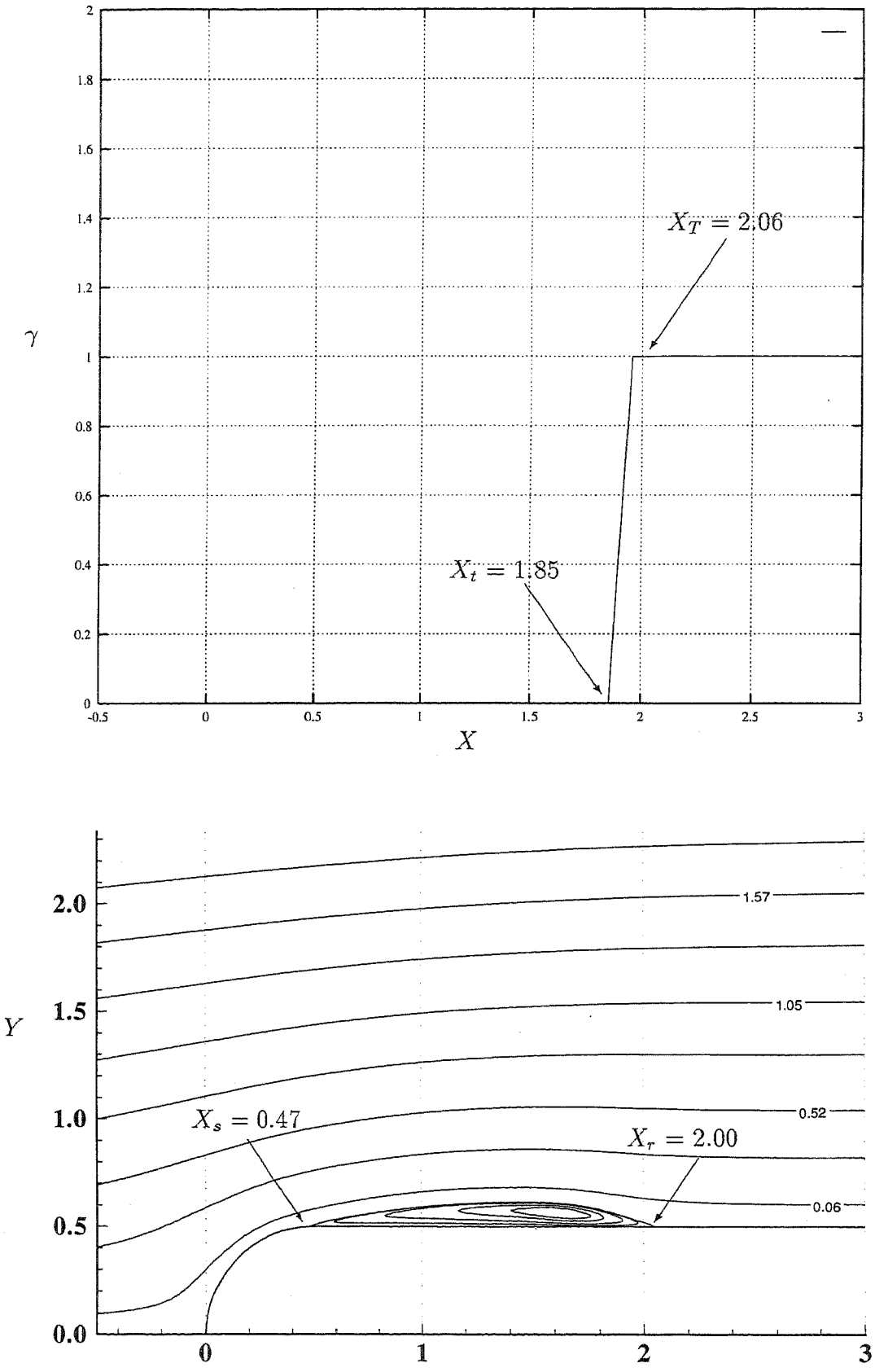

Fig. 13: Results for case 1d with $U_o = 5\ m/s$, $Tu_{\infty,6} = 5.56\ \%$.
Top : Intermittency $\gamma(x)$ - Bottom : Streamlines

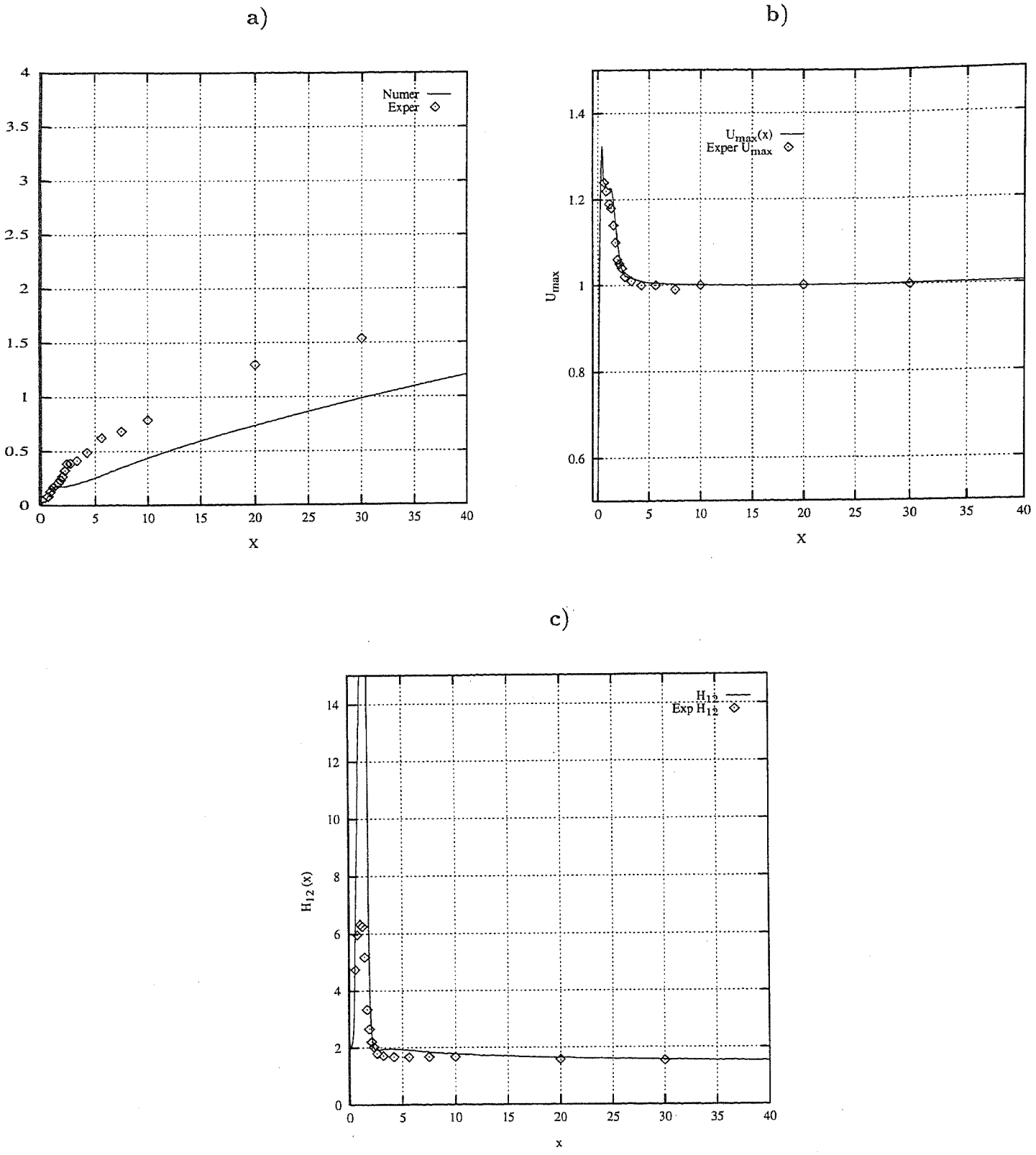

Fig. 14: Comparison between numerical (solid line) and experimental results (points) for case 1d, with $U_o = 5\ m/s$, $Tu_{\infty,6} = 5.56\ \%$.
a) Boundary-layer thickness vs. X b) Maximum velocity vs. X
c) Shape Factor H_{12} vs. X

a)

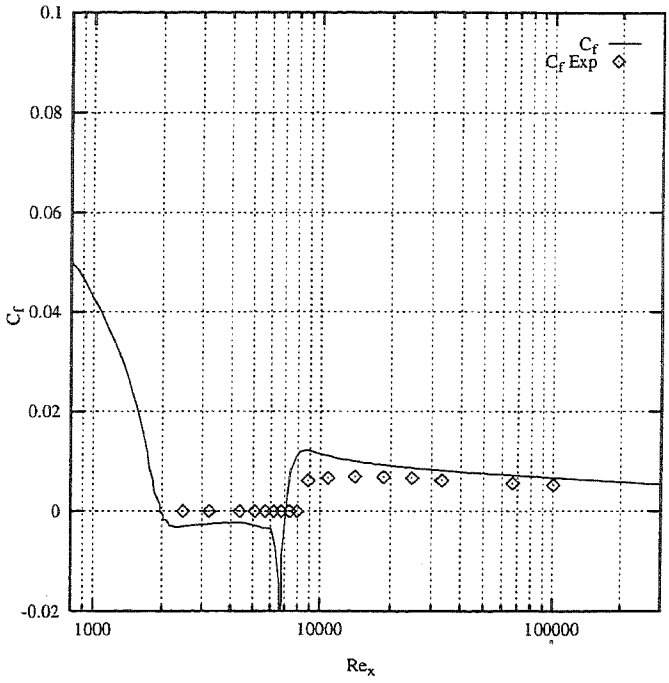

b)

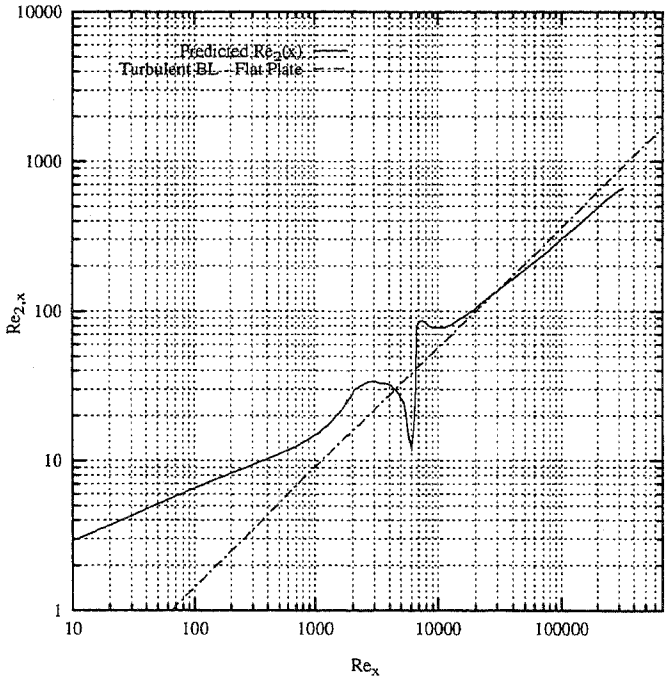

Fig. 15: Comparison between numerical (solid line), experimental results (points) and flat-plate correlations (dashed lines) for case 1d, with $U_o = 5\ m/s$, $Tu_{\infty,6} = 5.56\ \%$.

a) Skin friction coefficient C_f vs. Re_x

b) Momentum-thickness Reynolds number $Re_{2,x}$ vs. Re_x

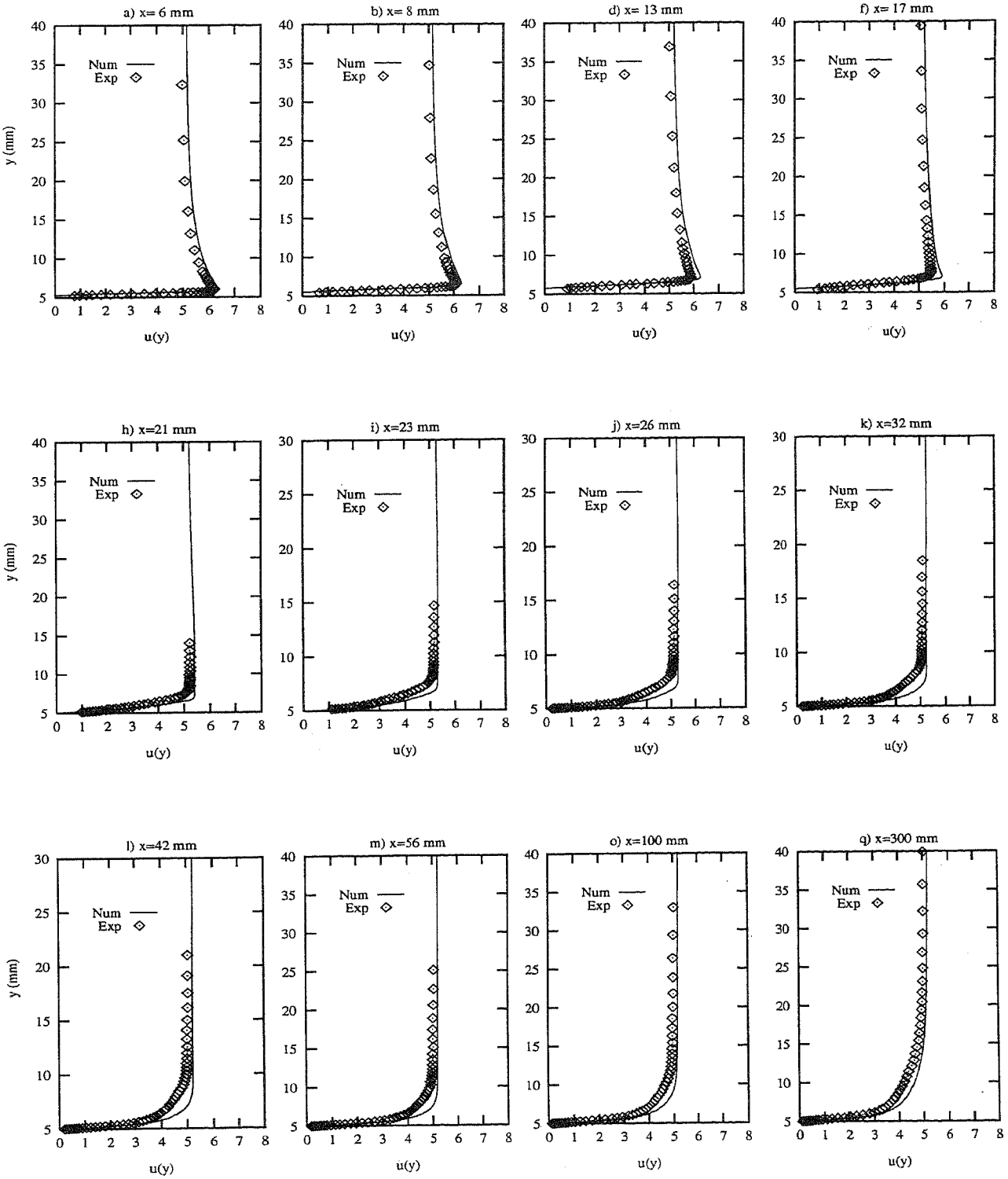

Fig. 16: Velocity $u(y)$ profiles (m/s) for case 1d with $U_o = 5\ m/s$, $Tu_{\infty,6} = 5.56\ \%$

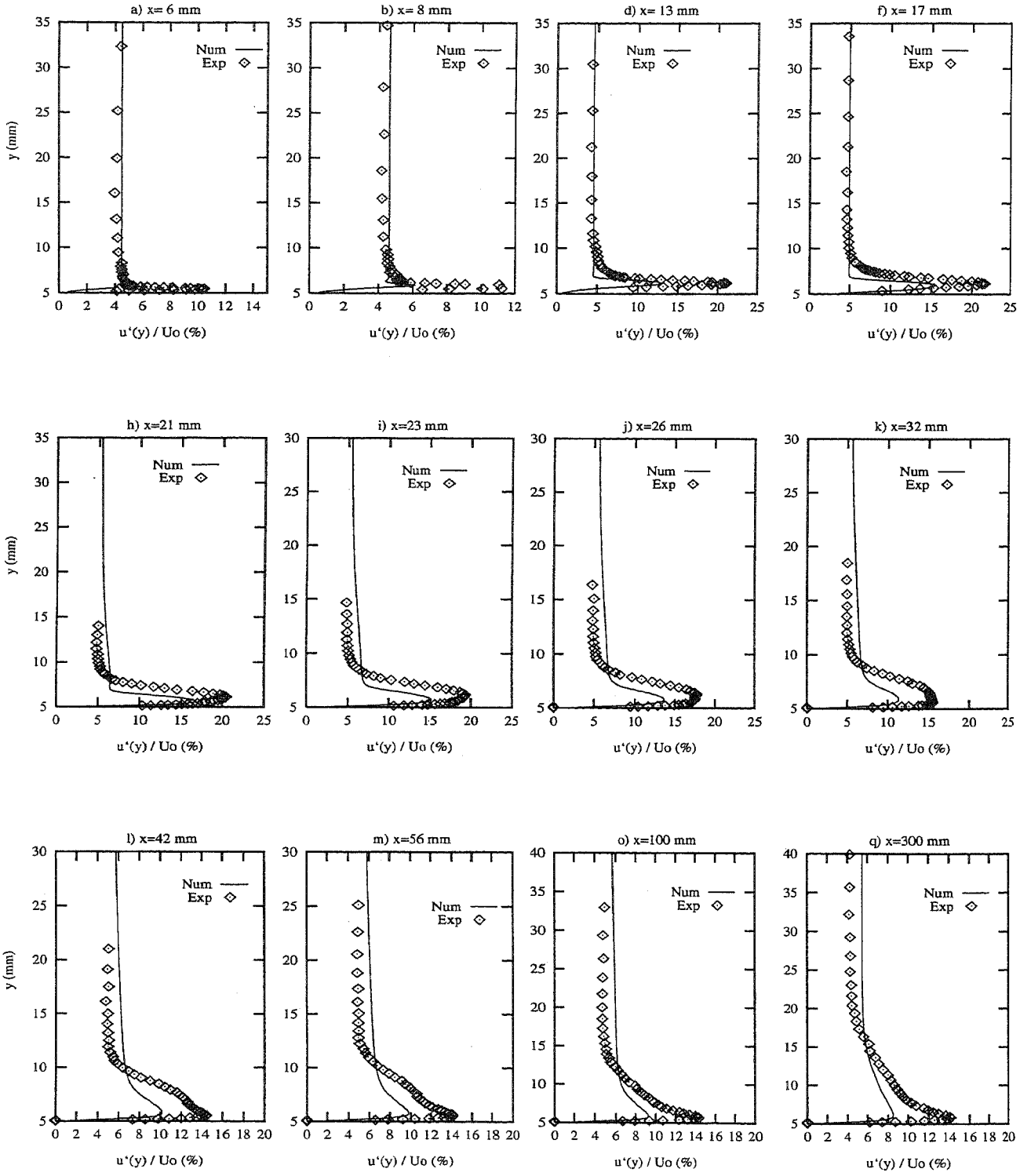

Fig. 17: Turbulence Intensity $\sqrt{\overline{u'^2}}/U_i$ profiles (%) for case 1d, with $U_o = 5\ m/s$, $Tu_{\infty,6} = 5.56\ \%$

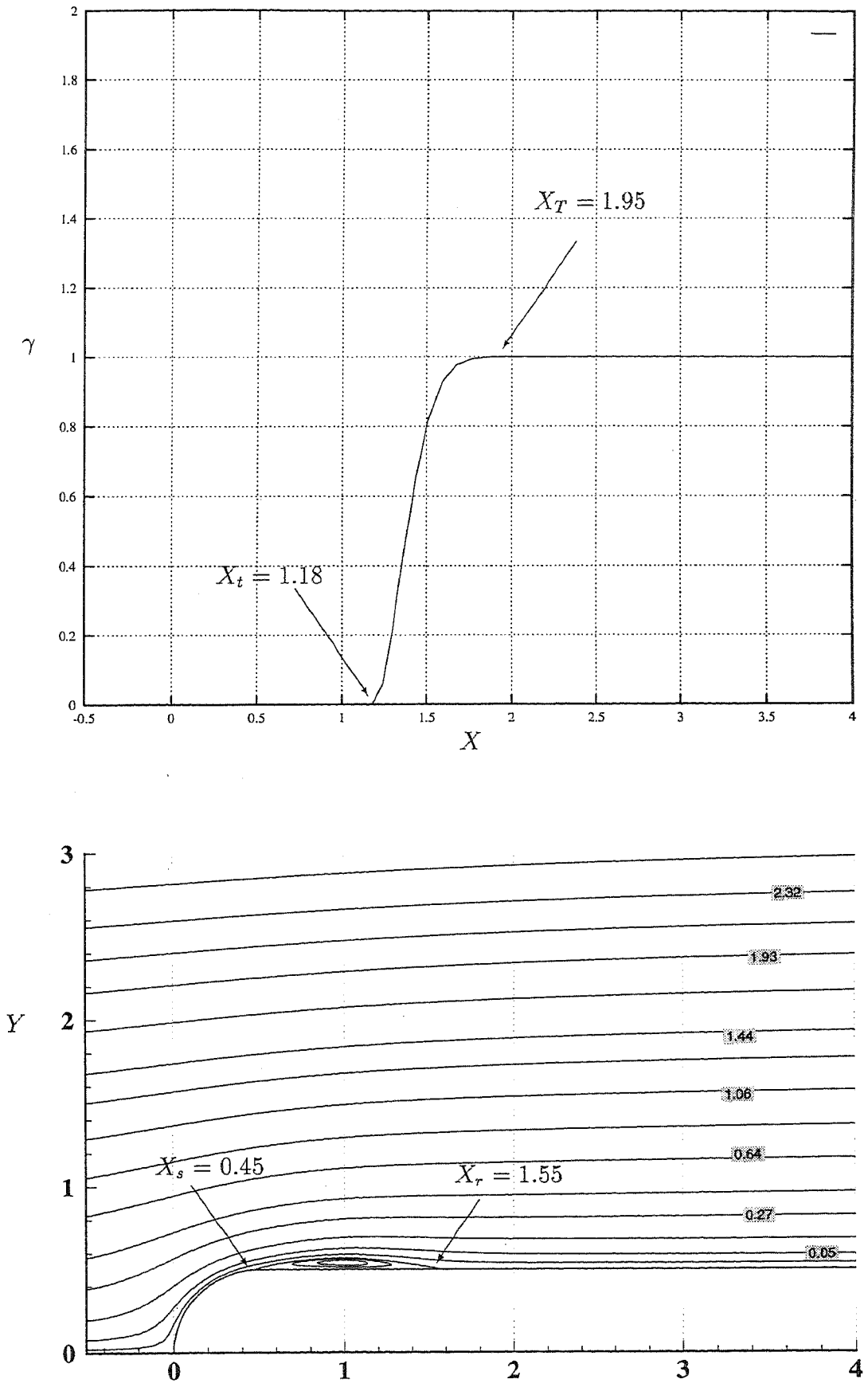

Fig. 18: Results for case 1f with $U_o = 10\ m/s$, $Tu_{\infty,6} = 2.5\ \%$.
Top : Intermittency $\gamma(x)$ - Bottom : Streamlines

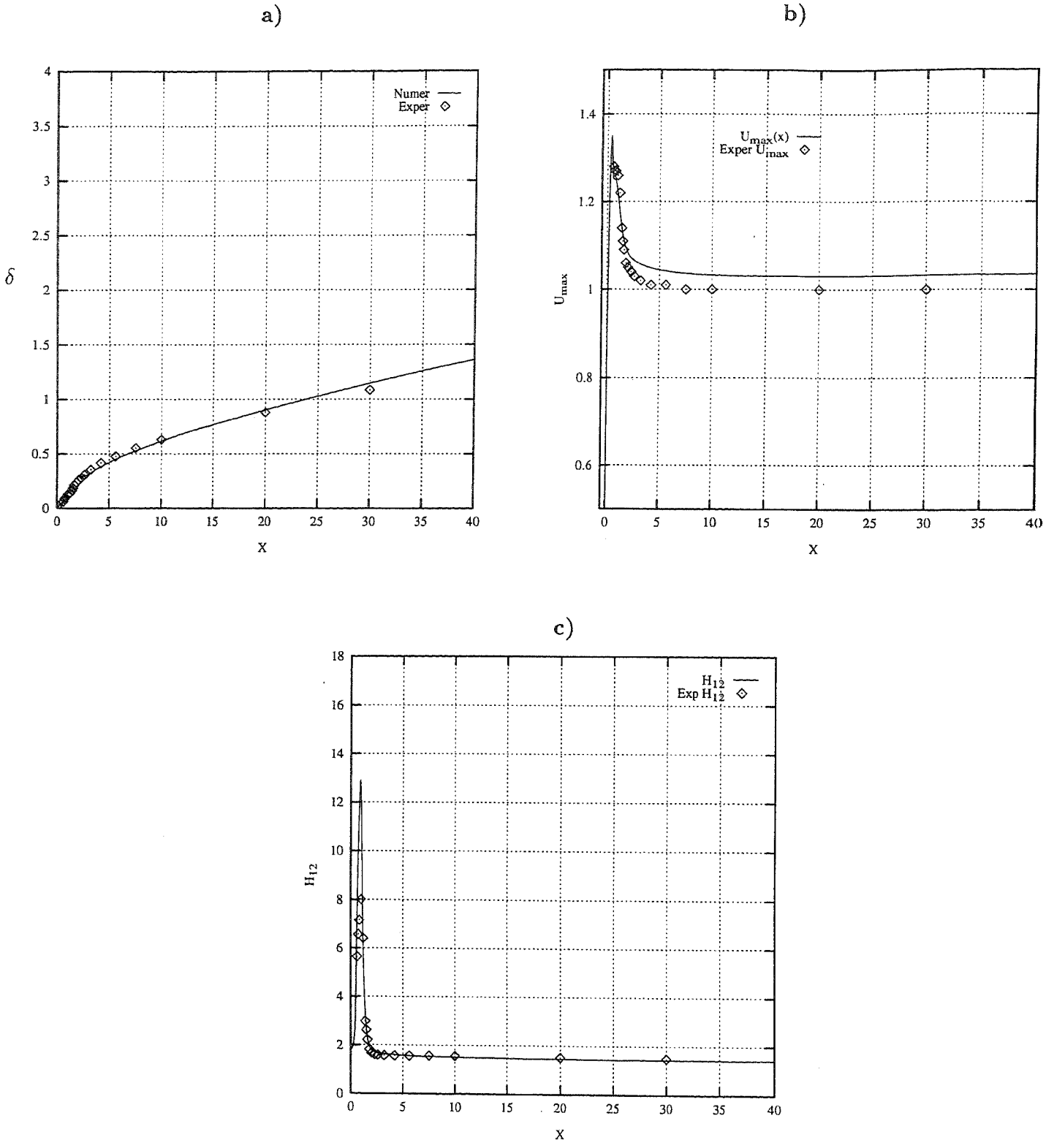

Fig. 19: Comparison between numerical (solid line) and experimental results (points) and flat-plate correlations (dashed lines) for case 1f, with $U_o = 10\ m/s$, $Tu_{\infty,6} = 2.5\ \%$.

a) Boundary-layer thickness vs. X b) Maximum velocity vs. X

c) Shape Factor H_{12} vs. X

a)

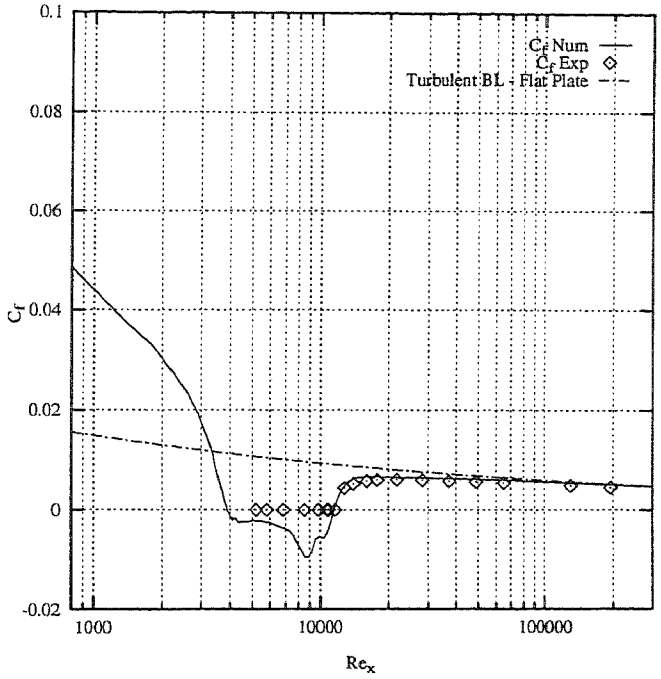

b)

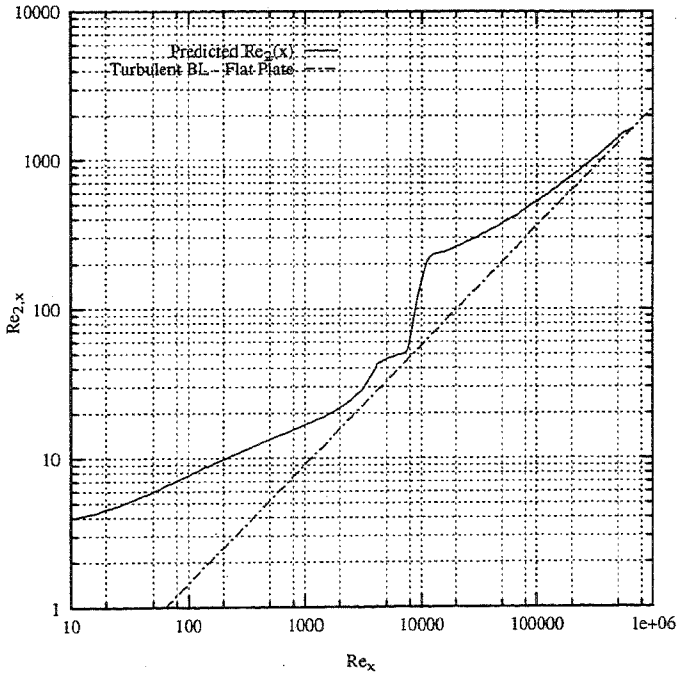

Fig. 20: Comparison between numerical (solid line), experimental results (points) and flat-plate correlations (dashed lines) for case 1f, with $U_o = 10\ m/s$, $Tu_{\infty,6} = 2.5\ \%$.

a) Skin-friction coefficient C_f vs. Re_x

b) Momentum-thickness Reynolds number $Re_{2,x}$ vs. Re_x

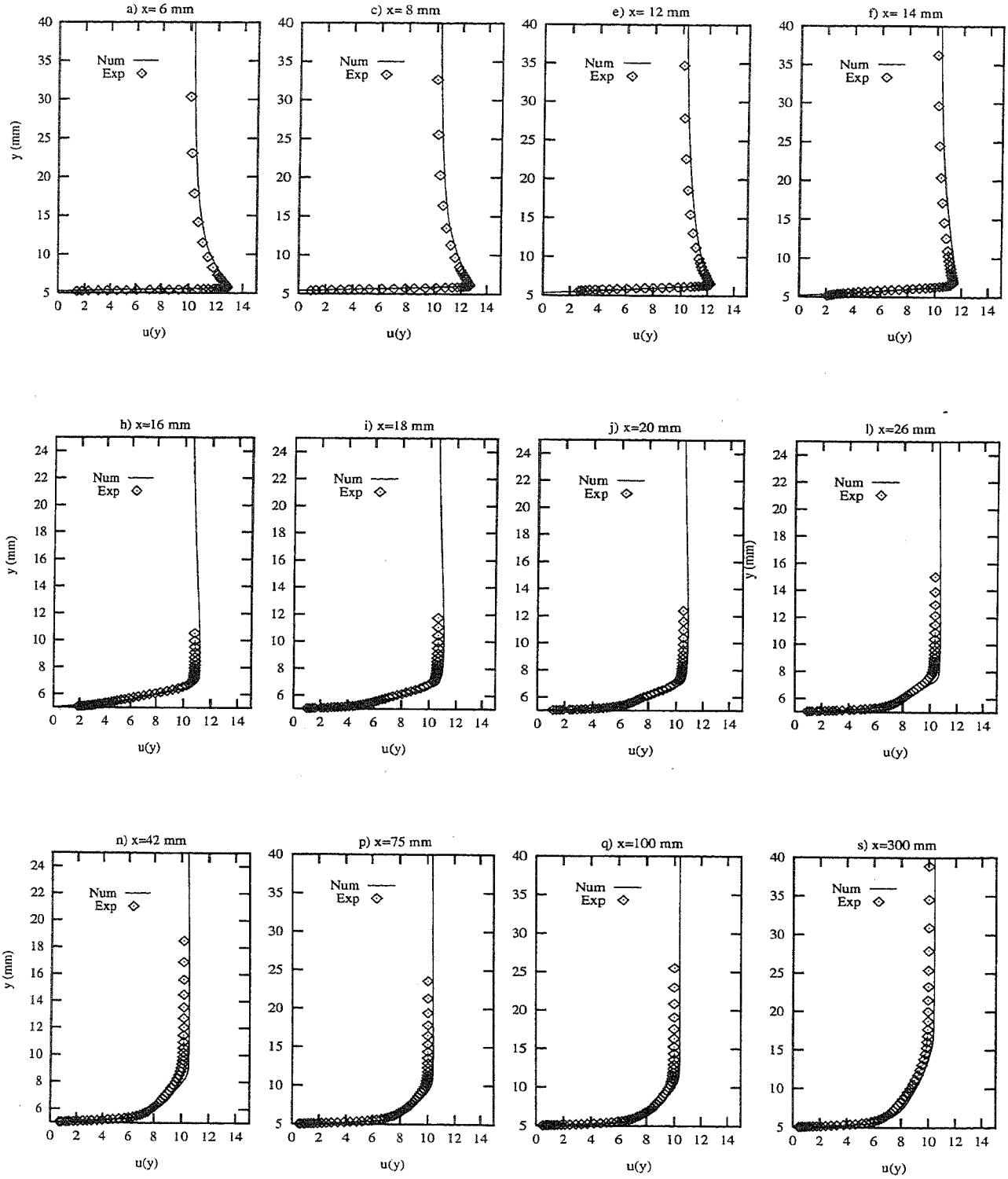

Fig. 21: Velocity $u(y)$ profiles (m/s) for case 1f with $U_o = 10\ m/s$, $Tu_{\infty,6} = 2.5\ \%$

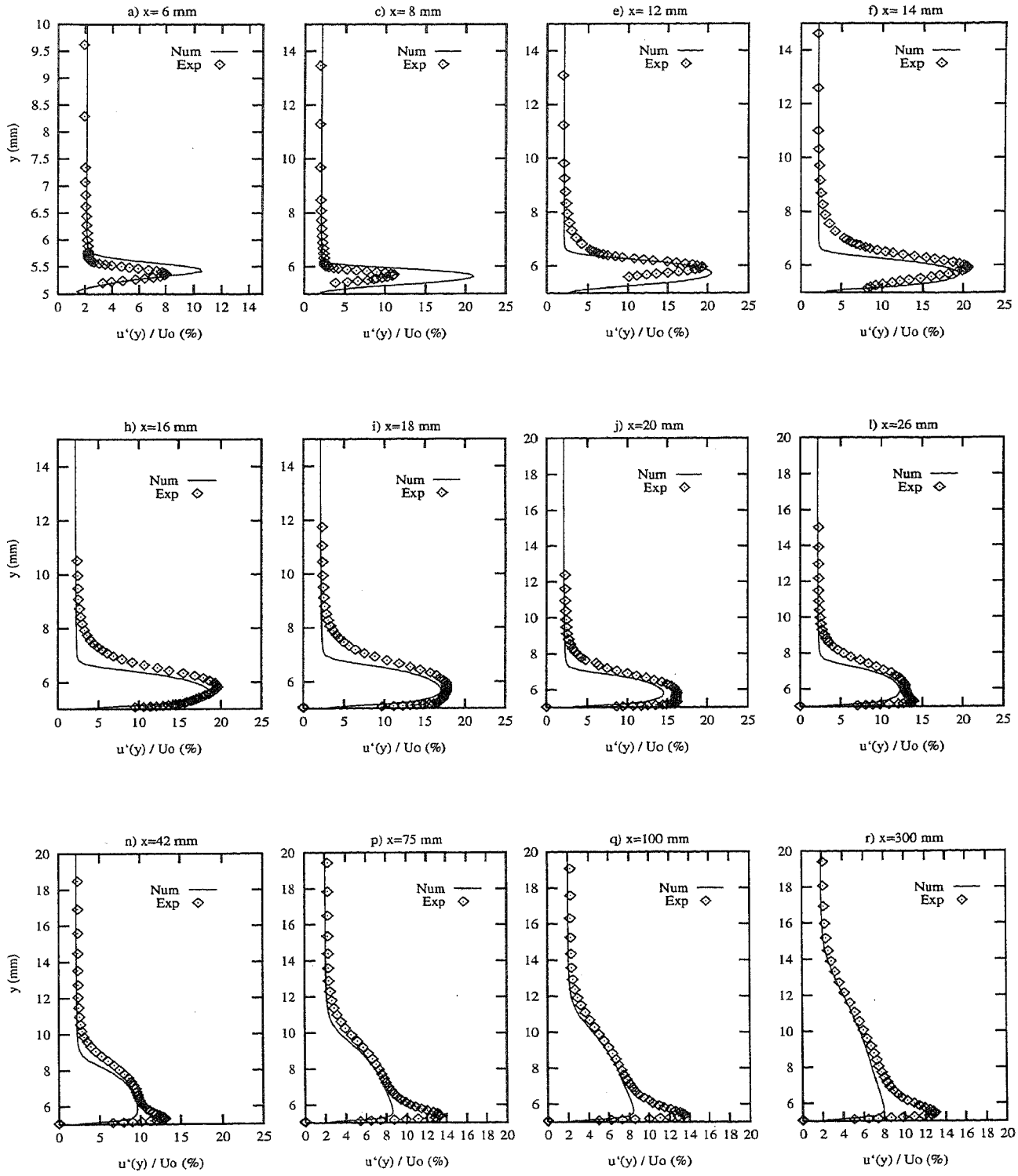

Fig. 22: Turbulence Intensity $\sqrt{\overline{u'^2}}/U_i$ profiles (%) for case 1f, with $U_o = 10\ m/s$, $Tu_{\infty,6} = 2.5\ \%$

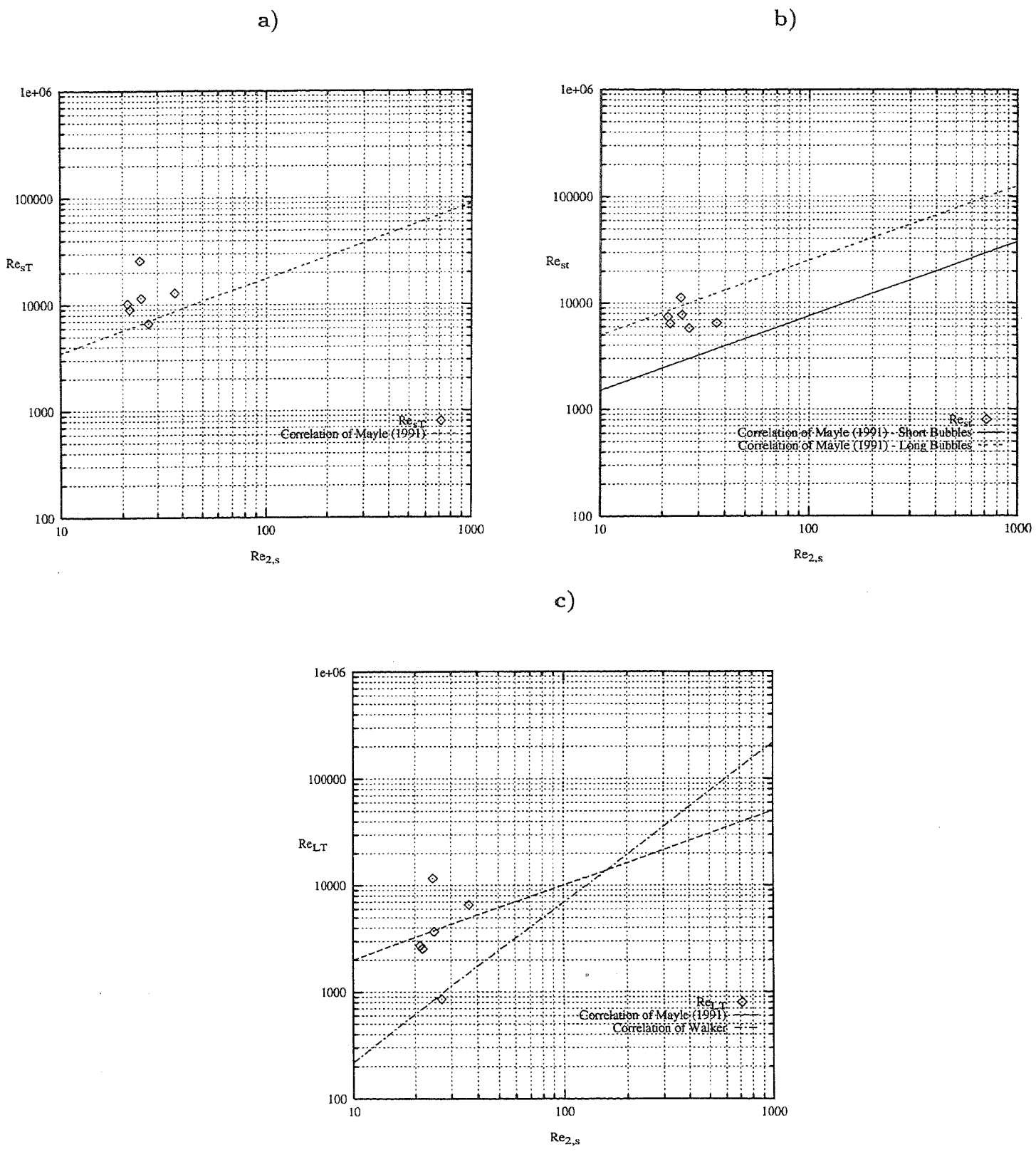

Fig. 23: Separation-bubble data for case 1, in terms of $Re2,s$ at separation compared against available correlations. The ordinate is a Reynolds number expressed in terms of :

a) The length of the constant-pressure region (Re_{sT}) b) The distance between separation and transition points (Re_{st}) c) The length of the transition region (Re_{LT})

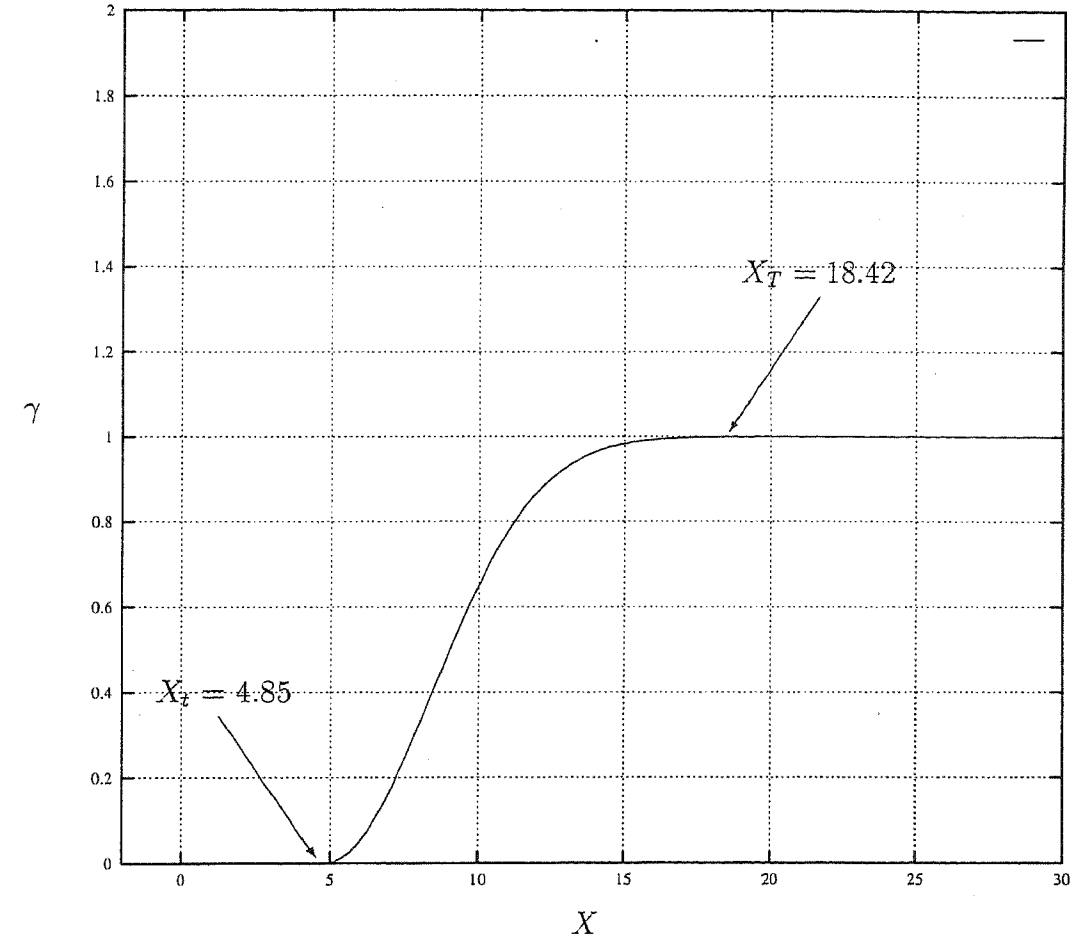

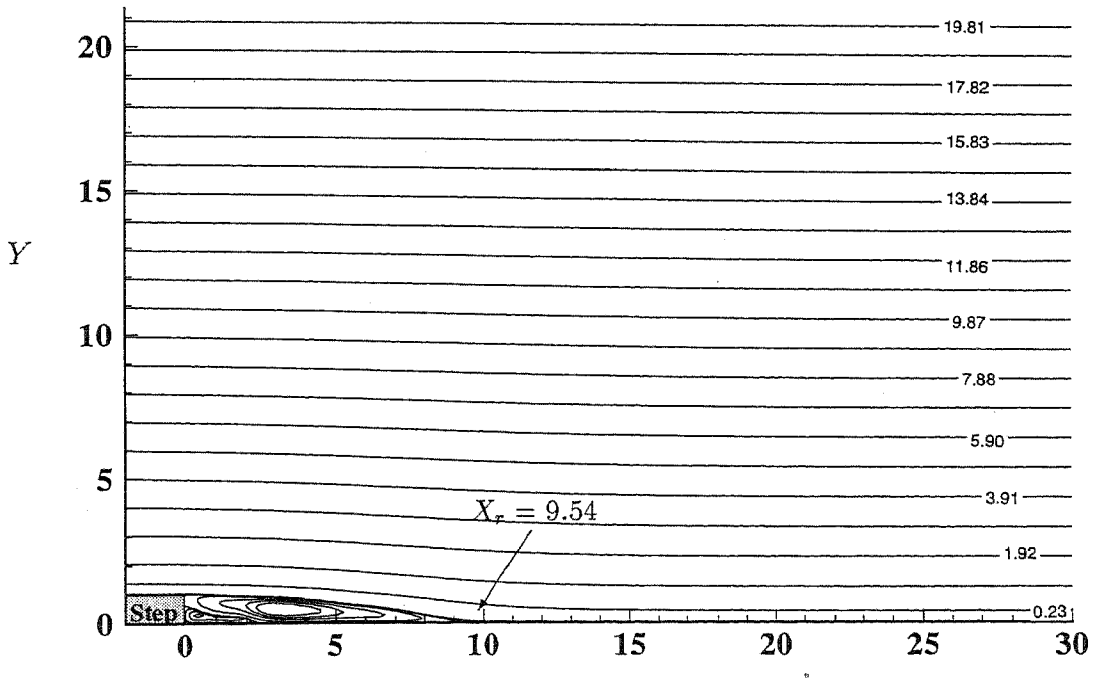

Fig. 24: Results for testcase 2 (backward-facing step) with $U_o = 11.38\ m/s$, $Tu_\infty = 1.11 \times 10^{-2}$ %.
Top : Intermittency $\gamma(x)$ - Bottom : Streamlines

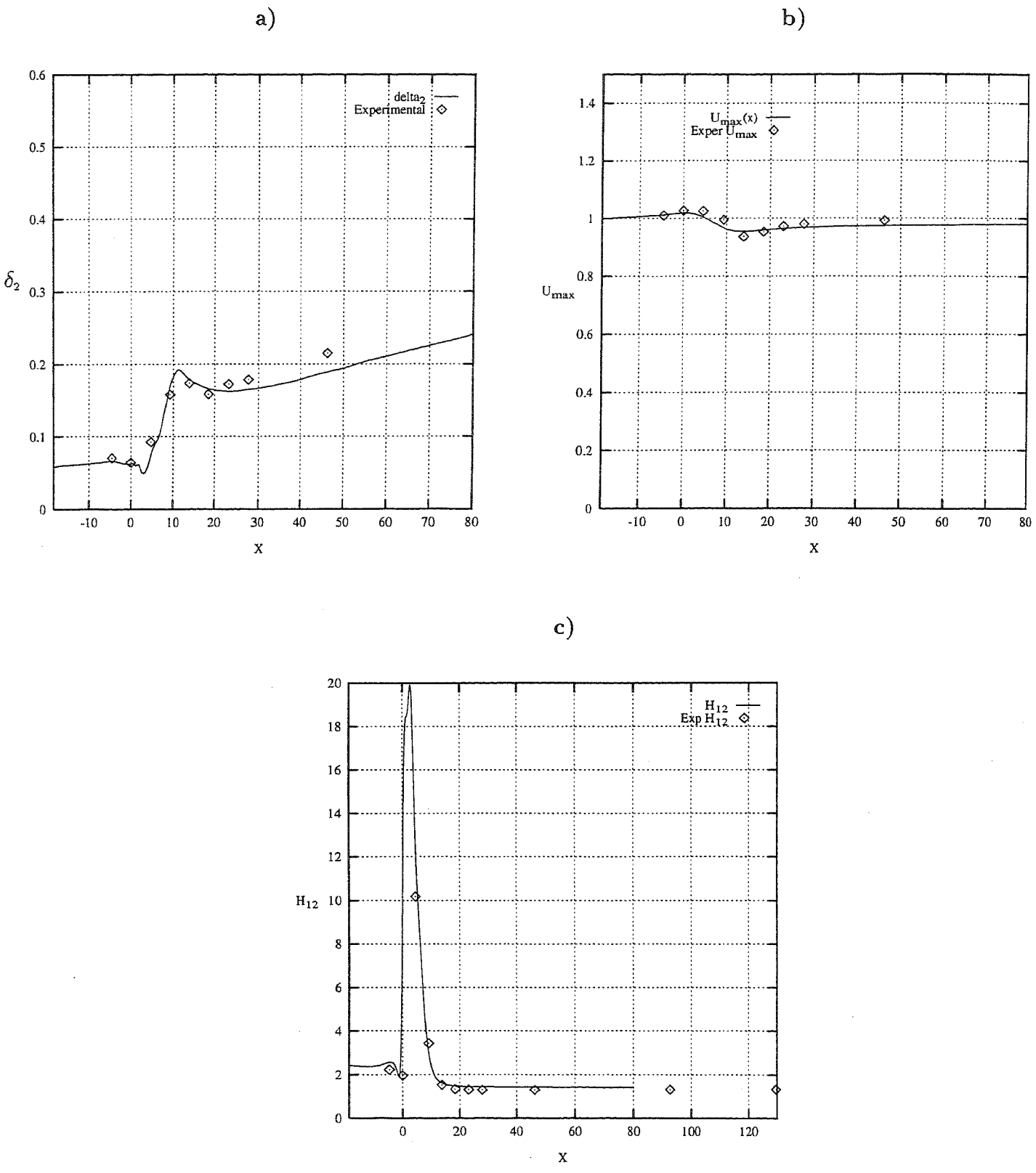

Fig. 25: Comparison between numerical (solid line) and experimental results (points) for testcase 2 (backward-facing step), with $U_o = 11.38\ m/s$, $Tu_\infty = 1.11 \times 10^{-2}$ %.

a) Momentum thickness δ_2 vs. X b) Maximum velocity vs. X

c) Shape Factor H_{12} vs. X

a)

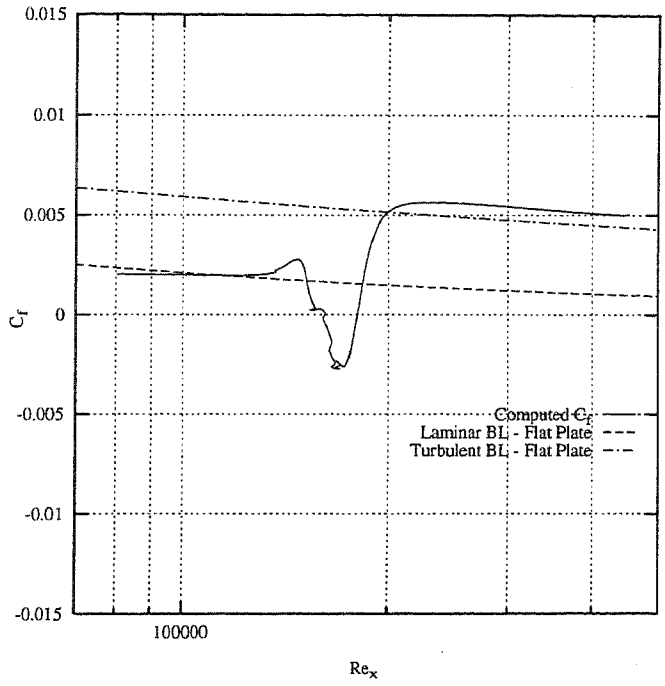

b)

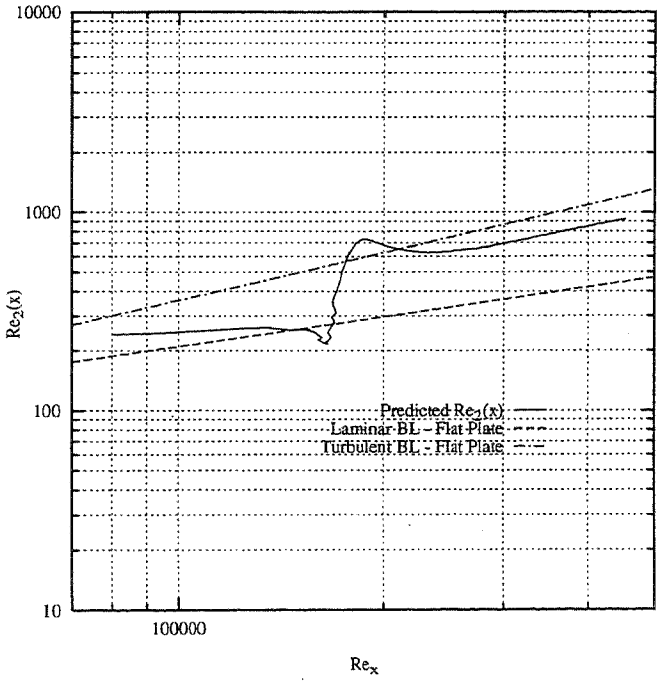

Fig. 26: Comparison between numerical (solid line), experimental results (points) and flat-plate correlations for testcase 2 with $U_o = 11.38\ m/s$, $Tu_\infty = 1.11 \times 10^{-2}$ %.

a) Skin friction coefficient C_f vs. Re_x

b) Momentum-thickness Reynolds number $Re_{2,x}$ vs. Re_x

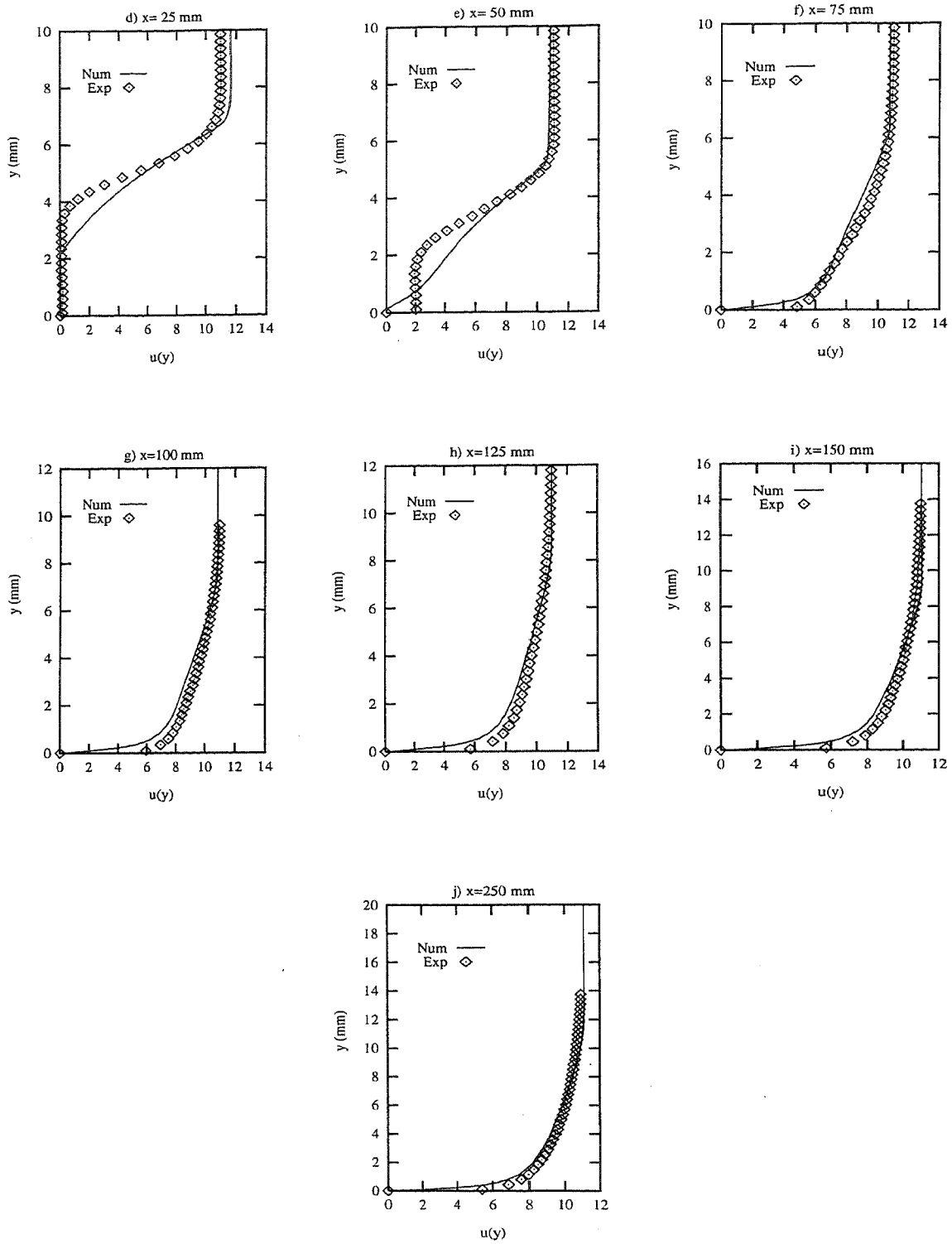

Fig. 27: Velocity $u(y)$ profiles (m/s) downstream of the step for testcase 2 (backward-facing step) with : $U_o = 11.38\ m/s$, $Tu_\infty = 1.11 \times 10^{-2}$ %

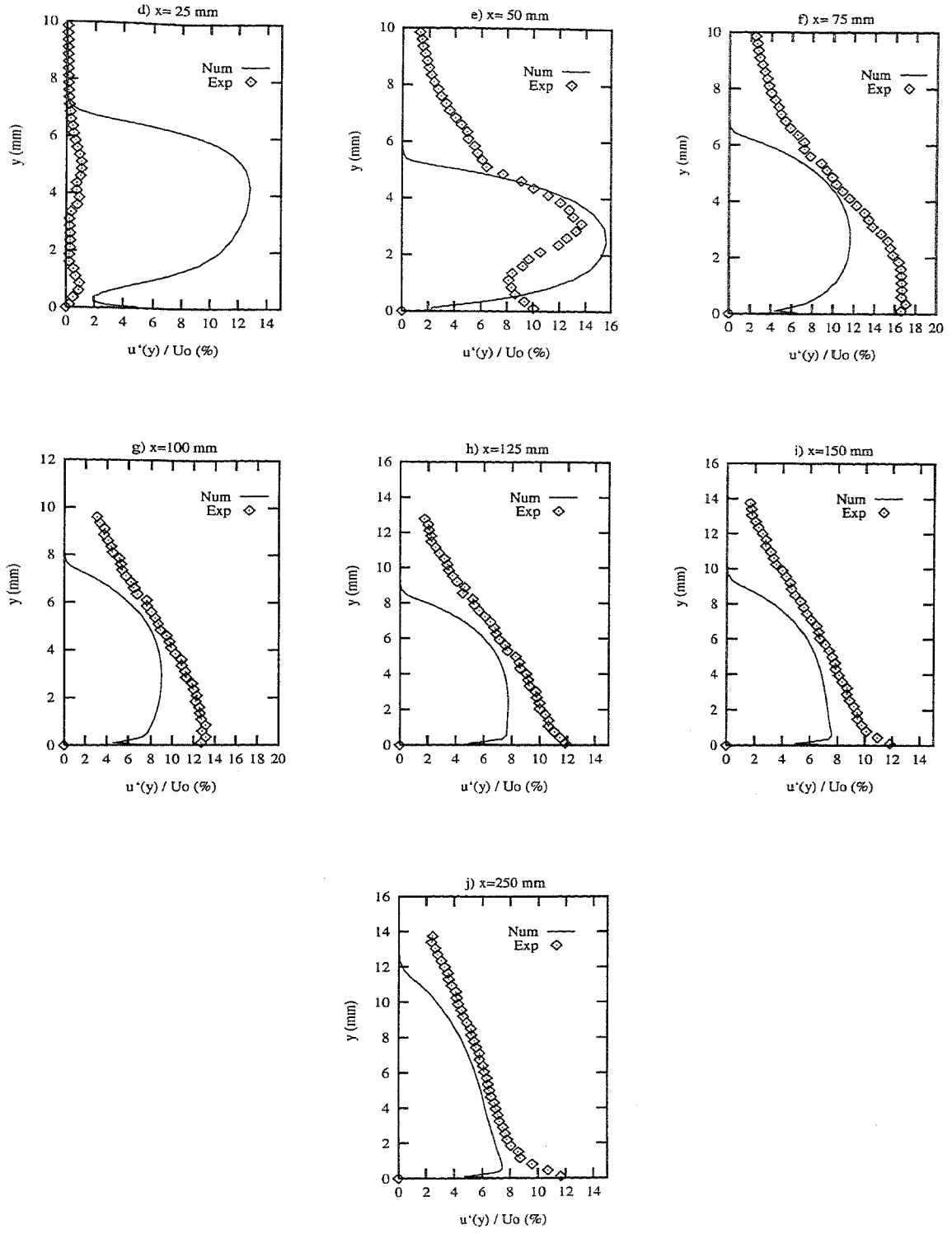

Fig. 28: Turbulence Intensity $\sqrt{\overline{u'^2}}/U_i$ profiles (%) downstream of the step for testcase 2 (backward-facing step), with $U_o = 11.38\ m/s$, $Tu_\infty = 1.11 \times 10^{-2}$ %

Anhang E

Turbulence and Transition Modelling in Transonic Turbine Flows

Institute for Hydromechanics
University of Karlsruhe

Report No. 728

Turbulence and Transition Modelling in Transonic Turbine Flows

Vittorio Michelassi*

February 1996

* on leave from the University of Florence, Italy

Acknowledgements

The authors wishes to gratefully acknowledge Dr. Georgios Theodoridis and Dr. Elias Papanicolaou for having supplied the updated version of the compressible pressure correction code for turbulent flow regime.

The author also wishes to thank Prof. Wolfgang Rodi and Prof. Francesco Martelli for the support and guide granted during the preparation of his work.

The work was sponsored by the German Federal Ministry of Education, Science, Research and Technology through Programme TURBOTECH under contract no. 0326801G.

List of contents

1 - INTRODUCTION

Gas turbine engines are becoming more and more popular in the field of energy conversion systems. The aerodynamic performances of the turbine stage is of primary importance because of its large impact on the overall efficiency of aeropropulsion engines and power plants. From a thermodynamic point of view the efficiency of gas turbine engines can be obtained by increasing the maximum cycle temperature. This technique requires appropriate blade cooling systems to prevent serious damages to the turbine stage. The effect of boundary layers on the performances of a turbine stage is also large, and becomes dramatic if flow separation is encountered in the blade vane. In both the heat transfer and boundary layer studies, turbulence and transition play a crucial role [14].

Turbulence modelling in transonic turbine flows is normally carried out by simple algebraic models, like the Baldwin-Lomax formulation. These models, while not altering the robustness and speed of the Navier-Stokes equation solvers, are often not able to guarantee a good degree of accuracy in a wide range of flows. Moving to more complex turbulence models does not guarantee itself an improvement in the fit with experiments and in the design applicability of the numerical models. Still, when leaving the so called zero-equation approach in the modelling of turbulence and moving towards two-equation or second moment closures, it is undeniably true that more "physics" is brought into the model. Second moment closures often require a very large computational effort due to the high non linearity of the transport equations involved. Moreover, second moment closures based on the wall functions as boundary conditions for solid walls are inadequate for flows with strong pressure gradients, like those normally encountered in turbine flows. Although second moment closures can, and have been formulated to allow the integration of the mean and turbulence quantities in the viscous and buffer layers, very often the large increase in computational effort is not accompanied by a proportional improvement in the quality of the results [21].

A good compromise between accuracy and computational efficiency is still given by the two-equation approach. Despite the theoretical limitations, the two-equation models are often able to give a good accuracy in terms of pressure distribution and head losses which are of primary importance for the evaluation of the blade load and efficiency. The latest versions of the two-equation models have been tuned with the Direct Numerical Simulation data. While the research in this field is still going on, the new two-equation models able to solve inside the viscous and buffer layers, thereby avoiding the cumbersome wall-function method, showed interesting results in a wide range of applications.

Transition to turbulence and reverse transition are additional problems encountered in the field of turbulence modelling in turbomachinery flows. Transition can take place in several ways, which will be discussed in the following sections, and can be controlled by the local turbulence level, pressure gradient, and the flow history. Savill [36] drawed a comprehensive summary of the research in the field of by-pass transition. In his review Savill considered the bypass transition on a flat plate in presence or not of pressure gradient and with variable turbulence level as modelled by two equation turbulence models with or without a transition model. Most the two-equation formulations fail to predict transition properly and it is necessary to introduce an extra model which should account for pressure gradients and turbulence level, as experiments indicate. In turbine flows, the effect of streamline curvature and the large pressure gradients often render the results obtained for flat plate boundary layers unreliable. Moreover, when compressibility effects play a significant role, transition may not occur via the by-pass mode, but through sudden transition induced by a shock-boundary layer interaction.

For these reasons, the investigation of the boundary layer transition phenomena in transonic turbine blades can have a considerable impact in the understanding of transonic accelerating flows. With this in mind, the availability of a wide set of measurements on a turbine rotor blade after DLR [5], [10] gave a good opportunity to verify the performances of well established Navier-Stokes solvers and turbulence models, together with a set of transition models.

2 - CHOICE OF THE TURBULENCE MODEL

The available literature provides a wide variety of turbulence models, ranging from simple algebraic expressions for the turbulent viscosity to more sophisticated forms of the two equation models. In view of the wide engineering applicability of the models, attention was focused on formulations based on the Boussinesq approximation, thereby not including in the present investigation any form of second moment closure.

The k-ε model [15], and its variations, like the k-τ [38], q-ω [3] and k-ω [40] formulations, has gained large popularity because of its intrinsic robustness and wide range of applicability. Still, a number of investigations proved that, apart from the well known theoretical limitations of the two-equation models, most of the formulations suffer from the following problems:

i) The wall functions have been removed by integrating the two transport equations for k and ε in the wall layer. This is often done through the introduction of damping functions related to the wall distance the definition of which is often problematic, especially in three dimensional flow configurations. The extra terms appearing in the equation for k and ε are called Low-Reynolds-number (LR) terms.

ii) In presence of stagnation points the models normally experience an overproduction of turbulent kinetic energy which has undesired effects on the development of the flow downstream of stagnation.

iii) The replacement of wall functions with a set of extra terms allows the computation of accelerating flows. The relaminarization process may be captured properly [8]. Still, the presence of adverse pressure gradient (APG), although in a limited portion of the flow field, may produced large overestimation of the turbulent viscosity which alters the natural boundary layer development [6], [18], [35].

iv) The two-equation model is often not able to predict transition, even though the introduction of the so called LR terms sometimes allows to predict a form of bypass transition in simple flow configurations.

v) The two-equation models do not always ensure realizability, insofar the turbulent kinetic energy may reach negative values.

vi) The dissipation rate budget in proximity of solid walls is often not realistic in view of the recent results of the direct numerical simulation (DNS) of simple flows [26], [27], [28].

Most of the problems encountered by the two-equation models in APG flows are due to the choice of the dissipation rate equation to provide the length scale of turbulence. Several proposals have been made to replace the ε equation by another transported quantity. Among these, one of the most popular attempt was done by Coakley[3] who replaced the dissipation rate equation by the ratio $1./\omega=k/\varepsilon$. The new transport equation, which was built on the basis of dimensional considerations, was definitely more robust than the standard dissipation rate equation. Still, the model did not bring large benefits with respect to the original k-ε formulation. The alternative form proposed by Wilcox is based on the introduction of a so called "specific dissipation rate" defined as $\omega \propto \varepsilon/k$, while keeping unaltered the transport equation for the turbulent kinetic energy. The choice of variables in the model by Wilcox introduces some improvements in accelerating flows, whereas problems still occur in APG [21]. Still this model avoids the cumbersome solution of the dissipation rate equation, which is

often the main cause of numerical problems, and does not introduce any additional term to the standard structure of the transport equations. Menter [17] proposed some modifications to the model by Wilcox to improve the performances in boundary layer flows. Still, the original formulation by Wilcox proved robust and able to give good predictions for compressible transonic flows.

A totally different approach is followed by Rodi et al. [33], who replaces the dissipation rate equation in proximity of the wall by the one equation model by Norris and Reynolds [29], or with a new formulation based on the analysis of the DNS results of channel and boundary layer flows (Rodi et. a. [33]). This approach considerably improves the predictions of the standard k-ε model in a number of flow configurations.

Because of their promising results in a wide variety of applications, the k-ω and two formulations of the two-layer models were selected for the computation of the transonic turbine blade flow designed by DLR. A brief description of the models follows.

2.1 - The k-ω model

The two equation model by Wilcox is based on the introduction of a transport equation for the specific dissipation rate $\omega = \frac{\varepsilon}{\beta^* \cdot k}$. The model equations are:

$$\begin{aligned}
\frac{\partial \rho k}{\partial t} + \frac{\partial \left(\rho u_j k\right)}{\partial x_j} &= \frac{\partial}{\partial x_j}\left[\left(\mu + \frac{\mu_t}{\sigma_k}\right)\frac{\partial k}{\partial x_j}\right] + P - \beta^* \rho \omega k \\
\frac{\partial \rho \omega}{\partial t} + \frac{\partial \left(\rho u_j \omega\right)}{\partial x_j} &= \frac{\partial}{\partial x_j}\left[\left(\mu + \frac{\mu_t}{\sigma_\omega}\right)\frac{\partial \omega}{\partial x_j}\right] + \gamma \frac{\omega}{k} P - \beta \rho \omega^2
\end{aligned} \tag{1}$$

in which the production rate for compressible flows is:

$$P = \left\{ 2\mu_t \left[\frac{1}{2}\left(\frac{\partial u_i}{\partial x_j} + \frac{\partial u_j}{\partial x_i} \right) - \frac{1}{3}\frac{\partial u_k}{\partial x_k}\delta_{ij} \right] - \frac{2}{3} k \delta_{ij} \right\} \frac{\partial u_i}{\partial x_j} \tag{2}$$

and the turbulent viscosity is computed as:

$$\mu_t = \gamma^* \frac{\rho k}{\omega} \tag{3}$$

The model constants are those specified by Wilcox in the original version of the k-ω model: $\beta=3/40$, $\beta^*=0.09$, $\gamma=5/9$, $\gamma^*=1$, $\sigma_\omega=\sigma_k=2$.

This model, as proposed by Wilcox, is supposed to perform well for the predictions of boundary layers in presence of pressure gradients.

2.2 - The two-layer model TLK

The two-layer model retains the standard high Reynolds number (Re) version of the k-ε model far from solid boundaries. In proximity of the wall the transport equation for ε is dropped in favour of an algebraic expression for the dissipation rate as suggested by Norris and Reynolds [29]. Accordingly, in the outer layer the standard k-ε equations are solved:

$$\frac{\partial \rho k}{\partial t}+\frac{\partial\left(\rho u_j k\right)}{\partial x_j}=\frac{\partial}{\partial x_j}\left[\left(\mu+\frac{\mu_t}{\sigma_k}\right)\frac{\partial k}{\partial x_j}\right]+P-\rho\varepsilon$$

$$\frac{\partial \rho \varepsilon}{\partial t}+\frac{\partial\left(\rho u_j \varepsilon\right)}{\partial x_j}=\frac{\partial}{\partial x_j}\left[\left(\mu+\frac{\mu_t}{\sigma_\varepsilon}\right)\frac{\partial \varepsilon}{\partial x_j}\right]+c_1\frac{k}{\varepsilon}P-c_2\rho\frac{\varepsilon^2}{k} \tag{4}$$

in which the turbulent viscosity is computed as:

$$\mu_t = c_\mu \frac{\rho k^2}{\varepsilon} \tag{5}$$

The model constants are the standard high-Re values: c_μ=0.09, c_1=1.44, c_2=1.92, σ_ε =1.3, σ_k=1.

In the flow layer close to the wall the dissipation rate equation is replaced by the following algebraic expression for ε due to Norris and Reynolds:

$$\varepsilon = \frac{k^{1.5}}{L}\left(1+\mu\frac{12.98}{\sqrt{k}\,L\rho}\right) \tag{6}$$

in which the length scale is given by:

$$L = K \cdot C_d \cdot y_{wall} \tag{7}$$

The turbulent viscosity in this layer is computed by:

$$\mu_t = c_\mu \cdot f_\mu \cdot L \cdot \sqrt{k} \cdot \rho \tag{8}$$

The damping function f_μ is introduced to ensure that $\mu_t = o\left(y^+\right)^3$. This function requires the definition of the distance from the solid wall:

$$f_\mu = 1-e^{-\left(0.0198 \cdot R_y\right)}$$

in which R_y is the turbulent Reynolds number based on the wall distance ($R_y = \frac{\rho \cdot y \cdot \sqrt{k}}{\mu}$). The model constants are K=0.41, C_d=6.085. The internal and external layer are matched where $f_\mu \approx 0.9$, which is equivalent to $\frac{\mu_t}{\mu} \approx 36$.

This model is supposed to cure the intrinsic overestimation of the turbulence length scale in low momentum and high shear regions (like in a boundary layer) predicted by the standard k-ε model in presence of APG.

2.3 - The two-layer model TLV

The TLK model was tuned before the availability of Direct Numerical Simulation data. The TLV model, proposed by Rodi et al. [33], maintains substantially unaltered the basic guidelines proposed in the TLK model, but replaces $\sqrt{k}$ as the velocity scale in the flow layer close to the wall by $\sqrt{\overline{v'^2}}$, which is the velocity fluctuation component in the direction normal to the wall. This velocity component fluctuation is correlated to R_y as follows:

$$\overline{v'^2} = \left(4.65 \cdot 10^{-5} \cdot R_y^2 + 4.00 \cdot 10^{-4} \cdot R_y\right) \cdot k \tag{9}$$

and the algebraic expression for the dissipation rate is:

$$\varepsilon = \frac{\sqrt{\overline{v'^2}}}{L_\varepsilon} \cdot \left(1 + \mu \frac{12.98}{\rho \cdot \sqrt{\overline{v'^2}} \cdot L_\varepsilon}\right) \tag{10}$$

in which $L_\varepsilon = 1.3 \cdot y_{wall}$. The turbulent viscosity in the inner layer is computed as:

$$\mu_t = \sqrt{\overline{v'^2}} \cdot L_\mu \tag{11}$$

and the turbulent viscosity length scale is $L_\mu = 0.33 \cdot y_{wall}$. Observe the lack of any damping function in equation (11). In fact, equation (9) plays the role of an algebraic damping function which is much better numerically behaved than the exponential damping function present in equation (8). Observe that this model adopts two different slopes for the dissipation and viscosity length scales, whereas the TLK model adopts the same slope for both. The internal and external layers are matched where $\frac{\mu_t}{\mu} \approx 15$ because equation (9) does not hold for $y^+ > 50$.

2.4 - Control of turbulence production in stagnation points

The overproduction of turbulence in stagnation points, or in flow regions with adverse pressure gradients is a very well known problem [4], [6], [9], [18], [35]. An adverse static

pressure gradient, like the one encountered close to the leading edge of a turbine blade, can give far excessive production due to mean strain which affects the entire evolution of the boundary layer on the blade. This problem can be cured in two ways.

The first way is to fix the turbulence length scale at the wall, as done in the two-layer models (see equation (7) for the TLK model). This approach proved to cure the problem, even though it does not limit the mean strain, but the turbulent viscosity level in the critical buffer layer.

In the k-ω model the former approach is precluded since the specific dissipation rate is solved till the solid wall. In this case it is possible to reformulate the production rate as proposed by Kato and Launder [9], or to introduce a sort of realizability constraint on the ratio k/ε as proposed by Durbin [4]. For the present set of tests it was decided to introduce the formulation proposed by Kato and Launder. Due to the excessive production rate in proximity of the leading edge of airfoils, Kato and Launder rewrote the production term as a sum of a rotational and irrotational terms. This decomposition is straightforward for incompressible flows, but is not straightforward for compressible flows where the not-divergence-free nature of the flow introduces some extra terms in the production, as shown in equation (2). The production rate is rewritten as:

$$S = \sqrt{\frac{1}{2}\left(\frac{\partial u_i}{\partial x_j} + \frac{\partial u_j}{\partial x_i}\right)^2} \quad , \quad \Omega = \sqrt{\frac{1}{2}\left(\frac{\partial u_i}{\partial x_j} - \frac{\partial u_j}{\partial x_i}\right)^2} \quad , \quad D = \left(\frac{\partial u_i}{\partial x_j} \cdot \delta_{ij}\right)$$

which are combined to give the production rate as:

$$P = \mu_t \cdot \left[S \cdot \Omega - \frac{2}{3} D \cdot D\right]$$

The extra contribution to the production rate is due to the velocity divergence D. This extra term, which is absent in a incompressible fluid formulation, was retained in the present set of calculations. The effect of such a decomposition of the mean strain terms in equation (2) causes a considerable reduction of the turbulence production rate. Still, this modification, while sorting positive effects, modifies the production term, as formulated according to the Boussinesq approximation, in a more or less arbitrary way. Nevertheless, the large improvements in the predictions of airfoils and turbine blades advised to replace the standard production rate of the k-ω model with that reformulated by Kato and Launder.

The Kato-Launder form of the production rate was not introduced in the two-layer formulations. In fact, in a set of three dimensional flow calculations of the flow past a square cylinder (Lakehal [13]), the use of the production decomposition in terms of S and Ω in conjunction with the two-layer approach gave far too long recirculation bubbles due to an excessive reduction of the turbulent viscosity.

3 - CHOICE OF THE TRANSITION MODEL

Transition from laminar to turbulent flow and reverse transition, or relaminarization, may both occur in turbine flows. In fact, the flow around turbine blades experiences regions of strong acceleration and deceleration which may have opposite effects on transition. As pointed out by Mayle [16], transition may occur in three different ways:

i) *Natural Transition*, which occurs when instabilities appear in the laminar boundary layer.
ii) *Bypass Transition*, caused by the disturbances to the boundary layer produced by the high free-stream turbulence.
iii) *Separated flow transition*, which takes place in presence of separation bubbles. This transition process may be started also by the presence of shocks which has such a disruptive effect on laminar boundary layers that transition occurs immediately.

Natural transition is unlike to take place in turbine flows because of the large disturbances usually associated with this kind of flows. In presence of high free-stream turbulence levels, transition takes place in the bypass mode. Still, for high Mach number flows, the presence of shocks, if accompanied by low turbulence levels, can be the main source of laminar boundary layer instabilities. In transonic turbine blades the trailing edge shock departing from the pressure side impinges on the suction side thereby interacting with the boundary layer. If the boundary layer is turbulent the impinging shock causes a thickening of the boundary layer with increased total pressure losses. Conversely, if the boundary layer is laminar, the flow can separate and still remain laminar throughout the separation bubble. Transition may start inside the laminar separation bubble or in proximity of the reattachment point. Although the turbulence level in real turbine blades is normally quite high (up to 5-10%), low turbulence level flows are interesting to study the separated flow transition in case of shock-boundary layer interaction.

In summary, of the three, bypass transition covers the widest range of interest in the field of turbine flows. Still, for low turbulence levels transition may take place following the third mechanism listed above.

Most of the models practically applied to turbine flows try to mimic bypass transition. These models evaluate a critical Reynolds number which, if exceeded, indicates that transition has started. One of the most common approaches for the computation of the critical Reynolds number is the one proposed by Abu-Ghannam and Shaw[1]. The length of transition can be modelled by a number of methods which are all aimed to the smooth introduction of turbulence into the boundary layer.

Models based on such approach normally fail in presence of laminar separation bubbles induced by a shock-boundary layer interaction. In fact the shock itself is enough to produce an abrupt transition with a steep increase in the turbulent viscosity which kills the laminar separation bubble. Still, there are ad-hoc models which are intended to mimic this particular phenomena for turbine blades.

Most of the transition models introduce a so-called intermittency function which intends to switch on turbulence when transition occurs. The intermittency function, f_t, is introduced in the general expression for the turbulent viscosity:

$$\mu_t = f_t \cdot c_\mu \cdot f_\mu \cdot \rho \cdot \frac{k^2}{\varepsilon} \tag{12}$$

In this view, different transition models, based on the intermittency function f_t can be selected for comparison with experiments. The models included in the investigation are those proposed by Cho et. al. [2], and by Sieger et. al. [37] for the bypass transition mode, and the model by Kwon and Pletcher [12], adopted by Rodi and Schönung [34] for the separated flow transition. A brief description of the various approaches follows.

3.1 - The transition model for TLK

The two-layer model TLK is particularly suited for the introduction of a transition model because of the structure adopted for the damping function f_μ which is modified as follows:

$$f_\mu = 1 - e^{-\left(0.0198 \cdot R_y \cdot \frac{25}{A^+}\right)} \tag{13}$$

in which the ratio $25/A^+$ acts as an intermittency function. The parameter A^+ is computed according to the onset of transition which is determined on the basis of the Abu-Ghannam and Shaw [1] correlation. Transition starts when the local Reynolds number based on the momentum thickness, Re_ϑ, exceeds the critical Reynolds number for the start of transition, Re_{tr}, which is defined as:

$$Re_{tr} = 163 + \exp\left[F(\lambda) - \frac{F(\lambda) \cdot Tu}{6.91}\right] \tag{14}$$

in which Tu is the free stream turbulence level, and

$$F(\lambda) = \begin{cases} 6.91 + 12.75 \cdot \lambda + 63.64 \cdot \lambda^2 & \text{if } \lambda \le 0 \\ 6.91 + 2.48 \cdot \lambda - 12.27 \cdot \lambda^2 & \text{if } \lambda > 0 \end{cases} \tag{15}$$

λ is the acceleration parameter defined following Polhausen as:

$$\lambda = -\frac{\vartheta^2 \cdot \frac{\partial p}{\partial x}}{\mu \cdot U_{be}} \tag{16}$$

The original correlation was determined for moderate pressure gradients. In fact the acceleration parameter λ was limited to $-0.1 \le \lambda \le 0.1$. Unfortunately, these values are often exceeded in turbine flows, especially in the high acceleration part. Although the correlation can be used outside its tuning range, it was decided not to extrapolate the validity of equation (15) outside the range used in its development, so that equation (16) was implemented by limiting to 0.1 the absolute value of the acceleration parameter.

ϑ is the momentum thickness, the pressure gradient and the velocity U_{be} parallel to the solid wall are computed at the edge of the boundary layer. The model by Cho et at. [2]

assumes transition is completed when $Re_\vartheta = 2 \cdot Re_{tr}$. From the onset of transition on, the parameter A^+ is computed as:

$$A^+ = A_t^+ + \left(300 - A_t^+\right)\left[1 - \sin\frac{\pi}{2}\left(\frac{Re_\vartheta - Re_{tr}}{Re_{tr}}\right)\right]^2 \tag{17}$$

The dependence of A_t^+ on the pressure gradient is neglected by imposing $A_t^+ = 25$. In laminar flow regions A^+ is approximately 300 and the damping function f_μ is small. In transitional boundary layers A^+ gradually grows to reach the asymptotic value of 25, characteristic of fully turbulent boundary layers.

Unfortunately, when using equation (14) for high speed low-turbulence-level flows, transition was never switched on, even when crossing the shock. This is due to the large value of the critical Reynolds number at low turbulence level. In order to avoid this problem in equation (14) the turbulence level Tu, which should be the free stream value, was replaced with the turbulence level at the edge of the boundary layer. This increased Tu, as will be seen in the discussion of the results, allowed the automatic switching on of transition across the shock. Equation (17) for the length of transition was left unaltered. Observe that in the present form, the model is theoretically able to predict relaminarization since equation (15) based on the acceleration parameter is tuned for favourable and adverse pressure gradients. Accordingly this model is implemented on both the suction and pressure sides of the blade.

The transition model is implemented in the boundary layer only. Outside the boundary layer the flow is assumed turbulent and the damping function given by equation (13) is set to unity.

3.2 - The transition model for TLV

The TLV formulation does not have any damping function so that the above transition model cannot be readily applied. Sieger et al. [37] proposed an alternative formulation based on equation (11) together with the introduction of an intermittency function:

$$\mu_t = f_t \cdot \sqrt{\overline{v'^2}} \cdot L_\mu \tag{18}$$

The intermittency function f_t is computed by the following complex expression:

$$f_t = \begin{cases} 0 & \text{for } Re_\vartheta < F \cdot Re_{tr} \\ 1 - \exp\left(-4.65 \cdot R^5 + R \cdot (1-R) \cdot \left(R^2 - R + 0.5\right)\right) & \text{for } F \cdot Re_{tr} \le Re_\vartheta \le Re_{en} \\ 1 & \text{for } Re_\vartheta \ge Re_{en} \end{cases} \tag{19}$$

in which:

$$R = \frac{Re_\vartheta - F \cdot Re_{tr}}{Re_{en} - F \cdot Re_{tr}}, \quad F = \exp\left(-0.01 \cdot Tu^4\right) \tag{20}$$

Observe that the turbulence level is defined as the average of the inlet and the local values as:

$$Tu = \frac{Tu_{in}+Tu(x)}{2} \tag{21}$$

The Reynolds number of the start of transition, Re_{tr}, and of the end of transition, Re_{en}, are computed by using a sort of modified version of the Abu-Ghannam and Shaw correlation. These two parameters are computed by:

$$Re_{tr} = \exp\left[5.094 - 25\left(\frac{Tu}{100}\right)^{1.6}\right] - 400\cdot\exp\left[-\frac{(Tu+2.5)^4}{100}\right] + \exp\left[F(\lambda) - \frac{F(\lambda)\cdot Tu}{6.91}\right] \tag{22}$$

$$Re_{en} = 540 + 183.5\cdot\left(15\cdot 10^{-5}\cdot\left(\frac{Re_{tr}}{0.664}\right)^{1.6} - 1.5\right)\cdot(1-1.4\cdot\lambda) \tag{23}$$

in which $F(\lambda)$ and λ are defined by equations (15) and (16). Equation (18) is used in the internal layer only, while in the outer layer the standard k-ε model holds.

The same deficiency found in the transition model for TLK was found for TLV. In fact, when using the free stream turbulence level, the transitional Reynolds number given by equation (22) was far too large and the model predicts no transition. Again, when taking Tu at the edge of the boundary layer, transition was correctly switched on at the shock. Unfortunately equation (23) could not be used for the present set of calculations. In fact the Reynolds number of the end of transition, as given by equation (23), does not directly feel the effect of the turbulence level, (while the equivalent equation in the TLK transition model does) and, consequently, the effect of the change in equation (22), thereby predicting an excessively long transition. So, for this model it was decided to set to zero the transition length.

3.3 - The transition model for k-ω

The k-ω model does not introduce any extra production or destruction term in the transport equations to account for wall effects. The absence of any damping function requires the introduction of an intermittency function in equation (3) which is modified as:

$$\mu_t = f_t\cdot\gamma^*\cdot\frac{\rho k}{\omega} \tag{24}$$

The onset of transition is determined by using the Abu-Ghannam and Shaw correlation, and transition is over when $Re_\vartheta = 2\cdot Re_{tr}$, as done in the transition model for TLK. The intermittency function is computed modifying equation (17) as:

$$f_t = \left(\frac{A_t^+}{A_t^+ + (300-A_t^+)\cdot\left(1-\sin\frac{\pi}{2}\left(\frac{Re_\vartheta - Re_{tr}}{Re_{tr}}\right)\right)}\right)^{\alpha} \tag{25}$$

in which α ranges in the interval 1-3. The intermittency function holds inside the boundary layer only, whereas the transition function is set to unity outside the boundary layer.

The effect of the parameter α in equation (25) is not negligible. When α is set to unity, equation (25) gives a smooth transition, whereas if α=2-3 the transition length is somewhat increased because of the decreased turbulent viscosity and growth of the boundary layer.

For this model, which is based on the Abu-Ghannam and Shaw correlation, it was necessary to use the critical Reynolds number correlation based on the turbulence level at the edge of the boundary layer, as done for the TLK and TLV models.

3.4 - The transition model for separation bubble

Rodi and Shönung [34] adopted the model proposed by Kwon and Pletcher [12] for the prediction of subsonic separation bubbles. In their investigation Rodi and Shönung computed laminar separation bubbles on airfoils and subsonic turbine blades. In their calculations, the low inlet turbulence level prevented the bypass transition in favour of the separation bubble transition. The viscous-inviscid interaction code used for the computations with the transition model proved adequate for subsonic flows. Following Kwon and Pletcher [12], there is no possibility of transition from laminar to turbulent unless a separation bubble develops. As soon as a separation point is detected on the suction side, transition is started when the local Reynolds number based on the momentum thickness, Re_ϑ, exceeds the critical Reynolds number given by:

$$Re_{tr} = \sqrt{\left(1+\frac{0.05}{\exp(0.365\cdot Tu)}\right)\cdot Re^2_{\vartheta,sep} + \frac{17000}{\exp(0.509\cdot Tu)}} \tag{26}$$

in which $Re_{\vartheta,sep}$ is the Reynolds number based on the momentum thickness ϑ at the separation point. The intermittency function is computed starting from the transition point as follows:

$$f_t = 1-\exp\left[-G\cdot(x-x_{tr})\int_{x_{tr}}^{x}\frac{dx}{U_e}\right] \tag{27}$$

in which:

$$G = \frac{\exp(0.99\cdot Tu)}{100}\cdot\frac{U_e^3}{\nu^2}\left(Re_{\vartheta,tr}\right)^{-8/3} \tag{28}$$

and U_e is the velocity at the boundary layer edge. The co-ordinate x and x_{tr} are defined along the blade surface from the flow separation point. This model clearly predicts no transition in case no separation bubble develops. The transition function tends to unity gradually as the distance of the current cross section from the point of the onset of transition ($x-x_{tr}$) increases in equation (27). The effect of the turbulence level is accounted for in equation (28), whereas the integral in equation (27) considers the local acceleration.

The separation bubble transition expressions are introduced in the k-ω turbulence model only. The intermittency function is introduced according to equation (24). When using this

transition model the pressure side was assumed laminar due to the absence of any recirculation bubble on this side of the blade.

3.5 - The boundary layer thickness for distorted velocity profiles

The computation of the boundary layer thickness and of the velocity at the edge of the boundary layer are not a trivial task in turbine flows. In fact, the velocity profile in the guide vane is highly distorted so that the edge of the boundary layer cannot be generally defined as the wall distance at which the velocity is 99% of the potential velocity on both the suction and pressure sides.

After intense numerical testing, Theodoridis [39] proposes to identify the boundary layer edge as the point at which:

$$\varpi \approx \varpi_{min} + (\varpi_{max} - \varpi_{min}) \cdot 0.01 \tag{29}$$

in which ϖ_{min} and ϖ_{max} are the minimum and maximum values of the vorticity ϖ in the cross section. This criteria ensures smooth and well behaved shapes of the boundary layer thickness and a reliable method to compute the velocity at the edge of the boundary layer.

4 - BRIEF DESCRIPTION OF THE SOLVERS

Although both the FASTC-3D and FLOS3D codes are three-dimensional Navier-Stokes solvers, they are used here in a 2D computational domain due to the two-dimensional nature of the geometry and flow field measured in DLR. A brief description of the two solvers follows.

4.1 - The pressure correction algorithm for compressible fluid flows

The present investigation was carried out by starting from the standard version of the FAST-3D code by Zhu [41]. This code is designed for the simulation of internal complex incompressible turbulent flows. Since the incompressible formulation is largely left unaltered for compressible fluids, a brief description of the original solver is given.

The transport equations are discretized by using second order accurate finite volumes. Convection is treated by the TVD scheme named HLPA, developed by Zhu [41], which largely decreases the extra numerical diffusion brought by the hybrid scheme, but is more stable than other existing second order upwind schemes. Further details on the code may be found in Zhu [41].

Special attention is devoted to the continuity equation. In fact, the cell centre location of the transported variable requires the evaluation of the cell face values to discretize the mass conservation relation. While a simple linear interpolation is suited for the momentum and the energy equations, the same technique cannot be used for the continuity equation since it results in the well known unphysical chequerboard pattern for the static pressure. To avoid this, the mass conservation equation is first modified to get the pressure correction equation. This is done following the idea by Patankar [30] for the SIMPLE family of algorithms according to which a link between cell centre pressure and cell face velocity is established by means of the momentum equation. The cell face velocities are not evaluated by linear interpolation of the cell centre velocities, but using the momentum interpolation technique by Rhie and Chow [32] which introduces some extra diffusion in order to prevent pressure wiggles.

Compressibility effects are accounted by retaining the Cartesian velocity components and not the momentums ρu_i as the unknown for the solution of the momentum equations, which remains substantially unaltered with respect to the incompressible fluid version. The pressure correction step requires some modifications while still retaining the SIMPLE algorithm. The continuity equation is discretized for a one dimensional problem as follows:

$$\left(\rho_e^* + \rho_e'\right)\left(u_e^* + u_e'\right)l_e - \left(\rho_w^* + \rho_w'\right)\left(u_w^* + u_w'\right)l_w = 0 \qquad (30)$$

in which the guessed density and velocity field are starred and the dashed variables are modification to the guessed field to ensure continuity, and l_w and l_e are the cell side surfaces. The subscripts e and w refer to the east and west sides of the control volume. In equation (30) the terms which imply a density change are related to the pressure change via an isothermal transformation and under the perfect gas hypothesis.

The cell face densities are computed by using a blended linear interpolation - first order upwind stencil:

$$\rho'_w = \frac{1}{R}\left\{(1-\mu_w)\underbrace{\left[f_x^+ \frac{p'_P}{T_P} + (1-f_x)\frac{p'_W}{T_W}\right]}_{\text{linear interpolation}} + \mu_w \underbrace{\left[M_P^+ \frac{p'_W}{T_W} + M_P^- \frac{P'_P}{T_P}\right]}_{\text{upwind}}\right\}$$

$$\rho'_e = \frac{1}{R}\left\{(1-\mu_e)\underbrace{\left[f_x^+ \frac{p'_E}{T_E} + (1-f_x^+)\frac{p'_P}{T_P}\right]}_{\text{linear interpolation}} + \mu_e \underbrace{\left[M_P^+ \frac{p'_P}{T_P} + M_p^- \frac{p'_E}{T_E}\right]}_{\text{upwind}}\right\} \qquad (31)$$

in which the biasing function μ is defined as:

$$\mu = \max\left(0, k\left[1-\left(\frac{M_{ref}}{M}\right)^2\right]\right) \qquad (32)$$

and

$$M_P^+ = \frac{1+\mathrm{sgn}(M_P)}{2}, \quad M_P^- = \frac{1-\mathrm{sgn}(M_P)}{2}$$

M_{ref} and k are of the order of one. The local Mach number M_p is computed as:

$$M_P = \frac{U_P}{a_P} = \frac{U_P}{\sqrt{\gamma R T}}$$

U_P is the local velocity module, a_p the local speed of sound, and

$$\mathrm{sgn}(f) = \begin{cases} 1 & \text{for } f \geq 0 \\ 0 & \text{for } f < 0 \end{cases}$$

f_x and f_x^+ are the linear interpolation functions used to compute the cell face value of the transported quantities. In equations (31) the density is linearly interpolated on the cell face for low subsonic flow conditions, yielding to the elliptic nature of the pressure correction equation with $\mu_e = \mu_w = 0$, whereas it is upwinded for supersonic flows, thereby increasing the hyperbolic nature of equation (30). Further details about the compressible pressure correction code may be found in Michelassi [20].

4.2 - The time marching code for compressible fluid flows

In order to compare the results computed by using the compressible pressure correction algorithm, the same test flows were also computed by using an implicit time marching code which solves for density, momentum, and total specific energy. The equations are discretized by centred finite differences in curvilinear non orthogonal co-ordinate systems.

The FLOS3D program (Michelassi et al., [22],[23]) is based on the scalar implicit algorithm proposed by Pulliam and Chaussée [31]. The program solves three-dimensional compressible flows with complex boundaries in inviscid, laminar and turbulent regime. In order to make the approximate factorisation method less computational costly Pulliam and Chaussée proposed a scalar form, adopted for the present set of calculations which decreases the number of operations per grid point. The introduction of a set of eigenvalues, Λ, and eigenvectors, T, allows writing:

$$T_\xi\left[I+\theta\Delta t\left(\delta_\xi\Lambda_\xi\right)\right]\cdot N\cdot\left[I+\theta\Delta t\left(\delta_\eta\Lambda_\eta\right)\right]\cdot P\cdot\left[I+\theta\Delta t\left(\delta_\zeta\Lambda_\zeta\right)\right]\cdot T_\zeta^{-1}\cdot\Delta Q=RHS \qquad (33)$$

in which $\Delta Q=Q^{n+1}-Q^n$, the matrices $N=T_\xi^{-1}T_\eta$ and $P=T_\eta^{-1}T_\zeta$ are solution independent and Θ allows weighting of the explicit-implicit nature of the space operator in round brackets. This formulation, which drops the viscous contribution to the implicit space operator, was found weak in internal viscous flows because of the presence of boundary layers. Unfortunately the diffusive operators cannot be included in the left hand side of equation (33) since they have a totally different set of eigenvectors. Nevertheless, to render the algorithm more efficient in presence of viscous boundary layers the implicit side of equation (33) is modified to account for an approximate expression of the viscous eigenvalues $\Lambda_{\xi,\eta,\zeta}$. The modified algorithm reads:

$$\begin{aligned}&T_\xi\cdot\left[I+\theta\Delta t\left(\delta_\xi\Lambda_\xi-\delta_\xi^2\Lambda_\xi^v\right)\right]\cdot\\&N\cdot\left[I+\theta\Delta t\left(\delta_\eta\Lambda_\eta-\delta_\eta^2\Lambda_\eta^v\right)\right]\cdot\\&P\cdot\left[I+\theta\Delta t\left(\delta_\zeta\Lambda_\zeta-\delta_\zeta^2\Lambda_\zeta^v\right)\right]\cdot T_\zeta^{-1}\cdot\Delta Q=RHS\end{aligned} \qquad (34)$$

The code implements a local time step strategy to march in time. Stability is ensured by introducing non linear damping terms as proposed by Jameson et al. [7]. Accordingly the right hand side (RHS) in equation (34) includes second and fourth order differences. Further details about the code may be found in Michelassi et al. [22],[24],[25].

4.3 - Boundary conditions

The boundary condition procedure applies to both the pressure correction and the time marching code. It is assumed that inlet and outlet axial Mach numbers are below unity. Accordingly, the experimental conditions are matched as follows:

• The isentropic outlet Mach number M_{ex} is fixed by the inlet total pressure to exit static pressure ratio. The inlet total pressure P_0^{in}, the exit static pressure P^{ex}, the inlet total temperature T_0^{in}, and the inlet flow angles α,β (in 3D flows two angles are needed) are fixed. This choice allows fixing directly the inlet total quantities that are very much often the only true data for compressible flow calculations. The inlet static pressure P^{in} is extrapolated at the inlet section from the interior points at every iteration, generally using a first order extrapolation, so that the local inlet Mach number is computed by the isentropic relation:

$$M_{in} = \sqrt{\frac{2}{\gamma-1}\left[\left(\frac{P_0^{in}}{P^{in}}\right)^{\frac{\gamma-1}{\gamma}} - 1\right]}$$

in which γ is the specific heat ratio.

• Consequently the inlet static temperature is given as:

$$T^{in} = \frac{T_0^{in}}{1+\frac{\gamma-1}{2}M_{in}^2}$$

which allows computing the inlet sound speed a_{in} and the inlet density ρ_{in}:

$$a_{in} = \sqrt{\frac{\gamma\ P^{in}}{\rho}} = \sqrt{\gamma\ R\ T^{in}}$$

$$\rho_{in} = \frac{P^{in}}{R\ T_{in}}$$

The inlet velocity module follows straightforward from the definition of the Mach number:

$$|U_{in}| = M^{in} \cdot a_{in}$$

The velocity module is then decomposed in the three components according to the inlet flow angles. In the exit section the static pressure is fixed to P^{ex} and all the other variables are extrapolated.

• On solid walls the slip condition is applied for the velocity components for inviscid flows, whereas the no-slip condition is imposed for viscous flow calculations. In presence

of viscosity, the walls are adiabatic, and the static pressure is computed setting to zero the pressure derivative in the direction normal to the wall.

• Periodic boundaries abandon the point-to-point periodic arrangement. This technique requires a sort of interpolation of the transported variables to enforce periodicity. Details may be found in Michelassi et al. [24], [25].

5 - RESULTS

5.1 - The set of Measurements

The two compressible Navier-Stokes solvers with the set of turbulence and transition models have been tested against an extensive data set produced by DLR [5],[10],[11]. The measurements refer to both the stator and the rotor blades of a transonic turbine stage. Both the stator and rotor blades have been measured in a linear cascade wind tunnel under variable pressure ratios. The flow around the two blades have been measured extensively in both the stator (T6.1) and the rotor (T5.1) blades. Measurements include:

- static pressure distribution around the blade profile
- profiles of total pressure, flow angle, and Mach number in the wake
- velocity and total pressure profiles in six cross sections in the blade vane

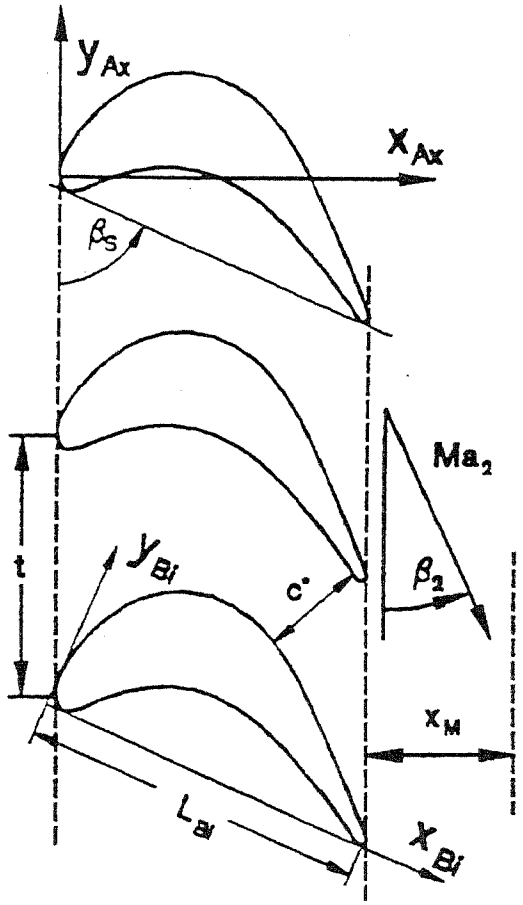

Figure 1. The T5.1 rotor profile from DLR [5]

The present set of calculations refer to the rotor blade T5.1, shown in figure 1. The overall flow conditions are set so as to have an isentropic Mach number M_{is} at the exit of approximately 1.1. The inlet flow angle is 40-deg with respect to the tangential direction. The blade chord is 80.00mm, the stagger angle 66.2-deg, with respect to the tangential direction, and the pitch-to-chord ratio is 0.755. Measurements have been taken by using pneumatic probes and laser doppler anemometry. The measured inlet turbulence level, Tu_{in}=0.6%, is extremely low. At such a low turbulence it is in fact questionable if bypass transition can take place. The transonic nature of the flow produces a fish tail shock departing from the trailing edge of the blade. One of the two shock waves impinges on the suction side. The shock boundary layer interaction is accompanied by an evident thickening of the boundary layer, but all the measurements, and the Schlieren flow visualisation, do not allow to verify the presence of a separation bubble on the suction side immediately downstream of the shock. Still, the flow visualisation shows a sort of complex shock-expansion wave pattern on the suction side, which will be discussed in the next sections. This pattern is not entirely periodic, as can be seen in figures 2,a and 2,b. In figure 2,a the knife edge is positioned parallel to the incoming flow, whereas figure 2,b shows the same flow visualisation with the knife perpendicular to the incoming flow direction. With different orientations of the knife, and in adjacent blade passages, the shock impinging on the suction side may give a simple reflection, (see the upper blade passage for both figures 2,a and 2,b), or a slightly more complex pattern (see the lower blade passage). In the latter the impinging shock causes two shocks, in between which a weak, and hardly visible, expansion wave indicates the presence of a small and thin separation bubble. This pattern is more evident in figure 2,a.

Although the turbulence level is very low, transition takes place on both the suction and pressure sides of the blade. While on the suction side transition is clearly located at the shock, on the pressure side transition takes place on the nose of the blade. The flow remains turbulent for approximately 50% of the blade. Then, due to the strong acceleration the flow reliminarizes and reaches the trailing edge still laminar. The experimental results are then particularly suited to verify the applicability of the above mentioned transition models to the mechanism of the separated flow transition, or transition induced by a shock wave.

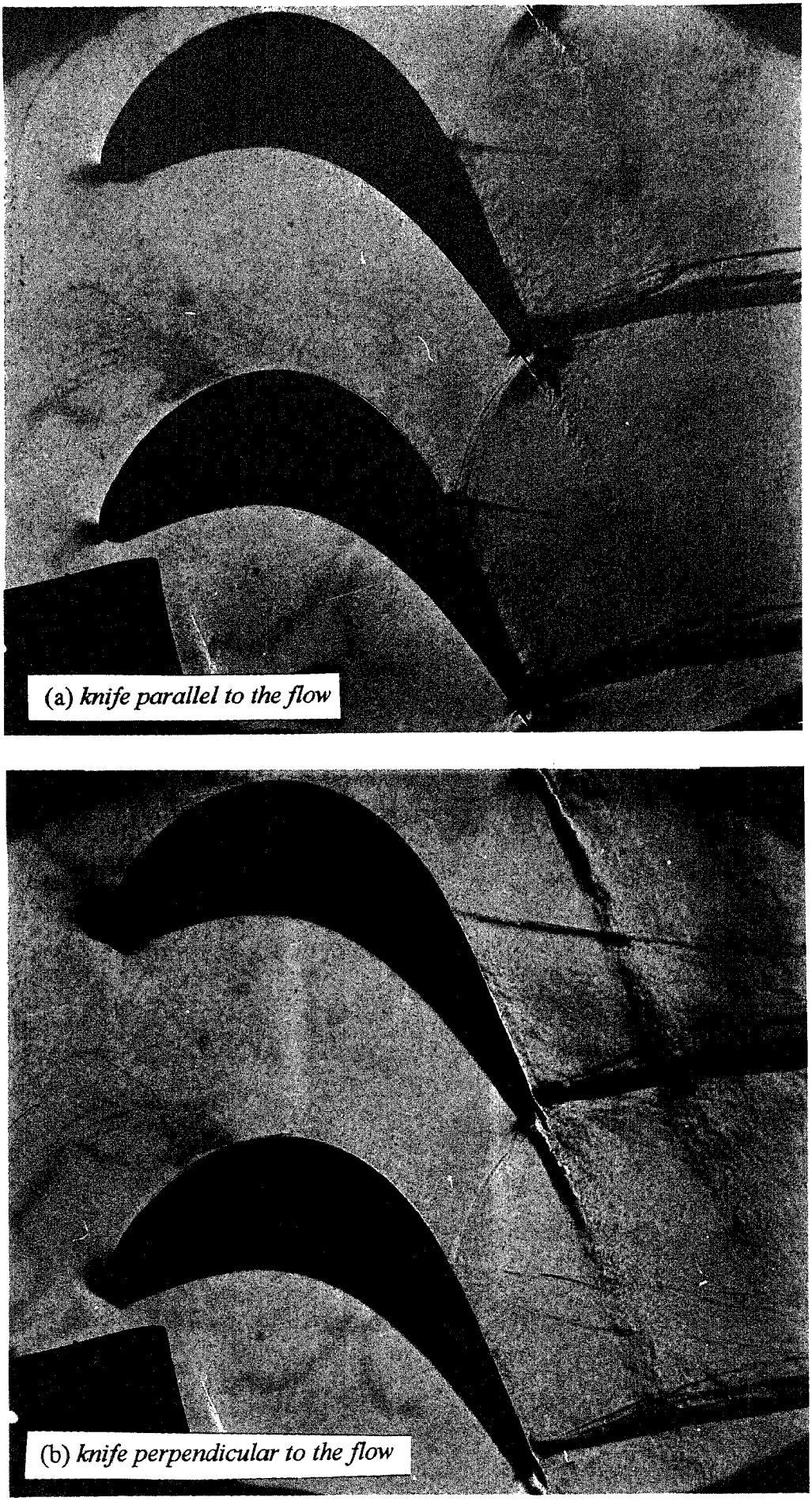

Figure 2. Schlieren Flow Visualization at M_{ex}=1.10 [5].

5.2 - The computer simulations

A wide set of computations was performed on the T5.1 profile by using both the FASTC-3D and FLOS3D codes with the turbulence and transition models listed above. Table 1 summarises the test runs. The two-layer models have been run on the compressible pressure correction solver, whereas the k-ω model was implemented in the time marching code only. The separated flow transition model (SFTM), described in section 3.4, was implemented in the FLOS3D code only. In fact, the SFTM can be applied only in the presence of a separation point, but, the absence of the separation bubble on the suction side of the turbine blade when using the two-layer model prevented from any transition. Conversely, the k-ω model was found able to predict a small and thin flow separation downstream of the impinging shock. The set of computations were not able to show if this difference in the flow pattern can be traced back to the solver or to the turbulence model. For the sake of a more complete comparison, the flow was also computed by using the standard k-ε model with wall functions and no transition.

Table 1

solver	k-ε with wall functions	TLK model with transition	TLV model with transition	k-ω model with transition	separated flow transition
FASTC-3D	√	√	√		
FLOS3D				√	√

Test runs on the T5.1 blade

A first set of preliminary runs were done in inviscid flow regime. Figure 3 shows a close-up view of the computational grid with 591×70 points. The I structure of the grid, with the blade placed inside the computational domain modelled as a set of blocked grid nodes, was retained for all the calculations. Observe the not point-to-point periodic nature of the periodic boundary which allows using a nearly orthogonal grid in the wake, thereby allowing a more accurate discretization of the transport equations.

For what concerns the viscous runs, several attempts have been made to compute a fully laminar flow case. Unfortunately, both the time marching and the pressure correction solver suffered from stability problems. In particular, the time marching solver soon developed a sort of vortex shedding downstream of the shock impinging on the suction side, which caused a large separated flow region. This shedding eventually brought to the uncontrolled growth of the numerical error. The pressure correction solver showed a very similar behaviour, which proved absolutely independent of the relaxation parameters used in the calculations (see Zhu [41]).

All the other tests were run in turbulent flow regime. The Reynolds number, based on the total sound speed and pitch (=45.3 mm) is approximately 10^6. The experimental inlet turbulence level is approximately 0.6% which was set according to the inlet velocity component. The inlet Reynolds stress components were not measured, so that the inlet dissipation rate ε when using the k-ε model, or the inlet specific dissipation rate when using the k-ω model, were set so as to have an inlet turbulent viscosity of approximately 10. Some tests have been performed to verify the sensitivity of the results to the inlet turbulent viscosity level. The tests showed that the inlet turbulence viscosity level has no, or very little, effect on the

development of the boundary layer around the blade. This must not be considered a general result since the lack of any significative response to the change of the inlet μ_t is probably due to the extremely low turbulence level which is the main responsible for the laminar nature of the pressure and suction side boundary layers, as will be seen in the next sections.

In order to verify the independence of the results from the grid, several I-meshes were generated by using the program MESHHO [19]. The simulations with the k-ε model and wall functions use two grids, a first 174×71 coarse one, and a 244×110 refined one, shown in figure 4. The refined grid showed no significant differences with respect to the coarse one. For the two-layer model it was necessary to resolve the boundary layer. The first coarse 244×71 grid, although very much stretched towards the blade walls, was not enough to resolve the viscous layer. The refined 273×115 proved adequate for this pourpose. The k-ω model has different grid requirements with respect to the two-layer models. In fact the TLK and TLV models do not solve the dissipation rate equation in proximity of solid walls, which is replaced by an algebraic expression based on a fixed growth rate of the turbulence length scale. So, the cumbersome solution of the dissipation rate at the wall, which exhibits very large gradients, is avoided. Conversely in the k-ω model, in which the specific dissipation rate tends to infinity at the wall (where $k \rightarrow 0$ and ε tends to a finite value), the grid requirements are more stringent. The proper resolution of the specific dissipation rate gradients at the wall required a 273×151 grid with a strong point stretching at the walls.

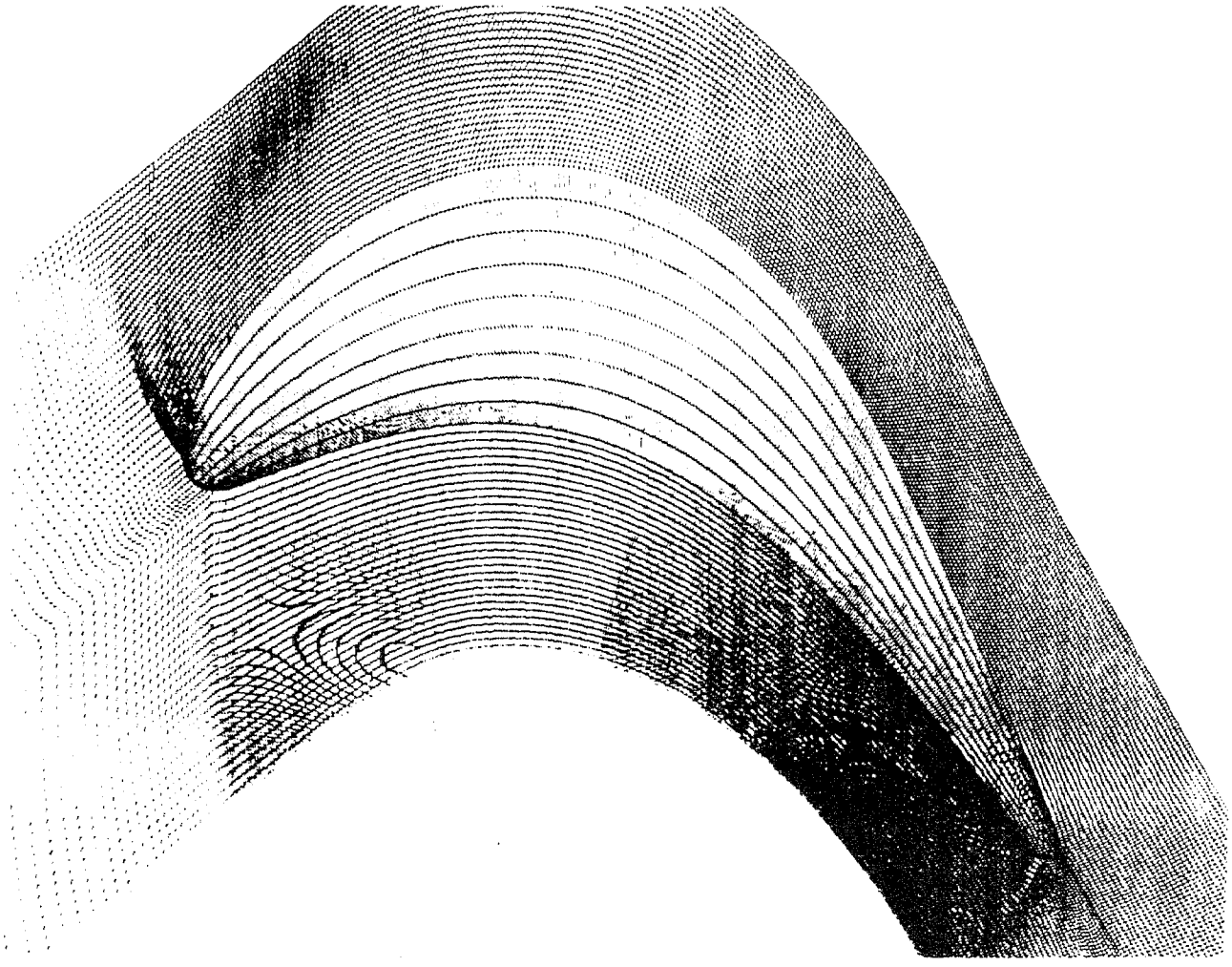

Figure 3. 591×70 grid points grid for inviscid flow calculations.

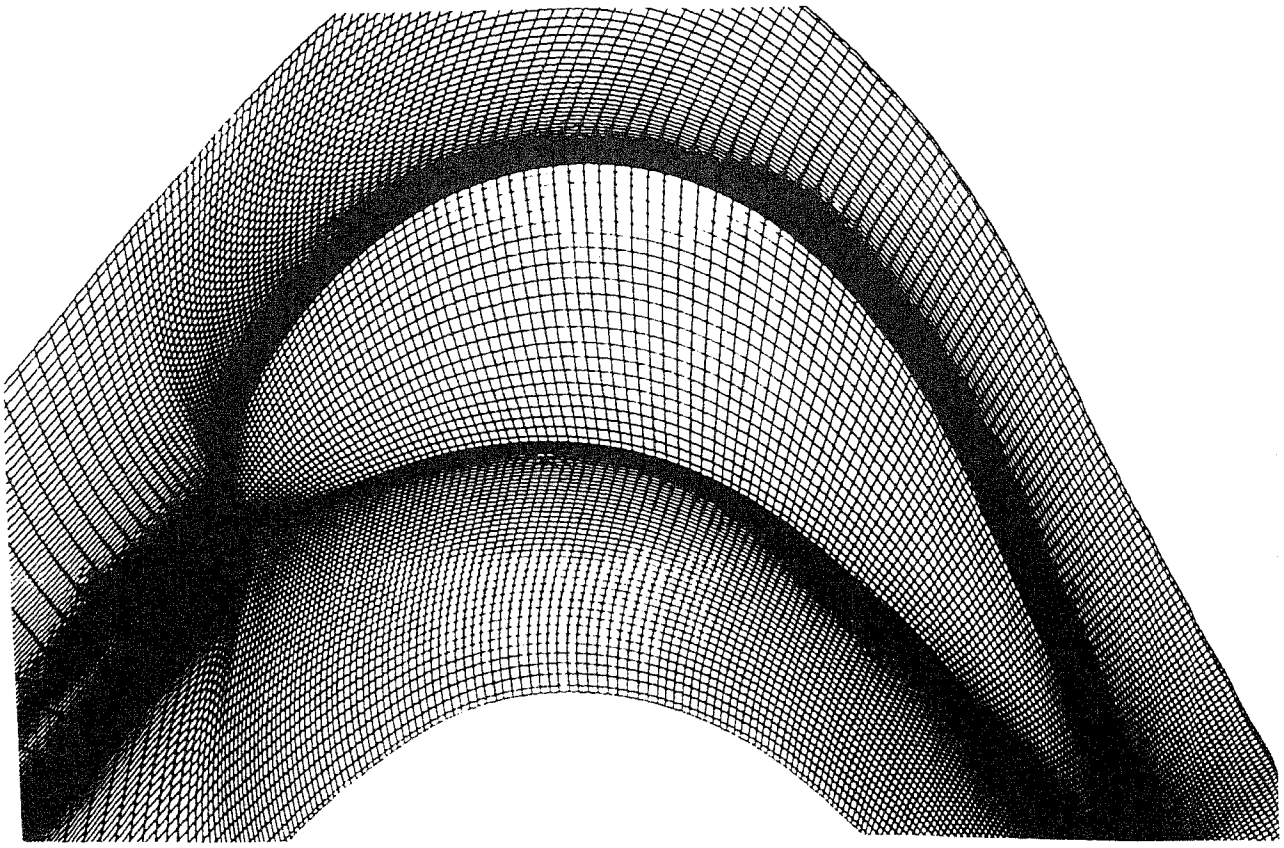

Figure 4. 244×110 grid points grid for turbulent flow calculations with wall functions.

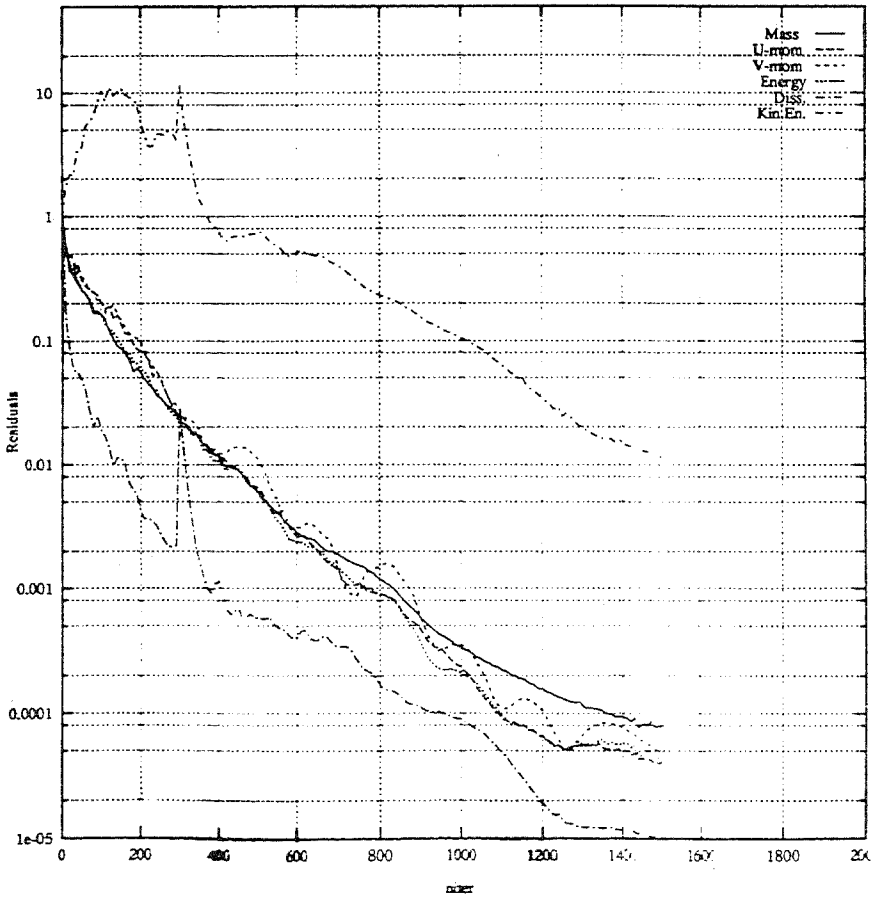

Figure 5. FLOS3D: a typical convergence history for turbulent flow regime.

Figure 5 shows a typical convergence history of the FLOS3D code run in turbulent flow regime with a coarse 273×115 grid. Approximately 1500 iterations (equivalent to 700s CPU time on a Fujitsu VP-800 supercomputer) are necessary to reduce the residual by 4 to 5 orders of magnitude, with the only exception of the turbulent kinetic energy equation which shows a slower convergence rate. The convergence rate of the pressure correction code are not as good as the time marching code, although the CPU times are quite similar.

5.2.1 - Isentropic Mach number distribution and flow pattern

The wall static pressure is measured at the blade mid span in 27 points. The measurements show a shock at approximately 80% of the axial chord, C. The oblique shock is weak and the flow, after having reached a maximum isentropic Mach number (M_{is}) of approximately 1.4, experiences a recompression which reduces the speed down to M_{is}=1.3. Further on, the trailing edge shock reduces the speed to M_{is}=1.1 downstream of the trailing edge. All the plots are arranged to have the axial co-ordinate x made non dimensional by using the axial chord C on the abscissa.

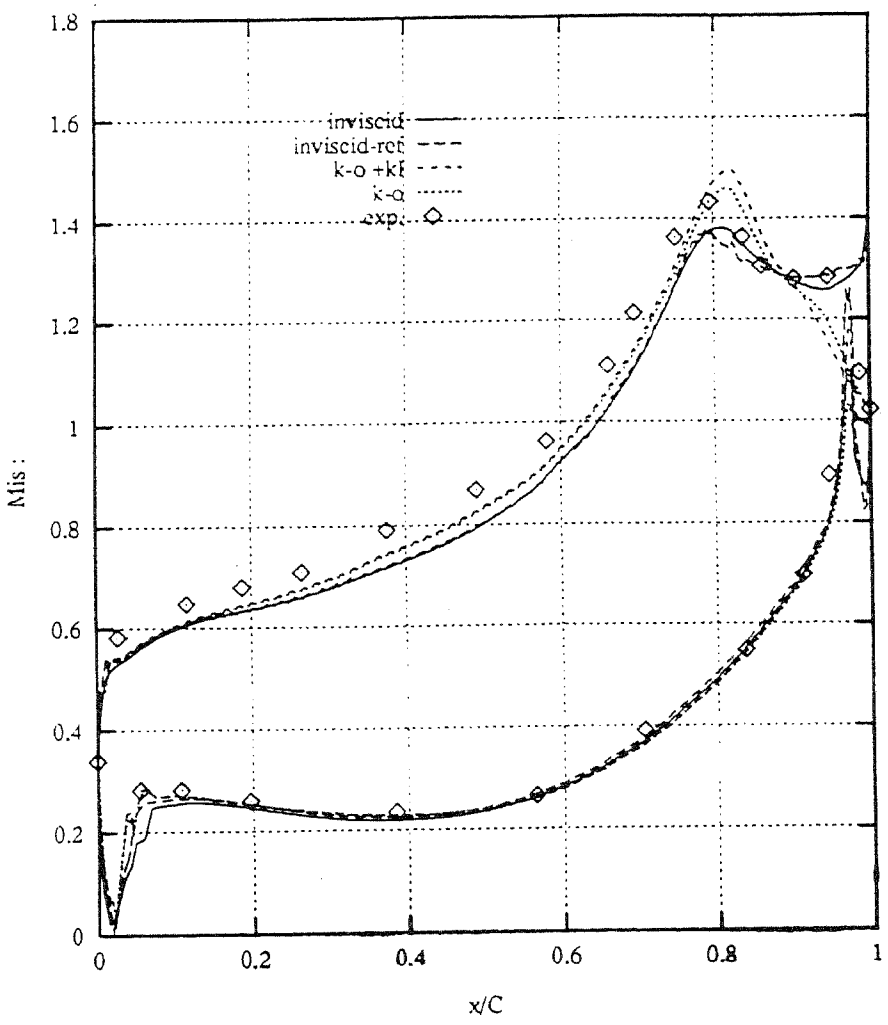

Figure 6. Isentropic Mach number distribution by FLOS3D, inviscid and fully turbulent flow.

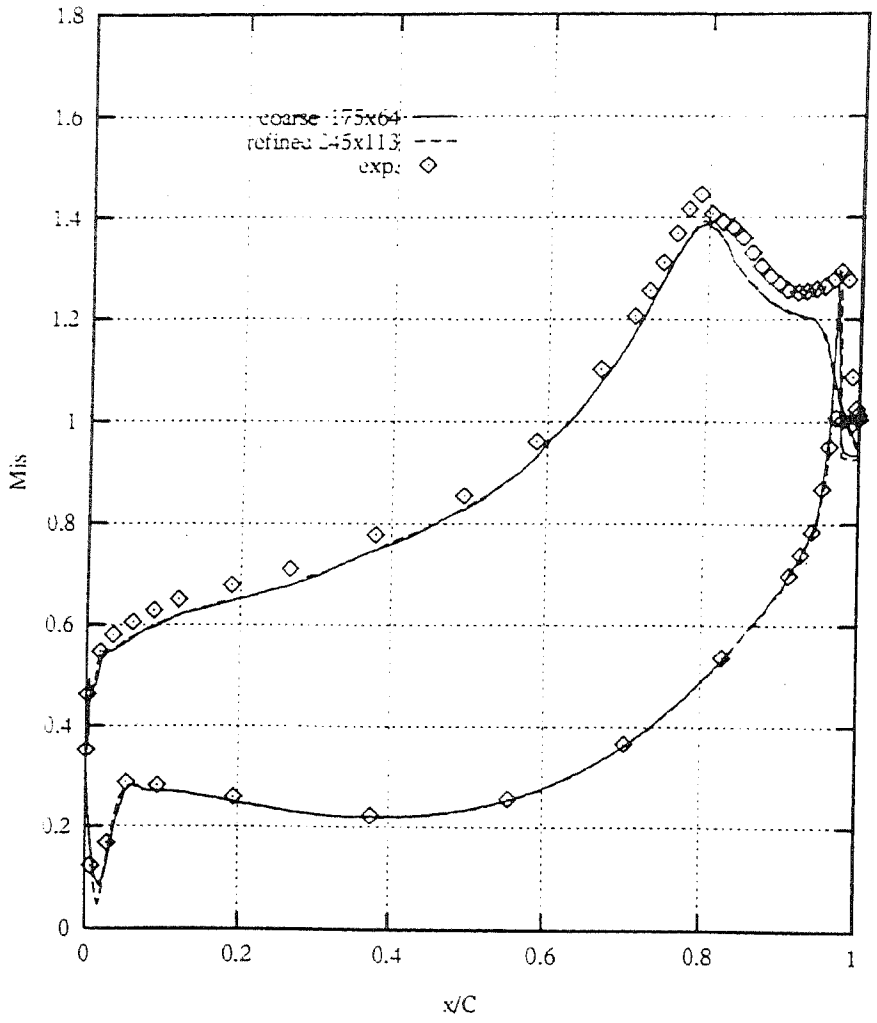

Figure 7. Isentropic Mach number distribution by FASTC-3D, turbulent wall-functions.

The first set of computed results refer to inviscid and fully turbulent calculations. Figure 6 shows the computed M_{is} profiles around the blade. The two inviscid flow calculations are almost identical, insofar they both capture correctly the shock position, although the shock strength is somewhat under predicted by using both the coarse and the refined grids. The pressure distribution downstream of the shock is very well captured, up to the trailing edge, where the refined grid allows following the measured isentropic Mach number profile.

When moving to the turbulent flow regime without any transition model large differences arise in the predictions. Figure 6 also shows the M_{is} profiles on the blade computed by the fully turbulent k-ω model (k-o) without and with (k-o+kl) the Kato-Launder approximation for the production rate. Firstly, both the turbulent calculations show an overestimation of the velocity peak, together with a small downstream shift of the shock position with respect to the experiments and to the inviscid flow calculations. Immediately downstream of the shock, the turbulent flow calculations show a strong decrease of the isentropic Mach number evidently caused by an excessive pressure recovery. A close up view of the flow field showed that the trailing edge vortex on the suction side tends to move towards the suction side shock. The excessive thickening of the boundary layer downstream of the shock, still in supersonic flow regime, is responsible for the strong pressure recovery. The measurements do not show such a

trend, which is clearly caused by the fully turbulent, and not transitional, nature of the boundary layer. The Kato-Launder form of the production term does not seem to play a significant role. In fact, the decomposition of the production rate has a negative effect on the predictions of this transonic turbine blade since it does enhance the velocity overestimation and the pressure recovery.

When retaining the fully turbulent boundary layer the situation slightly improves if moving to the pressure correction solver with the standard k-ε model and wall functions, or the TLK and TLV models. Figure 7 shows the isentropic Mach number computed by the high Re k-ε model on both the coarse and the refined grids. The two grids give identical results, and the shock strength is slightly underestimated. Still, downstream of the shock the flow does not decelerate as fast as in the k-ω model. Figure 8 shows the refined grid predictions obtained by using the TLK and TLV models under the assumption of fully turbulent boundary layer. The M_{is} profiles do not differ much from those given by the high-Re k-ε model with wall functions. The trend is, in fact, very similar, although the shock location given by the two-layer models is in perfect agreement with experiments. The shock strength is again slightly underestimated, although the TLK model moves a little closer to experiments, and the pressure distribution is reasonably well predicted on the suction side downstream of the shock.

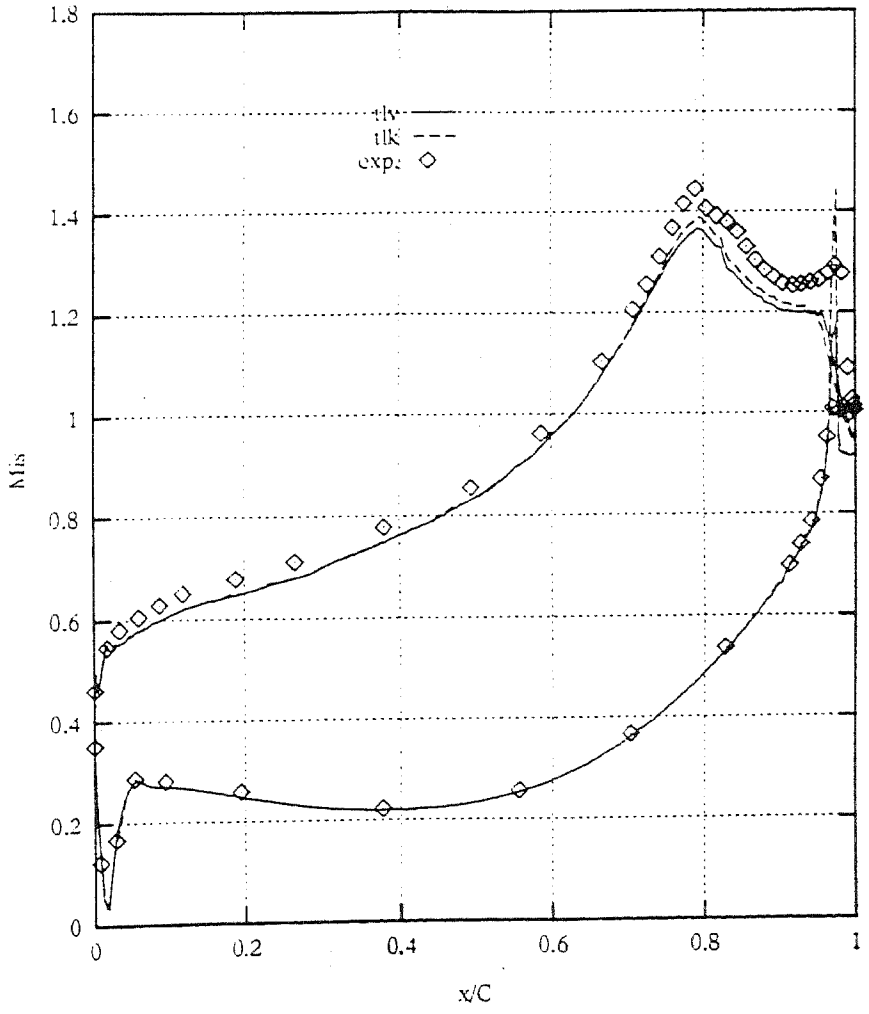

Figure 8. Isentropic Mach number distribution by FASTC-3D, TLK and TLV.

In figures 6,7,8 the pressure side profile of the isentropic Mach number is always well reproduced. Conversely, all the profiles show that the models have some difficulty in following the flow acceleration on the suction side, especially in proximity and immediately downstream of the leading edge.

The introduction of the transition models in the two-layer and k-ω turbulence models does not largely alter the predictions, but brings about changes in the flow region downstream of the shock. While the details of the transitional flow calculations will be given in the following sections, the effects of transition on the isentropic Mach number profile around the blade will be discussed here. Figure 9 shows a close up view of the M_{is} profile on the suction side in the shock region. The wall-functions, turbulent TLK and transitional TLK predictions are compared with experiments. Observe that the transition model is implemented on both the pressure and suction sides of the blade. Figure 9 shows that the introduction of the transition model slightly changes the pressure distribution while approaching the trailing edge. It seems that the transition model allows capturing the tendency towards a flow acceleration. This acceleration is captured only qualitatively since the velocity is still underestimated. This change in the predictions is solely due to the introduction of the transition model, and it repeats in all the other transitional flow calculations. Figure 10 shows the similar trend experienced when introducing various transition options in the TLV model (see section 5.2.3). While the isentropic Mach number is still somewhat underestimated in the supersonic region, the shape of the predicted M_{is} closely resembles the measured one. In all the computations with the two-layer model without and with transition model, no suction side separation was ever detected. This is the reason why the separated flow transition model could not be successfully applied.

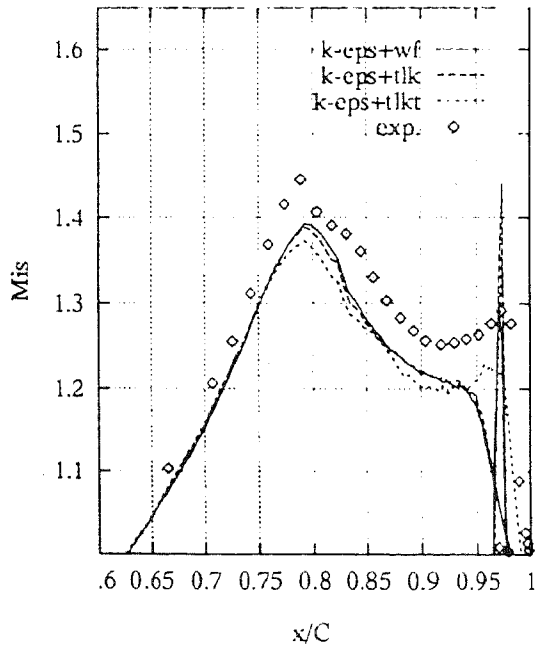

Figure 9. Isentropic Mach number distribution by FASTC-3D, TLK+transition.

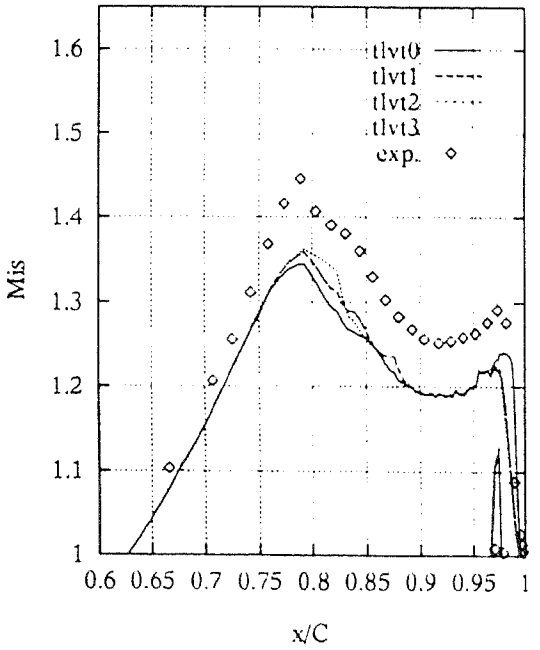

Figure 10. Isentropic Mach number distribution by FASTC-3D, TLV+transition.

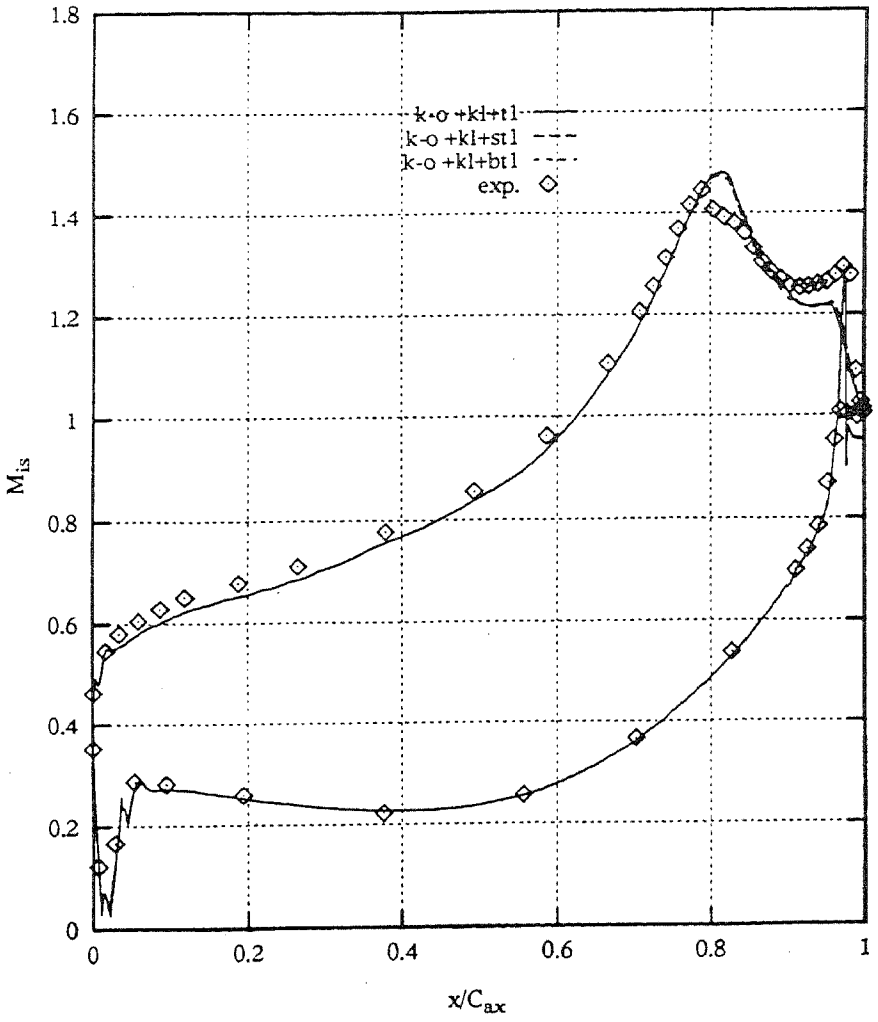

Figure 11. Isentropic Mach number distribution by FLOS3D with transition, laminar pressure side.

With the FLOS3D solver some differences arose in the supersonic flow region. The k-ω model was tested with both the bypass and separation bubble transition models. Both formulations implements the Kato-Launder approximation of the production rate. In all the following runs the parameter α in equation (25) was set to unity. Figure 11 compares the experiments with the M_{is} profiles computed by using the bypass transition model (k-o+kl+st1), by using the same model but with zero transition length (k-o+kl+t1), and by using the separation transition model (k-o+kl+bt1). These three profiles refer to calculations in which the pressure side boundary layer was assumed fully laminar till the trailing edge. Although the M_{is} peak is still overestimated, but by a smaller amount with respect to the fully turbulent calculations (see figure 6), there is a considerable improvement in the region downstream of the shock insofar the isentropic Mach number does not drop abruptly as in figure 6 and follows the experimental values much better. Observe that three totally different transition models give very similar, although not identical results.

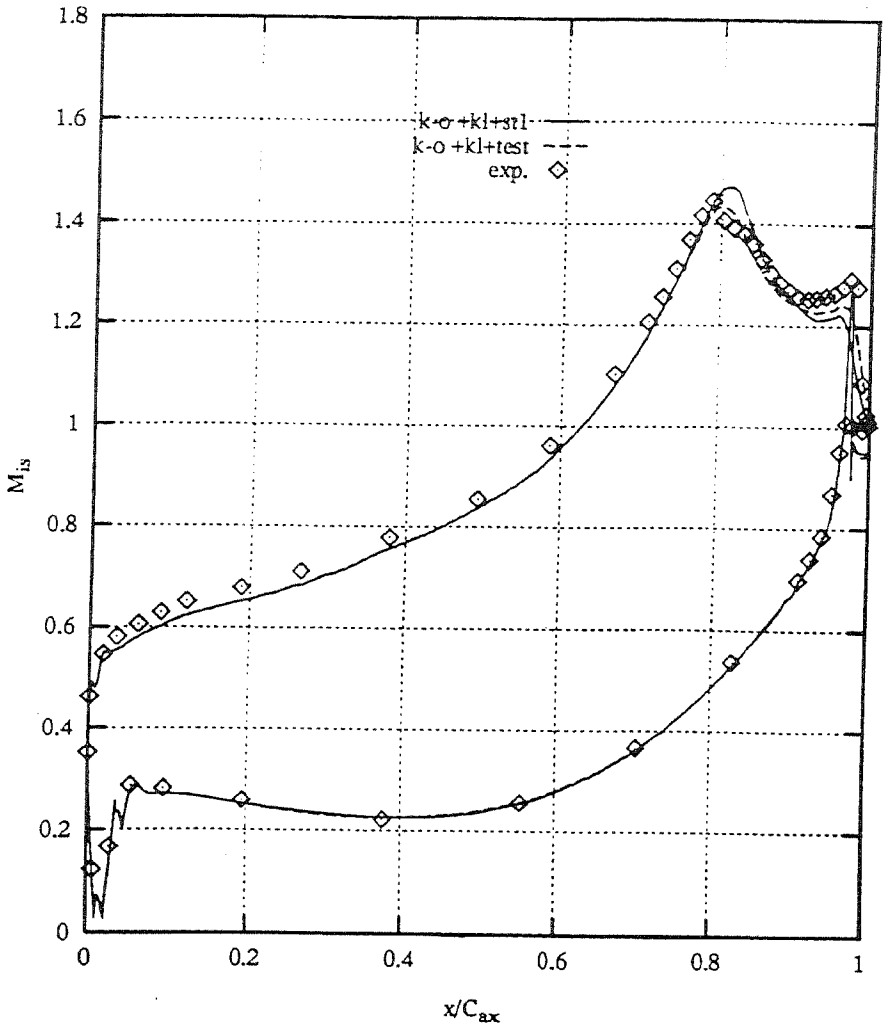

Figure 12. Isentropic Mach number distribution by FLOS3D with transition, transitional pressure side.

Figure 12 proves that the assumption of a fully laminar boundary layer on the pressure side is not realistic. The plot compares the experiments with the bypass transition model predictions (k-o+kl+st1) with the same model in which the transition criteria is applied to the pressure side also (k-o+kl+test). The predicted isentropic Mach number clearly moves towards the measurements in the critical region immediately downstream of the shock. Both the M_{is} peak and the M_{is} level between the shock and the trailing edge are well predicted when introducing the transition model on the pressure side also. Although it might appear surprising that the transitional boundary layer on the pressure side has such a large impact on the pressure distribution on the suction side of the blade, it must be observed that the expansion wave-shock pattern which departs from the trailing edge and moves towards the suction side is governed by the trailing edge recirculation. The shape and size of this recirculation is governed by the thickness and the nature of the approaching boundary layer. When the pressure side is assumed laminar the shock strength is clearly overestimated, and consequently the total pressure loss caused by the shock-boundary layer interaction is also overestimated with respect to the experimental values. The excessive total pressure loss is the main responsible for the

strong flow deceleration downstream of the shock. Figure 12 proves that the changes in the pressure side boundary layer caused by the transition model reduces the strength of the shock with a positive effect on the overall quality of the predictions.

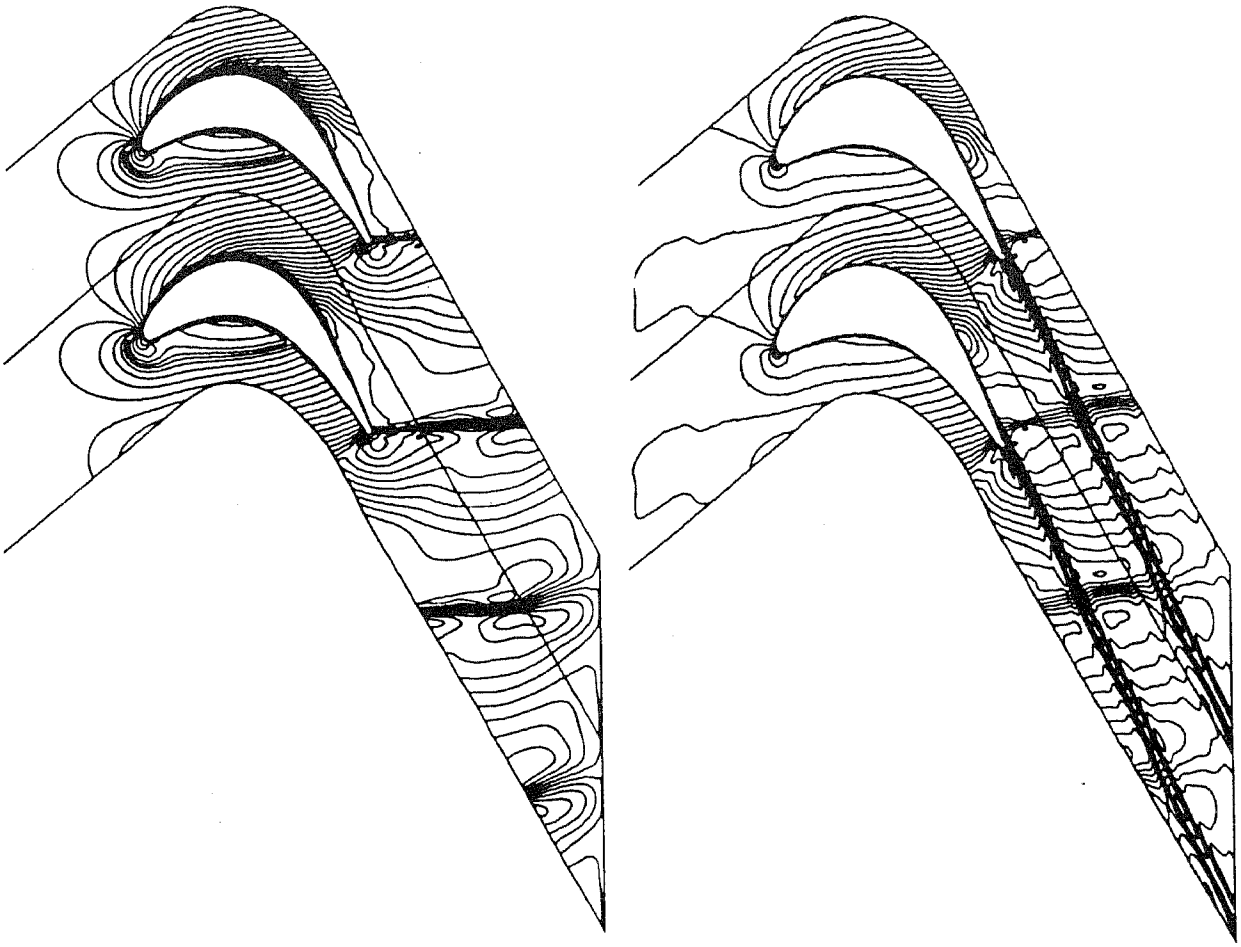

(a) inviscid flow (isentropic) (b) transitional flow (local)

Figure 13. FLOS3D, Mach number isolines.

The local Mach number isolines predicted by FLOS3D in inviscid and transitional flow regime are given in figures 13.a and 13.b respectively. The transitional flow calculation refers to the bypass transition model in which the pressure side is also transitional. Still, the overall flow pattern is substantially not altered by the changes in the nature of the transition model. The inviscid calculation shows that the shock is generated exactly at the trailing edge of the blade. The pressure side shock is very weak and hard to detect, as proved by the Schlieren pictures shown in figures 2.a and 2.b. When moving to the turbulent flow regime, the shock angle is slightly changed. Still, the most important change with respect to the inviscid flow regime calculation is the position from which the shock departs on the suction side. Figure 13.b shows that the shock is generated upstream of the inviscid flow position on the suction side.

Figures 14.a and 14.b show the local Mach number isolines computed by the transitional TLK and TLV models respectively. The two plots show identical patterns with only marginal

differences across the shock. Figures 13 and 14 show that, as already found by Michelassi et al. [24], the time marching code suffers more than the pressure correction solver of some shock smearing, especially in complex flows. Moreover the plots show that the boundary layer remains very thin as long as the shock is reached. At the shock, the boundary layer experiences an evident thickening. Figure 15 shows the experimental shock pattern. While the pressure side shock departs from the trailing edge, on the suction side the shock is generated somewhat upstream of the trailing edge. This is in perfect agreement with the predictions of both the time marching and the pressure correction solver, and it does indicate that the overall boundary layer development is correctly modelled.

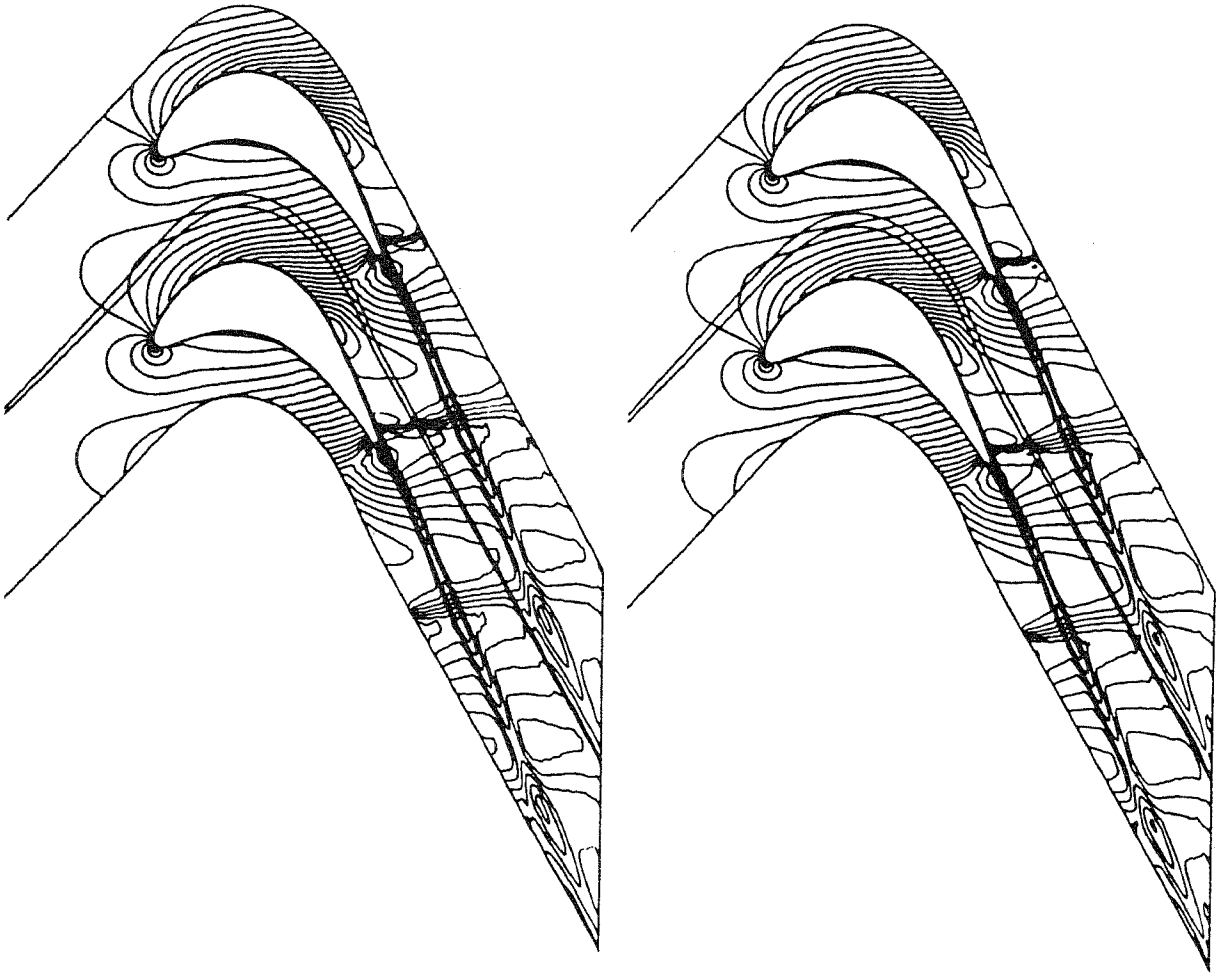

(a) transitional TLK (b) transitional TLV

Figure 14. FASTC-3D, local Mach number isolines.

Figure 16 shows the small and thin separation bubble predicted by using the FLOS3D solver in conjunction with the separated flow transition model. While fully laminar calculations soon develop an unsteady behaviour, the transition model is able to stabilise the solution. The laminar separation bubble, visible on the suction side, starts where the shock impinges on the blade. This reverse flow region remains stable and, although the boundary layer thickness is increased, the separation bubble does not tend to merge together with the trailing edge vortex

on the suction side. When using the bypass transition model with k-ω a very small separation bubble was also observed when setting a laminar pressure side. Still, this recirculation disappears when introducing the transition model on the pressure side also, which proved to improve the predictions of the isentropic Mach number profile.

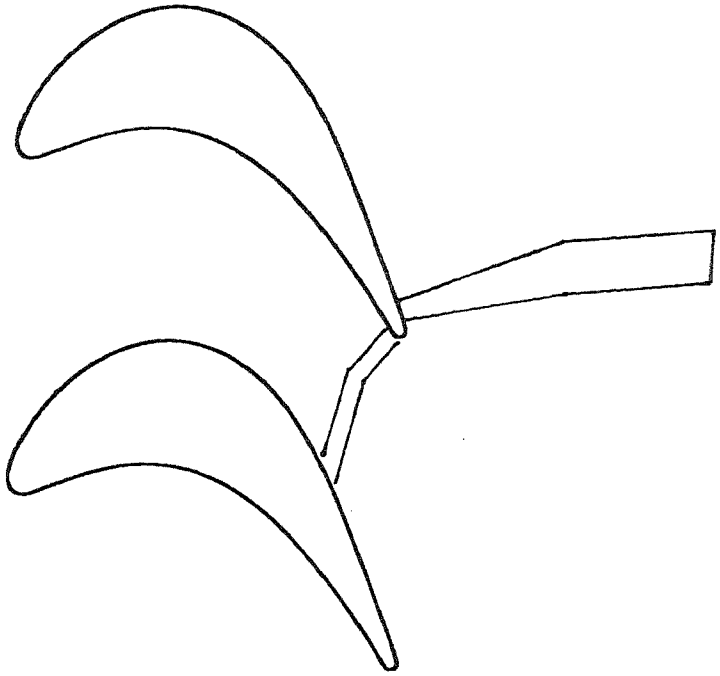

Figure 15. Experimental shock pattern.

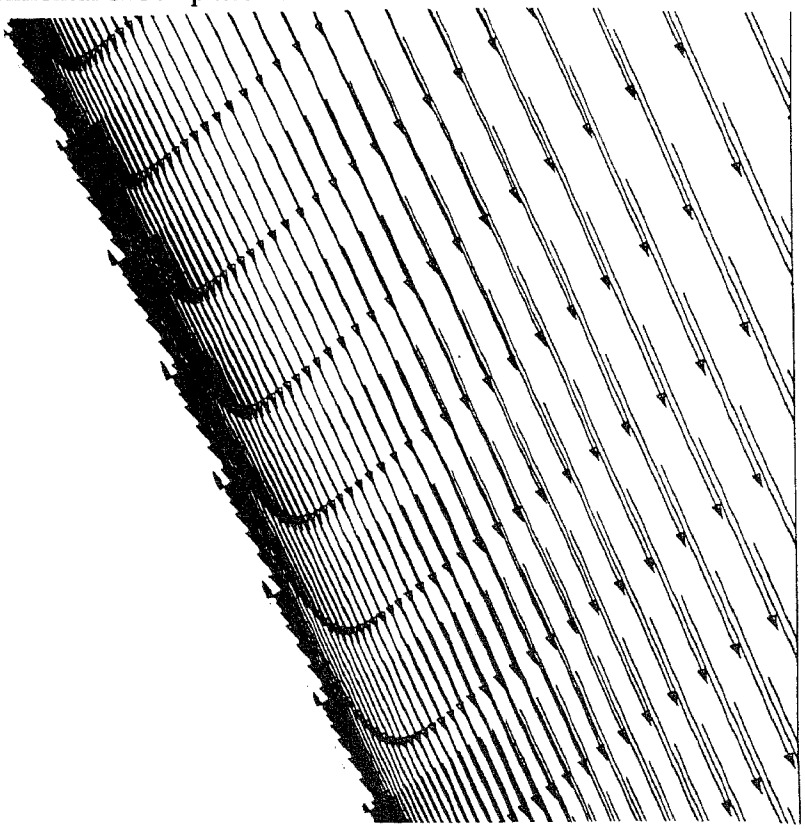

Figure 16. Shock-boundary layer interaction induced separation on the suction side. FLOS3D with separated flow transition model.

5.2.2 - Wake profiles

The exit flow angle, Mach number and total pressure profiles have been measured at x≈ 1.46·C, in which C is the axial chord, and the x origin is located on the blade leading edge. As a general remark before entering the details of the comparison with experiments, it is necessary to observe that the transition models have very little impact on the profiles far downstream the trailing edge. This is probably due to the great amount of turbulence generated in the trailing edge vortices, the overwhelming importance of which greatly diminished the influence of the boundary layer thickness on both the suction and pressure sides.

The plots are made in such a way y/pitch=-2.5, -1,5, -0.5 corresponds to the portion of the flow downstream of the trailing edge, whereas the periodic boundaries are located at y/pitch=-2.0, -1.0, -0.0.

Figures 17,a,b,c compare the computed exit flow angle, local Mach number, and total pressure ratio in the wake (P_{01} is the inlet total pressure, P_{02} is the local total pressure) with experiments. Observe that experiments show an extremely good periodicity for the two experimental vanes under consideration. The turbulent boundary layer calculation (k-o+kl) differ very little from the bypass transition model with α=1 (k-o+kl+trans) and the separated flow transition model (k-o+kl+btrans). The exit flow angle in figure 17,a is well captured especially for the portion of the flow which is coming from the pressure side (for -2.0 < (y/pitch) < -1.5). The only remarkable difference between the various predictions takes place on the portion of the flow coming from the suction side. The fully turbulent calculation is expected to predict a thicker boundary layer on the suction side, which increases the portion of the profile which is affected by the wake. The overall trend is correctly followed by the computations. The computed and experimental local Mach number profiles, visible in figure 17,b show a slight overestimation of the peak value for all the computations (at y/pitch≈-2.0 and -1.0). For the portion of the flow coming from the suction side the agreement with experiments is again generally good, it does not deteriorate for the pressure side also, even though, for this flow region the transitional calculation shows a better fit with experiments. The up-down shape of the profiles deep in the wake is thinner in the transitional flow calculation than in the fully turbulent ones. This difference is clearly caused by the different boundary layer thickness predicted in the two cases. Figure 17.c compares the computed and experimental total pressure profiles. This plot clearly shows that the computed total pressure wakes are much deeper and thinner than the experimental ones. This feature of the computed wakes is absolutely independent of the transitional or fully turbulent nature of the boundary layer. Although this phenomena still lacks a definite explanation, the paper by Kost and Gieβ [11] can help to explain this disagreement. In their paper, Kost and Gieβ measured the wake downstream of the profile T6.1, which is the stator blade of the T5.1 profile under consideration in this work. The flow downstream of the trailing edge of the stator blade clearly show some trailing edge vortex shedding which yielded to instationary flow conditions in the near wake. From specific studies in the field, vortex shedding is known to largely increase the momentum diffusion in high shear flow regions. Although it is not sure that the shedding is present on the T5.1 blade also, this extra diffusion is probably the main responsible for the smooth experimental total pressure wakes. The steady nature of the computer simulations does not allow for accounting of such a complex phenomena. Accordingly, the lack of any sort of numerical vortex shedding might well explain the thinner and deeper wakes computed by the FLOS3D code.

Figure 18 shows the flow angle, local Mach number and total pressure ratio profiles for the FASTC-3D code when using the high-Re k-ε model and the TLK model under the assumption of fully turbulent or transitional boundary layers. The results obtained with the

TLV model are not reported since they nearly collapse with those given by the TLK formulation. Observe that most of the comments made about the FLOS3D calculations can be repeated here as well. The k-ε model with wall functions (k-eps+wf), the TLK model (k-eps+tlk), and the transitional TLK model (k-eps+tlkt) show almost identical results. In figure 18.a the exit flow angle show the same trend exhibited by the FLOS3D simulations. The introduction of the transition model in the TLK formulation slightly improves the fit between the computed and measured flow angles. The local Mach number profiles given in figure 18.b show that the maximum value of Ma is here underestimated by the computations, which is opposite to what found in the k-ω simulations. This also fits with the isentropic Mach number profiles around the blade in which the k-ω model always gave higher velocity peaks. The up-down shape in the wake is present here as in the k-ω predictions. The situation of the total pressure profiles does not improve much when moving from the time marching code to the pressure correction algorithm. Figure 18.c shows that the total pressure wakes are not as deep and thin like in the time marching algorithm. Still the shape of the computed total pressure wakes is far from the experimental one. The introduction of the transition model plays here a similar role to that found for the k-ω model. In fact the total pressure wake thickness is reduced for the portion of the flow coming from the suction side (-1.5 < y/pitch < -1.0), but the improvement of the fit with experiments is marginal.

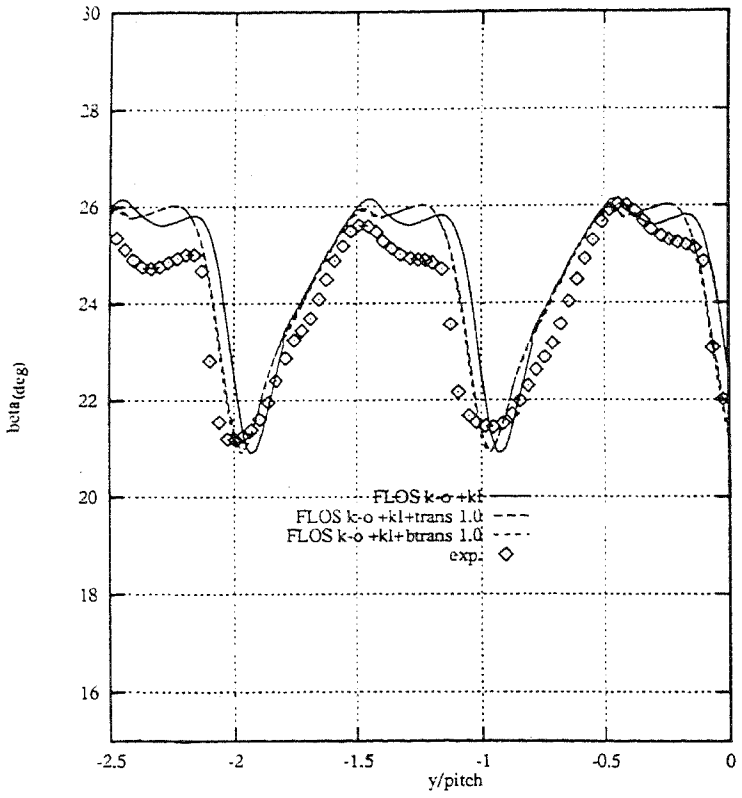

(a) flow angle

Figure 17. FLOS3D, wake profiles for fully turbulent and transitional boundary layer.

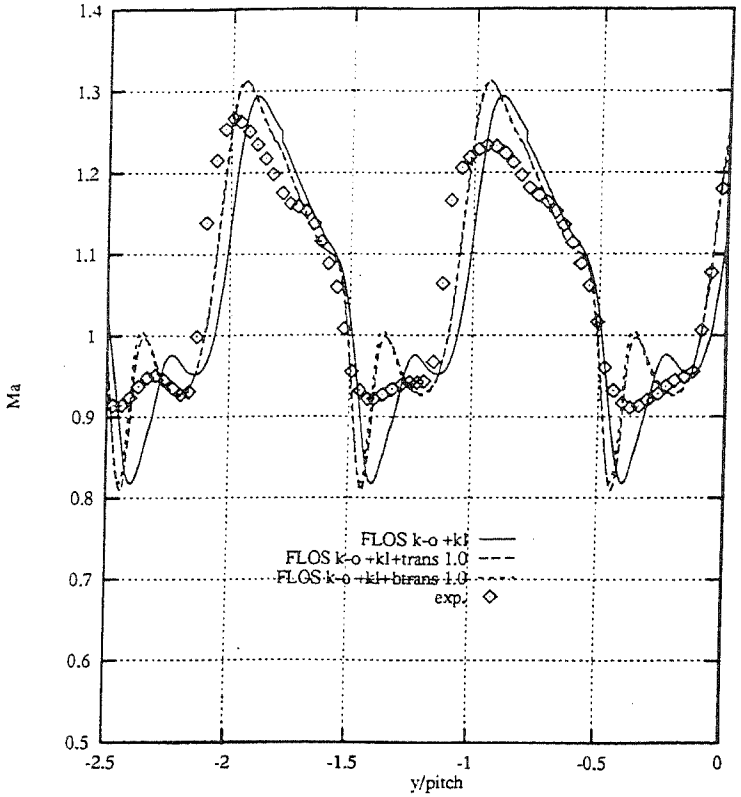

(b) local Mach number

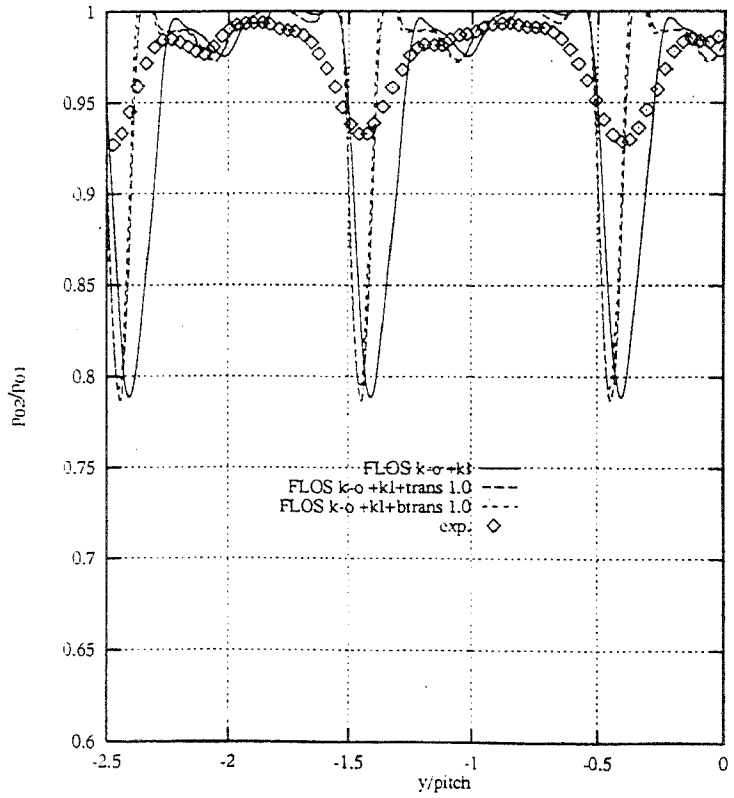

(c) total pressure ratio

Figure 17 (cont).FLOS3D, wake profiles for fully turbulent and transitional boundary layer.

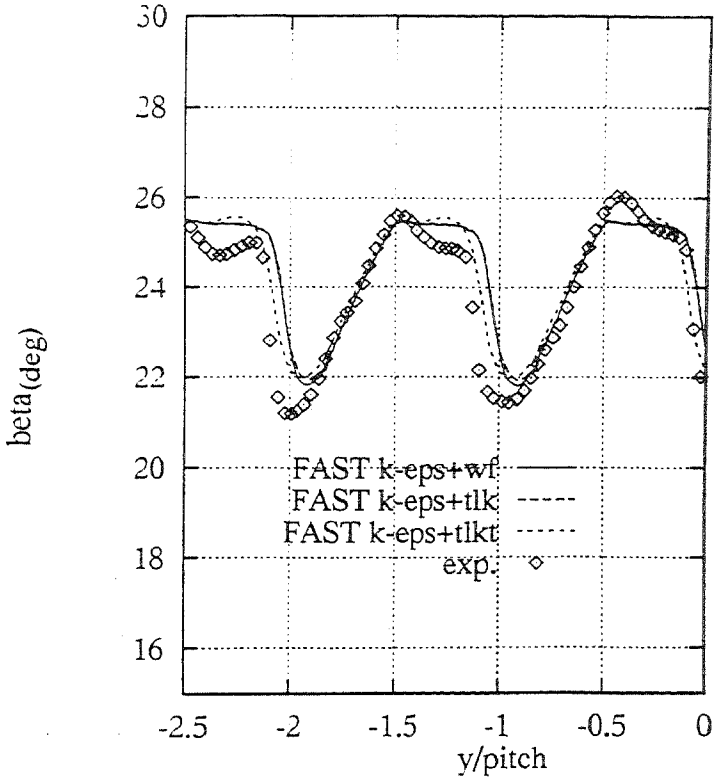

(a) flow angle

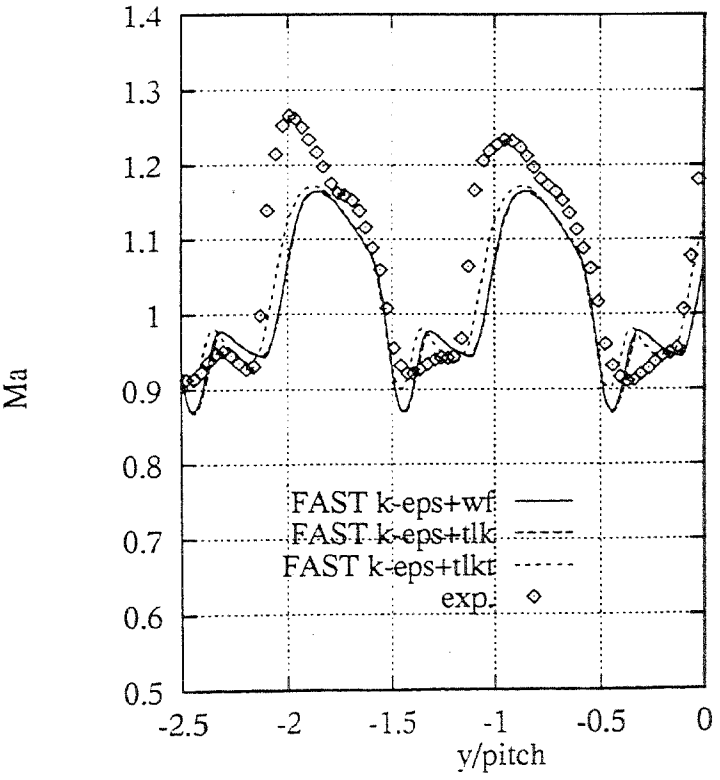

(b) local Mach number

Figure 18. FASTC-3D, wake profiles for fully turbulent and transitional boundary layer.

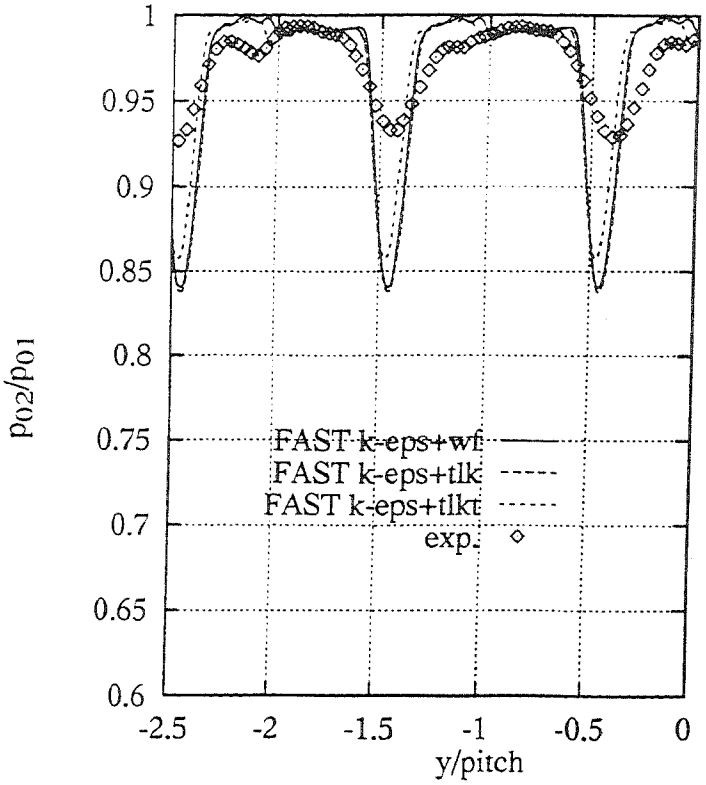

(b) total pressure ratio

Figure 18 (cont). FASTC-3D, wake profiles for fully turbulent and transitional boundary layer.

5.2.3 - Velocity and Total Pressure profiles in the guide vane

The set of measurements include six Mach number and total pressure profiles in the guide vane. Four of them are taken on the suction side and refer to sections upstream and downstream of the shock, and the other two are taken close to the trailing edge on the pressure side. For these six sections, located as shown in figure 19, the boundary layer thickness is also available. The four sections on the suction side will be referred to by Ass, Bss, Css, Dss, whereas those on the pressure side are Aps, Bps. The computed velocity and total pressure profiles will be analysed in conjunction with the features of the transition models.

Only some of the profiles computed by assuming a fully turbulent boundary layer will be shown because they are often completely off the measured ones. The fully turbulent boundary layer hypothesis causes an overestimation of a factor 2 to 3 of the boundary layer thickness on the suction side. The discrepancy on the pressure side is reduced by the natural tendency towards the flow relaminarization in presence of favourable pressure gradients, which is approximately captured by the turbulence models without the aid of a transition model. Still, the best fit with experiments is obtained by switching on the transition models.

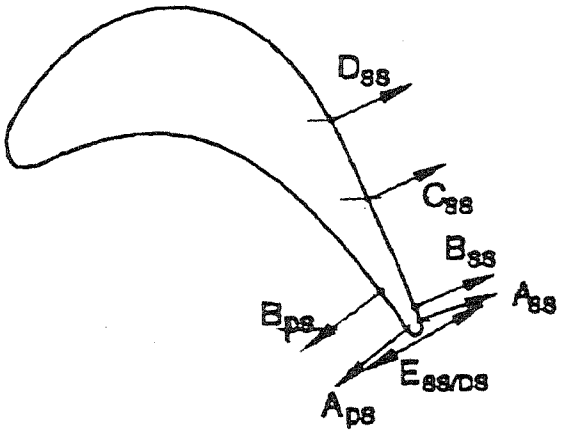

Figure 19. Location of the experimental velocity profiles.

Figures 20,a,b compares the measured total pressure profiles with those computed by the wall-function approach (wf) and the TLK model without transition (tl1), and the TLK model with transition (ttl1) on both the suction and pressure sides. For the Css and Dss profiles, which are located upstream of the shock on the suction side, the effect of the transition model is very large. In these two sections the boundary layer is still laminar and the fully turbulent assumption provokes a large overestimation of the boundary layer thickness. The transitional flow calculations are in best agreement with experiments especially downstream of the shock (see sections Ass and Bss). On the pressure side the fully turbulent flow calculations are in better agreement with experiments than the transitional one. This is due to the early relaminarization predicted by the TLK model in conjunction with the transition model on the pressure side. Apparently, the effect of the strong flow acceleration on the boundary layer is better modelled by using the fully turbulent assumption than by implementing the transition model. Still, this disagreement with the experimental profiles remains located on the pressure side close to the trailing edge, where the effect of the flow acceleration and history is maximum. Not much can be asserted on what happens further upstream on the pressure side because of the lack of measurements.

Figures 21,a,b compare the computed and measured boundary layer thicknesses on both the suction and the pressure sides. The boundary layer thickness is defined according to equation (29). On the Suction side the transitional flow calculation are in excellent agreement with experiments. The sudden growth of the boundary layer across the shock is correctly modelled. On the pressure side the agreement is not as good since the computed thickness is less than the experimental one. Figure 21,b qualitatively agrees with the total pressure profiles on the pressure side given in figure 20,b. At a first glance, figure 21,a shows that the boundary layer remains laminar up to x_{ax}=0.04, and transition develops from this abscissa on, which is the approximate position in which the shock impinges on the boundary layer. On the pressure side the flow behaves differently. The boundary layer thickness, which reaches its maximum at $x_{ax}\approx$0.025, is evidently turbulent. After this point, the effect of the strong acceleration, typical of transonic turbine flows, causes a strong relaminarization. Still, the importance of this phenomena is overestimated by the computations.

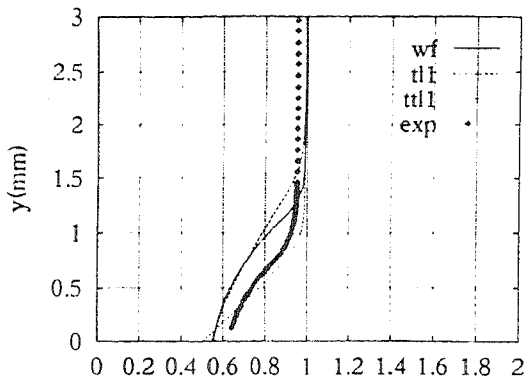

Ass

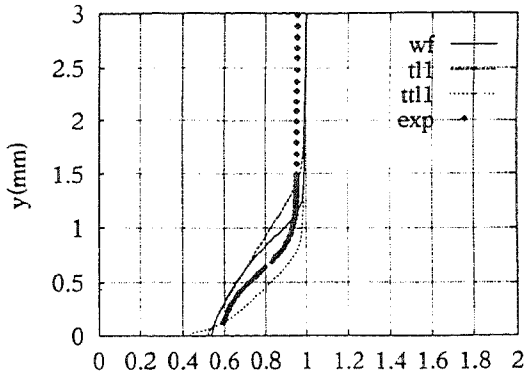

Bss

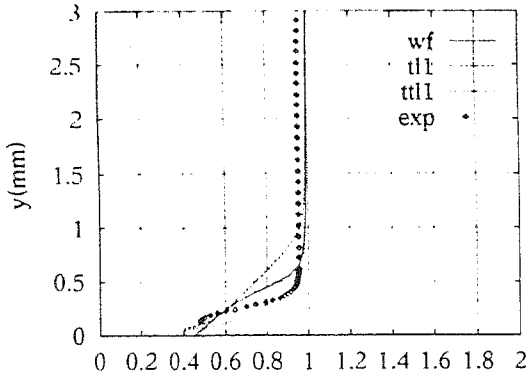

Css

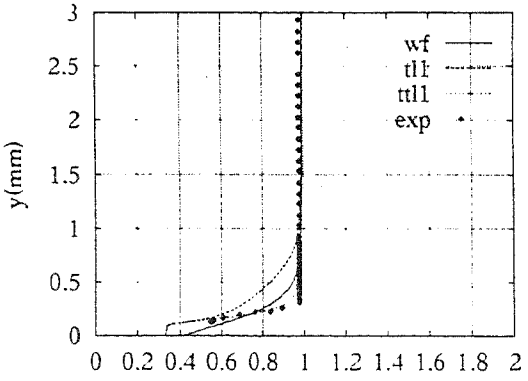

Dss

(a) suction side

Figure 20. FASTC-3D, Total pressure profiles.

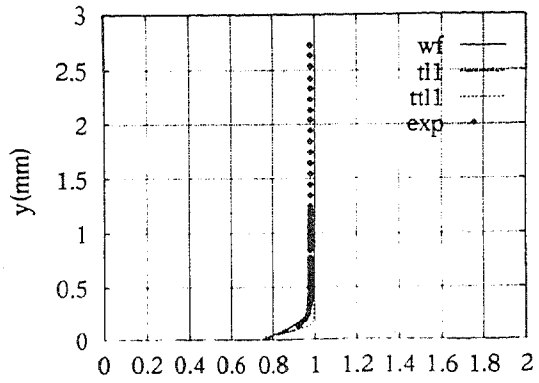

Aps

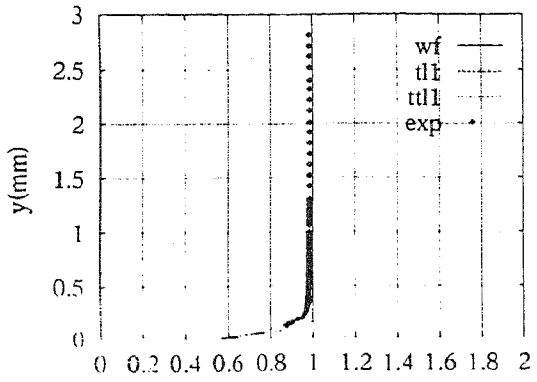

Bps

(b) pressure side

Figure 20 (cont). FASTC-3D, Total pressure profiles.

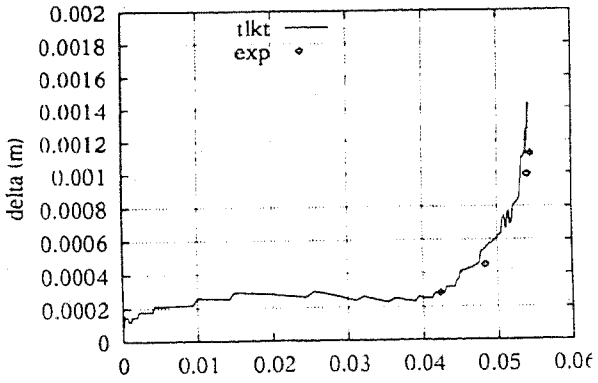

(a) suction side

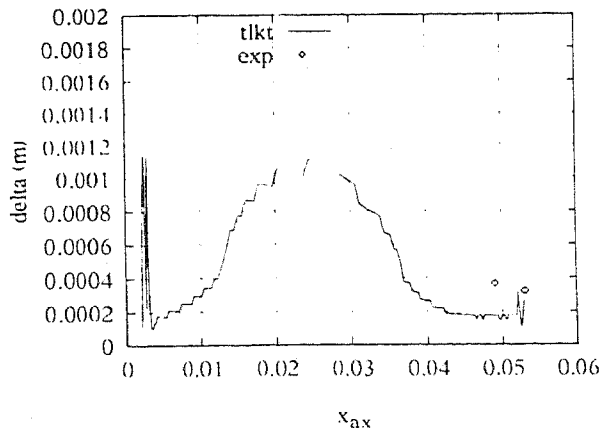

(b) pressure side

Figure 21. FASTC-3D, Boundary layer thickness, transitional TLK model.

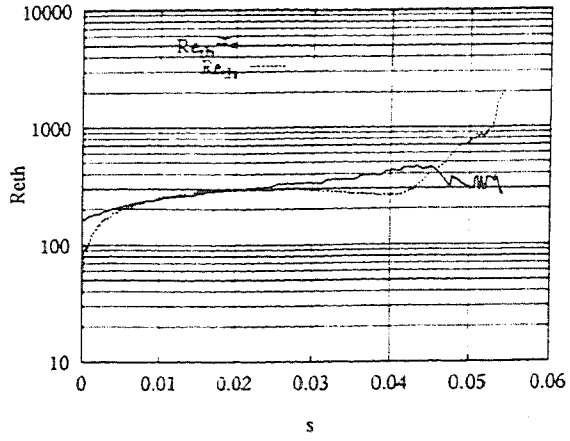

(a) suction side

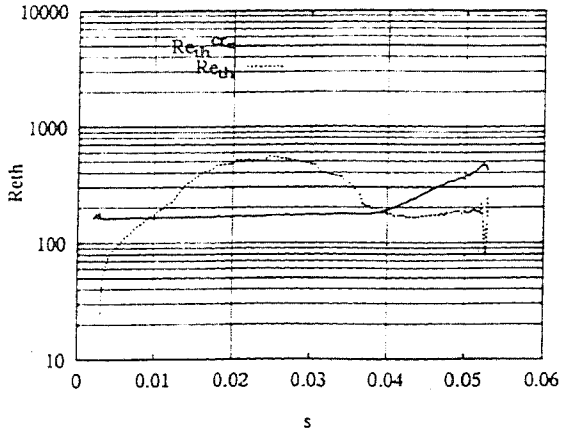

(b) pressure side

Figure 22. Local and critical Re_ϑ profiles, transitional TLK model.

Figures 22 and 23 explain the behaviour the transition model. Figure 22,a,b show the computed profiles of the local and critical Re_ϑ on the suction and pressure sides respectively. The local Re_ϑ is larger than the critical Reynolds number up to the shock. From there on, the total pressure losses induced by the shock determines an increase in the boundary layer thickness which is the main responsible for the onset of transition. Remember that is was necessary to use the turbulence level at the edge of the boundary layer, and not the core flow value, to have transition. When using the free stream value of the turbulence level, the model predicted a fully laminar boundary layer down to the trailing edge. On the pressure side the flow behaves very differently. The critical Reynolds number is exceeded very early on the blade surface and the model predicts a transition from laminar to turbulent. Then, the flow acceleration largely decreases the value of Re_ϑ which falls again below the critical value at $s \approx 0.04$. From here on the boundary layer reverts to laminar till the trailing edge. The relative shapes of the intermittency function, which is the squared expression in square brackets present in equation (17), is reported in figures 23,a,b for the suction and pressure sides respectively. On the suction side transition is quite sharp, and it takes place across the shock, after which the intermittency function reaches unity. On the pressure side, transition is slightly smoother, but the flow does not stay turbulent till the trailing edge. In fact, as observed already in the Re_ϑ profiles, the strong flow acceleration causes a sharp reverse transition, and A^+ in equation (17) becomes 300 again.

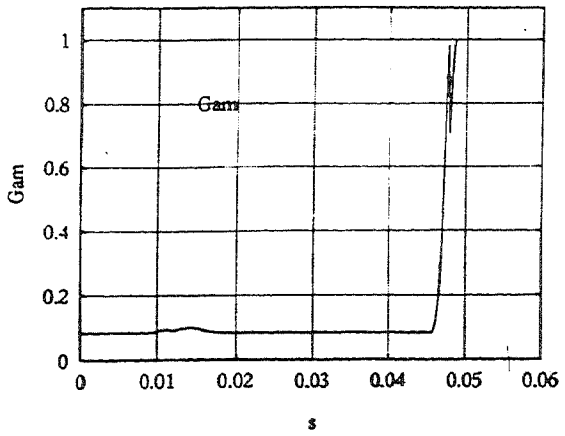

(a) suction side

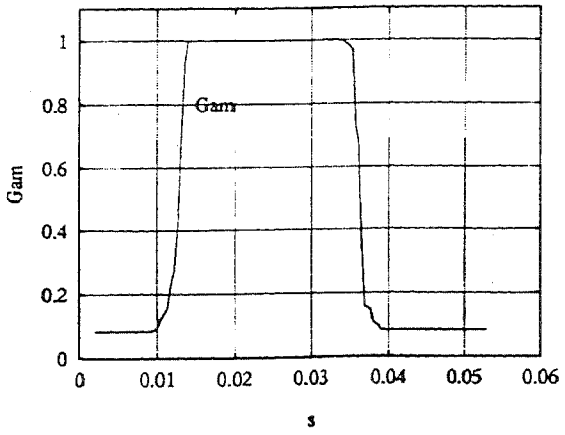

(b) pressure side

Figure 23. Intermittency function, transitional TLK model.

When moving to the transitional TLV model some problems arise. As already mentioned in section 3.2, the correlation for the Reynolds number at the end of transition could not be used. This caused a series of problems in the implementation of the transition model which are somewhat summarised in figures 24,a,b, which show some attempts to tune the transitional TLV formulation The various cross sections refer to: ttv0 corresponds to results obtained by using the correlation for the end of transition as it is: the ttv1, ttv2, ttv3 profiles are obtained by setting the intermittency function to unity as soon as the critical Reynolds number is exceeded, and by using three different matching points between the internal and external layers, at $\frac{\mu_t}{\mu} = 12, 18, 30$ respectively. Unfortunately, despite the various attempts, the combination of the TLV model and the transition model by Sieger et al. [37] does not ensure the same accuracy given by the transitional calculations by the TLK model. With the relation for the end of transition the boundary layer clearly stays laminar, and the situation is only marginally improved by switching to turbulent boundary layer as soon the critical Reynolds number is exceeded. The various profiles are virtually identical upstream of the leading edge and on the pressure side where the effect of the transition model is less severe. Despite the large discrepancies in the velocity profiles, figure 25,a,b show the satisfactory fit between the computed and measured boundary layer thicknesses. The profiles refer to the ttv0 formulation, although the differences with the other attempts are negligible. Figures 26,a,b show the profiles of Re_ϑ, the critical Reynolds number and the Reynolds number of the end of transition. On the

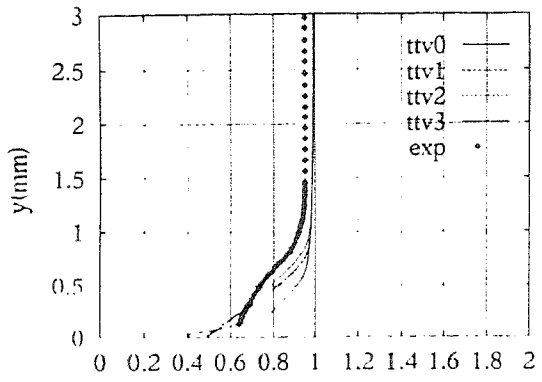

Ass

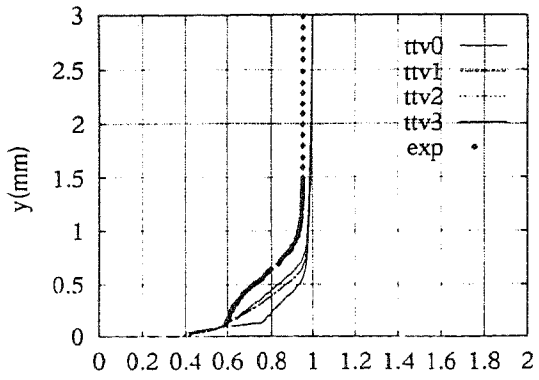

Bss

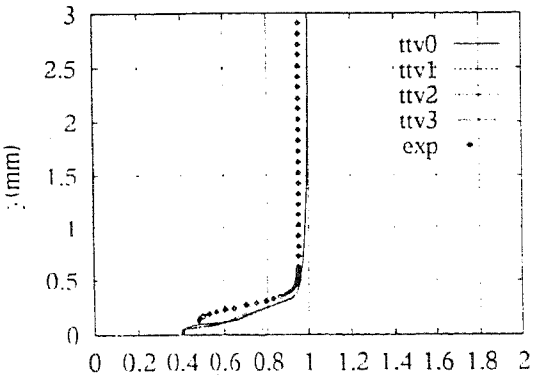

Css

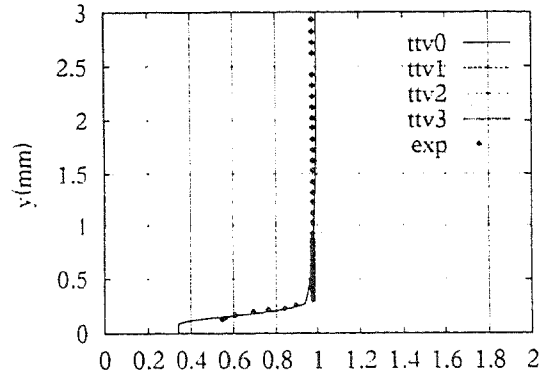

Dss

(a) suction side

Figure 24. FASTC-3D, Total pressure profiles, transitional TLV model.

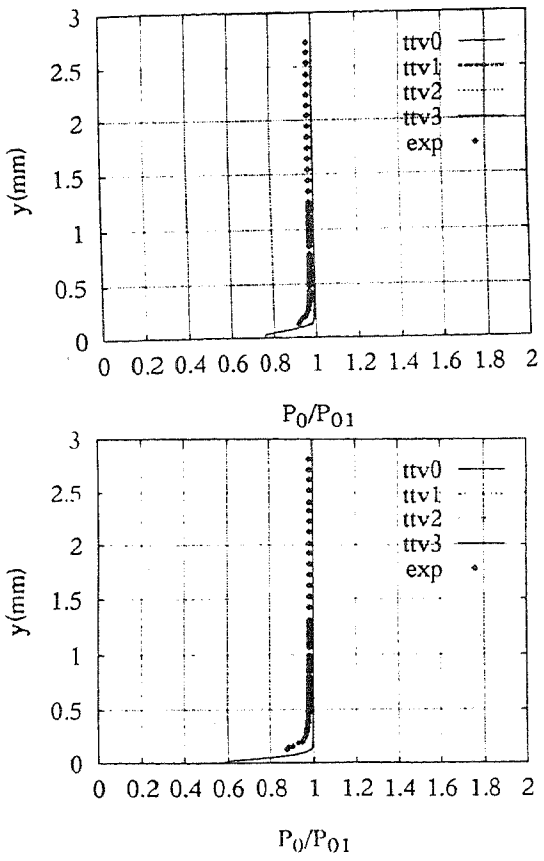

(b) pressure side

Figure 24 (cont). FASTC-3D, Total pressure profiles, transitional TLV model.

suction side (see figure 26,a) Re_ϑ stays below the critical Reynolds number until the shock is reached, but then it grows too slowly so that the boundary layer stays practically laminar. On the pressure side (see figure 26,b) the model seems to predict both transition and reverse transition, as predicted by the TLK model, without any difficulty.

The agreement with experiments is not substantially altered when switching to the FLOS3D code and the k-ω model. The profiles obtained by assuming a fully turbulent boundary layer are not given here, but attention will be focused on the profiles obtained with the separated flow transition model and the bypass transition model. After intense numerical testing, it was found that, when using the by-pass transition model the best fit with experiments was ensured by introducing the transition model on the pressure side also, as already observed in the discussion of the Isentropic Mach number distribution. Figure 27 compares the computed and measured total pressure profiles in the blade vane in the same six cross sections mentioned above. The agreement with experiments is good on both the pressure side and the first two sections of the suction side upstream of the shock. The two profiles downstream of the shock (ass and bss) show that the computed boundary layer thickness is still too small as compared with experiments. This is due to the smooth growth of the intermittency function when transition is started. Since transition is always completed when using equation (25), although too late, it was decided not to set f_t=1 as soon as the critical Reynolds number was exceeded. A direct comparison with the predictions given by the separated flow transition model is possible when looking at figure 28. This run was performed assuming a laminar boundary layer on the pressure side. The aps and bps profiles are in good agreement with

experiments, as in figure 27, although the laminar boundary layer assumption underestimates the boundary layer thickness. Still, the separated flow transition model seems to perform very well downstream of the shock, as visible in sections ass and bss.

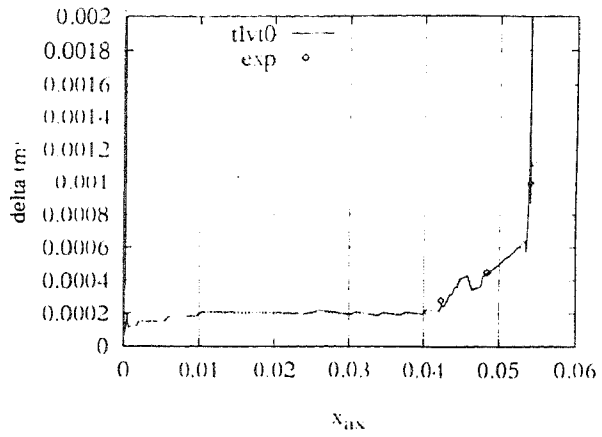

(a) suction side

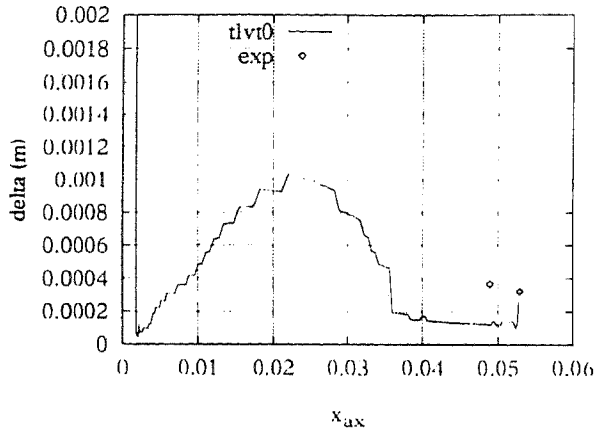

(b) pressure side

Figure 25. FASTC-3D, Boundary layer thickness, transitional TLV model.

Figures 29,a,b compare a typical computed and measured boundary layer thickness on both the suction and pressure side with those predicted by the by-pass transition model in conjunction with the k-ω turbulence model. The agreement on the pressure side is quite good, while the boundary layer thickness is slightly underestimated upstream of the shock on the suction side.

The plots of the intermittency function allows understanding the results of the simulation better. On the suction side with the by-pass transition model (figure 30,a) transition takes place approximately at the same position predicted by using the two-layer models with the FASTC-3D code. Still, the growth of Re_ϑ, after the critical Reynolds number is exceeded, is not as sharp as in the two-layer models. On the pressure side (figure 30,b) the situation is very much different: the boundary layer first becomes turbulent and than it experiences a reverse transition, as evidenced by the two-layer models. When switching to the separated flow transition model the critical Reynolds number is exceeded in correspondence with the reattachment position, and in approximately the same position predicted by the by-pass transition model (see figure 31,a). Observe that in figure 31,a, in proximity to the leading edge

Re_ϑ exceeds the critical Reynolds number with no effect on transition because of the lack of separation bubble in the region of the blade nose.

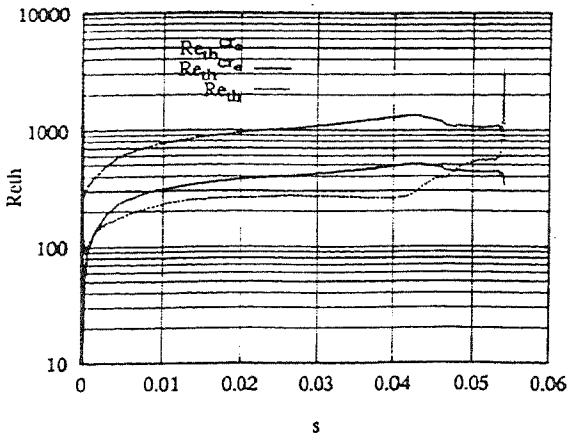

(a) suction side

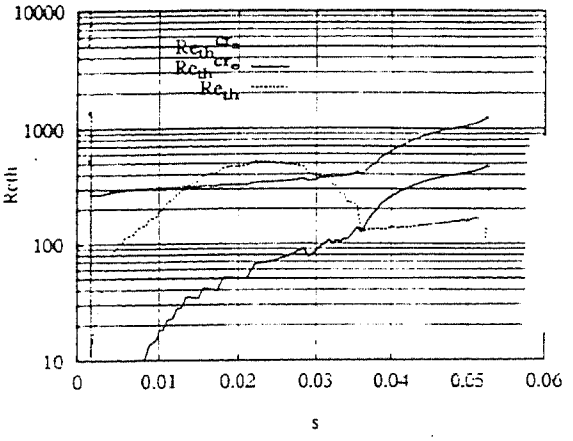

(b) pressure side

Figure 26. Local and critical Re_ϑ profiles, transitional TLV model.

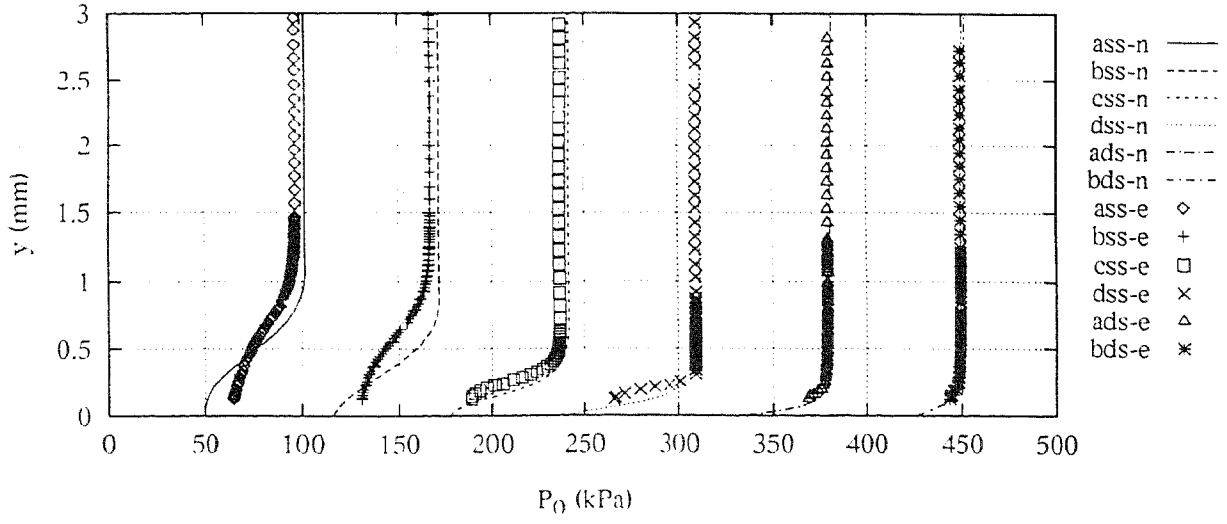

Figure 27. FLOS3D, Total pressure profiles, by-pass transition model.

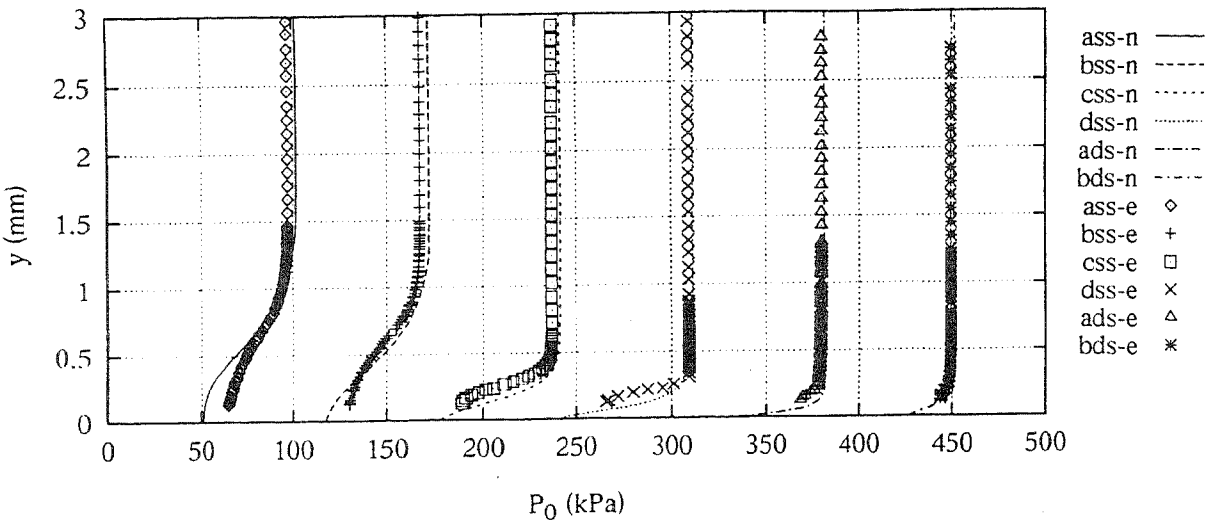

Figure 28. FLOS3D, Total pressure profiles, separated flow transition model.

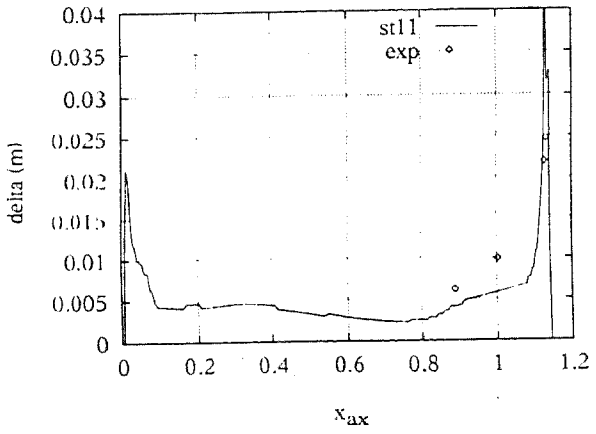

(a) suction side

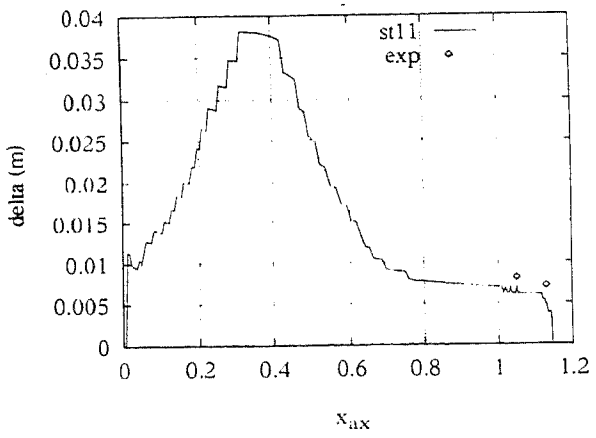

(b) pressure side

Figure 29. FLOS3D, boundary layer thickness, FLOS3D, by-pass transition model.

The intermittency functions relative to the by-pass and separated flow transition models are plotted in figures 32 and 33. On the suction side (figure 32,a) the by-pass transition model predicts too slow a growth of the intermittency function, which reaches unity only in proximity of the trailing edge. On the pressure side (see figure 32,b), the shape of the intermittency function is very much irregular. After transition to turbulence in the first half of the blade, the model predicts a sharp reverse transition, as given by the two-layer models. Then, while the flow remained laminar till the trailing edge with the two-layer models, here the intermittency function grows again showing an up down behaviour which is difficult to explain. Figure 33 shows the intermittency function predicted by using the separated flow transition model. The shape of this function is different from that predicted by the by-pass transition model, mostly because of the sharp growth to unity experienced immediately after the transition point. Despite the large differences in the intermittency functions, the results from the two transition models in the k-ω turbulence models are quite similar. Observe that in the separated flow transition model the separation bubble is laminar and transition is switched on after the reattachment point.

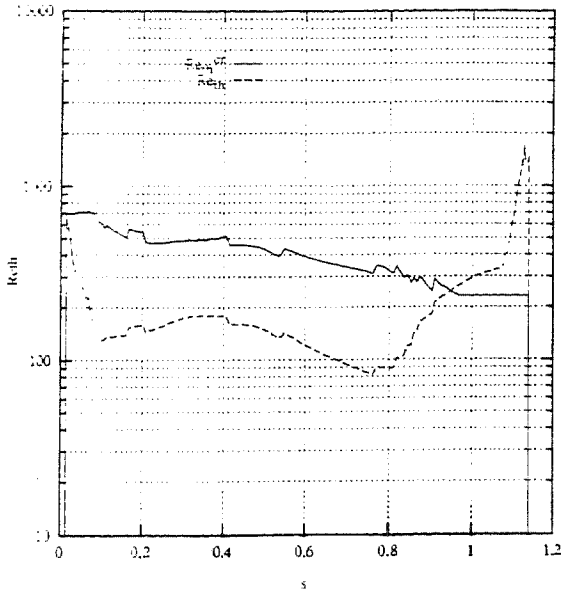

(a) suction side

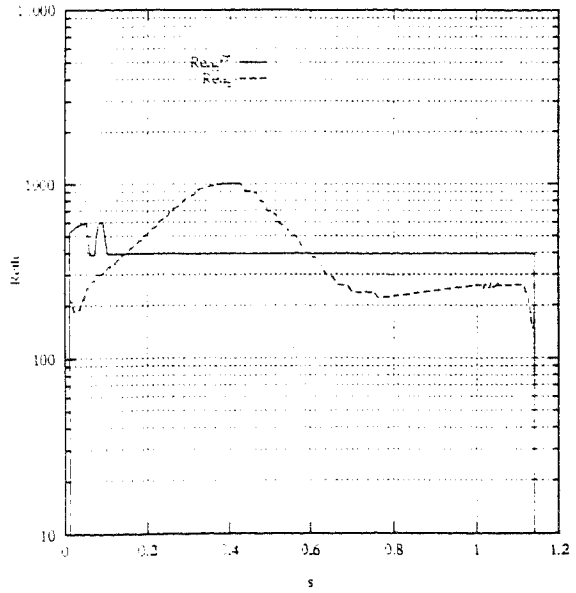

(b) pressure side

Figure 30. Local and critical Re_ϑ profiles, FLOS3D by-pass transition model.

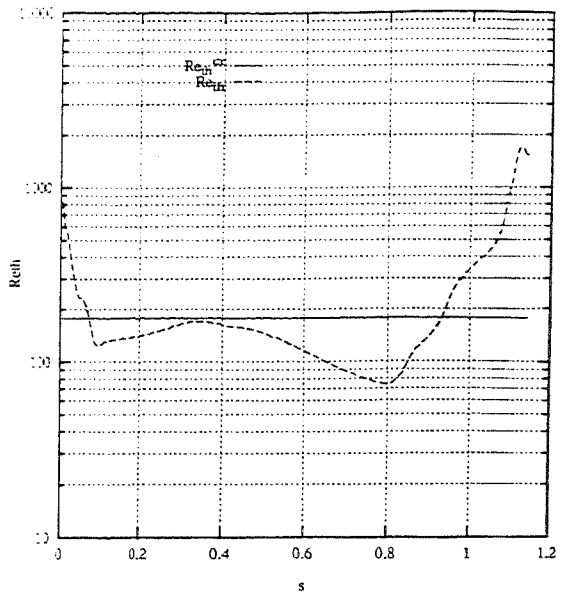

(a) suction side

Figure 31. Local and critical Re_ϑ profiles, FLOS3D separated flow transition model.

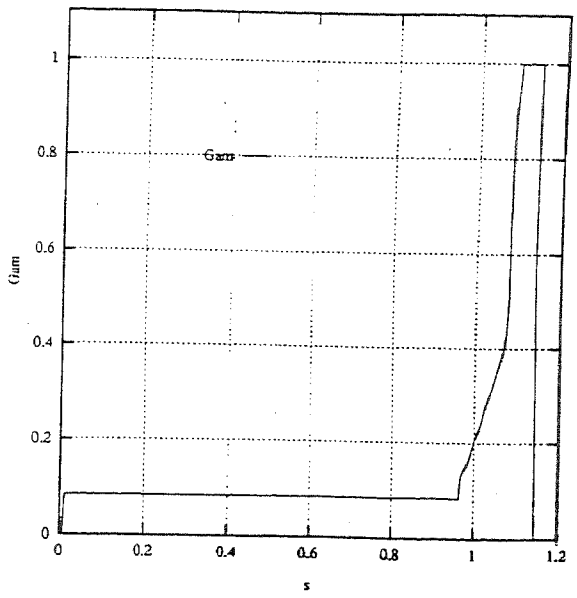

(a) suction side

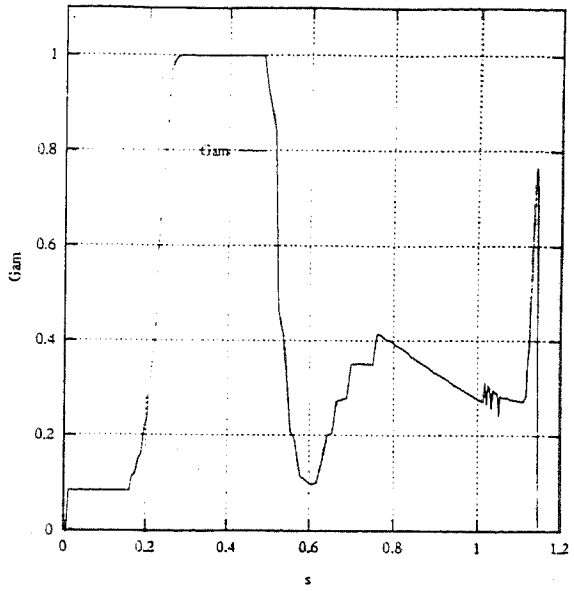

(b) pressure side

Figure 32. Intermittency function, FLOS3D by-pass transition model.

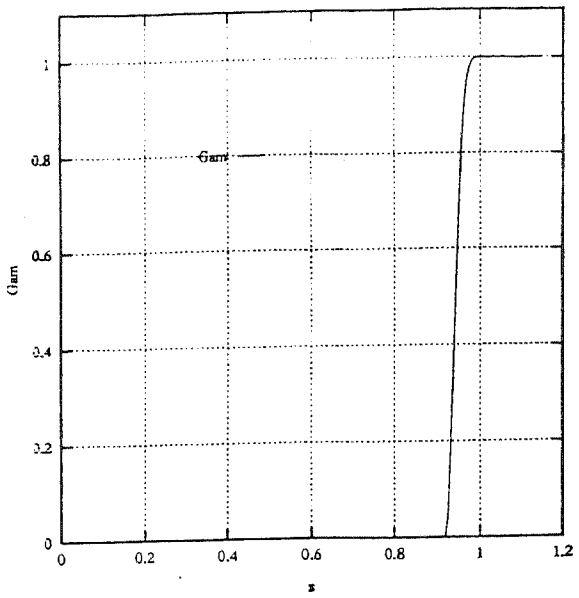

(a) suction side

Figure 33. Intermittency function, FLOS3D separated flow transition model.

6 - CONCLUSIONS

The wide set of computer simulations were mostly aimed to verify the applicability of existing transition models to transonic turbine flows. The experimental data set provided a challenging opportunity for the verification of the accuracy of both by-pass and separation bubble transition models. The very low experimental turbulence intensity, which was approximately 0.6% limited the validity of the existing by-pass transition models. It is in fact questionable whether at such a low turbulence intensity by-pass transition is possible and, in case it is, if the existing correlations are adequate. In fact, all the transition models based on the Abu-Ghannam and Shaw correlation failed to predict any transition, natural or across the shock wave which impinges on the suction side of the blade. The by-pass approach managed to predict a sort of transition when replacing the core flow turbulence intensity with the turbulence intensity encountered at the edge of the boundary layer. This procedure introduces another source of uncertainty in the correlation for the determination of the critical Reynolds number, which is now directly sensitive to the way the boundary layer thickness is defined. Still, this ad-hoc modification proved able to switch transition on in the three turbulence models under investigation with the relative transition models. Although this result would require a wider validation, it seems that the turbulence level at the edge of the boundary layer is a good sensor for transition across shocks.

The separated flow transition model also proved adequate for this kind of flow. The model, applied to a highly compressible transonic flow, allowed computing a laminar separation bubble. The computed results indicated that transition starts after the reattachment point, even though transition was expected to start inside the separation bubble. When considering that experiments do not allow to draw a final conclusion about the presence or not of the separation bubble, and, if a separation bubble is present, about its size, the results of the transition model can be regarded as satisfactory because the predictions are in overall good agreement with experiments.

All the models give a satisfactory description of the wake and the profile of the isentropic Mach number around the blade. The transition model, when applied on the pressure side of the blade, has an effect on the shock and boundary layer interaction on the suction side. It was found that the isentropic Mach number profile immediately after the velocity peak on the suction side and until the trailing edge was affected by the nature and thickness of the boundary layer on the pressure side. This can be explained by observing that the expansion wave and shock strength are influenced by the size of the two counter rotating trailing edge vortices, the size of which is affected by the nature of the boundary layer leaving the blade at the trailing edge. This important feature of the flow evidences that the prediction of the pressure distribution around the blade can suffer from an incorrect description of the boundary layer, especially in case its nature is highly transitional, like the ones encountered on the suction and pressure sides of the blade under consideration.

The computations also indicated that both the two-layer models and the k-ω model correctly mimic the relaminarization process on the pressure side of the blade. The introduction of the bypass transition correlation on the pressure side of the blade did not give any positive effect in terms of fit with the experimental profiles.

In view of a next set of tests, the effect of the pressure gradient on the fully turbulent value of A_t^+(=25) needs to be investigated. The effect of sharp pressure gradients on A_t^+ is a known problem, especially in presence of favourable pressure gradients.

7 - REFERENCES

[1] Abu-Ghannam, B.J., Shaw, R., "Natural Transition of Boundary Layers - The effects of Turbulence, Pressure Gradient, and Flow History", Journal of Mechanical Engineering Science, Vol.22, No.5, pp.213-228.

[2] Cho, N.-H., Liu, X., Rodi, W., Shönung, B., "Calculation of Wake-Induced Unsteady Flow in a Turbine Cascade", ASME Journal of Turbomachinery, October 1993, Vol.115, pp. 675-686.

[3] Coakley, T.J., "Turbulence Modelling Methods for the Compressible Navier-Stokes Equations", AIAA paper 83-1693, 1983.

[4] Durbin, P.A., "On the k-ε Stagnation Point Anomaly", to appear in the Int. J. Heat and Fluid Flow, 1996.

[5] Gieβ, P.-A., "Grenzschichtmessungen auf der Schaufeloberfläche bei transsonischer und incompressibler Durchströmung ebener Turbinengitter", DLR Institute für Strömungsmechanik, Report IB 223 - 94 A 08, 1994.

[6] Hanjalic, K., Launder, B.E., "Sensitising the Dissipation Equation to Irrotational Strains", ASME Journal of Fluids Engineering, 102, 1980, pp. 34-40.

[7] Jameson, A., Schmidt, W., Turkel, E., 1981 : "Numerical Solutions of the Euler Equations by Finite Volume Methods Using Runge-Kutta Time-Stepping Schemes", AIAA 81-1259.

[8] Jones, W.P., Launder, B.E., "The Calculation of Low-Reynolds Number Phenomena with a Two-Equation model of Turbulence". International Journal of Heat and Mass Transfer, Vol. 16, 1973, pp. 1119-1130.

[9] Kato, M., Launder, B.E., "The Modelling of Turbulent Flow around Stationary and Vibrating Square Cylinders", Proceedings Ninth Symposium of "Turbulent Shear Flows", Kyoto, Japan, August 16-18, 1993.

[10] Kost, F., "Messungen des Geschwindigkeitsfeldes nit dem L2F-Velocimeter bei transsonischer und inkompressibler Durchströmung ebener Turbinengitter", DLR Institute für Strömungsmechanik, Report IB 223 - 94 A 09, 1994.

[11] Kost, F., Gieβ, P.-A., "Incompressible and Transonic Turbine Wake Flow Influenced by Vortex shedding". VDI Berichte NR. 1186, 1995, pp. 63-77.

[12] Kwon, O.K., Pletcher, R.H., "Prediction of subsonic separation bubbles on airfoils by viscous-inviscid interaction". Second Symposium on Numerical and Physical Aspects of Aerodynamic Flows, Iowa State University, Ames, Iowa, USA, 1992.

[13] Lakehal, D. Private Communication, Institute for Hydromechanick, University of Karlsruhe, 1995.

[14] Lakshminarayana B., 1991, "An Assessment of Computational Fluid Dynamic Techniques in the Analysis and Design of Turbomachinery - The 1990 Freeman Scholar Lecture", ASME J. of Fluids Eng., Vol. 113, pp. 315-352.

[15] Launder, B.E., Spalding, D.B., "The Numerical Computation of Turbulent Flows", Comp. Match. App. Mech. Engg. Vol. 3, 1974, pp. 269-289.

[16] Mayle, R.E., "The Role of Laminar-Turbulent Transition in Gas Turbine Engines", ASME Journal of Turbomachinery, vol. 113, October 1991, pp. 509-537.

[17] Menter, F. R., "Two-equation Eddy-Viscosity Turbulence Models for Engineering Applications", AIAA Journal, Vol.3, No. 8, August 1994, pp. 1598-1605.

[18] Michelassi, V., "Adverse Pressure Gradient Flow Computation by Two-Equation Turbulence Models", Proceedings 2 nd International Symposium on Engineering Turbulence Modelling and Measurements", May 31-June 2, 1993, Florence, Italy.

[19] Michelassi, V., 1994, "The Meshho program 1.06", Rept no. 1-1994, Dept. of Energetics, University of Florence, Italy.

[20] Michelassi, V., "A pressure correction algorithm for all speed flows", Report No.718, Institute for Hydromechanik, University of Karlsruhe, Germany, 1994.

[21] Michelassi, V., Chiaramonti, D., Contribution to the 4-th ERCOFTAC/IAHR Workshop on Refined Flow Modelling, University of Karlsruhe, Karlsruhe, Germany, April 3-7, 1995.

[22] Michelassi, V., Liou, M.-S., Povinelli, L.A., Martelli, F., 1990, "Implicit Solution of Three-Dimensional Internal Turbulent Flows", NASA CP-10045.

[23] Michelassi, V., Martelli, F., (1993), "3-D Implicit Navier-Stokes Solver for Internal Turbulent Compressible Flows", Journal de Phys. III, France 3, pp. 223-235.

[24] Michelassi, V., Papanicolaou, E., Theodoridis, G., "A Comparison of Time Marching and Pressure Correction Algorithms for Transonic Turbine Blades", 1995 International Mechanics Engineering Congress and Exposition, November 12-17, 1995, San Francisco, California, USA.

[25] Michelassi, V., Theodoridis, G., Papanicolaou, E., "Low Speed Turbine Computation by Pressure Correction and Time Marching Methods", 1995 International Mechanics Engineering Congress and Exposition, November 12-17, 1995, San Francisco, California, USA.

[26] Michelassi, V., Rodi, W., Scheuerer, G., "Testing a Low Reynolds Number k-Turbulence Model Based on Direct Numerical Simulation Data", presented at the 8 th Symposium on Turbulent Shear Flows, Munich, Sept. 1991.

[27] Michelassi, V., Rodi, W., Zhu, J., "Testing a low Reynolds number k-ε turbulence model based on direct simulation data", AIAA Journal Vol.31 N.9, September 1993., and Rept. SFB/210/T/83, University of Karlsruhe, Germany, 1992.

[28] Michelassi, V., Shih, T.-H., "Low Reynolds Number Two-Equation Modelling of Turbulent Flows", NASA TM-104368, ICOMP 91-06, CMOTT 91-01.

[29] Norris, L.H., Reynolds, W.C., "Turbulent Channel Flow with Moving Wavy Boundary", Rept. No. FM-10, 1975, Stanford University, Dept. of Mech. Eng..

[30] Patankar, S.V., (1980), "Numerical Heat Transfer and Fluid Flow", Mc Graw-Hill Book Company.

[31] Pulliam,T.H., Chaussée, D.S., 1981, "A Diagonal Form of an Implicit Approximate-Factorisation Algorithm". Journal of Computational Physics, N. 39.

[32] Rhie, C.M., Chow, W.L., (1983), "Numerical Study of the Turbulent Flow Past an Airfoil with Trailing Edge Separation", AIAA Journal, No. 11, November 1983, pp. 1525-1532.

[33] Rodi, W., Mansour, N.N., Michelassi, V., "One-Equation Near-Wall Modelling with the Aid of Direct Simulation Data", ASME Journal of Fluids Engineering, vol.115, June 1993, pp.196-205.

[34] Rodi, W., Shönung, B., "Interaktives-Inverses Grenzschichtverfahren zur Berechnung von lokalen Ablöseblasen an Turbinenschaufeln", Z. Flugwiss. Weltraumforsch. 11, 1987, pp. 271-280.

[35] Rodi, W., Scheuerer, G., "Scrutinizing the k-ε Turbulence Model Under Adverse Pressure Gradient Conditions", ASME Journal of Fluids Engineering, 108, 1986, pp. 174-179.

[36] Savill, A.M., "Further Progress in the Turbulence Modelling of By-Pass Transition", Proceedings 2-nd International Symposium on Engineering Turbulence Modelling and Measurements", May 31-June 2, 1993, Florence, Italy.

[37] Sieger, K., Schiele, R., Kaufmann, F., Wittig, S., Rodi, W., "A Two-Layer Turbulence Model for the Calculation of Transitional Boundary-Layers", ERCOFTAC Bullettin no. 24, March 1995, pp. 21-25.

[38] Speziale, C.G., Abid, R., Anderson, E.C., "A Critical Evaluation of Two-Equation Models for Near Wall Turbulence", AIAA paper 90-1481, 1990.

[39] Theodoridis, G. S., Private Communication, Institute for Hydromechanick, University of Karlsruhe, 1995.

[40] Wilcox, D.C., 1988, "Reassessment of the Scale-Determining Equation for Advanced Turbulence Models", AIAA Journal, Vol. 26, No. 11, pp. 1299-1310.

[41] Zhu, J., (1992), "An Introduction and Guide to the Computer Program FAST-3D", Report No. 691, Institute for Hydromechanik, University of Karlsruhe.